Ab initio investigation of hybrid molecular-metallic interfaces as a tool to design surface magnetic properties for molecular spintronics

Rico Friedrich

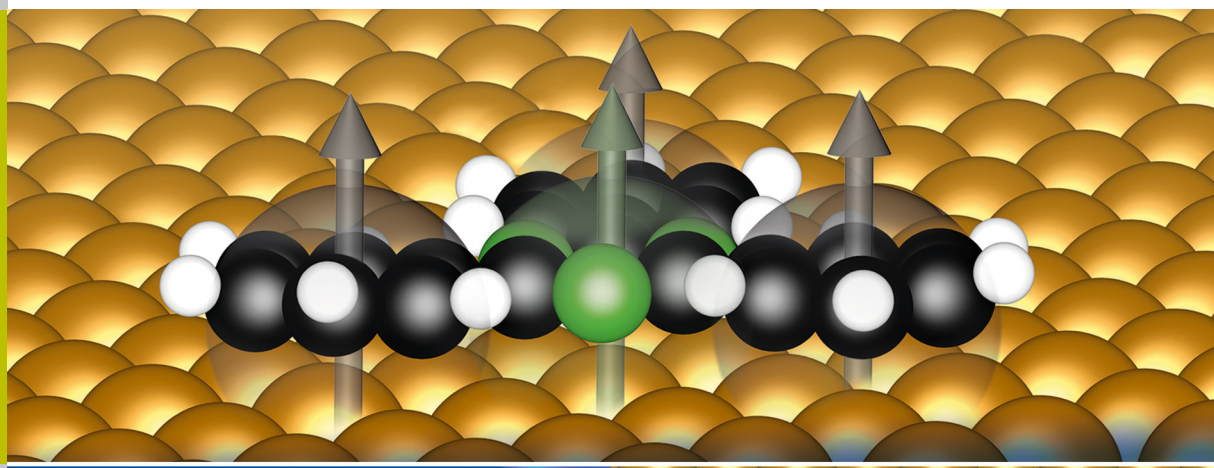

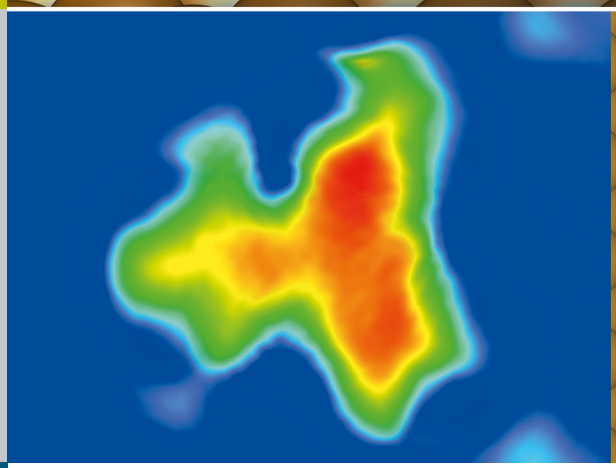

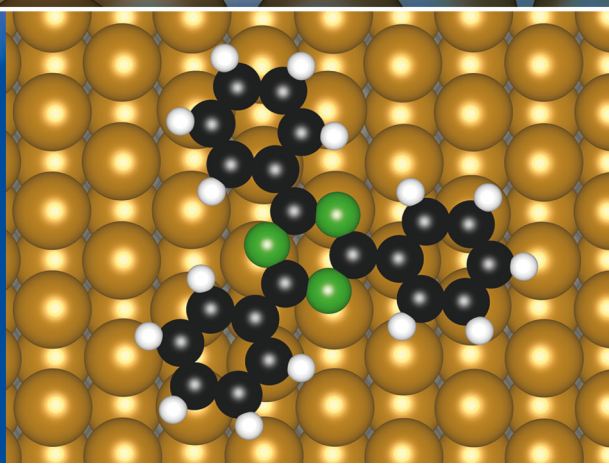

Schlüsseltechnologien /
Key Technologies
Band / Volume 138
ISBN 978-3-95806-194-1

JÜLICH
FORSCHUNGSZENTRUM

Member of the Helmholtz Association

Schriften des Forschungszentrums Jülich
Reihe Schlüsseltechnologien / Key Technologies Band / Volume 138

Forschungszentrum Jülich GmbH
Peter Grünberg Institute (PGI)
Quantum Theory of Materials (PGI-1 / IAS-1)

Ab initio investigation of hybrid molecular-metallic interfaces as a tool to design surface magnetic properties for molecular spintronics

Rico Friedrich

Schriften des Forschungszentrums Jülich
Reihe Schlüsseltechnologien / Key Technologies Band / Volume 138

ISSN 1866-1807 ISBN 978-3-95806-194-1

Bibliographic information published by the Deutsche Nationalbibliothek.
The Deutsche Nationalbibliothek lists this publication in the Deutsche
Nationalbibliografie; detailed bibliographic data are available in the
Internet at http://dnb.d-nb.de.

Publisher and Distributor:	Forschungszentrum Jülich GmbH Zentralbibliothek 52425 Jülich Tel: +49 2461 61-5368 Fax: +49 2461 61-6103 Email: zb-publikation@fz-juelich.de www.fz-juelich.de/zb
Cover Design:	Grafische Medien, Forschungszentrum Jülich GmbH
Printer:	Grafische Medien, Forschungszentrum Jülich GmbH
Copyright:	Forschungszentrum Jülich 2016

Schriften des Forschungszentrums Jülich
Reihe Schlüsseltechnologien / Key Technologies, Band / Volume 138

D 82 (Diss. RWTH Aachen University, 2016)

ISSN 1866-1807
ISBN 978-3-95806-194-1

The complete volume is freely available on the Internet on the Jülicher Open Access Server (JuSER)
at www.fz-juelich.de/zb/openaccess.

Kurzfassung

Die molekulare Spintronik zielt darauf ab, Informationen, die im Elektronenspin kodiert sind, auf der Grundlage von einzelnen, molekülbasierten magnetischen Einheiten zu übertragen und zu speichern. In dieser Arbeit werden die magnetischen Eigenschaften hybrider molekular-metallischer Grenzflächen mit Hilfe der *ab initio* Dichtefunktionaltheorie, der erfolgreichsten Methode zur Berechnung der elektronischen Struktur von Materialien über die letzten Jahrzehnte, untersucht.

Die meiste Forschungstätigkeit in diesem Feld konzentrierte sich bisher auf die magnetischen Eigenschaften des molekularen Anteils der untersuchten Systeme. Hier wird ein komplementärer Ansatz vorgeschlagen, bei dem hybride molekular-metallische Grenzflächen als Instrument zur Einstellung magnetischer Oberflächeneigenschaften benutzt werden. Zuerst werden die beiden Effekte des (i) in-plane magnetic hardening, d. h. die Verstärkung der Austauschkopplung zwischen den magnetischen Zentren der Oberflächenlage unter dem Molekül und des (ii) inter-layer magnetic softening, d. h. die Verringerung der Austauschkopplung zwischen magnetischen Zentren der ersten und zweiten Oberflächenlage lokal unter dem Molekül, im Detail untersucht:

1. Der in-plane magnetic hardening Effekt kann durch einen chemischen Funktionalisierungsprozess selektiv angepasst werden, wie die Untersuchung einer Reihe von π-Elektronensystemen absorbiert auf 1 Monolage Fe/W(110) zeigt, was zu einer spezifischen Einstellung der magnetischen Hysterese-Kurven führt.

2. Der inter-layer magnetic softening Effekt ist allgemein mit einem molekülinduzierten skyhook Mechanismus verknüpft wie durch die Adsorption von Dioxan und Dioxin auf 1 und 2 Monolagen Fe/W(110) demonstriert wird: Eine Ablösung der magnetischen Oberflächenatome der ersten von der zweiten Lage lokal unter dem Molekül wird durch die Abstoßung der peripheren Wasserstoffatome des Moleküls vom Substrat und die gleichzeitige attraktive Wechselwirkung zwischen dem Substrat und dem zentralen Teil des Moleküls hervorgerufen.

3. Räumlich ausgdehnte zweidimensionale π-Elektronensysteme wie Graphen und hexagonales Bornitrid führen zu einem in-plane magnetic hardening auf Co(111), aber verursachen kein inter-layer softening, was zeigt, dass der skyhook Mechanismus ein Charakteristikum finiter molekularer Adsorbate ist.

4. Ein Molekül bestehend aus verschiedenen Ringen wie Triphenyl-triazin kann multiple intramolekulare magnetische Einheiten auf 2 Monolagen Fe/W(110) in einer Einzelmolekül-Oberfläche Hybrid-Struktur induzieren, was einen Ausblick auf molekülbasierte Spin-Logik Elemente eröffnet.

Im Folgenden wird gezeigt, dass das Konzept der molekülinduzierten Modifikation von magnetischen Oberflächeneigenschaften auf Oberflächen-Rashba-Systeme verallgemeinert werden kann:

5. Die Adsorption von chemisch verschiedenen Molekülen auf der $BiAg_2$/Ag(111) Oberfläche erlaubt es, die Spinpolarisation der Oberflächen-Rashba-Zustände von einer Orientierung bevorzugt in der Oberflächenebene zu einer Orientierung senkrecht zu dieser Ebene zu schalten.

Demzufolge etabliert diese Arbeit die Nutzung der Molekül-Adsorption zur systematischen Einstellung von magnetischen Oberflächeneigenschaften als verallgemeinertes neues Konzept in der molekularen Spintronik.

Abstract

Molecular spintronics aims to store and transmit information encoded in the electron spin using single molecular based magnetic units. In this thesis the magnetic properties of hybrid molecular-metallic interfaces are investigated by *ab initio* density functional theory, the most successful electronic structure method over the last decades.

Most of the research in molecular spintronics has been devoted to the magnetic properties of the molecular part of the investigated systems. Here a complementary approach is proposed in which hybrid molecular-metallic interfaces are used as a tool to design surface magnetic properties. Firstly, two effects: (i) in-plane magnetic hardening, i. e. the increase of the exchange coupling between the first layer magnetic surface atoms below the molecule and (ii) inter-layer magnetic softening, i. e. the reduction of the exchange coupling between first and second magnetic surface layer locally below the molecule, are investigated in detail:

1. The in-plane magnetic hardening effect is tuned through a chemical functionalization process by investigating a series of π-bonded molecules adsorbed onto 1 monolayer Fe/W(110) that give rise to specifically tailored magnetic hysteresis curves.

2. The inter-layer magnetic softening effect is generally connected to a molecular induced skyhook mechanism as shown for dioxan and dioxin adsorbed onto 1 and 2 monolayers Fe/W(110): The first layer magnetic atoms below the molecule are locally detached from the second layer due to the repulsion of the peripheral hydrogen atoms of the molecule from the surface and the attraction of the central molecular part to the surface.

3. Spatially extended two-dimensional π-electron systems as graphene and hexagonal boron nitride lead to an in-plane magnetic hardening on Co(111) but do not cause the inter-layer softening revealing that the skyhook mechanism occurs only for finite-size molecular adsorbates.

4. A molecule made up of different rings as triphenyl-triazine can induce multiple intramolecular magnetic units on 2 monolayers Fe/W(110) within a single molecule-surface hybrid system offering prospects for molecular based spin logic devices.

In the following it is demonstrated that the concept of molecular induced manipulation of surface magnetic properties can be generalized to surface Rashba systems:

5. The adsorption of chemically different molecules on the $BiAg_2$/Ag(111) surface allows to switch the spin polarization of the surface Rashba states from predominantly in-plane to out-of-plane.

Hence this thesis establishes molecular adsorption to be employed to systematically tune surface magnetic effects as a generalized novel concept in molecular spintronics research.

‘Ohne den Glauben daran, daß es grundsätzlich möglich ist, die Wirklichkeit durch unsere theoretischen Konstruktionen begreiflich zu machen, ohne den Glauben an die innere Harmonie unserer Welt, könnte es keine Naturwissenschaft geben.’

Albert Einstein

Contents

1 Introduction

The phenomenon of magnetism is known to mankind already since ancient times when it was observed that iron is attracted to the mineral loadstone [1]. It took, however, until the 20th century till it was realized that magnetism is intrinsically a quantum mechanical effect. The observed magnetic moments are due to the intrinsic property of the electron called spin conceptually representing the angular momentum of this particle and being a consequence of relativistic quantum mechanics, i. e. the Dirac equation. At the individual atomic centers the moments eventually arise as a consequence of many-body effects from constraints concerning the filling of the electronic states as the Hund's rules or due to an energy gain coming from the spontaneous spin splitting in band magnets. These effects are predominantly a result of the on-site Coulomb interaction between the electrons at each atomic center.

However, for collective magnetic phases as ferromagnetism, antiferromagnetism and ferrimagnetism to occur, the moments of the individual atoms in a solid need to be coupled. In this sense collective magnetism is a many-body effect since the quantum mechanical exchange interaction communicates this coupling between all the electrons of the solid. This inter-atomic exchange interaction originates from the indistinguishability of the electrons and the Coulomb interaction among them. Hence, when all moments are coupled to align in the same spatial direction, ferromagnetic order can be established.

Nevertheless an additional ingredient is needed which couples the directions of the moments to the lattice potential, i. e. so that particular spatial directions are preferred along which all moments orient. This is provided by the magnetic anisotropy arising from spin-orbit coupling. Consequently, an energy barrier, called anisotropy barrier, is found when jointly tilting away all moments from such a preferred direction. These combined effects lead to the known characteristics of a ferromagnet to exhibit a stable magnetization below a certain critical temperature called Curie temperature and showing hysteretic behavior, i. e. that the magnetic properties of the sample in a certain magnetic field range can depend on its history. The latter feature can be characterized by the field needed to demagnetize a sample when all moments were fully aligned before known as coercive field strength.

Modern research in the field of magnetism is largely motivated by its practical relevance, i. e. for instance by the fact that currently about 90% of all data on earth are stored magnetically [2]. This situation naturally generates the intrinsic quest for the discovery and investigation of magnetic phenomena and their physical understanding to meet the upcoming challenges in the fields of data storage and processing. In this framework the role of *ab initio* methods in solid state physics in general and in magnetism in particular is of special importance. On the one hand quantum-chemical methods based on Hartree-Fock theory and subsequent approaches to include electronic correlations can yield accurate results. Even more

importantly density functional theory has been developed to a level where it is not only able to explain a large number of experimental findings but it also has the power to predict undiscovered quantum phenomena. Especially the field of surface magnetism is currently a heavily investigated research area since, due to the reduced dimensionality on a surface, new physical effects can be expected. Examples for this include the recent discovery of non-collinear magnetic structures at surfaces as spin spirals [3] and nanoskyrmion lattices [4]. *Ab initio* density functional theory has been essential in these cases to outline the competing magnetic interactions which give rise to the formation of the complex magnetic phases. This research is also motivated from an application point of view since magnetic surface structures can offer a favorable spatial scalability of the active magnetic units.

One possible route to advance in the direction of exploiting novel physical effects for application purposes is provided by the research area of spintronics, i. e. to use the intrinsic magnetic moment (spin degree of freedom) of the electron to store and transmit information. The discovery of the giant magnetoresistance effect [5, 6] by Grünberg and Fert in 1988 for which they were awarded the Nobel Prize in physics 2007 can be considered as the major kick-off of this field. This effect, based on the giant resistance change of a layer stack made up of alternating ferromagnetic and nonmagnetic metal films in a magnetic field, has revolutionized the field of data storage. It was developed further [7] and evolved into the standard technology exploited in read heads of hard disks within a record time of about 10 years [1].

The discovery of giant magnetoresistance can be seen as the nucleus of spintronics to evolve as a whole new scientific field pushing forward novel device concepts and measuring magnetoresistances using different types of materials. Alternatively to the nonmagnetic metallic spacer separating the ferromagnetic layers, an insulating material could be used leading to the tunneling magnetoresistance effect [8–10]. In this case even higher magnetoresistance values were observed especially when using MgO based tunneling barriers [11–15]. In addition also research has been devoted to implement spintronic functionalities into devices built from inorganic semiconductors [16, 17].

In particular carbon-based materials are promising in terms of spintronics on the one hand because of the small spin-orbit coupling present in light elements and the weak hyperfine interactions both favoring long spin coherence times [18]. These characteristics hence offer the prospect to transmit the information encoded in spin currents over larger distances as compared to non carbon-based materials. On the other hand especially carbon-based (organic) molecules allow to form atomic-scale hybrid molecule-surface units and give rise to a chemical functionalization of surface magnetic properties [19, 20]. Systematically investigating this latter approach and establishing novel ways to design surface magnetic properties in single molecule-surface hybrid systems is the topic of this thesis.

When focusing on carbon-based spintronics, the field can be subdivided into approaches

dealing with pure carbon structures, using organic thin films or implementing the spintronic functionality into single (organic) molecular based devices. Especially the latter two approaches are highly relevant in the context of this work. In organic thin film devices the volume effects associated with a large number of molecules play an important role for the spintronic properties and this area is therefore termed organic spintronics. Molecular spintronics on the other hand tries to store and transmit the spin information using single molecular based magnetic units being the area where this thesis is assigned to. However in large part the two fields have emerged in parallel and are to a certain degree conceptually interconnected.

In the area of organic spintronics pioneering works have been presented by Dediu and coworkers [21] and Xiong and coworkers [22] demonstrating magnetoresistance in devices where an organic spacer was placed between two ferromagnetic electrodes, so-called organic spin-valves. Moreover, in Refs. [23, 24] it was also reported that magnetic order could be induced into a molecular monolayer deposited onto a ferromagnetic substrate. The first studies using single molecules were mainly theoretically driven [25–32] till later on spin filtering for a single molecule on a ferromagnetic surface was demonstrated by spin-polarized scanning tunneling microscopy [33].

Since these early works the field has evolved and seen important further developments which include the detection of the spin injection efficiency through an organic/ferromagnetic interface and the spin diffusion length in organic materials by new techniques as two-photon photoemission [34] and low-energy muon spin rotation [35]. The first method could later on be used to outline the role of interface states as spin dependent traps [36]. Transport studies through very thin organic films showed long spin relaxation times from milliseconds up to seconds in organic nanowire spin valves [37], room-temperature tunneling magnetoresistance and spin-polarized tunneling through an organic barrier [38] as well as a large spin diffusion length for amorphous rubrene [39]. Moreover, it was demonstrated that organic molecules can invert the surface spin polarization by a $p_z - d$ interaction between molecule and substrate [19, 40] offering the possibility to pattern the spin polarization of the surface on the molecular scale. The importance of the organic-ferromagnetic interface and especially the $p_z - d$ interaction was further highlighted by others [41–43] demonstrating for instance giant magnetoresistance through a single molecule [43]. Also single-molecule magnets were proposed as a possible playground for molecular spintronics in that they directly implement the magnetic functionality on the molecular site [44]. Soon afterwards indeed a supramolecular spin valve was demonstrated for single-molecule magnets anchored to carbon nanotubes [45]. In addition Fe_4 based single-molecule magnets could be attached onto a gold surface without destroying its magnetic properties [46] eventually allowing to detect quantum tunneling of magnetization [47]. Recently, it could be demonstrated that the nuclear spin state of a single-molecule magnet can be read [48] and switched [49] electronically.

However, all these studies concentrated on the molecular part of the investigated structure, i. e. how the electronic and magnetic properties of the molecule are affected. The complementary influence of the molecules onto the underlying substrate attracted less attention. This point of view changed in 2013 when a new approach to manipulate surface magnetic exchange interactions by the adsorption of nonmagnetic molecules was established [50–52]. Specifically, two effects caused by adsorbates containing π-electrons were introduced: (i) in-plane magnetic hardening and (ii) inter-layer magnetic softening. The in-plane magnetic hardening effect describes the enhancement of the magnetic exchange coupling between the first layer magnetic surface atoms below the π-electron system [50, 52]. It was revealed to lead to the formation of strongly exchange coupled magnetic units below (cyclic) molecules and was outlined to give rise to both an enhanced coercive field as well as an increased Curie temperature. On the contrary, the inter-layer magnetic softening effect refers to the weakening of the exchange coupling between the first and second magnetic surface layer below a molecule [51]. This decoupling of the interface magnetic unit from the bulk magnetization was highlighted to cause an experimentally measured interface magnetoresistance effect where the bulk magnetization switches with respect to the interface magnetic layer.

These developments and ideas set the starting point for this thesis. The advancement of this work lies in generalizing these concepts by proposing hybrid molecular-metallic interfaces to be used as a tool to design surface magnetic properties for molecular spintronics. The objectives of this theoretical study are to apply *ab initio* density functional theory on the one hand to systematically bring fundamental understanding to the observed effects at a quantum level. On the other hand it serves to investigate the outreach of this novel approach, i. e. to study whether the concept of tuning surface magnetic properties by the adsorption of nonmagnetic molecules can be generalized beyond a modification of the surface magnetic exchange interaction. More specifically, the investigated issues can be summarized in terms of the following questions: (i) Can the in-plane magnetic hardening effect be tuned by a chemical functionalization of the adsorbed molecule? (ii) What is the mechanism of the inter-layer magnetic softening effect? (iii) What is the effect of extended, two-dimensional π-electron systems such as graphene onto the surface magnetic exchange interactions? (iv) Can the concept be extended to form different magnetic units for logic operations using molecules with different molecular rings? (v) Is it possible to generalize the principle of molecular induced surface manipulation to other surface magnetic properties than exchange?

In order to present the results of this work, this thesis is structured into a first part containing the basics, a second part comprising the results and a third part for the appendix. In the first part important preliminaries on electronic structure theory mainly focusing on density functional theory are presented in Chapter 2, a summary on magnetic interactions is given in Chapter 3 whereas Chapter 4 is devoted to an introduction on molecular spintronics. In

the second part the questions (i) to (v) are addressed in Chapters 5 to 9, respectively and a summary as well as an outlook are presented in Chapter 10. Finally, the appendix includes the computational details in Chapter A and additional results obtained for triphenyl-triazine on 2 monolayers of Co on Cu(111) in Chapter B and for graphene on 1 monolayer Fe or Co on Cu(111) in Chapter C.

Part I.

Basics

2 Survey of Electronic Structure Theory

In this chapter basic ideas and principles of modern electronic structure theory will be reviewed. Firstly, the origin of electronic structure in solids is outlined by starting from the general many-body Hamiltonian of the Schrödinger equation. Subsequently, the Born-Oppenheimer approximation as a fundamental way of explicit decoupling of electronic and nuclear motion on the basis of the large mass difference between electrons and cores is presented. After giving an overview over different approaches to electronic structure, density functional theory (DFT) is introduced. Based on the theorems of Hohenberg and Kohn and the Kohn-Sham equations it is outlined as an in principle exact theory to treat the electronic structure problem. Efficient and at the same time accurate approximations to the exchange correlation functional allow to calculate the properties of real materials from ab initio. In addition the generalization of the theory to spin polarized systems as well as a brief account on selected extensions and recent developments are included. In terms of practical applications of DFT an overview on basis functions, pseudopotentials and the Korringa-Kohn-Rostoker Green's function method is given. Finally, it is emphasized how DFT results can aid as an input for electronic transport calculations.

2.1. The Many-body Problem in Electronic Structure Theory

2.1.1. The Many-body Hamiltonian

The starting point for the exact quantum mechanical treatment of materials was given by the time-independent Schrödinger equation which treats quantization as an eigenvalue problem as introduced by Schrödinger [53] in 1926:

$$\hat{H}\Psi = E\Psi, \tag{2.1}$$

where the Hamiltonian $\hat{H}$ acts on the wave function Ψ describing the state of the system and yields the wave function multiplied by the energy E of the system in this state. According to quantum theory the wave function that solves (2.1) contains all possible information about the time-independent, i. e. stationary states of the system having a well defined energy. For the treatment of time-dependent problems the time-dependent Schrödinger equation needs to be considered [54] although by making use of perturbation theory certain time-dependent properties can be estimated from the stationary states by applying Fermi's Golden rule [54].

For the hydrogen atom containing one electron and one proton the solution of the Schrödinger equation is a standard problem that can be solved rather straightforwardly by separa-

tion of spherical coordinates which leads to an analytical solution [55]. However for a system out of many electrons (e. g. molecules or solids) one has to take into account the interaction between the N_K cores and the N_e electrons giving rise to the general form of the many-body Hamiltonian [56]:

$$H = \underbrace{-\frac{\hbar^2}{2m_e}\sum_i^{N_e}\Delta_i}_{T_e} \underbrace{-\frac{\hbar^2}{2}\sum_K^{N_K}\frac{1}{M_K}\Delta_K}_{T_K} \underbrace{-\sum_{i,K}\frac{Z_K e^2}{|\mathbf{R}_K-\mathbf{r}_i|}}_{V_{e-K}} \underbrace{+\frac{1}{2}\sum_{K,L}\frac{Z_K Z_L e^2}{|\mathbf{R}_K-\mathbf{R}_L|}}_{V_{K-K}} \underbrace{+\frac{1}{2}\sum_{i,j}\frac{e^2}{|\mathbf{r}_i-\mathbf{r}_j|}}_{V_{e-e}}, \tag{2.2}$$

where the first term (T_e) represents the kinetic energy of the electrons (indexed by i), the second term (T_K) the kinetic energy of the nuclei (indexed by K), the third term (V_{e-K}) the attractive interaction between a nucleus at $\mathbf{R}_K$ and an electron at $\mathbf{r}_i$, the fourth term (V_{K-K}) the repulsion between the nuclei and the last term (V_{e-e}) the repulsion between the electrons ($\hbar$ is Planck's constant divided by 2π, m_e is the electron mass, M_K and Z_K are mass and atomic number of nucleus K, e is the elementary charge and the dielectric constant is set to $\varepsilon_0 = \frac{1}{4\pi}$).

To assess the importance of each term in (2.2), the Hamiltonian can be transformed into atomic units which will henceforth be used for all expressions by scaling all distances by one Bohr radius $a_0 = \hbar^2/m_e e^2$, i. e. $\mathbf{r} = a_0\tilde{\mathbf{r}}$ and measuring the energies in units of Hartree $E_{\mathrm{Ha}} = m_e e^4/\hbar^2$. This transforms the Hamiltonian into [56]:

$$H/E_{\mathrm{Ha}} = -\frac{1}{2}\sum_i^{N_e}\frac{\partial^2}{\partial\tilde{\mathbf{r}}_i^2} - \frac{1}{2}\sum_K^{N_K}\frac{m_e}{M_K}\frac{\partial^2}{\partial\tilde{\mathbf{R}}_K^2} - \sum_{i,K}\frac{Z_K}{|\tilde{\mathbf{R}}_K-\tilde{\mathbf{r}}_i|} + \frac{1}{2}\sum_{K,L}\frac{Z_K Z_L}{|\tilde{\mathbf{R}}_K-\tilde{\mathbf{R}}_L|} + \frac{1}{2}\sum_{i,j}\frac{1}{|\tilde{\mathbf{r}}_i-\tilde{\mathbf{r}}_j|}. \tag{2.3}$$

The remarkable point about this expression is that it essentially only depends on the nuclear charges Z_K and the mass ratio m_e/M_K. Hence a theory has been established where one only needs to specify the elements to be treated and any property can at least in principle be calculated by using the Hamiltonian (2.3). The important conclusion from this transformation of the Hamiltonian is that the kinetic energy of the nuclei is small due to the prefactor m_e/M_K which is due to the fact that the proton is about 1836 times heavier than the electron. It is therefore physical to consider the kinetic energy term of the nuclei as a perturbation [57]. The basic idea is hence to assume that the electrons can spontaneously adapt to a change of the nuclear positions and are therefore always in the electronic ground state during the movement of the cores which allows to decouple the electronic motion from the nuclear motion.

2.1.2. The Born-Oppenheimer Approximation

To show this more explicitly the Hamiltonian (2.2) is subdivided [56, 58]:

$$H = H_e + T_K \tag{2.4}$$

$$H_e = T_e + V_{e-K}(\underline{\mathbf{r}},\underline{\mathbf{R}}) + V_{e-e}(\underline{\mathbf{r}}) + V_{K-K}(\underline{\mathbf{R}}), \tag{2.5}$$

where $\underline{\mathbf{r}}$ and $\underline{\mathbf{R}}$ stand for all electronic and nuclear coordinates, respectively. Now it is assumed that a solution to the electronic Schrödinger equation [59]:

$$H_e\Phi_\alpha = E_\alpha^{\mathrm{el}}\Phi_\alpha \tag{2.6}$$

is available with α being a full set of electronic quantum numbers and E^{el} being the total energy of the electronic system. As this is only a differential equation with respect to the electronic coordinates, the electronic wave function depends only parametrically on the nuclear coordinates $\Phi_\alpha = \Phi_\alpha(\underline{\mathbf{r}};\underline{\mathbf{R}})$ and can be calculated for every static arrangement of the nuclei. For each of these arrangements the $\Phi_\alpha(\underline{\mathbf{r}};\underline{\mathbf{R}})$ form a complete set of wave functions. Hence without introducing an approximation the wave function $\Psi(\underline{\mathbf{r}},\underline{\mathbf{R}})$ of the full Hamiltonian (2.2) in (2.1) can be expanded into these electronic wave functions [57]:

$$\Psi(\underline{\mathbf{r}},\underline{\mathbf{R}}) = \sum_\alpha \chi_\alpha(\underline{\mathbf{R}})\Phi_\alpha(\underline{\mathbf{r}};\underline{\mathbf{R}}). \tag{2.7}$$

Inserting this into (2.1) yields:

$$(H-E)\Psi(\underline{\mathbf{r}},\underline{\mathbf{R}}) = \sum_\alpha (H_e + T_K - E)\chi_\alpha(\underline{\mathbf{R}})\Phi_\alpha(\underline{\mathbf{r}};\underline{\mathbf{R}}) = \sum_\alpha (E_\alpha^{\mathrm{el}}(\underline{\mathbf{R}}) + T_K - E)\chi_\alpha(\underline{\mathbf{R}})\Phi_\alpha(\underline{\mathbf{r}};\underline{\mathbf{R}}) = 0. \tag{2.8}$$

Multiplying from the left with $\Phi_\beta^*(\underline{\mathbf{r}};\underline{\mathbf{R}})$ and integrating over all electronic coordinates gives [56]:

$$(T_K + E_\beta^{\mathrm{el}}(\underline{\mathbf{R}}))\chi_\beta(\underline{\mathbf{R}}) + \sum_\alpha A_{\beta,\alpha}(\underline{\mathbf{R}})\chi_\alpha(\underline{\mathbf{R}}) = E\chi_\beta(\underline{\mathbf{R}}) \tag{2.9}$$

where according to the product rule [57]:

$$A_{\beta,\alpha}(\underline{\mathbf{R}}) = -\sum_K \frac{m_e}{2M_K}\int d\underline{\mathbf{r}}\left[\Phi_\beta^*(\underline{\mathbf{r}};\underline{\mathbf{R}})\Delta_K\Phi_\alpha(\underline{\mathbf{r}};\underline{\mathbf{R}}) + 2\Phi_\beta^*(\underline{\mathbf{r}};\underline{\mathbf{R}})\nabla_K\Phi_\alpha(\underline{\mathbf{r}};\underline{\mathbf{R}})\nabla_K\right]. \tag{2.10}$$

The Born-Oppenheimer approximation [60] is now to neglect the term $A_{\beta,\alpha}(\underline{\mathbf{R}})$ which accounts for transitions between electronic states due to nuclear motion, i. e. the coupling of electronic and nuclear motion[1]. This results in a Schrödinger equation for the nuclear wave

[1] However a fine difference between the adiabatic and the Born-Oppenheimer approximation is that in the adiabatic approximation the diagonal terms of (2.10) are still included although they are neglected in case

function $\chi_\beta(\underline{\mathbf{R}})$ [55]:

$$(T_K + E_\beta^{\mathrm{el}}(\underline{\mathbf{R}}))\chi_\beta(\underline{\mathbf{R}}) = E\chi_\beta(\underline{\mathbf{R}}). \tag{2.11}$$

Here the energy of the electronic system $E_\beta^{\mathrm{el}}(\underline{\mathbf{R}})$ acts as a potential on the nuclear states. In other words, the electronic energy forms a potential energy landscape on which the nuclei move [59]. This equation incorporates the full quantum nature of the nuclear motion and its solution would yield energy levels for vibrations and rotations [59]. However in most practical calculations one treats the nuclei essentially as classical objects and forces on the nuclei $\mathbf{F}_K$ for geometry optimizations can be obtained from the Hellman-Feynman theorem [57, 61–63]:

$$\mathbf{F}_K = -\frac{\partial E_\alpha^{\mathrm{el}}}{\partial \mathbf{R}_K} = -\int d^3r\, n(\mathbf{r})\frac{\partial v_{e-K}(\mathbf{r},\mathbf{R}_K)}{\partial \mathbf{R}_K} - \frac{\partial V_{K-K}(\mathbf{R}_K)}{\partial \mathbf{R}_K}, \tag{2.12}$$

where $n(\mathbf{r})$ is the electron density and $V_{e-K} = \sum_i v_{e-K}(\mathbf{r}_i,\mathbf{R}_K) = -\sum_{i,K}\frac{Z_K}{|\mathbf{R}_K-\mathbf{r}_i|}$.

The Born-Oppenheimer approximation turns out to be a very good approximation in most practical situations and leads to an accurate description of most systems. However it does not hold any more when different potential energy landscapes come very close or cross or when more than one electronic surface is involved as in photochemical reactions [55–57, 59]. Nevertheless it is often valid for the electronic ground state [58]. An example where the approximation becomes poor is in case of the dissociation of LiF [59]. At the equilibrium distance the ground state of the system has mainly ionic character (Li^+F^-) but it dissociates into two neutral atoms (Li· F·). The transition between the two electronic states occurs within a short distance range of the bond length for which consequently the Born-Oppenheimer approximation breaks down [59].

On the basis of the Born-Oppenheimer approximation the electronic structure problem reduces to the electronic Schrödinger Equation (2.6) with the Hamiltonian (2.5). However this problem is not exactly solvable essentially due to the electron-electron interaction V_{e-e}. This term incorporates all the many-body effects of the problem which are namely exchange and correlation [64]. The exchange interaction is a consequence of the indistinguishability of elementary particles [55] and lies at the heart of magnetism [57]. The electron correlation is due to the fact that the state of one electron depends on the position of all other electrons in the system. More clearly speaking, a change of the state of one electron at one point in space immediately causes a reaction of all other electrons acting back on the initial change. This complex behavior poses the hardest problem for electronic structure theory [57] and is the reason why no exact solution is possible. It eventually leads to the breakdown of the orbital picture [59] since an electron cannot be assigned to a single state any more. The whole system is, due to these many-body effects, more than just the sum of its parts, or as Anderson has put it: 'More Is Different' [65].

of the Born-Oppenheimer approximation [59]. Nevertheless it can be shown that the contribution of these diagonal terms is small and is essentially connected to the mass ratio m_e/M_K [57, 59].

2.1.3. Approaches to Electronic Structure

During the last century several methods have been developed both from the physical and the chemical side to treat the electronic structure problem (2.6) with different degrees of accuracy. These approaches can mainly be categorized into wave function based methods and density based methods. The starting point of all wave function methods is Hartree-Fock (HF) theory [66, 67] later on simplified by Slater [68][2]. This theory solves the electronic Schrödinger equation within a mean field approach as it optimizes the orbital for each electron in the static field of all other electrons [59]. Thereby it fully takes into account exchange but completely neglects correlations [61]. Within a practical scheme it tries to find the best description of the electronic ground state by using a single Slater determinant[3]. The main weakness of HF theory is the neglect of the electron correlations. Although this energy contribution is much smaller than all other contributions to the total energy, it can be of great importance. For instance without taking into account correlation the F_2 molecule would not be stable [55].

In order to systematically improve on HF results the main strategy of quantum chemical methods is to take the HF results as a reference for more elaborate and at the same time numerically much more expensive techniques. Among these are Configuration Interaction (CI), Møller-Plesset perturbation theory (e. g. MP2), Coupled Cluster (CC) or Quantum Monte Carlo (QMC) that try to estimate the correlation contribution by taking into account more electronic configurations based on the HF orbitals [55, 59]. Furthermore it can also be of importance to start the initial calculation with more than one determinant which leads to multi-configuration self-consistent-field (MCSCF) approaches which is e. g. necessary for systems with degenerate states [55]. Although these methods demand great computational resources, their main advantage is that they form a strictly hierarchical structure which can be utilized to systematically improve the results towards an exact solution [59].

Alternatively to the wave function based methods, a density based theory as DFT can provide a shortcut both conceptually as well as in terms of performance since the electron density $n(\mathbf{r})$ depends only on three spatial coordinates whereas the all-electron wave function would depend on $3N_e$ spatial coordinates [64]. From this perspective a density based scheme can make computations much more efficient. However the main challenge of the electronic structure problem is then shifted to finding appropriate approximate functional expressions for the energy contributions in the Hamiltonian (2.5) in terms of the density.

A further advantage of the DFT formalism is that it shortens the quantum chemical procedure of first performing a HF calculation and then a post-HF scheme on top as according to the theoretical foundations both exchange and correlation are included in the functional

[2] Remarkably, the so-called X_α-approach resulting from this suggestion of Slater fits into the frame of DFT [61].
[3] A Slater determinant is an antisymmetrized product of single particle wave functions [55].

$E_{xc}[n]$ right from the beginning [61]. For many practical cases DFT is at least as fast as HF theory and provides at the same time more accurate results. This is one of the major reasons why DFT has become the standard method of computational solid state physics and quantum chemistry [59, 69, 70] and it is in the spirit of Dirac who demanded that for performing actual calculations 'approximate practical methods' [71] need to be developed.

A further remarkable point for a density based theory was given by Kohn [72] by arguing that the density is a much better key variable than the all-electron wave function for large systems. His argument, which will be sketched in a slightly modified form here, is based on the finding that the electronic wave function Φ is never known exactly due to physical approximations or numerical inaccuracies. What can be calculated is only an approximate wave function $\tilde{\Phi}$. One might now consider the guess accurate if:

$$|\langle\tilde{\Phi}|\Phi\rangle| \gg 0.5. \tag{2.13}$$

Let now ϕ be the accurate single electron wave function for one electron of a many electron system. This wave function can only be estimated by a $\tilde{\phi}$ with finite accuracy, say:

$$|\langle\tilde{\phi}|\phi\rangle| = 1-\epsilon \quad \text{where} \quad \epsilon = 10^{-2}. \tag{2.14}$$

Let's now assume that the system consists of $N_e = 100$ electrons. Due to the antisymmetrized product structure of a Slater determinant ansatz to the all-electron wave function this leads to:

$$|\langle\tilde{\Phi}|\Phi\rangle| = (1-\epsilon)^{N_e} \approx e^{-N_e\epsilon} \approx e^{-1} \approx 0.37, \tag{2.15}$$

not any more fulfilling the accuracy criterion (2.13). Although the accuracy values in Equations (2.13) and (2.14) were chosen arbitrarily, this reasoning essentially outlines that smallest errors in the single particle states potentiate to large errors in the all-electron wave function for large systems denoted by Kohn as an 'exponential wall'[72]. A drastic formulation of this result is: 'the many-electron wave function $\Psi(r_1,\ldots,r_N)$ for a system of N electrons is not a legitimate scientific concept, when $N \geq N_0$' [72], where N_0 depends on the specific approach[4]. DFT is at least in principle able to circumvent this issue. Based on these arguments an explicit account on the DFT method will be presented in the next section as it forms the theoretical foundation of this thesis.

[4] Nevertheless Kohn himself admitted that from certain 'bad' wave functions good results for observables might still be computed [72].

2.2. Density Functional Theory

This section will give an overview of the DFT formalism. A special focus will be put on the key theorems of Hohenberg and Kohn [73] setting a strict justification of the theory and on the Kohn-Sham equations [74] making the approach useful in practice. Also some standard approximations for the exchange-correlation functional will be shortly described.

2.2.1. The Thomas-Fermi Approach

The first approach for calculating properties of matter from a density based theory was introduced by Thomas [75] and Fermi [76] in 1927. The basic challenge of this ansatz was to find an energy functional in terms of the electron density, i. e. to express the energy contributions T_e, V_{e-K} and V_{e-e} of the Hamiltonian (2.5) in terms of the density. Easily, the energy contribution $V_{e-K}[n]$ that comes from the external potential $v_{e-K}(\mathbf{r}) = -\sum_K \frac{Z_K}{|\mathbf{r}-\mathbf{R_K}|}$ is expressed as [61]:

$$V_{e-K}[n] = \int d^3r\, n(\mathbf{r})\, v_{e-K}(\mathbf{r}). \tag{2.16}$$

However the kinetic energy contribution $T_e[n]$ is already much harder to express in terms of the density. Within Thomas-Fermi (TF) theory $T_e[n]$ is approximated by locally taking the kinetic energy density $t^{\text{hom}}(n(\mathbf{r})) = \frac{3}{10}(3\pi^2)^{\frac{2}{3}} n(\mathbf{r})^{\frac{5}{3}}$ [61] of a homogeneous interaction-free electron gas (local density approximation (LDA)) and integrating over all space to obtain the kinetic energy [64]:

$$T_e[n] \approx T_{\text{s}}^{\text{LDA}}[n] = \int d^3r\, t^{\text{hom}}(n(\mathbf{r})), \tag{2.17}$$

where the index 's' stands for 'single particle' since the term comes from a theory of independent particles. The electron-electron interaction energy $V_{e-e}[n]$ is approximated by the Hartree energy [61]:

$$V_{e-e}[n] \approx V_{\text{H}}[n] = \frac{1}{2}\int d^3r \int d^3r'\, \frac{n(\mathbf{r})\, n(\mathbf{r}')}{|\mathbf{r}-\mathbf{r}'|}. \tag{2.18}$$

These terms can be summarized to the TF energy functional $E_{\text{TF}}^{\text{el}}[n]$ [64]:

$$E^{\text{el}}[n] = T_e[n] + V_{e-K}[n] + V_{e-e}[n] \approx T_{\text{s}}^{\text{LDA}}[n] + V_{e-K}[n] + V_{\text{H}}[n] = E_{\text{TF}}^{\text{el}}[n]. \tag{2.19}$$

The variation of this expression with respect to the density $\frac{\delta E_{\text{TF}}^{\text{el}}}{\delta n}$ and the introduction of a Lagrange multiplier λ that keeps track of charge conservation ($N_e = \int d^3r\, n(\mathbf{r})$) leads to the TF equation [61]:

$$\frac{5}{3}\frac{3}{10}(3\pi^2)^{\frac{2}{3}} n(\mathbf{r})^{\frac{2}{3}} + v_{e-K}(\mathbf{r}) + \int d^3r'\, \frac{n(\mathbf{r}')}{|\mathbf{r}-\mathbf{r}'|} + \lambda = 0. \tag{2.20}$$

Later on Dirac suggested [77] to add a correction term to the TF energy functional that appro-

ximately accounts for the exchange interaction $W_x[n]$ by locally applying the exchange energy density of a homogeneous electron liquid [61]:

$$W_x[n] \approx -\frac{3}{4}\left(\frac{3}{\pi}\right)^{\frac{1}{3}} \int d^3r\, n^{\frac{4}{3}}(\mathbf{r}). \tag{2.21}$$

However to this end the TF theory still completely neglects correlation effects. Nevertheless TF theory is a well defined mathematical model, gives reasonable total energies for atoms and is exact in the limit of large atomic numbers $Z \to \infty$ [61, 70, 72]. On the other hand it has serious shortcomings in that atoms do not bind to form molecules or solids, no shell structure for atoms occurs and atoms shrink for increasing atomic numbers [61, 64, 78]. It also turned out that the correction term (2.21) does not improve the results [61]. The major defect of TF theory is due to the bad description of the kinetic energy in Equation (2.17) [61]. The great achievement of Kohn and Sham described later on was to find a substantially better expression for this energy contribution.

2.2.2. The Hohenberg-Kohn Theorems

Remarkably, already Dirac noted in 1930 that 'the whole state of the atom is completely determined by this electric density; it is not necessary to specify the individual three-dimensional wave functions that make up the total electric density' [77]. The formal proof of this statement now called the first Hohenberg-Kohn (HK) theorem was however only given 34 years later by Hohenberg and Kohn who showed by *reductivo ad absurdum* that the electron density $n(\mathbf{r})$ determines the external potential $v_{e-K}(\mathbf{r})$ uniquely up to an arbitrary constant, i. e. there can be no two external potentials that yield the same ground state density $n_0(\mathbf{r})$ [73].

The proof of Hohenberg and Kohn is based on the assumption that two external potentials $v^1_{e-K}(\mathbf{r})$ and $v^2_{e-K}(\mathbf{r})$ exist that lead to the same density and subsequently showing that this leads to a contradiction based on the Rayleigh-Ritz minimal principle [72]. In conclusion, the quantum mechanical treatment of materials in terms of the electron density is completely appropriate. In this sense the electron density is a fully sophisticated variable incorporating all possible information about the system at least for the ground state [5].

By specifying the external potential, also the many-body Hamiltonian of Equation (2.6) is specified and thereby the ground state density determines the many-body wave function[6]. Hence the ground state wave function $\Phi_0(\mathbf{r}_1, \mathbf{r}_2 \ldots, \mathbf{r}_N)$ is a unique functional of the ground

[5] It is however important to realize that although the density depends only on three spatial variables and the ground state wave function depends on $3N_e$, no information is lost as the ground state wave function has to reproduce the ground state density *and* minimize the energy [64].

[6] Consequently, also excited states of the system are in principle determined by n_0 [64].

state density [64]:

$$\Phi_0(\mathbf{r}_1, \mathbf{r}_2 \ldots, \mathbf{r}_N) = \Phi_0[n_0(\mathbf{r})]. \tag{2.22}$$

Consequently, also the expectation value of any ground state observable is a unique functional of $n_0(\mathbf{r})$ [64] which especially holds for the ground state total energy of the system:

$$E_0^{\mathrm{el}} = E_0^{\mathrm{el}}[n_0]. \tag{2.23}$$

Even more importantly, Hohenberg and Kohn were able to show that there exists a variational principle for the total energy in terms of the density[72, 73]:

$$E_0^{\mathrm{el}}[n_0] \leq E^{\mathrm{el}}[n'], \tag{2.24}$$

i. e. the energy evaluated from the ground state density is a lower bound for the energy evaluated from any other density with a possible equality in case of degeneracy. The proof is based on the variational principle for the many-body wave function that is a functional of the ground state density according to Equation (2.22) [72]. It is a very valuable property for practical applications of DFT and is therefore called the second HK theorem.

The HK energy functional can now be written in the following form [61]:

$$E_{\mathrm{HK}}^{\mathrm{el}}[n] = T_e[n] + V_{e-e}[n] + V_{e-K}[n] := F[n] + V_{e-K}[n], \tag{2.25}$$

where the internal-energy functional $F[n]$ incorporates the kinetic and interaction energy contributions of the electronic system and is a universal functional, i. e. it is the same for any system [64]. On the other hand the system specific contribution $V_{e-K}[n]$ is given in terms of the density by Equation (2.16). The minimization of the functional has to be done under the constraint that the number of electrons in the system is equal to N_e by using a Lagrange multiplier. In order for this scheme to work, the energy contributions in Equation (2.25) have to be expressed appropriately in terms of the density.

2.2.3. The Kohn-Sham Equations

The significant contribution of Kohn and Sham in 1965 was the way they accounted for the energy contributions in Equation (2.25) and reformulated the many-body problem into a single-particle problem including in principle all interactions of the real system [74]. It forms the basis for most of the practical implementations of DFT into scientific computer programs.

As pointed out in Subsection 2.2.1 the main defect of TF theory lies in the approximation of the kinetic energy contribution in terms of the local treatment as a homogeneous electron gas. Kohn and Sham pointed out that the problem of expressing the kinetic energy of the electron

system $T_e[n]$ directly in terms of the density could be avoided by expressing it in terms of auxiliary single particle wave functions $\phi_i(\mathbf{r})$ of non-interacting electrons [57]:

$$T_\mathrm{s}[\{\phi_i[n]\}] = -\frac{1}{2}\sum_i^{N_e}\int d^3r\,\phi_i^*(\mathbf{r})\Delta\phi_i(\mathbf{r}), \tag{2.26}$$

where the index 's' represents once again 'single particle' and the expression is an indirect density functional as the orbitals of this non-interacting system depend on the ground state density. The full kinetic energy of the interacting system is then given by the sum of Equation (2.26) and a correction $T_\mathrm{c}[n]$ due to correlation effects [7] [64]:

$$T_e[n] = T_\mathrm{s}[\{\phi_i[n]\}] + T_\mathrm{c}[n]. \tag{2.27}$$

With the usage of this construction the total energy of the electronic system is now expressed by the Kohn-Sham (KS) energy functional as [61]:

$$E_\mathrm{KS}^\mathrm{el}[n] = T_e[n] + V_{e-K}[n] + V_{e-e}[n] = T_\mathrm{s}[\{\phi_i[n]\}] + V_{e-K}[n] + V_\mathrm{H}[n] + E_{xc}[n]. \tag{2.28}$$

This energy functional defines the exchange-correlation functional $E_{xc}[n]$ which includes both the difference between the kinetic energy of the interacting and the non-interacting system $T_\mathrm{c} = T_e - T_\mathrm{s}$ and the exchange and correlation contributions to the electron-electron interaction $W_{xc} = V_{e-e} - V_\mathrm{H}$. One can thus say that the complications of the many-body system have been shifted into the unknown functional $E_{xc}[n]$ for which up to the present day no exact expression is known and it needs to be approximated for practical purposes. A major reason for the success of DFT is the finding that for most practical applications simple approximations to $E_{xc}[n]$ are accurate enough to obtain a reliable treatment of the system [64].

In order to obtain the ground state, the KS energy functional (2.28) has to be minimized in terms of the density: $0 = \frac{\delta E_\mathrm{KS}^\mathrm{el}[n]}{\delta n(\mathbf{r})}$, which has to be done indirectly for $T_\mathrm{s}[\{\phi_i[n]\}]$. The conservation of the total electron number N_e is taken into account by a Lagrange multiplier ε. This leads to a Schrödinger-like equation for the eigenstates $\phi_i(\mathbf{r})$ of the auxiliary system [72]:

$$\left[-\frac{1}{2}\Delta + v_\mathrm{s}(\mathbf{r})\right]\phi_i(\mathbf{r}) = \varepsilon_i\,\phi_i(\mathbf{r}). \tag{2.29}$$

The effective potential $v_\mathrm{s}(\mathbf{r})$ includes all potential contributions of the interacting system [57]:

$$v_\mathrm{s}(\mathbf{r}) = v_{e-K}(\mathbf{r}) + v_\mathrm{H}(\mathbf{r}) + v_{xc}(\mathbf{r}), \tag{2.30}$$

[7] Exchange contributions are fully accounted for by a Slater determinant ansatz for the all-electron wave function (of the auxiliary electron system) in practical schemes [64].

where $v_{\mathrm{H}}(\mathbf{r}) = \frac{\delta V_{\mathrm{H}}[n]}{\delta n(\mathbf{r})} = \int d^3r' \frac{n(\mathbf{r}')}{|\mathbf{r}-\mathbf{r}'|}$ is the Hartree potential and $v_{xc}(\mathbf{r}) = \frac{\delta E_{xc}[n]}{\delta n(\mathbf{r})}$ is the exchange-correlation potential. By introducing this effective external potential Kohn and Sham transformed the interacting many-body problem into a non-interacting single-particle problem with potential v_{s}. This reformulation guarantees that the solution of the auxiliary single-particle problem reproduces the density of the real system by summing over all states [64]:

$$n(\mathbf{r}) = \sum_i f_i |\phi_i(\mathbf{r})|^2, \tag{2.31}$$

with f_i indicating the occupation of the i'th orbital.

The three Equations (2.29), (2.30) and (2.31) are the so-called KS equations. They form a nonlinear system of equations as the operator of Equation (2.29) depends on the density itself and therefore they need to be solved self-consistently. Because of this, Equation (2.29) is not a real Schrödinger equation since a linear operator would be required in this case. This nonlinearity of the KS equations complicates their solution also in the sense that they cannot be solved directly in the spirit of the Banach fixed-point theorem by taking the solutions of Equation (2.29) directly to calculate the new potential. Instead mixing schemes have been developed that mix old and new densities (or potentials) to obtain a self-consistent solution [57, 79–82].

The ground state total energy of the system according to the KS formalism is then given by [72]:

$$E_0^{\mathrm{el}}[n] = \sum_i^{N_e} \varepsilon_i - \frac{1}{2} \int d^3r\, d^3r' \, \frac{n_0(\mathbf{r})\, n_0(\mathbf{r}')}{|\mathbf{r}-\mathbf{r}'|} - \int d^3r\, v_{xc}(\mathbf{r})\, n_0(\mathbf{r}) + E_{xc}[n_0]. \tag{2.32}$$

Obviously, it is not simply the sum of the orbital energies ε_i of the auxiliary system. In order to account for the interactions present in the real system it has to include similar as in the HF formalism [55] correction terms that account for the double counting of the electron-electron interaction. Owing to this fact, the eigenvalues calculated from Equation (2.29) have no direct physical meaning as they are calculated from an auxiliary single-particle problem that in principle only has the task to reproduce the correct density according to Equation (2.31). However an important exception to this is the highest occupied KS eigenvalue which gives the correct ionization potential I of the system $\varepsilon_{N_e}(N_e) = -I$ [83]. Accordingly, the electron affinity can be calculated as the highest occupied eigenvalue of the N_e+1 system [64]. For all other eigenvalues no such relation holds but experience shows that in many practical cases the eigenstates and eigenvalues give a remarkably good description of the electronic structure of the system [64, 84–86]. This is especially exploited in electronic band structure calculations [57] and can even be rationalized if DFT is considered as a mean field theory and comparing it with other self-consistent equations of many-body physics as the HF equation or Dyson's equation [64]. When arguing along this line one should note that DFT calculations typically underestimate

the band gap in solids or the energy gap between highest occupied molecular orbital (HOMO) and lowest unoccupied molecular orbital (LUMO) in molecular systems which is due to the so-called derivative discontinuity introduced below and has become known as the 'band-gap problem' of DFT [57, 64, 87]. In extreme cases it can even lead to the finding that semiconductors are predicted to be metals as in case of germanium [57]. In addition, the KS eigenvalues and eigenfunctions can also be used as a starting point for perturbation expressions to evaluate excitation energies [57].

2.2.4. Approaches to the Exchange-correlation Functional

The exchange-correlation functional $E_{xc}[n]$ of Equation (2.28) is a very complicated object as it includes by definition all the many-body effects of the problem. The usefulness of DFT in practice is largely based on the fact that the energy contribution due to that functional is rather small and that simple and efficient approximations allow for an accurate description of many systems. It is these approximations where now physics enters the formally mathematical theory of Hohenberg, Kohn and Sham [72]. After outlining some known exact properties of the functional, an overview of selected approaches to $E_{xc}[n]$ and some recent developments to include dispersion forces and van der Waals interactions will be given.

Some Exact Properties

Although the exact exchange-correlation functional of KS DFT is unknown, some exact relations for this functional have been found. One of the most important concepts in this regard is the so-called exchange-correlation hole $n_{xc}(\mathbf{r},\mathbf{r}')$. It expresses the effect that the presence of one electron at $\mathbf{r}$ reduces the probability to encounter another electron at $\mathbf{r}'$ due to exchange and correlation, i. e. the electron at $\mathbf{r}$ digs a hole in the probability of another electron at $\mathbf{r}'$. This xc-hole can be defined in terms of a Hartree-like interaction with the density [61]:

$$E_{xc}[n] = \frac{1}{2}\int d^3r \int d^3r' \frac{n(\mathbf{r})\, n_{xc}(\mathbf{r},\mathbf{r}')}{|\mathbf{r}-\mathbf{r}'|}. \tag{2.33}$$

An important property of this xc-hole is that it satisfies the sum rule[8] [72]:

$$\int d^3r'\, n_{xc}(\mathbf{r},\mathbf{r}') = -1, \tag{2.34}$$

which means that exactly one electron is missed in the exchange-correlation hole independent of the position $\mathbf{r}$ [61].

[8] The xc-hole can be divided into an exchange hole and a correlation hole $n_{xc}(\mathbf{r},\mathbf{r}') = n_x(\mathbf{r},\mathbf{r}') + n_c(\mathbf{r},\mathbf{r}')$ for which the exchange hole integrates to -1 and the correlation hole to 0 [64].

A further important relation is given by the one-electron limit [64]:

$$E_c[n^{(1)}] \equiv 0 \tag{2.35}$$

$$E_x[n^{(1)}] \equiv -V_{\mathrm{H}}[n^{(1)}], \tag{2.36}$$

where $n^{(1)}$ is the one-electron density. These relations avoid the self-interaction of an electron with itself.

Moreover there are also general boundaries for the correct functional. The upper bound is given by the TF theory which completely neglects exchange and correlation:

$$E_{xc}[n] \leq E_x[n] \leq 0. \tag{2.37}$$

A lower limit is set by the Lieb-Oxford bound [64]:

$$E_x[n] \geq E_{xc}[n] \geq -1.68 \int d^3r\, n(\mathbf{r})^{\frac{4}{3}}. \tag{2.38}$$

A property of the xc-functional which is extremely hard to describe is its derivative discontinuity with respect to the total electron number [64, 87]:

$$\left.\frac{\delta E_{xc}[n]}{\delta n(\mathbf{r})}\right|_{N_e+\delta} - \left.\frac{\delta E_{xc}[n]}{\delta n(\mathbf{r})}\right|_{N_e-\delta} = \Delta_{xc}, \tag{2.39}$$

where δ stands for an infinitesimal change of the electron number. As many standard functionals neglect this discontinuity, they underestimate the fundamental (many-body) gap of the system Δ_{MB} as mentioned above since [64]:

$$\Delta_{\mathrm{MB}} = \Delta_{\mathrm{KS}} + \Delta_{xc}, \tag{2.40}$$

where Δ_{KS} is the energy difference between highest occupied and lowest unoccupied state of the KS system, i. e. the KS gap.

In physics related approaches these and many other exact properties act as constraints during the construction of new functionals. In chemistry new functionals are often obtained by fitting the results for special test sets of molecules to even more accurate quantum chemical calculations[64].

The Local Density Approximation

The local density approximation (LDA) was historically the first approach to deal with $E_{xc}[n]$ in practice and was already introduced by Kohn and Sham [74]. Conceptually similar to TF theory, within this ansatz the system is considered as being locally homogeneous by integra-

ting over the exchange-correlation energy density $\epsilon_{xc}^{\mathrm{LDA}}(n(\mathbf{r}))$ of a homogeneous electron liquid [64]:

$$E_{xc}^{\mathrm{LDA}}[n] = \int d^3r\, \epsilon_{xc}^{\mathrm{LDA}}(n(\mathbf{r})). \tag{2.41}$$

As already described in Subsection 2.2.1 the exchange energy of the homogeneous electron liquid can be calculated exactly by Equation (2.21) and was suggested by Dirac [77] as a correction term to the TF theory. Thus the LDA exchange energy reads:

$$E_{x}^{\mathrm{LDA}}[n] = -\frac{3}{4}\left(\frac{3}{\pi}\right)^{\frac{1}{3}} \int d^3r\, n(\mathbf{r})^{\frac{4}{3}}. \tag{2.42}$$

As the correlation energy of the homogeneous electron liquid is not known exactly, it is usually included via parametrization of accurate QMC calculations [64]. Despite of the relatively simple conceptual construction, the LDA approach works remarkably well for many systems [57] and particularly yields bond lengths with only about 1% error [72]. The success of LDA accurately describing even in part inhomogeneous electron systems was later shown to be due to the fact that the LDA exchange-correlation hole fulfills the exact sum rule Equation (2.34) and that the exchange-correlation energy depends on the isotropic part of the exchange-correlation hole only [61, 70, 88–90]. Nevertheless often bonding distances are underestimated by LDA (overbinding) and especially for very inhomogeneous and correlated electron systems the method usually fails [57]. One of the most severe failures of LDA is that within spin-polarized DFT it predicts iron to have a nonmagnetic hcp structure in the ground state [91].

The Generalized Gradient Approximation

In order to improve on the LDA results and to make the method applicable to a broader range of materials, a systematic gradient expansion of the exchange-correlation functional was investigated [64]. The approach was driven by the idea that not only the density at a given point $\mathbf{r}$ in space as exploited by LDA might be important but also the rate of change of the density, i. e. its gradient $\nabla n(\mathbf{r})$. The systematic inclusion of gradient corrections termed 'generalized gradient expansion' turned out to be less useful as it often worsened LDA results since the real density gradients in materials are usually large [57, 64, 70]. However a major improvement of the results could be obtained if not a power-series in terms of the density gradient is used but a more general function $f(n(\mathbf{r}), \nabla n(\mathbf{r}))$ of the density and an 'effective' gradient which is constrained by the exact properties mentioned at the beginning of this subsection [64]:

$$E_{xc}^{\mathrm{GGA}}[n] = \int d^3r\, f(n(\mathbf{r}), \nabla n(\mathbf{r})). \tag{2.43}$$

This ansatz gives rise to the so-called generalized gradient approximation (GGA) which due to the freedom in the function f represents a large class of functionals. Because of their dependence on the gradient, these functionals are termed semilocal. A frequently used example of a GGA functional is the one developed by Perdew, Burke and Ernzerhof (PBE) in which all parameters are fundamental constants [92]. This functional has been used to obtain most of the results of this thesis. In general GGAs provide reliable results for nearly all types of chemical bonds and give reliable structures [57, 64]. However sometimes GGAs overcorrect the bond lengths of the LDA approach yielding too long bond lengths (underbinding) [92]. An interaction type that cannot be described by the GGA are van der Waals interactions [64].

The LDA+U Approach

The aforementioned LDA and GGA approaches tend to have problems treating systems with localized and strongly interacting electrons such as in transition metal oxides or rare-earth metals [57]. In such systems for instance metal-insulator transitions can occur. It has therefore been tried to incorporate the relevant strong correlation effects into the functional by simple means. For this purpose the LDA+U approach accounts for LDA or GGA type calculations into which an additional orbital-dependent interaction is introduced [57]. This additional interaction is then only applied onto highly localized atomic orbitals, i. e. a Hubbard 'U' term is added onto a correlated l shell as for example d or f states. The LDA+U total energy functional can be expressed as [93]:

$$E^{\mathrm{LDA}+U}[n,\{n_i\}] = E^{\mathrm{LDA}}[n] + \frac{1}{2}U\sum_{i\neq j} n_i n_j - \frac{U(N_e^{\mathrm{ss}}-1)N_e^{\mathrm{ss}}}{2}, \tag{2.44}$$

where n_i is the occupation number of orbital i and $N_e^{\mathrm{ss}} = \sum_i n_i$ is the number of electrons in the correlated subspace. The last term is a double counting correction as it subtracts the total Coulomb energy within the subspace that is also accounted for in $E^{\mathrm{LDA}}[n]$. This functional then shifts the orbital energies $\varepsilon_i^{\mathrm{LDA}}$ of the correlated subspace with respect to the other orbitals and induces a (stronger) splitting between occupied and unoccupied states [93]:

$$\varepsilon_i = \frac{\partial E^{\mathrm{LDA}+U}}{\partial n_i} = \varepsilon_i^{\mathrm{LDA}} + U\left(\frac{1}{2} - n_i\right). \tag{2.45}$$

The induced splitting can be used to correct the calculated gap of the system [57]. It should however be noted that the resulting orbitals are correlated model orbitals and not KS orbitals any more [61]. Within this scheme an adjustable parameter is introduced into the calculations but it can also be obtained from 'constrained density functional' calculations [57].

Orbital Functionals and Nonlocal Approximations

For further improvement of the approximations to $E_{xc}[n]$ orbital dependent quantities as for instance the kinetic energy density $\tau(\mathbf{r})$:

$$\tau(\mathbf{r}) = \frac{1}{2}\sum_i |\nabla\phi_i(\mathbf{r})|^2 \tag{2.46}$$

were included into the functional development to obtain so-called meta-GGAs [64]. These functionals are in principle able to improve upon GGA results [70].

Moreover the calculation of exact exchange from the Kohn-Sham states by means of the Fock-term:

$$E_x[\{\phi_i[n]\}] = -\frac{1}{2}\sum_{j,k}\int d^3r \int d^3r' \, \frac{\phi_j^*(\mathbf{r})\phi_k^*(\mathbf{r}')\phi_j(\mathbf{r}')\phi_k(\mathbf{r})}{|\mathbf{r}-\mathbf{r}'|} \tag{2.47}$$

was introduced and mixing a fraction of it into the GGA-exchange resulted in the so called hybrid functionals [57]. This type of functionals profits from a certain error-cancellation effect since DFT-calculations typically underestimate the gap and HF-calculations, where the Fock-term originates from, overestimate it [57]. A suitable mixing of both exchange types will hence improve the gap. However this procedure of introducing weighting factors for the different exchange contributions can be to a certain extent empirically driven which makes this approach not any more fully *ab initio* [64]. Nevertheless especially for chemical systems the approach seems to be successful [64] although it should be noted that due to the Fock-term the scaling of the calculation with system size is similar to the HF formalism and consequently less favorable compared to GGA DFT.

Moreover it has been realized that also non-local functionals purely in terms of the density could lead to improved results. There the density at different points influences the density at point $\mathbf{r}$ (average density approximation (ADA) or weighted density approximation (WDA)) [57, 64, 94]:

$$E_{xc}^{\mathrm{ADA}}[n] = \int d^3r \, n(\mathbf{r})\varepsilon_{xc}^{\mathrm{hom}}(\bar{n}(\mathbf{r})), \tag{2.48}$$

where $\varepsilon_{xc}^{\mathrm{hom}}$ is the exchange-correlation energy of the homogeneous electron liquid per particle and $\bar{n}(\mathbf{r})$ is an averaged density [9] [57]:

$$\bar{n}(\mathbf{r}) = \int d^3r' \, n(\mathbf{r}') \, w[n](|\mathbf{r}-\mathbf{r}'|), \tag{2.49}$$

where $w[n](|\mathbf{r}-\mathbf{r}'|)$ is a weighting function that averages the density over a certain physically relevant part of space [64]. The WDA is based on a similar approach. Consequently, this means that the density at any point $\mathbf{r}$ is determined by the character of the density at other

[9] In LDA one would take $\bar{n}(\mathbf{r}) \equiv n(\mathbf{r})$.

points in space. Although this fully non-local treatment turns the computation costly, favorable results can be expected [64].

Approaches to Include the van der Waals Interaction

LDA and GGA usually reliably describe the electronic properties and bonding of overlapping density distributions (see Fig. 2.1(a)). However non-local bonding contributions as the van der Waals (vdW) interaction posed a difficulty onto DFT in this respect. The vdW interaction accounts for the interaction between two systems due to charge fluctuations leading to induced dipole moments [95] as indicated in Fig. 2.1(b). As a strictly non-local long range correlation effect it is not described properly within LDA or GGA DFT. Nevertheless these interactions are of outstanding importance especially in condensed organic phases or condensed nobel gas phases which only bind due to the vdW force [96]. Another typical example where inter-layer vdW forces are important, is bulk graphite for which GGA consequently fails to predict inter-planar bonding[10] [97]. Furthermore, also in case of molecule-surface hybrid systems the vdW interaction can be decisive [40, 98].

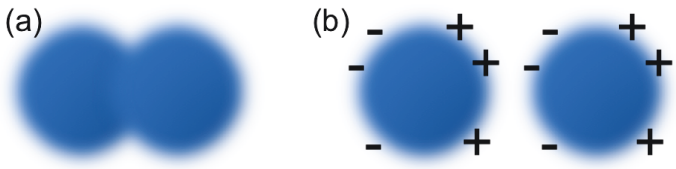

Figure 2.1.: Schematic visualization of overlapping (a) and non-overlapping (b) density distributions. In (b) charge fluctuations can give rise to induced dipole moments contributing to the vdW interaction.

One of the first approaches to include the vdW interaction into DFT was to take into account the strictly non-local character of this correlation effect by constructing an explicit van der Waals density functional (vdW-DF) for general geometries as suggested by Dion and coworkers [99]. In the proposed form the non-local correlation-energy part E_c^{nl} of the exchange-correlation functional is given by a density-density interaction formula [99]:

$$E_c^{\mathrm{nl}} = \frac{1}{2}\int d^3r \int d^3r'\, n(\mathbf{r})\Phi(\mathbf{r},\mathbf{r}')n(\mathbf{r}'), \tag{2.50}$$

where the kernel function $\Phi(\mathbf{r},\mathbf{r}')$ is a general function of $\mathbf{r}-\mathbf{r}'$ determined such as to mimic the correct long-range correlation behavior. In Ref. [99] an approximate expression for this kernel function was derived. Test calculations on nobel gas dimers and benzene dimers showed a

[10] LDA does however predict interplanar bonding.

considerably better description of these systems by the vdW-DF compared to GGA. Nevertheless, a rather strong dependence of the results on the chosen exchange part of the functional was pointed out. For this purpose specifically optimized exchange functionals for the vdW-DF have been proposed and tested [100–102]. Moreover an improved version of the non-local correlation functional has been developed [103]. To reduce the computational effort in the evaluation of the double spatial integral in Equation (2.50), Román-Pérez and Soler studied the effective implementation of the proposed non-local correlation functional in Ref. [104]. The double spatial integral scales as $\mathcal{O}(\mathcal{N}^2)$ where $\mathcal{N}$ denotes the number of grid points in the calculation. In Ref. [104] the integral is reformulated by factorizing the kernel function and using Fast Fourier Transforms to achieve a speedup to $\mathcal{O}(\mathcal{N}\log\mathcal{N})$. A major disadvantage of this approach is that no explicit spin-polarized version of the vdW-DF had been developed until recently and in case of spin-polarized calculations the correlation energy is evaluated on the sum of spin up and spin down densities [105]. However very recently an explicit spin dependent variant of the vdW-DF was proposed [106].

An alternative strategy when taking into account the stated drawbacks of the vdW-DF is to incorporate the interaction via a correction term instead of an explicit functional. This scheme was introduced by Grimme within the DFT-D approach [69, 107] and later on a non-empirical ansatz to obtain the needed C_6 coefficients was presented by Tkatchenko and Scheffler [108]. Within this scheme the electronic energy E^{el} is written as the sum of the KS DFT energy $E^{\mathrm{el}}_{\mathrm{KS}}$ and a dispersion correction E_{disp} [69]:

$$E^{\mathrm{el}} = E^{\mathrm{el}}_{\mathrm{KS}} + E_{\mathrm{disp}}. \tag{2.51}$$

The dispersion correction is obtained by the summation of pairwise $C_6 R^{-6}$ interaction terms [69]:

$$E_{\mathrm{disp}} = -s_6 \frac{1}{2} \sum_{i,j} \frac{C_6^{ij}}{R_{ij}^6} f_{\mathrm{damp}}(R_{ij}), \tag{2.52}$$

where the sums over i and j run over the number of atoms in the system, s_6 is a global scaling factor depending on the applied density functional, C_6^{ij} denotes the pairwise C_6-coefficient between atoms i and j[11], R_{ij} labels the inter-atomic distance between atoms i and j and $f_{\mathrm{damp}}(R_{ij})$ indicates a damping function taking care to cut the interaction at short distances and eliminating singularities[12]. Remarkably, the expression (2.52) does not explicitly include electronic coordinates and will therefore primarily change atomic distances and thereby alter equilibrium geometries as a result of the modified potential energy landscape. Consequently, the electronic structure will also be modified via the KS equations.

[11] The C_6 coefficient can be related to static dipole polarizabilities of atoms [69].

[12] These damping functions incorporate the vdW radii of the atoms, that can be obtained from the electron density contour [69, 108].

To obtain the specific shape of the DFT-D functional, Grimme utilized a fitting procedure using a training set of molecules in which the original xc-functional is corrected for correlation effects allowing to determine the s_6 value [69]. Furthermore the C_6^{ij}-coefficients are obtained from a geometric mean of the corresponding homonuclear C_6-coefficients that are elucidated from ionization potentials and dipole polarizabilities of free atoms [69]. In a refined version of the approach the parameters are computed from first principles and an eighth order dispersion correction is included in addition to the sixth order dispersion correction of Equation (2.52) [109]. Notably, the coefficients are introduced as geometry dependent quantities in the latter scheme.

The approach of Tkatchenko and Scheffler [108] makes use of obtaining the C_6-coefficients from the ground-state electron density and free-atom reference data of Chu and Dalgarno [110]. The coefficients are computed from a limited series expansion of frequency-dependent polarizabilities. The development was extended to correctly describe van der Waals interactions important for modeling hybrid inorganic-organic systems such as molecules on surfaces [111]. The many-body collective response (screening) properties of the substrate electrons were taken into consideration within Lifshitz-Zaremba-Kohn theory. Very recently, the method was extended to a self-consistent treatment of the vdW interaction [112].

2.2.5. Generalization to Spin-polarized Systems

Up to this point, DFT has only been presented in terms of the spin unpolarized density $n(\mathbf{r})$. The theory can however be generalized according to von Barth and Hedin [113] to a spin-polarized variant called spin-DFT (SDFT) for collinear spin structures which is now used almost synonymous to DFT. Within this framework one introduces an additional spin index $\sigma = \uparrow, \downarrow$ and deals with a density for each spin, $n_\uparrow(\mathbf{r})$ and $n_\downarrow(\mathbf{r})$ and two effective potentials $v_{s,\uparrow}(\mathbf{r})$ and $v_{s,\downarrow}(\mathbf{r})$ [61, 64]. Alternatively, the charge density $n(\mathbf{r}) = n_\uparrow(\mathbf{r}) + n_\downarrow(\mathbf{r})$ and the magnetization density $m(\mathbf{r}) = \mu_B(n_\uparrow(\mathbf{r}) - n_\downarrow(\mathbf{r}))$, where μ_B is the Bohr magneton, can be used as fundamental variables [64]. The KS differential Equation (2.29) is then given by:

$$\left[-\frac{1}{2}\Delta + v_{s\sigma}(\mathbf{r})\right]\phi_{i\sigma}(\mathbf{r}) = \varepsilon_{i\sigma}\phi_{i\sigma}(\mathbf{r}). \tag{2.53}$$

A subtle point of the SDFT formalism is however that there is no spin dependent analogue to the original theorem of Hohenberg and Kohn and only a one-to-one correspondence between the spin densities and the wave function can be proven [64]. The external spin dependent potential is however not any more a unique functional of the spin density [61]. This can be seen form the fact that the Zeeman energies in an external magnetic field shift without any change in the wave functions (in non-relativistic approximation) until level crossing [61]. This means that within a large range of the external potential the spin density is the same. In

addition, special care must be taken when constructing spin polarized exchange-correlation functionals as for example von Barth and Hedin generalized the LDA to the local spin density approximation (LSDA) by interpolating between an unpolarized and a fully polarized electron gas [64, 113].

The formalism can also be extended to treat non-collinear magnetic systems by taking into account that the magnetization density is a three-component vector, i. e. $\mathbf{m}(\mathbf{r})$ whose direction can vary locally [57, 61, 64].

Relativistic effects such as spin-orbit coupling (SOC) in general originate from the Dirac equation. SOC is responsible for phenomena as magnetic anisotropy, the Rashba effect and non-collinear magnetism [57]. These effects can be taken into account by first evaluating the scalar relativistic equation and including SOC thereafter as a perturbation when the spin polarized bands and wave functions are available from the scalar relativistic equation [114, 115]. The Hamiltonian of spin-orbit coupling can be expressed in atomic units as [57]:

$$H_{\mathrm{SO}} = \frac{1}{2M^2c^2}\frac{1}{r}\frac{dv_{\mathrm{s}}}{dr}\mathbf{L}\cdot\vec{\sigma}, \tag{2.54}$$

where $M(r) = 1 + \frac{\varepsilon - c^2 - v_{\mathrm{s}}(r)}{2c^2}$ is a radially varying mass, c is the speed of light in vacuum, $\mathbf{L}$ is the total angular momentum and $\vec{\sigma}$ is a vector of Pauli matrices. Importantly, since the term $\frac{1}{r}\frac{dv_s}{dr}$ is only large in the core region close to the nucleus, the evaluation of the spin-orbit contribution can be performed within a spherically symmetric environment [57].

2.2.6. Extensions and Recent Developments

The DFT formalism presented so far has been extended in several ways. However, the description of these extensions is beyond the scope of this thesis. This subsection aids to outline at least some important developments. The extension of DFT to time-dependent problems to accurately treat excitations and response functions, is made possible by time-dependent density functional theory (TDDFT) introduced by Runge and Gross [116]. One of the main issues within this theory is that the exchange-correlation functional is in principle also non-local in time since the density at a certain time t depends on all earlier times $t' \leq t$ [57].

A prominent approach to treat excitations is to use the eigenvalues and eigenfunctions of the KS equations as input for many-body perturbation theory approaches [57] as for instance the GW-scheme introduced by Hedin [117].

Another major development in modern electronic structure theory was the introduction of 'quantum molecular dynamics' by Car and Parrinello [118]. It allows for a combined treatment of electronic structure and nuclear motion which opened the way to treat liquid phases or disordered solid systems [57].

2.3. Practical Considerations for Actual Calculations

This section is devoted to the approaches that need to be considered when actually performing calculations. First, usually basis functions are used to expand the wave functions of the system which then leads to secular equations that are solved for the coefficients of this expansion. In practice the bare Coulomb potential of the cores acting on the valence electrons is too strong and the substitution of this real potential by a pseudopotential (PP) leads to smooth potentials and valence states that can be treated with reduced numerical effort. A formal exactification of this approach is the projector augmented-wave (PAW) method. Alternatively, the problem of solving the KS-equations can be treated by a Green's function method as the Korringa-Kohn-Rostoker (KKR) formalism. Furthermore DFT results offer the possibility to be used as an input for electronic transport calculations in the framework of the DFT-non-equilibrium Green's function (NEGF) formalism and can be utilized to simulate scanning tunneling microscopy (STM) results.

2.3.1. Basis Sets

The usual way to solve the differential KS Equation (2.29) is to expand the wave functions $\phi_i(\mathbf{r})$ into a suitably chosen set of basis functions. This then transforms the differential problem into an algebraic matrix-vector equation (secular equation), i. e. into a (generalized) eigenvalue problem, where the coefficients of the expansion are the variational parameters that need to be determined. For this scheme to work mathematically rigorously the basis set should be complete. Since in practice every basis is naturally finite, the challenge is to use a suitable set of functions to describe the states within this finite set as appropriately as possible. Therefore different approaches for the basis functions have been proposed and the suitable choice of the type of basis functions can depend on the system under study [55, 57].

In computational chemistry often isolated systems as free molecules are studied which can be described accurately by localized basis functions representing atomic orbitals [55, 59]. By this procedure one constructs molecular orbitals out of a linear combination of atomic orbitals known as linear combination of atomic orbitals to molecular orbitals (LCAOMO) approach. When remembering the solutions of the hydrogen atom, it might at first sight seem appropriate to use a class of functions called Slater-type orbital (STO) as basis functions since the exponential decay of these functions is typical for the radial part $R(r)$ of atomic orbitals [55]:

$$R^{\mathrm{STO}}(r) = A\, r^{\nu-1} e^{-\gamma r}, \tag{2.55}$$

where A is a normalization constant, γ determines the spread of the orbital and ν is the main quantum number. The great disadvantage of these STOs is that they are hard to treat nu-

merically [64]. A solution to this problem is to express the STOs with their reasonable radial behavior by a set of functions called Gaussian-type orbital (GTO). Gaussians have individually a less favorable radial behavior [64]:

$$R^{\mathrm{GTO}}(r) = A\, r^{2\nu-2-2l} e^{-\gamma r^2}, \tag{2.56}$$

where l stands for the angular momentum quantum number. By using an appropriate set of GTOs one can fit an STO relatively well besides the cusp at the nucleus [55]. This linear combination of GTOs to approximate an STO has become known as contracted Gaussian-type orbital (CGTO) [64]. The advantage of such basis functions is, that products of GTOs are again GTOs that can be integrated analytically. The continuous effort in quantum chemistry lead to the construction of very accurate basis sets formed out of GTOs [119]. In addition, also numerical approaches for localized orbitals have been presented [57, 120]. One major disadvantage of such type of basis functions is that it is often difficult to systematically improve the basis set.

On the other hand in computational solid state physics one often treats periodic systems which can be represented by a unit cell and periodic boundary conditions. In this context plane waves are a natural choice for the basis functions in periodic systems according to the Bloch theorem [121], which states that for a periodic potential each eigenfunction $\phi_{i,\mathbf{k}}$, indexed by its set of quantum numbers i and the wave vector $\mathbf{k}$, can be expressed as the product of a plane wave times a lattice periodic function $u_i(\mathbf{r})$ [122]:

$$\phi_{i,\mathbf{k}} = e^{i\mathbf{kr}} u_i(\mathbf{r}); \qquad u_i(\mathbf{r}) = u_i(\mathbf{r}+\mathbf{M}), \tag{2.57}$$

where $\mathbf{M}$ is a lattice vector. Then the wave function $\phi_{i,\mathbf{k}}$ can be expanded according to [123]:

$$\phi_{i,\mathbf{k}} = \sum_{\mathbf{g}} a_{i,\mathbf{g}} |\mathbf{k}+\mathbf{g}\rangle = \sum_{\mathbf{g}} a_{i,\mathbf{g}}\, e^{i(\mathbf{k}+\mathbf{g})\mathbf{r}}, \tag{2.58}$$

where $\mathbf{g}$ is a reciprocal lattice vector. Often this approach is used in conjunction with PPs (see Subsection 2.3.2) or the PAW method (see Subsection 2.3.3) which create smooth pseudo wave functions that can be treated by a small number of plane waves. The matrix elements of the potential $v_{\mathrm{s}}(\mathbf{r})$ can then be determined by Fourier components $v_{\mathrm{s},\mathbf{g}}$ [123]:

$$v_{\mathrm{s},\mathbf{g}} = \frac{1}{\Omega} \int_{\Omega} d^3 r\, v_{\mathrm{s}}(\mathbf{r}) \exp[-i\mathbf{gr}], \tag{2.59}$$

where Ω is the volume of the primitive unit cell. These Fourier components are also known as potential form factors that can be used in combination with structure factors to describe the potential within the unit cell [123]. Finally, this treatment leads to the secular equation in the

plane wave basis [57]:

$$\sum_{\mathbf{g}'} H_{\mathbf{g},\mathbf{g}'}(\mathbf{k})\, a_{i,\mathbf{g}'}(\mathbf{k}) = \varepsilon_i(\mathbf{k})\, a_{i,\mathbf{g}}(\mathbf{k}), \tag{2.60}$$

where

$$H_{\mathbf{g},\mathbf{g}'}(\mathbf{k}) = \langle \mathbf{k}+\mathbf{g}|H_\mathrm{s}|\mathbf{k}+\mathbf{g}'\rangle = \frac{1}{2}(\mathbf{k}+\mathbf{g})^2\delta_{\mathbf{g},\mathbf{g}'} + v_{\mathrm{s},\mathbf{g}-\mathbf{g}'} \tag{2.61}$$

and $H_\mathrm{s} = -\frac{1}{2}\Delta + v_\mathrm{s}(\mathbf{r})$ is the single-particle KS Hamiltonian. The advantage of choosing plane waves as basis functions is that in a natural way the basis set can be improved by increasing the number of plane waves used. The basis set is then defined by giving the kinetic energy cutoff E_cutoff [57]:

$$E_\mathrm{cutoff} = \frac{1}{2}(\mathbf{k}+\mathbf{g})^2. \tag{2.62}$$

It is also possible to perform the calculation using the values of the wave functions and densities on a real space grid which are then the variational parameters of the calculation [124]. The accuracy of the calculation can be systematically improved by reducing the grid spacing h. Derivatives as needed for instance for the kinetic energy are calculated by finite differences over neighboring grid points to mth order at grid point (x_i, y_j, z_k)[57]:

$$\left[\frac{\partial^2\phi}{\partial x^2}\right]_{x_i,y_j,z_k} = \sum_{-m}^{m} C_m \phi(x_i + mh, y_j, z_k) + \mathcal{O}(h^{2m+2}), \tag{2.63}$$

where the coefficients C_m are obtained from suitable algorithms. The grid spacing can be expressed as a nominal cutoff energy [124]:

$$E_\mathrm{cutoff}^\mathrm{RS} = \frac{\pi^2}{2h^2}. \tag{2.64}$$

Usually in real space methods a higher nominal cutoff than the energy cutoff in plane wave methods is needed as the plane wave form is already suitable to describe the Bloch states but in the grid methods no functional shape is assumed. This real space method allows for real space parallelization by dividing the space into suitable cells. The approach is especially favorable when treating large systems from first principles [124].

There are also methods that use energy-dependent basis functions for the description of the systems as for instance the augmented plane wave (APW) method [64]. Details about these methods can be found in Ref. [57] and references therein.

2.3.2. The Pseudopotential Approach

A fundamental observation when studying the physical properties of solids is, that most of these properties (e. g. electrical conduction, specific heat or optical properties) are governed by the behavior of the valence electrons around the Fermi energy E_F rather than the core electrons [56, 122]. Hence there is the need in view of a theoretical description and understanding of these properties to describe those valence states as accurately as possible. The great drawback in this context is, that the valence states behave very differently in different regions of space [57, 123, 125]. In the physically relevant region far from the cores, where bonding occurs, the valence states are rather smooth and could be described accurately by a small number of basis functions (i. e. Fourier components when utilizing a plane wave basis). On the other hand close to the nuclei the valence states need to be orthogonal to the core-states which leads to strong spatial oscillations and hence high kinetic energies of these states due to the associated curvature [57].

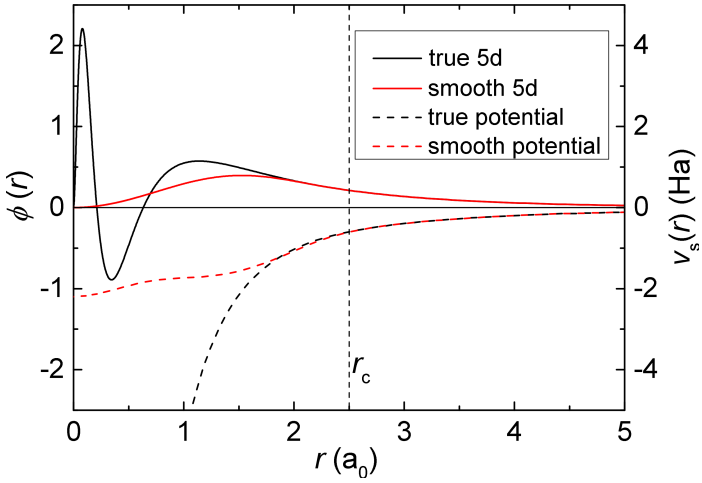

Figure 2.2.: Visualization of the PP approach for the W atom. The true effective potential is singular at the origin whereas the associated smooth potential has a finite value at $r = 0$ and is much smoother and weaker than the true potential. Consequently, the radial part of the true $5d$ state of W varies much more rapidly than the corresponding nodeless smooth part. The data was obtained from the GPAW setup for W [126].

The idea of the PP method is to substitute the true strong Coulomb potential by a smoother PP that leads to smooth pseudo (PS) wave functions. These PS wave functions are identical to the true wave functions beyond a certain (angular momentum dependent) cutoff radius r_c and resemble a smooth continuation inside as demonstrated in Fig. 2.2 for the exemplary

case of the $5d$ state of W. This PP method is rigorously based on two findings: (i) The scattering properties of a localized spherical potential can be described by the scattering phase shifts which determine all properties of the wave function outside the localized region [57]. Hence the wave function outside the core region is the same for any potential leading to the same phase shift (modulo 2π). This freedom can be used to choose a PP with desired smooth properties. (ii) The screening of the nuclear potential by the core electrons results in a weaker potential (PP) acting on the valence electrons which can be proven mathematically by the so-called 'cancellation theorem' [123, 127, 128]. One could also say that the valence electrons are nearly free [123]. Taking advantage of the PP approach can only be expected when both properties are used since they allow to choose the PP both smoother and weaker than the bare nuclear potential [57]. However the drawback of this PP transformation is that the new potential is inherently a more complicated non-local operator [57]. Nevertheless, within the calculation effectively only the valence electrons are taken into account but it is in principle possible to reconstruct the core states from a PP calculation [57].

The use of PPs for solid state calculations originated from the introduction of the orthogonalized plane wave (OPW) approach [129, 130] where the valence states were separated into a smooth part and a localized part. However considerable progress had to be made to make the PPs transferable from one system to another. For model ion potentials every l was treated differently which lead to non-local l-dependent model PPs [57]. From the point of view of *ab initio* PPs especially two approaches turned out to be successful, which will be described subsequently.

Norm-conserving Pseudopotentials

A major breakthrough in terms of accuracy and transferability was achieved when norm-conservation was introduced for generating the PPs. This means that the resulting PS wave function should have the same norm as the correct wave function which eventually leads to charge conservation inside the cutoff radius [57]. Moreover the norm-conservation condition secures that the first energy derivative of the logarithmic derivative of the pseudo wave function $\tilde{\phi}_{nl}(r,\varepsilon)$ is the same as for the true wave function $\phi_{nl}(r,\varepsilon)$ at energy ε_{nl} chosen for the construction of the PP [57]:

$$\frac{d}{d\varepsilon}\frac{d}{dr}\ln[\tilde{\phi}_{nl}(r,\varepsilon)]|_{r_c,\varepsilon_{nl}} = \frac{d}{d\varepsilon}\frac{d}{dr}\ln[\phi_{nl}(r,\varepsilon)]|_{r_c,\varepsilon_{nl}}. \tag{2.65}$$

Therefore the resulting norm-conserving (NC) PP has correct scattering properties not only at the reference energy at which it was constructed, but also in the energy range around. Particularly this leads to increased transferability between different environments as the energetic positions of the atomic valence states are modified within a compound [56]. Additional ideas

have been developed to extend the energy range in which the phase shifts are reproduced correctly [57]. Furthermore the PS wave functions of NC PPs are orthonormalized with respect to state and spin index leading to a standard eigenvalue problem for the KS-equations [57].

A further significant contribution concerning the applicability of PPs was given by Kleinman and Bylander by showing that a separable PP operator v_{e-K}^{KB} can be constructed [131]:

$$v_{e-K}^{\mathrm{KB}} = v_{\mathrm{loc}} + \sum_{L} |p_L\rangle D_l \langle p_L|, \tag{2.66}$$

where v_{loc} is the local part of the potential and the projectors p_L localized around the nucleus are constructed out of spherical harmonics $Y_{l,m}$ and a contribution from the difference between local and nonlocal part [132]. The coefficients D_l are chosen such that the action of v_{e-K}^{KB} is the same as the one of the semilocal potential it tries to approximate. This procedure reduces the computational cost as the calculation of matrix-elements now requires only products of projection operations [57].

Ultrasoft Pseudopotentials

To improve on the results of NC PPs which still yielded hard PS wave functions for states of a new angular momentum channel (e. g. $2p$ and $3d$ elements [57]), Vanderbilt [133] and Blöchl [134] introduced a scheme where auxiliary localized functions are utilized to split up the initial PS wave function into a very smooth PS part (that is not norm-conserving) and a rapidly varying function which is localized around the core [57]. The difference in the norm-conservation is incorporated into a new non-local potential operating on the PS wave functions. Hence the PS wave functions are orthonormal with respect to the specific overlap operator $\hat{S}$ [57]:

$$\langle \tilde{\phi}_i | \hat{S} | \tilde{\phi}_j \rangle = \delta_{ij}. \tag{2.67}$$

Consequently, one needs to solve the corresponding generalized eigenvalue problem for the smooth wave function. Within this procedure the strict norm-conservation condition is relaxed. This allows to form each PS function independently from all others [57]. In this way the method of ultrasoft PPs offers the possibility to increase the cutoff radius compared to NC PPs.

Ghost States

Following Kleinman and Bylander [131] semilocal PPs which are local in the radial part but non-local in the angular part can be transformed into a separable form which is useful in terms of efficient calculations. However for such a separable PP it is not guaranteed anymore that it does not cause additional eigenstates with very low energies [132]. Such 'ghost states'

are especially common for very attractive PPs [135] which should therefore be avoided. In this framework it can sometimes be necessary to treat semicore states (e. g. $3s$ and $3p$ states in case of $3d$ elements) as valence states to avoid ghost states [57].

Generation of Pseudopotentials

For the actual construction of PPs many different approaches have been proposed (see for example [57, 133, 134, 136–141] and references therein) as there is in general not one best PP for all systems but the suitable choice can be problem dependent [57].

In general the PPs are derived from all-electron calculations on the specific atom of the element for which it is then applied in other systems. After the all-electron calculation the valence states are identified and PPs and PS orbitals are generated so as to match the results of the all-electron calculation beyond the cutoff radius. Thereby a 'screened' PP acting on the valence states of the atom is found which eventually needs to be 'unscreened' to be transferable [57]. This is done by subtracting from the total angular momentum dependent PP $v_{l,\mathrm{total}}(r)$ the sum of Hartree and exchange-correlation potential $v_{\mathrm{H}xc}^{\mathrm{PS}}$ of the valence electrons in their PS orbitals[13]:

$$v_l(r) = v_{l,\mathrm{total}}(r) - v_{\mathrm{H}xc}^{\mathrm{PS}}. \tag{2.68}$$

In fact there are many different possibilities to construct a specific PP as already mentioned before either by varying parameters or inverting the Schrödinger equation [57], which is partly due to the fact that the shape of the potential in the core region is less significant [123]. In that regard the scheme proposed by Troullier and Martins in Ref. [141] is one widely used approach to obtain smooth NC PPs in the core region. Within that scheme the PS orbitals are chosen such as to have the correct radial behavior (r^{l+1}) around the nucleus, are as smooth as possible in the other regions and depend on seven adjustable parameters:

$$\tilde{\phi}_l(r) = \begin{cases} \phi_l(r) & \text{if} \quad r \geq r_c \\ r^{(l+1)} \exp[p(r)] & \text{if} \quad r \leq r_c \end{cases}, \tag{2.69}$$

with $p(r)$ being a six order polynomial in r^2:

$$p(r) = c_0 + c_2 r^2 + c_4 r^4 + c_6 r^6 + c_8 r^8 + c_{10} r^{10} + c_{12} r^{12}. \tag{2.70}$$

The parameters are obtained from continuity requirements of the pseudo orbital and its first four derivatives at the cutoff radius, the norm-conservation condition and a zero-curvature condition for the screened PP at the nucleus. The PP is then given by inversion of the radial Schrödinger equation [141].

[13] As the exchange-correlation potential is not a linear functional of the density, non-linear core corrections might need to be included which can be of importance in case of magnetic systems [57].

By actually constructing a PP one always has to make a compromise since high accuracy and transferability demand hard PPs whereas smoothness of the PS wave functions requires smooth PPs [57].

2.3.3. The Projector Augmented-wave Method

The PAW method was initially introduced by Blöchl [142] and it was shown by Kresse and Joubert that ultrasoft PPs can be derived by a well defined approximation [135]. The PAW formalism provides in this sense the formal exactification of the PP method and puts it onto a more reliable ground. The big advantage of the PAW method is that it is in principle an explicit all-electron method which can therefore be used to obtain information on the core states as the all-electron wave functions can always be reconstructed from the smooth PS wave functions [57]. Within the scheme space is divided into atom-centered augmentation spheres in which both the true and the smooth PS wave functions are represented by partial waves, and an interstitial region between the spheres (bonding region) where the PS wave function is identical to the true wave function [125]. Both parts of the wave function are matched at the sphere boundary.

Basic Formalism

The basic idea is to find a *linear* operator $\hat{T}$ that transforms smooth auxiliary wave functions $|\tilde{\phi}_n\rangle$, which are the actual variational parameters within the calculation, into the true single particle wave functions $|\phi_n\rangle$ [125]:

$$|\phi_n\rangle = \hat{T}|\tilde{\phi}_n\rangle, \tag{2.71}$$

where n is the label of the state (**k** index, band index, spin index). Now $\hat{T}$ needs to be defined in such a way that the auxiliary wave functions become smooth. Similar to the PP method the transformation shall only affect the wave functions within a spherical part around the nuclei (augmentation sphere) as beyond the sphere the wave functions are already smooth. Therefore [57]:

$$\hat{T} = 1 + \sum_a \hat{T}^a, \tag{2.72}$$

where a is the atom label and the atom-centered transformation $\hat{T}^a$ is zero outside an *atom-specific* cutoff radius r_c^a. Overlap between the spheres should be avoided as this would result in a double counting due to a double augmentation.

Within the augmentation sphere one expands the atom centered true wave function ϕ_n^a into partial waves ψ_i^a [125]:

$$|\phi_n^a\rangle = \sum_i P_{ni}^a |\psi_i^a\rangle. \tag{2.73}$$

For every partial wave a corresponding smooth partial wave $\tilde{\psi}_i^a$ is defined that fulfills:

$$|\psi_i^a\rangle = (1 + \hat{T}^a)|\tilde{\psi}_i^a\rangle \tag{2.74}$$

which defines the transformation operator $\hat{T}^a$ uniquely [125]. As the operator is zero outside the sphere, true partial wave and smooth partial wave are identical in this region of space.

The smooth atom-centered wave functions $\tilde{\phi}_n^a$ can then for a complete set of smooth partial waves be expanded inside the augmentation sphere [124]:

$$|\tilde{\phi}_n^a\rangle = \sum_i P_{ni}^a |\tilde{\psi}_i^a\rangle \tag{2.75}$$

where the coefficients P_{ni}^a are the same as in Equation (2.73) since the operator is linear [125]:

$$|\phi_n^a\rangle = (1 + \hat{T}^a)|\tilde{\phi}_n^a\rangle = \sum_i P_{ni}^a |\psi_i^a\rangle. \tag{2.76}$$

The coefficients are now determined from the projection of $|\tilde{\phi}_n^a\rangle$ onto atom specific smooth projector functions $\tilde{p}_i^a$ [124]:

$$P_{ni}^a = \langle \tilde{p}_i^a | \tilde{\phi}_n^a \rangle. \tag{2.77}$$

Since the spheres should not overlap and the smooth partial waves should reproduce the smooth wave function within the expansion (2.75) inside the sphere there is the completeness relation [125]:

$$\sum_i |\tilde{\psi}_i^a\rangle\langle\tilde{p}_i^a| = 1 \tag{2.78}$$

which also implies the orthonormality of the projector functions to the smooth partial waves [125]:

$$\langle \tilde{p}_{i1}^a | \tilde{\psi}_{i2}^a \rangle = \delta_{i1,i2}. \tag{2.79}$$

Usually the projector functions are defined to be localized inside the augmentation sphere.

With the aid of the completeness relation and Equation (2.74) the atom-centered transformation can be shown to be given by [57]:

$$\hat{T}^a = \sum_i (|\psi_i^a\rangle - |\tilde{\psi}_i^a\rangle)\langle\tilde{p}_i^a|. \tag{2.80}$$

Hence for the total transformation operator we need to take into account all atomic contributions according to Equation (2.72):

$$\hat{T} = 1 + \sum_a \sum_i (|\psi_i^a\rangle - |\tilde{\psi}_i^a\rangle)\langle\tilde{p}_i^a|. \tag{2.81}$$

Consequently, the transformation between true and smooth wave function can be written[14] [125]:

$$\phi_n(\mathbf{r}) = \tilde{\phi}_n(\mathbf{r}) + \sum_a \sum_i (\psi_i^a(\mathbf{r}) - \tilde{\psi}_i^a(\mathbf{r})) \underbrace{\langle \tilde{p}_i^a | \tilde{\phi}_n^a \rangle}_{P_{ni}^a}. \tag{2.82}$$

The smooth wave function is obtained by solving a transformed KS equation and can in principle be used to reconstruct the true wave function [57]. The double sum in Equation (2.82) can be considered as a correction to the smooth wave function to achieve the true wave function. Within this scheme the true and smooth partial waves must form a complete set of functions and the projectors must fulfill the completeness relation (2.78) [124]. These sets of functions can be precalculated and tabulated for each element [125]. The atom-centered parts with superscript a incorporate the rapid oscillations and are represented on a *radial grid*, whereas the smooth wave functions are represented on a rather *coarse real space grid* (or Fourier grid) [125]. The PAW method is hence in principle an all-electron method but demands the computational cost of a PP calculation.

The Frozen Core Approximation

The frozen core approximation is based on the observation that the core states of the atom do only change slightly during the formation of a chemical bond in molecules and solids. Hence the potential induced by them onto the valence states stays basically the same. Therefore one can approximately take the core states from the specific atom a for each core state α as core state of the system under study [125]:

$$|\phi_n^c\rangle = |\phi_\alpha^{a,\text{core}}\rangle \tag{2.83}$$

assuming that they are well localized in the core region and that there is no significant change in the actual situation. However the frozen core approximation can also be relaxed within the PAW framework [142, 143].

Transformation of Operators

The expectation value of an operator $\hat{O}$ can be converted into an expectation value of a transformed operator $\hat{T}^\dagger \hat{O} \hat{T}$ [124]:

$$\langle \hat{O} \rangle = \langle \phi_n | \hat{O} | \phi_n \rangle = \langle \hat{T} \tilde{\phi}_n | \hat{O} | \hat{T} \tilde{\phi}_n \rangle = \langle \tilde{\phi}_n | \hat{T}^\dagger \hat{O} \hat{T} | \tilde{\phi}_n \rangle. \tag{2.84}$$

[14] Note that the relationship between $\phi_n(\mathbf{r})$ and $\phi_n^a(\mathbf{r})$ is the following:

$$\phi_n(\mathbf{r}) = \tilde{\phi}_n(\mathbf{r}) + \sum_a (\phi_n^a(\mathbf{r} - \mathbf{R}^a) - \tilde{\phi}_n^a(\mathbf{r} - \mathbf{R}^a)),$$

where $\mathbf{R}^a$ is the position of atom a [125].

This can then be further evaluated by inserting Equation (2.82) (see [125]). It turns out that the expression splits up into a local part and a non-local part. Hence for purely local operators a specific local expression can be derived to evaluate for instance the density, the kinetic energy or the exchange correlation energy for local and semilocal xc-functionals [124, 125]. The non-local contribution comes to matter e. g. in case of the Hartree term or for nonlocal exchange-correlation functionals. This leads then to more extensive expressions involving the introduction of compensation charges for which details can be found in Refs. [124, 125, 135, 142]. The atom centered compensation charges are added to the density as an intelligent zero on different grids. The charges are constructed such that the atom centered density has no multipole moments and the corresponding potential outside the sphere is therefore zero [125]. This allows to resolve all problems usually associated with the evaluation of the Hartree term as it avoids matrix elements between quantities on different grids, badly scaling double summation and numerical problems with densities of nonzero total charge [124, 125]. The final expressions can then be used to solve the transformed KS equations.

However, in every case the specific quantity splits up into two parts. The first only includes the contribution of the smooth wave functions and the other term includes atom-centered corrections inside the sphere. For instance the density reads [125]:

$$n(\mathbf{r}) = \tilde{n}(\mathbf{r}) + \sum_a (n^a(\mathbf{r}) - \tilde{n}^a(\mathbf{r})), \tag{2.85}$$

where $n^a(\mathbf{r})$ and $\tilde{n}^a(\mathbf{r})$ include the contributions from the partial waves and smooth partial waves, respectively.

Projected Density of States

In the PAW formalism the projection of the all electron wave functions onto the all electron wave functions of the isolated atom (the all electron partial waves) can be approximated by [125]:

$$\langle \psi_i^a | \phi_n^a \rangle \approx \langle \tilde{p}_i^a | \tilde{\phi}_n^a \rangle = P_{ni}^a. \tag{2.86}$$

Hence this can be used to obtain information about the l, m-character of the all electron wave functions and allows to define the projected density of states (PDOS) at each site a [125]:

$$\rho_i^a(\varepsilon) = \sum_n \delta(\varepsilon - \varepsilon_n) |P_{ni}^a|^2. \tag{2.87}$$

PAW Datasets

For each element of the periodic table one needs to provide a specific amount of data in order to perform a calculation within the PAW formalism. Once again an all-electron DFT program

is needed for the generation of the basis sets [125]. The unavoidable fact that the partial wave expansions are always finite in a practical calculation demands careful preparation of these basis functions. Furthermore the position dependent basis around the atoms causes a force contribution arising from the wave functions called Pulay forces [142].

The (all electron) partial waves are chosen as the eigenstates of the isolated atom [125]:

$$\psi_i^a(\mathbf{r}) = \psi_{nl}^a(r)\, Y_{lm}(\mathbf{e}_r), \tag{2.88}$$

where $\mathbf{e}_r$ denotes the direction of the vector $\mathbf{r}$. Also unbound states can be included as partial waves since the diverging tail is canceled outside the sphere by the smooth partial waves.

The smooth partial waves can for instance be represented by either 6'th order polynomials of even order, Bessel functions or Gaussians and they are identical to the true partial waves outside the cutoff radius [125].

The only formal requirement for the projector functions is, that they are orthonormal to the smooth partial waves. One way to determine them is by the action of the radial KS operator onto these smooth partial waves [125]:

$$|\tilde{p}_i^a\rangle = (-\frac{1}{2}\nabla^2 + \tilde{v}_\mathrm{s} - \varepsilon_i)|\tilde{\phi}_i^a\rangle, \tag{2.89}$$

where $\tilde{v}_s$ is the smooth KS potential of the atom. Afterwards orthogonality can be enforced for instance by a Gram-Schmidt procedure.

The compensation charges can be described via a multipole expansion of products of spherical harmonics and radial functions. The radial functions can be chosen as generalized Gaussians [125].

The all-electron core density follows directly from the partial waves and the smooth core densities can for instance be expanded in a few Bessel functions, Gaussians or polynomials [125].

Furthermore the PAW scheme offers the possibility to add a potential localized within the augmentation sphere to the effective potential without changing the energy when suitable corrections are added to the energy term and the Hamiltonian [125]. This allows to make the potential around the nuclei even smoother. The localized potential is expanded in some basis and adjusted to achieve a maximally smooth potential [125].

To obtain the desired properties, the adjustable parameters within a PAW calculation are [125]:

- cutoff radius r_c^a
- frozen core states
- number of basis functions (partial waves)

- energies of unbound partial waves.

The parameters should be adjusted such that the dataset is transferable to all environments and the resulting PS wave functions are smooth [125].

As a concluding remark of these subsections, the significant speed up in the calculations using PPs and the PAW method is not only due to the reduced amount of electrons treated explicitly but is rather a consequence of the smaller amount of basis functions needed to express smooth wave functions.

2.3.4. The Green's Function Approach of Korringa, Kohn and Rostoker

As an alternative to methods directly dealing with the singe-particle wave functions of the KS Equation (2.29) and expressing them in a suitable basis set, a conceptually different approach is based on Green's functions. As the KS Equation(2.29) is a differential equation, it can be solved by a Green's function method. This Green's function can then be used to calculate all physical properties of a system. An efficient way to obtain the Green's function of a crystal or surface is the KKR approach. The elegance of this theory is based on the separation of the single-site scattering problem and the structural problem.

The Green's Function Approach

The method of Green's functions is an elegant scheme to obtain the solution of an inhomogeneous differential equation. For the linear operator $\varepsilon - H$ with a complex number ε the Green's function $G(x,x';\varepsilon)$ is formally defined as [144]:

$$(\varepsilon - H)G(x,x';\varepsilon) = \delta(x,x'). \tag{2.90}$$

The Green's function is thus the inverse of the operator $(\varepsilon - H)$:

$$G(x,x';\varepsilon) = (\varepsilon - H)^{-1}. \tag{2.91}$$

If one now takes the inhomogeneous differential equation:

$$(\varepsilon - H)\phi(x) = h(x), \tag{2.92}$$

with an inhomogeneity h, the solution is immediately given by:

$$\phi(x) = \phi_0(x) + \int dx' G(x,x';\varepsilon)h(x'), \tag{2.93}$$

with $\phi_0(x)$ being the solution of the homogeneous problem $(\varepsilon - H)\phi_0(x) = 0$. If now the inhomogeneity is identified as the effective potential and the homogeneous problem as the free-particle Schrödinger or KS equation, this Green's function method provides a convenient way to obtain the solution of the general problem including the potential.

An advantageous feature of the Green's function is that it can be related to the Green's function of a reference system that is known. If one assumes that the Green's function G_0 to the operator H_0 is known and that the operator H is related to H_0 by:

$$H = H_0 + V, \tag{2.94}$$

with an additive contribution V. Then the Green's function of H is obtained by the so-called Dyson equation [144, 145]:

$$G = G_0 + G_0 V G = G_0 [1 - V G_0]^{-1}. \tag{2.95}$$

This is a central relation within KKR theory. A second important equation is the Lippmann-Schwinger equation which relates the eigenstate $\phi(x)$ of the perturbed system to the eigenstate $\phi_0(x)$ of the unperturbed system [144]:

$$\phi(x) = \phi_0(x) + G_0 V \phi(x). \tag{2.96}$$

The (energy-dependent) T-matrix of the scattering system $T(\varepsilon)$ is defined as [145]:

$$V\phi(x) = T(\varepsilon)\phi_0(x). \tag{2.97}$$

Using this relation the Lippmann-Schwinger equation can immediately be written as:

$$\phi(x) = \phi_0(x) + G_0 T(E)\phi_0(x) \tag{2.98}$$

and the Dyson equation can be transformed into [145]:

$$G = G_0 + G_0 T(E) G_0. \tag{2.99}$$

These relations show that also the T-matrix contains the full information about the system as the Green's function does and so either of the two can be calculated. Within the description of the single-site scattering properties below, the T-matrix will be indicated as t.

Obtaining Physical Quantities from the Green's Function

The Green's function $G(\mathbf{r},\mathbf{r}';\varepsilon)$ of a physical system is formally connected to the eigenstates ϕ_i and the eigenenergies ε_i by the so-called spectral representation [145]:

$$G(\mathbf{r},\mathbf{r}';\varepsilon) = \sum_i \frac{\phi_i(\mathbf{r})\phi_i^*(\mathbf{r}')}{\varepsilon - \varepsilon_i}, \tag{2.100}$$

which shows that $G(\mathbf{r},\mathbf{r}';\varepsilon)$ has poles at the eigenenergies. Importantly, the sum runs over both occupied and unoccupied states. The Green's function is thus directly related to the spectrally- and spatially-resolved density of states $\rho(\mathbf{r};\varepsilon)$ [145, 146]:

$$\rho(\mathbf{r};\varepsilon) = -\frac{2}{\pi}\mathrm{Im}\, G(\mathbf{r},\mathbf{r};\varepsilon). \tag{2.101}$$

Consequently, the spectral density of states $\rho_\Omega(\varepsilon)$ of an atom in volume Ω is obtained by integrating the imaginary part of the Green's function over this volume [145, 146]:

$$\rho_\Omega(\varepsilon) = -\frac{2}{\pi}\int_\Omega d^3r\, \mathrm{Im}\, G(\mathbf{r},\mathbf{r};\varepsilon) = -\frac{2}{\pi}\mathrm{Im}\,\mathrm{Tr}\, G(\varepsilon). \tag{2.102}$$

Furthermore, the charge density is obtained by an energy integration up to the Fermi energy E_F [146]:

$$n(\mathbf{r}) = 2\sum_i^{\varepsilon_i \le E_\mathrm{F}} |\phi_i(\mathbf{r})|^2 = -\frac{2}{\pi}\int_{-\infty}^{E_\mathrm{F}} d\varepsilon\, \mathrm{Im}\, G(\mathbf{r},\mathbf{r};\varepsilon) = -\frac{2}{\pi}\mathrm{Im}\int_{-\infty}^{E_\mathrm{F}} d\varepsilon\, \mathrm{Tr}(\hat{\mathbf{r}}G(\varepsilon)), \tag{2.103}$$

where $\hat{\mathbf{r}}$ is the position operator. Thus the evaluation of the states ϕ_i can be avoided in order to obtain physical properties and it can even be shown that the expectation value of any operator $\hat{A}$ can be evaluated using the Green's function [145]:

$$\langle\hat{A}\rangle = -\frac{2}{\pi}\mathrm{Im}\int_{-\infty}^{E_F} d\varepsilon\, \mathrm{Tr}\left[\hat{A}\,G(\varepsilon)\right]. \tag{2.104}$$

Hence the Green's function contains the full information about the system and any physical property can be calculated from it. However the strongly energy-dependent structure of the density of states makes the evaluation of the energy integrals difficult [146]. This complication can be circumvented by using that the Green's function is an analytic function in the upper part of the complex plane [145]. Therefore one can make a substitution $\varepsilon \to \varepsilon + i\Gamma$ and take an integration path over the upper part in the complex plane where the Green's function is much smoother due to the broadening induced by the imaginary part Γ and the integration can be carried out with a strongly reduced amount of energy points [146].

Basics of the KKR Formalism

The KKR formalism was initially developed by Korringa [147], Kohn and Rostoker [148]. The reformulation of this theory using Green's functions works with a natural separation of the Green's function into a single-site part (local part) and a structural part (global part) connecting the local solutions [144]. In order for this approach to work, the space needs to be partitioned into so-called Voronoi cells by constructing the Wigner-Seitz cell around each center (Voronoi construction). Within this procedure also the potential is partitioned into local potentials for each cell. For each of these cells the single-site scattering problem is solved first and subsequently the structural arrangement of these scattering centers is taken into account by the determination of a structural Green's function.

A natural choice for the reference system upon which all further calculations can be based on, is the free-electron system, i. e. a system without potential contributions for which the Green's function is known analytically [57]:

$$g(\mathbf{r},\mathbf{r}';\varepsilon) = -\frac{1}{4\pi}\frac{e^{ik|\mathbf{r}-\mathbf{r}'|}}{|\mathbf{r}-\mathbf{r}'|}, \tag{2.105}$$

where $k = \sqrt{2\varepsilon}$. This free-space Green's function can be expanded as [145]:

$$g(\mathbf{r},\mathbf{r}';\varepsilon) = \sum_L Y_L(\mathbf{r}) g_l(\mathbf{r},\mathbf{r}';\varepsilon) Y_L(\mathbf{r}'), \tag{2.106}$$

where $L := (l,m)$ is a combined angular momentum index, Y_L are real spherical harmonics and

$$g_l(\mathbf{r},\mathbf{r}';\varepsilon) = -i\sqrt{\varepsilon} j_l(\sqrt{\varepsilon} r_<) h_l(\sqrt{\varepsilon} r_>), \tag{2.107}$$

where j_l are spherical Bessel functions, $h_l = j_l + i n_l$ are spherical Hankel functions containing the spherical Neumann functions n_l and $r_<$ ($r_>$) is the smaller (larger) of the radii r and r'.

The actual calculation starts with a suitable guess for the input potential v_{in} for the single-site problem. Then one sets up the radial Schrödinger-like equation for each single-site problem [145]:

$$\left[-\frac{1}{r}\frac{\partial^2}{\partial r^2} r + \frac{l(l+1)}{r^2} + v_{\text{in}} - \varepsilon\right] R_l(r;\varepsilon) = 0 \tag{2.108}$$

with radial wave function $R_l(r;\varepsilon)$. This radial equation has two linearly independent solutions, a regular one R_l (converging for $r \to 0$) and an irregular one H_l (diverging for $r \to 0$) which are in practice obtained by numerical outwards and inwards integration from the origin to the spatial boundary S of the potential [145]. These radial solutions correspond to spherical Bessel and Hankel functions in case of the potential-free radial equation [144]. Thus the

Green's function for the scattering from a central potential is given by [145]:

$$G(\mathbf{r},\mathbf{r}';\varepsilon) = -i\sqrt{\varepsilon}\sum_{L} R_l(r_<;\varepsilon)H_l(r_>;\varepsilon)Y_L(\mathbf{r})Y_L(\mathbf{r}'). \tag{2.109}$$

In addition, the t-matrix element which is related to the scattering phase shift is given in angular momentum representation by [146]:

$$t_l(\varepsilon) = \int_0^S dr\, r^2\, j_l(\sqrt{\varepsilon}r)\, v_{\text{in}}(r) R_l(r;\varepsilon). \tag{2.110}$$

After this treatment of the single-site problem, the multiple-scattering properties are taken into account by first calculating the so-called structure constants (of free-space) [145]:

$$g_{LL'}^{nn'}(\varepsilon) = -(1-\delta_{nn'})4\pi\sqrt{\varepsilon}\sum_{L''} i^{l-l'+l''} C_{LL'L''} h_{L''}(\mathbf{R}^n - \mathbf{R}^{n'};\varepsilon), \tag{2.111}$$

where n is a site index of the n'th scattering site, $\mathbf{R}^n$ is the vector pointing to the n'th site, $h_L(\mathbf{r};\varepsilon) = h_l(\sqrt{\varepsilon}r)Y_L(\mathbf{r})$ and $C_{LL'L''}$ are the so-called Gaunt coefficients:

$$C_{LL'L''} = \int d\Omega Y_L(\mathbf{r})Y_{L'}(\mathbf{r})Y_{L''}(\mathbf{r}), \tag{2.112}$$

where Ω indicates the volume in real space. These structure constants are then transformed into Fourier space [145]:

$$g_{LL'}(\mathbf{k};\varepsilon) = \sum_{n\neq n'} g_{LL'}^{nn'}(\varepsilon) e^{i\mathbf{k}(\mathbf{R}^n - \mathbf{R}^{n'})}. \tag{2.113}$$

The total Green's function of the system can now be expressed as [145]:

$$G(\mathbf{r}+\mathbf{R}^n,\mathbf{r}'+\mathbf{R}^{n'};\varepsilon) = -i\sqrt{\varepsilon}\sum_{L} R_L^n(\mathbf{r}_<;\varepsilon)H_L^n(\mathbf{r}_>;\varepsilon)\delta_{nn'} + \sum_{LL'} R_L^n(\mathbf{r};\varepsilon)G_{LL'}^{nn'}(\varepsilon)R_{L'}^{n'}(\mathbf{r}';\varepsilon) \tag{2.114}$$

where $R_L^n(\mathbf{r};\varepsilon) = R_l^n(r;\varepsilon)Y_L(\mathbf{r})$ with an analogous expression for $H_L^n(\mathbf{r};\varepsilon)$. The coefficients $G_{LL'}^{nn'}(\varepsilon)$ represent the structural Greens function which needs to be determined. It can be obtained from the following Dyson equation using free-space as the reference system [145]:

$$G_{LL'}^{nn'}(\varepsilon) = g_{LL'}^{nn'}(\varepsilon) + \sum_{n'',L''} g_{LL''}^{nn''}(\varepsilon)\, t_{l''}^{n''}(\varepsilon) G_{L''L'}^{n''n'}(\varepsilon) \tag{2.115}$$

by matrix inversion and integration over the Brillouin zone (BZ) in k-space [145]:

$$G_{LL'}^{nn'}(\varepsilon) = \frac{1}{\Omega_{\text{BZ}}}\int_{\text{BZ}} d^3k e^{i\mathbf{k}(\mathbf{R}^n - \mathbf{R}^{n'})}\left[\left(1-\underline{g}(\mathbf{k};\varepsilon)\underline{t}(\varepsilon)\right)^{-1}\underline{g}(\mathbf{k};\varepsilon)\right]_{LL'}, \tag{2.116}$$

where Ω_{BZ} is the volume of the BZ and underlined quantities are matrices in L and L'.

By using the total Green's function (2.114) the valence electron density $n^{\mathrm{v}}(\mathbf{r})$ can be obtained from Equation (2.103) by integrating from the bottom of the valence band ε_{B} to E_{F} [145]:

$$n^{\mathrm{v}}(\mathbf{r}) = -\frac{2}{\pi}\mathrm{Im}\int_{\varepsilon_B}^{E_F} d\varepsilon\, G(\mathbf{r},\mathbf{r};\varepsilon). \tag{2.117}$$

In addition, the core-electron density $n^{\mathrm{c}}(\mathbf{r})$ is obtained from the core-states localized at the atomic sites so that the total density $n = n^{\mathrm{c}} + n^{\mathrm{v}}$. Finally, the output potential v_{out} is obtained by solving the Poisson equation and adding the exchange-correlation potential [145]. If v_{in} and v_{out} coincide within the demanded accuracy, observables can be calculated from the obtained Green's function, otherwise the potentials are mixed by a proper scheme to obtain a new input potential for the radial equation. The cycle is performed until convergence is achieved. Remarkably, due to the expansion of the Green's function into the energy-dependent solutions of the radial equation $R_l(r;\varepsilon)$, the KKR formalism can be regarded as operating with an energy-dependent basis.

The KKR formalism can be extended to a variant containing the full anisotropic potential within the crystal which is needed for accurate force calculations [145]. Furthermore, an improvement of the KKR method has been suggested now called the screened or tight-binding KKR formalism [149, 150]. By the help of a screening transformation the Green's function of the reference system falls off exponentially leading finally to sparse matrices within the calculation. This decoupling of distant atomic sites is possible due to the freedom of choice in the reference system and allows for linear scaling of the computing time with system size [145]. Finally, also the accurate treatment of impurities in an infinite host can be accomplished by the KKR method. A Dyson equation can be used to compute for instance the Green's function of a system with an impurity on a surface when the clean surface Green's function is taken as a reference [144]. The embedding of the impurity on the surface ('embedding problem') is correctly described within the Green's function formalism [146].

2.3.5. Connection of DFT to Electronic Transport

DFT results also turned out to be useful for the study of electronic transport properties of nanoscale systems. At first sight this might seem surprising as practical DFT is a theory for the ground state but electronic transport is a non-equilibrium process. However, the most important point is that the KS Hamiltonian can be used as an input for electronic transport theory and DFT therefore provides a useful starting point for specific approaches concerning transport [151]. In addition, for the theory of STM and scanning tunneling spectroscopy (STS), the measured quantity is the local density of states (LDOS) for which the density of states (DOS) obtained from DFT can be a good approximation [152]. It is the objective of this subsection to outline the basic principles of these connections between DFT and electronic transport.

The nanoscale devices considered at this point are made up of a left and a right lead between which the active device component (scattering region) is positioned. This active component can for example consist of a molecule or a metallic nanowire [153]. One of the most extensively studied approaches for the ballistic transport regime, i. e. electrons traveling freely without scattering, to calculate the bias dependent current $I(U)$ through such a nanojunction, is the so called Landauer formula[15] [154, 155]:

$$I(U) = 2\int_{-\infty}^{+\infty} d\varepsilon\, T(\varepsilon, U)[f_{\mathrm{L}}(\varepsilon) - f_{\mathrm{R}}(\varepsilon)], \tag{2.118}$$

where $T(\varepsilon, U)$ is the energy and bias dependent transmission function and f_{L} and f_{R} are the Fermi functions for the left and right lead, respectively. The bias dependence of the transmission function reflects the fact that the applied bias voltage leads to a change in potential energy within the scattering region as this is the part of the device where the voltage drops. The transmission function can be interpreted as the probability amplitude for an electron to tunnel from the left to the right lead [156]. In a simple model presented in Ref. [155] for the transport through a single energy level, it is connected to the DOS $\rho(\varepsilon)$ of the active device component [155]:

$$T(\varepsilon, U) = \rho(\varepsilon - U)\frac{\gamma_{\mathrm{L}}\gamma_{\mathrm{R}}}{\gamma_{\mathrm{L}} + \gamma_{\mathrm{R}}}, \tag{2.119}$$

where $\gamma_{\mathrm{L/R}}$ describes the coupling of the scattering region to the left/right lead and can therefore be interpreted as hopping matrix element between the specific lead and the scattering region. In addition, the difference of the chemical potentials[16] μ_{L} and μ_{R} of left and right lead represents the applied voltage:

$$\mu_{\mathrm{L}} - \mu_{\mathrm{R}} = U. \tag{2.120}$$

For very low temperatures close to $T = 0$ K the expression can be simplified as the Fermi functions in Equation (2.118) in this case are sharp, step-like functions which effectively reduces the integral range to energies between μ_{L} and μ_{R} [155]:

$$I(U) = 2\int_{\mu_{\mathrm{R}}}^{\mu_{\mathrm{L}}} d\varepsilon\, T(\varepsilon, U). \tag{2.121}$$

This form highlights the special significance of the electronic structure of the active device region near the Fermi level for small bias voltages. Clearly, to make use of these equations a certain amount of input from the electronic structure theory dealing with the active device component within the junction is needed. This data could in principle be obtained using different quantum chemical methods [154], but particularly DFT results are appealing because

[15] Note that atomic units are used and that the current expression refers to a nonmagnetic system.
[16] The chemical potential is identical to the Fermi energy E_{F} at $T = 0$ K.

of the good balance between accuracy and computational effort [157].

For an exact treatment of devices with many levels contributing to the transport a more general approach is needed that can also take into account incoherent transport processes and is provided by the so called non-equilibrium Green's function (NEGF) formalism [155, 156]. Within this method the quantities characterizing the system are expressed by matrices rather than scalar functions. The non-equilibrium Green's function $G(\varepsilon)$ containing all information of the scattering region connected to the leads is given by [158]:

$$G(\varepsilon) = \lim_{\eta \to 0} [(\varepsilon + i\eta) - H_S - \Sigma_L - \Sigma_R]^{-1}, \tag{2.122}$$

where H_S is the Hamiltonian of the scattering region and $\Sigma_{L/R}$ represents the self-energy for the left/right lead, respectively. These self-energies describe the effects of the leads coupled to the scattering region. They can be evaluated using the surface Green's function of the leads which can be constructed efficiently using an algorithm presented in Ref. [157].

As the bias modifies the charge distribution over the scattering region, the potential profile over this region must be calculated self-consistently since a change in density again affects the potential. A self-consistency scheme can be established in which one first obtains the Hamiltonian H_S from a trial density using for instance DFT. Then the precomputed surface Green's functions of the leads are used to calculate the self-energies to obtain the Green's function (2.122). Using this Green's function, a lesser Green's function can be evaluated from which a new density is obtained [157]. This cycle is repeated until convergence is achieved. The current can subsequently be calculated from [158]:

$$I(U) = 2 \int_{-\infty}^{+\infty} d\varepsilon \, \mathrm{Tr}[G\Gamma_L G^\dagger \Gamma_R][f_L(\varepsilon) - f_R(\varepsilon)], \tag{2.123}$$

where $\Gamma_{L/R}$ is now the matrix accounting for the broadening of the states of the active device region due to its coupling to the leads. It is the anti-Hermitian part of the self-energies whereas the Hermitian part adds to the Hamiltonian and shifts the energies [155]. $G^\dagger$ is the Hermitian conjugate of G. Formally, the transmission function $T(\varepsilon, U)$ of Equation (2.118) is replaced by the term $\mathrm{Tr}[G\Gamma_L G^\dagger \Gamma_R]$ to obtain the current although it has been outlined in Ref. [159] that for inelastic scattering processes any relation between those two quantities is improbable. However, a detailed introduction to the NEGF formalism is beyond the scope of this thesis and comprehensive accounts can be found in Refs. [156, 160].

A slightly different experimental scheme concerning transport where DFT can supply extremely useful information is provided by STM and STS where a voltage is applied between a substrate and an (ideally atomically sharp) STM tip which is positioned closely above the substrate. The resulting tunneling current is then measured and can provide insight into the

electronic properties of the substrate and possible adsorbates on the substrate with high lateral resolution down to the atomic level [161].

An early study to model tunnel junctions was proposed by Bardeen [162] who developed a theory for the time evolution of the wave function in these junctions. According to Bardeen and with direct relation to the STM setup the tunneling probability per unit time $P_{\mu\nu}(t)$ between a state of the substrate S labeled by μ and a state of the tip T labeled by ν is given by [152]:

$$P_{\mu\nu}(t) = 4\pi\delta(\varepsilon_\mu^{\mathrm{S}} - \varepsilon_\nu^{\mathrm{T}})|M_{\mu\nu}|^2, \tag{2.124}$$

where $M_{\mu\nu} = \langle\phi_\nu^{\mathrm{T}}|\upsilon_{\mathrm{T}}|\phi_\mu^{\mathrm{S}}\rangle$ is the transition matrix element of the junction with the potential υ_{T} on the side of the tip. It describes the projection of the initial state ϕ_μ^{S} affected by the potential υ_{T} onto the state ϕ_ν^{T} [152]. Equation (2.124) is essentially Fermi's Golden rule which is a general result of first order time-dependent perturbation theory and in which the elastic character of the tunneling is explicitly secured by the δ-function. The tunneling current is then proportional to $P_{\mu\nu}$ summed over all states contributing to the transport [152]:

$$I = 4\pi\sum_{\mu\nu}[f_{\mathrm{S}} - f_{\mathrm{T}}]|M_{\mu\nu}|^2\delta(\varepsilon_\nu^{\mathrm{T}} - \varepsilon_\mu^{\mathrm{S}} - U), \tag{2.125}$$

where $f_{\mathrm{S/T}}$ is the Fermi function of the substrate/tip and U is the applied voltage. In general the sum can be replaced by an energy integration taking into account the DOS of the substrate ρ^{S} and the DOS of the tip ρ^{T} [152]:

$$I = 4\pi\int d\varepsilon[f_{\mathrm{S}} - f_{\mathrm{T}}]\rho^{\mathrm{T}}(\varepsilon - U)\rho^{\mathrm{S}}(\varepsilon)|M(\varepsilon, \varepsilon - U)|^2. \tag{2.126}$$

This relation shows that in general the tunneling current includes both the electronic structure of the substrate and of the tip via their respective DOS. The dependence on the DOS also indicates that STM can address occupied and unoccupied states of the substrate. Notably, also inelastic contributions to the tunneling can be included into the formalism [152]. The problematic part in the evaluation of Equations (2.125) and (2.126) is how to obtain the matrix elements $M_{\mu\nu}$. Within Bardeen's approach these are obtained by a surface integral being only related to the unperturbed wave functions of tip and substrate at the tunnel junction [152]:

$$M_{\mu\nu} = \frac{1}{2}\int dxdy\left[\phi_\mu^{\mathrm{S}}\frac{\partial\phi_\nu^{\mathrm{T}*}}{\partial z} - \phi_\nu^{\mathrm{T}*}\frac{\partial\phi_\mu^{\mathrm{S}}}{\partial z}\right]. \tag{2.127}$$

These matrix elements include an energy dependence important for the spectroscopic mode, i. e. STS.

Although the presented scheme can be carried out in principal, the main drawback is that the tip structure needed for the description is usually not available. Therefore models for the

electronic structure of the tip have been proposed.

Tersoff and Hamann [163] modeled the tip as a geometrical point in space allowing to eliminate the tip from the actual calculation. The tip is considered as a locally spherical potential at $\mathbf{R}_\mathrm{T}$. Thereby it is treated as a single atom with an s-orbital. The tunneling matrix elements in the Tersoff-Hamann model are then given by [152]:

$$M_{\mu\nu}(\mathbf{R}_\mathrm{T}) = -\frac{2\pi C}{\kappa}\phi_\mu^\mathrm{S}(\mathbf{R}_\mathrm{T}), \tag{2.128}$$

where C is the normalization constant of the tip wave function and κ is a decay constant describing the penetration of the tip wave function into the vacuum barrier. The tunneling matrix element is hence proportional to the value of the sample wave function ϕ_μ^S at the position of the tip [152]. The tunneling current at low temperature (which reduces the integral again to states within the bias window) is then given by [152]:

$$I = \frac{16\pi^3 C^2}{\kappa^2}\rho^\mathrm{T}\int_0^U d\varepsilon\, \rho^\mathrm{S}(\mathbf{R}_\mathrm{T},\varepsilon), \tag{2.129}$$

where ρ^T is constant since it originates from an s-state. Consequently, all states of the sample at the location of the tip within the bias window are important which means that the current effectively measures the integrated LDOS within a specific energy interval. For small voltages the integral can be further simplified by considering the sample DOS to be constant which means that spectroscopic images effectively depict the DOS of the sample [152]. The basic assumption of the Tersoff-Hamann model is that the tip can be modeled solely by an s-state. However, Chen has proposed a method to extend the formalism to include the influence of other tip states [164, 165]. It turns out that for tip states of higher angular momentum spatial derivatives of the sample wave functions have to be taken into account.

Finally, for magnetic tips and substrates the tunneling current includes also information about the spin polarization of the sample. This variant of STM is called spin-polarized STM (SP-STM). For the modeling of this technique two-component spinor wave functions are needed within Bardeen's approach and the current in the Tersoff-Hamann model can be decomposed into a non spin-polarized and a spin-polarized contribution originating from the fact that in most cases the spin quantization axes of tip and sample are not aligned in parallel [152].

3 Magnetic Interactions

This chapter introduces the basic interactions responsible for the collective magnetic phenomena such as ferro-, ferri- and antiferromagnetism observed in magnetic materials. Firstly magnetism is outlined as a purely quantum mechanical phenomenon since by the virtue of the Bohr-van Leeuwen theorem it can be rigorously shown that in a classical system no magnetization can occur. The magnetic moments eventually arise from the inclusion of relativistic effects into quantum mechanics in terms of the Dirac equation leading to the spin of the electron and from aufbau principles as the Hund's rules or the energy gain resulting from the spontaneous spin splitting in band magnets. Thereafter the exchange interaction is presented as the driving mechanism to couple different magnetic moments and the Heisenberg, Ising and Hubbard models of magnetism are briefly introduced. In the following, the typical exchange mechanisms as direct, super-, double and RKKY exchange are described shortly. Finally, an account on selected non-standard exchange contributions as higher order exchange and the Dzyaloshinskii-Moriya interaction as well as the magnetic anisotropy is given.

3.1. Origin of Magnetism and Theoretical Models

3.1.1. Origin of Magnetism

The origin of magnetism is a purely quantum mechanical one. For a classical system it can be rigorously shown based on the Bohr-van Leeuwen theorem that there can be no magnetization in thermal equilibrium [166, 167]. The proof is based on the reasoning that the partition function $\mathcal{Z}$ of a classical system of N particles with charge q is proportional to [166]:

$$\mathcal{Z} \propto \int\int\cdots\int \exp(-\beta E(\{\mathbf{r}_i,\mathbf{p}_i\}) d\mathbf{r}_1\cdots d\mathbf{r}_N d\mathbf{p}_1\cdots d\mathbf{p}_N), \tag{3.1}$$

where $\beta = \frac{1}{k_B T}$, k_B is the Boltzmann constant, T is the temperature and $E(\{\mathbf{r}_i,\mathbf{p}_i\})$ stands for the energy of the N charged particles with positions $\mathbf{r}_1,\ldots,\mathbf{r}_N$ and momenta $\mathbf{p}_1,\ldots,\mathbf{p}_N$. A magnetic field $\mathbf{B}$ will shift the momentum associated with each particle by $q\mathbf{A}$ where $\mathbf{A}$ is the magnetic vector potential for which $\mathbf{B} = \nabla\times\mathbf{A}$ applies. But since the momentum integration in Equation (3.1) for each particle is carried out from $-\infty$ to $+\infty$, the effect of the shifted momentum can be canceled by just shifting the origin in the integration. This means that the partition function is independent of the magnetic field which is then also true for the free energy $F = -k_B T\log\mathcal{Z}$ and consequently all other physical quantities [166]. Thus magnetism is outside the realm of classical physics.

Due to quantum mechanics the magnetic moments predominantly originate from the spin of the electrons since the moment due to the orbital motion of the electrons is quenched in

many systems [166]. The spin degree of freedom of the electron itself is obtained by including the relativistic energy-momentum relation into quantum mechanics as it is done in the Dirac equation [167]. The moments at different atomic centers are eventually due to the rules that determine how to fill the electronic levels in terms of aufbau principles as the Hund's rules originating from on-site Coulomb exchange [168]. In band magnets the moments at each ion are formed as a consequence of the energy gain obtained by a spontaneous spin splitting of the bands at the Fermi energy [166].

As it turns out, the interaction of these moments can also not be understood from a classical magnetostatics point of view. The magnetostatic energy contribution due to the dipole-dipole interaction between the two magnetic moments $\mathbf{m}_1$ and $\mathbf{m}_2$ separated by $\mathbf{d}$ reads [167]:

$$E = \frac{\mu_0}{4\pi d^3}\left\{\mathbf{m}_1 \cdot \mathbf{m}_2 - \frac{3}{d^2}(\mathbf{m}_1 \cdot \mathbf{d})(\mathbf{m}_2 \cdot \mathbf{d})\right\}, \tag{3.2}$$

where μ_0 is the magnetic permeability of free space. If one estimates the energy scale of this interaction based on two moments of one Bohr magneton $m_1 = m_2 = 1\ \mu_B$ each and a separation of $d \approx 1$ Å then one obtains about 1 K (about 86 μeV) in pronounced disagreement with the magnetic ordering temperatures (Curie temperatures) of about 1000 K for Fe and Co [166]. Hence the origin of the effective coupling of magnetic moments in a material is also purely quantum mechanical. The indistinguishability of elementary particles and the associated antisymmetrization of the many particle wave function for Fermions finally leads to the quantum mechanical exchange interaction which is the driving mechanism coupling the moments and giving rise to long-range magnetic order and collective magnetic phases. The exchange interaction is specifically included in the *ab initio* approaches to electronic structure described in Chapter 2 due to the construction of the many body wave function out of antisymmetrized Hartree products, i. e. a Slater determinant which inherently incorporates exchange contributions.

However for the coupled magnetic moments to align along a preferred spatial direction another interaction is needed which is given by the magnetic anisotropy. It originates predominantly from SOC and leads to the fact that an alignment of the magnetization along certain spatial directions according to the lattice potential is preferred over others. This gives rise to an energy barrier called anisotropy barrier when the magnetization is tilted away from this direction.

These ingredients are responsible for the characteristic magnetic properties of especially ferromagnets to exhibit a stable magnetization up to the Curie temperature and to show a magnetic hysteresis, i. e. a dependence of the magnetic properties of the sample on its history within a certain range magnetic field characterized by the coercive field strength. In the following first a general account on the coupling of spins will be outlined before different types of exchange and magnetic anisotropy will be introduced in detail.

3.1.2. Exchange Coupling of Two Spins

For the simple case of two spin-$\frac{1}{2}$ particles a and b the exchange coupling can be analyzed in detail [166]. Therefore one considers the Hamiltonian:

$$\hat{H}^{\text{spin}} = -K\,\hat{\mathbf{S}}_a \cdot \hat{\mathbf{S}}_b, \tag{3.3}$$

where $\hat{\mathbf{S}}_a$ and $\hat{\mathbf{S}}_b$ stand for the spin operators of particles a and b and K is a constant. Consequently, the resulting spin quantum number s of the two particle system has the values $s = 0$ or $s = 1$. Therefore the square of the total spin operator

$$\hat{\mathbf{S}}_{\text{tot}} = \hat{\mathbf{S}}_a + \hat{\mathbf{S}}_b \tag{3.4}$$

has eigenvalues 0 or 2 according to $s(s+1)$. By taking the square of Equation (3.4) [166]:

$$\hat{\mathbf{S}}^2_{\text{tot}} = \hat{\mathbf{S}}^2_a + \hat{\mathbf{S}}^2_b + 2\hat{\mathbf{S}}_a \cdot \hat{\mathbf{S}}_b \tag{3.5}$$

the eigenvalues of the above Hamiltonian can be derived. Both the eigenvalues of $\hat{\mathbf{S}}^2_a$ and $\hat{\mathbf{S}}^2_b$ are $\frac{3}{4}$ as the eigenvalue of each squared Cartesian spin component is equal to $\frac{1}{4} = (\pm\frac{1}{2})^2$. This results in:

$$\langle \hat{\mathbf{S}}_a \cdot \hat{\mathbf{S}}_b \rangle = \begin{cases} \frac{1}{4} & \text{for} \quad s = 1 \\ -\frac{3}{4} & \text{for} \quad s = 0. \end{cases} \tag{3.6}$$

The coupled system has consequently two energy levels:

$$E = \begin{cases} -\frac{K}{4} & \text{for} \quad s = 1 \\ \frac{3K}{4} & \text{for} \quad s = 0. \end{cases} \tag{3.7}$$

The degeneracy of each of the two levels is $2s+1$ fold. Hence the first one is a triplet state and the second one is a singlet state. The z-component of the coupled spins associated with quantum number m_s then takes the values from $-s$ to $+s$. A symbolic representation of the eigenstates can be obtained based on the general coupling of angular momenta yielding [54]:

$$|s, m_s\rangle = \begin{cases} |1,1\rangle & = |\uparrow\uparrow\rangle \\ |1,0\rangle & = \frac{|\uparrow\downarrow\rangle + |\downarrow\uparrow\rangle}{\sqrt{2}} \\ |1,-1\rangle & = |\downarrow\downarrow\rangle \\ |0,0\rangle & = \frac{|\uparrow\downarrow\rangle - |\downarrow\uparrow\rangle}{\sqrt{2}}, \end{cases} \tag{3.8}$$

where the first arrow refers to the z-component of the first spin and the second arrow to the z-component of the second spin.

3.1.3. Heisenberg Model

To outline basic aspects of exchange, the simplest case is to consider two electrons at $\mathbf{r}_1$ and $\mathbf{r}_2$ in orbitals ϕ_a and ϕ_b for which the total wave function Φ has to be antisymmetric [169]. As a consequence, either the spatial part is symmetric and the spin part is an antisymmetric singlet state χ_S:

$$\Phi_S = \frac{1}{\sqrt{2}}[\phi_a(\mathbf{r}_1)\phi_b(\mathbf{r}_2) + \phi_a(\mathbf{r}_2)\phi_b(\mathbf{r}_1)]\chi_S \tag{3.9}$$

or otherwise the spatial part is antisymmetric and the spin contribution is a symmetric triplet state χ_T:

$$\Phi_T = \frac{1}{\sqrt{2}}[\phi_a(\mathbf{r}_1)\phi_b(\mathbf{r}_2) - \phi_a(\mathbf{r}_2)\phi_b(\mathbf{r}_1)]\chi_T. \tag{3.10}$$

The energy of each state can be evaluated by the expectation value of the two-electron Hamiltonian $\hat{H}$ assuming that the spin functions are normalized [166]:

$$\begin{aligned} E_S &= \langle\Phi_S|\hat{H}|\Phi_S\rangle \\ E_T &= \langle\Phi_T|\hat{H}|\Phi_T\rangle. \end{aligned} \tag{3.11}$$

Then the energy-difference between E_S and E_T can be expressed as [169]:

$$E_S - E_T = 2\int \phi_a^*(\mathbf{r}_1)\phi_b^*(\mathbf{r}_2)\hat{H}\phi_a(\mathbf{r}_2)\phi_b(\mathbf{r}_1)\, d^3r_1\, d^3r_2 := J, \tag{3.12}$$

which defines the exchange integral J[1]. This result can be used in conjunction with the expectation value of the coupling term given in Equation (3.6) to obtain a parametrized effective form of the Hamiltonian [166]:

$$\hat{H} = \frac{1}{4}(E_S + 3E_T) - (E_S - E_T)\hat{\mathbf{S}}_1 \cdot \hat{\mathbf{S}}_2. \tag{3.13}$$

The first part of this Hamiltonian only shifts the energy scale by a constant and can therefore be set to zero. The second part can be expressed using the exchange coupling constant J defined in Equation (3.12) leading to the effective spin Hamiltonian:

$$\hat{H}^{\text{spin}} = -J\hat{\mathbf{S}}_1 \cdot \hat{\mathbf{S}}_2. \tag{3.14}$$

This result reveals that ferromagnetic (FM) alignment of the spins is realized if $J > 0$ whereas antiferromagnetic (AFM) alignment is favored for $J < 0$. Hence the sign of the exchange coupling constant is directly related to the type of magnetic ordering. This Hamiltonian can be generalized assuming analogous interactions between all neighboring spins [166, 169] leading

[1] Notably, it is also possible to define the exchange integral to be half of the present value[166].

to the Heisenberg model[2]:

$$\hat{H}_{\mathrm{HB}}^{\mathrm{spin}} = -\frac{1}{2}\sum_{i,j} J_{ij}\hat{\mathbf{S}}_i \cdot \hat{\mathbf{S}}_j, \tag{3.15}$$

where the exchange coupling constant J_{ij} indicates the strength of the exchange coupling between spins i and j. It is completely determined by the overlap of the corresponding wave functions at the different centers [167]. The Heisenberg model is one of the most important approaches used to describe and analyze magnetic properties of materials. If only the z components, i. e. $\hat{S}_{z,i}$, $\hat{S}_{z,j}$, are taken into account in Equation (3.15) the Heisenberg model reduces to the Ising model which is frequently used to analyze phase transitions [167, 169].

Importantly, in the classical limit of the above Heisenberg model the quantum mechanical spin operators $\hat{\mathbf{S}}_i$ and $\hat{\mathbf{S}}_j$ are substituted by their expectation values $\mathbf{S}_i$ and $\mathbf{S}_j$[3]. These are directly related to the magnetic moments obtained from DFT via $\mathbf{m}_i = 2\mu_{\mathrm{B}}\mathbf{S}_i$ and this therefore establishes a connection to the results obtained from *ab initio* calculations. Hence in the following all spin Hamiltonians will be considered in their respective classical limit.

3.1.4. Calculation of the Exchange Coupling Constant

There are different ways to calculate the exchange coupling constants J_{ij} of the Heisenberg model from DFT results. A first approach would be to perform individual calculations for the FM and suitably chosen AFM configurations of the coupled moments and to deduce the coupling constants from the resulting algebraic problem in the spirit of the so-called 'broken-symmetry approach' introduced by Noodleman [170]. For example in case of the coupling of two Ising spins S_1 and S_2 the following equation can be derived based on the Heisenberg Hamiltonian:

$$E_{\mathrm{FM}} - E_{\mathrm{AFM}} = -2J_{12}S_1S_2, \tag{3.16}$$

where S_1 and S_2 are the values of the first and second spin and E_{FM} (E_{AFM}) is the energy of the (anti-)ferromagnetic configuration from which the coupling constant J_{12} can be easily obtained as: $J_{12} = \frac{E_{\mathrm{FM}}-E_{\mathrm{AFM}}}{-2S_1S_2}$.

In another approach suggested by Liechtenstein and coworkers [171] the exchange coupling constants are calculated by the method of infinitesimal rotations. It relates the energy change of the Heisenberg Hamiltonian due to a small tilting of the directions of the magnetic moments by an angle θ with respect to each other to the change of the DFT total energy [171]. The exchange coupling constants are finally expressed as [171, 172]:

$$J_{nn'} = \frac{1}{4\pi}\mathrm{Im}\int^{E_{\mathrm{F}}} \mathrm{Tr}_{lm}\{G^{\uparrow}_{nn'}(\varepsilon)[t^{\uparrow}_{n'}(\varepsilon) - t^{\downarrow}_{n'}(\varepsilon)]G^{\downarrow}_{n'n}(\varepsilon)[t^{\uparrow}_{n}(\varepsilon) - t^{\downarrow}_{n}(\varepsilon)]\}d\varepsilon = \int^{E_{\mathrm{F}}} j_{nn'}(\varepsilon)d\varepsilon, \tag{3.17}$$

[2] In order to avoid double counting, the prefactor $\frac{1}{2}$ has been included.
[3] Note that the spins correspond to angular momenta in units of $\hbar$.

where $G^{\uparrow,\downarrow}_{nn'}(\varepsilon)$ is the inter-site structural Greens function for spin up ($\uparrow$) or spin down ($\downarrow$) as obtained from the KKR formalism (see Subsection 2.3.4), $t^{\uparrow,\downarrow}_n$ are the spin dependent scattering matrices of sites n and n' and Tr_{lm} is a trace over angular momentum quantum numbers. The integrand of Equation (3.17) can be identified as an exchange coupling density $j_{nn'}(\varepsilon)$ which can be used for analyzing purposes [172]. By performing the energy integration in Equation (3.17) up to different energies (below and above E_F), an energy-dependent exchange coupling constant $J(\varepsilon)$ can be obtained which can be used to assess the influence of the states crossing the Fermi level onto the magnetic coupling [172].

According to the model of Alexander and Anderson [173] FM coupling is favored when (only) one of the spin split d-bands has large weight at the Fermi energy due to the effective energy saving by the formation of bonding and antibonding states [174] (see Fig. 3.1(a)). On the other hand AFM coupling is dominant when the Fermi level lies in the region between the spin split d-bands since then a net energy gain is possible due to the energetic lowering of the occupied d-bands [174] (see Fig. 3.1(b)).

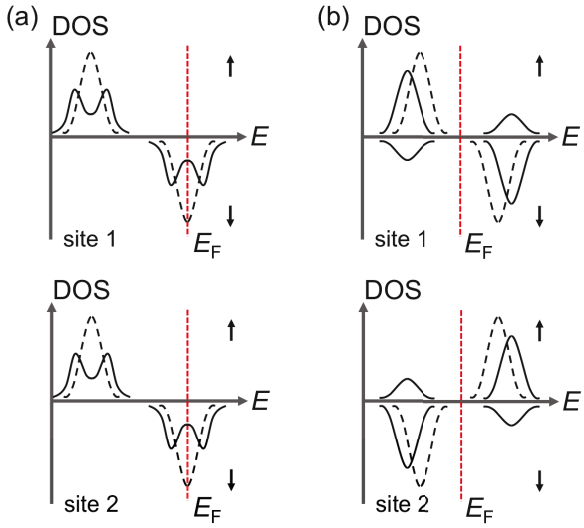

Figure 3.1.: Interaction of two magnetic sites according to the Alexander-Anderson model [173]. For a high DOS of for instance minority spin electrons at the Fermi level (a) FM alignment of the moments leads to a splitting of the states into bonding and antibonding states which gives rise to an energy gain not present for AFM alignment. However when the Fermi level lies between the spin-split bands (b) AFM coupling leads to an energy gain not found in the FM case. Full lines: DOS of the interacting sites and broken lines: DOS of the individual sites neglecting interaction (based on a figure in Ref. [174]).

Nevertheless it is important to realize that the two approaches to calculate the exchange coupling constants correspond to different physical regimes. A complete switching of selected moments from a parallel to an antiparallel configuration as done in the first method can in certain cases be related to the switching of the moments in an applied magnetic field when recording a hysteresis loop or to the large spin fluctuations close to the Curie temperature. On the contrary, the second method that relies on only slightly tilting the spins with respect to each other is rather characteristic for the regime of spin wave propagation or certain spiral spin-density waves. Therefore a comparison of the exchange coupling constants obtained with the different methods should be done with care.

3.1.5. Hubbard Model

There is another important model for the description and qualitative understanding of magnetic properties which is called the Hubbard model. It is especially suited for the treatment of band magnets such as Fe, Co and Ni in which the magnetism arises from the relatively narrow $3d$ bands [167]. The Hamiltonian of the (one band) Hubbard model can be expressed as [167]:

$$\hat{H} = \sum_{ij\sigma} t_{ij} c^{\dagger}_{i\sigma} c_{j\sigma} + \frac{1}{2} U \sum_{i\sigma} n_{i\sigma} n_{i-\sigma}, \tag{3.18}$$

where t_{ij} is the hopping integral (hopping matrix element) between the states centered at lattice sites i and j, $c^{\dagger}_{i\sigma}$ is the creation operator for an electron at site i with spin σ, $c_{j\sigma}$ is the corresponding annihilation operator at site j, U symbolizes the on-site Coulomb repulsion energy and $n_{i\sigma} = c^{\dagger}_{i\sigma} c_{i\sigma}$ is the occupation number operator of the state at site i. So only if two electrons with opposite spin are present at the same center i then the on-site Coulomb repulsion term U is 'activated'. In general, the ratio of U to the bandwidth W of the considered band determines whether a system is insulating ($U > W$) or metallic ($W > U$) or in a transition region ($U \sim W$) [166]. The Hubbard model is frequently used to treat for instance band magnetism and metal-insulator transitions (Mott transitions) [167].

3.2. Exchange Mechanisms

3.2.1. Direct Exchange

The most natural first approach to exchange is to consider a direct exchange interaction between the atoms carrying the magnetic moments. This direct interaction through space is connected to the bonding between those centers as the formation of bonds allows the electrons to delocalize and thereby minimize the kinetic energy (kinetic exchange) [175]. As an

electron within a bonding state can only hop to a neighboring site if the spin of the electron is aligned antiparallel to the electron at this receiving center due to the Pauli principle, the direct exchange interaction usually leads to antiferromagnetism [166, 168]. This process is visualized in Fig. 3.2. For this direct exchange interaction an effective Hamiltonian of the Heisenberg type acting on the spins:

$$H_{\text{direct}}^{\text{spin}} = -\frac{1}{2}\sum_{i,j} J_{ij}^{\text{direct}} \mathbf{S}_i \cdot \mathbf{S}_j, \tag{3.19}$$

can be derived based on first order perturbation theory of the electron-electron interaction with the Heitler-London method [167] or by explicitly taking into account ionic contributions to the states within a model describing the hopping process of the electrons [168]. In the second case the exchange coupling constant can be parametrized for large on site Coulomb interaction U as:

$$J^{\text{direct}} = -\frac{4t^2}{U}, \tag{3.20}$$

where t is the hopping matrix element between the interacting states [168].

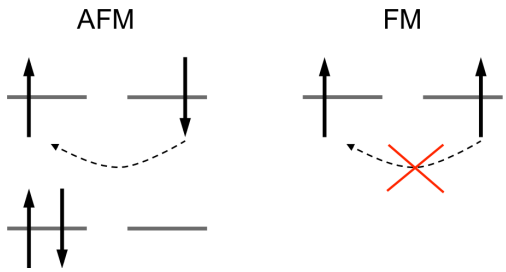

Figure 3.2.: The direct exchange mechanism. In the case of an AFM alignment of the spins, hopping is allowed and the electrons can be delocalized to save kinetic energy. On the contrary, for FM alignment the hopping process is suppressed due to the Pauli principle (based on a figure in Ref. [168]).

There is however also a FM contribution to the coupling when the spins are aligned parallel in different orbitals as this minimizes the potential energy (potential exchange) [168, 175]. If in a metallic system the Fermi energy lies at a pronounced peak of the DOS, the kinetic energy cost to transfer spin down electrons into spin up electrons is relatively small as they stay close to the Fermi level. If in addition the on-site Coulomb interaction U is high and intensively screened, then a considerable amount of potential energy can be saved by aligning the moments parallel to one another [167]. Thereby the gain in potential energy can outweigh the cost in kinetic energy which is expressed by the Stoner criterion for ferromagnetism [166]:

$$U\rho(E_{\text{F}}) \geq 1, \tag{3.21}$$

i. e. the product of the on-site Coulomb interaction and the DOS at the Fermi energy should be larger than one. This then leads to spontaneously spin split bands and gives a qualitative and at the same time physically insightful explanation for metallic ferromagnetism.

However the direct exchange mechanism depends on the direct overlap of the interacting states and it is therefore of short range as it decreases exponentially with the distance between the centers [167]. Hence it cannot be the only mechanism leading to magnetic coupling in a variety of systems. Particularly in materials containing rare earth elements, the magnetic f-states are strongly localized close to the atomic center rendering direct overlap between neighboring magnetic centers unlikely [166]. The situation turns out to be a bit different in case of transition metal elements. The d-states are naturally more delocalized than the f-states of rare earth elements but nevertheless the direct exchange mechanism can be overcompensated by band structure effects in metals or other exchange mechanisms [166]. Consequently, the direct exchange mechanism can only be of special importance in materials with short distances between the magnetic centers.

3.2.2. Superexchange

The superexchange mechanism describes the indirect exchange between magnetic centers proceeding along a path over intermediate non-magnetic ions. This mechanism is of special relevance for the magnetic coupling occuring within both ionic solids (especially oxides) and molecular magnets [166, 167, 175].

A prominent superexchange mechanism present for instance in MnO is the so called 180° superexchange interaction. In Fig. 3.3(a) it is shown for the exemplary case of two $d_{x^2-y^2}$-states coupled by a p_x-orbital of a diamagnetic element situated between the two magnetic centers. In the figure selected spin configurations for a FM as well as an AFM alignment of the moments at the two magnetic centers are listed. In the AFM case the hopping is allowed and the system can minimize its kinetic energy due to the delocalization of the electrons. However in the FM case the hopping processes are not allowed as they would yield configurations that violate the Pauli principle [166]. The procedure can be extended to take into account more configurations as done in Ref. [168] but the result is always that for an AFM alignment of the moments more configurations are allowed and hence the lowering in energy is larger and the interaction is AFM. In general the superexchange mechanism is derived from second order perturbation theory [166]. Based on a cluster model an effective Hamiltonian for the superexchange interaction between the spins can be derived which in lowest order is of Heisenberg type [167]:

$$H_{\mathrm{SE}}^{\mathrm{spin}} = -J_{12}^{\mathrm{SE}} \mathbf{S}_1 \cdot \mathbf{S}_2, \tag{3.22}$$

where 'SE' stands for 'superexchange'. The exchange coupling constant of the model can be

expressed as [167]:

$$J_{12}^{\mathrm{SE}} = -\frac{2t^4}{S^2U^2(U+V)}, \tag{3.23}$$

where t is again the hopping matrix element between the configurations taken into account, S is the absolute value of the interacting spins, U measures the on-site Coulomb repulsion of the electrons in the d-states and V is the on-site Coulomb repulsion of the electrons in the d-states taking into account an empty p orbital at the intermediate ion.

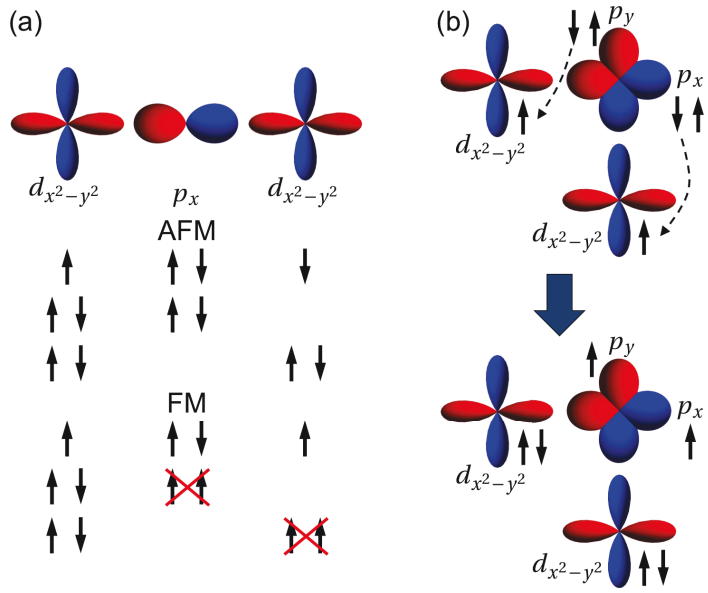

Figure 3.3.: (a) 180° superexchange mechanism between two $d_{x^2-y^2}$-states mediated by a p_x-state at an intermediate center. For the AFM configuration the hopping of the electrons is allowed whereas in the FM configuration it is suppressed due to the Pauli principle. (b) 90° superexchange mechanism between two $d_{x^2-y^2}$-states mediated by a p_x- and a p_y-state of an intermediate center. If the spins in the d-states are initially aligned ferromagnetically, then two electrons from the occupied p-states can hop such that an energetically favorable FM alignment (first Hund's rule) of the spins at the intermediate center is achieved. Blue colored parts of the orbitals correspond to negative sign of the wave function and red colored parts to positive sign of the wave function ((a) based on a figure in Ref. [166]), (b) based on a figure in Ref. [168]).

A different superexchange scenario occurs when the two $d_{x^2-y^2}$-states are positioned at a 90° angle relative to one another. Then the interaction cannot be described anymore by a single p-orbital at the intermediate ion but two p-states (here p_x and p_y) have to be taken into account. Fig. 3.3(b) shows that for a FM alignment of the unpaired spins in the $d_{x^2-y^2}$-

states (upper part of Fig. 3.3(b)) the spin down electrons can hop from the p-orbitals at the intermediate ion into the d-orbitals to form electron pairs (lower part of Fig. 3.3(b)). As a consequence, the remaining spins in the two p-orbitals at the intermediate ion are aligned ferromagnetically which is preferred over AFM alignment according to the first Hund's rule. Such a FM alignment at the intermediate ion after hopping cannot be realized for an AFM initial alignment at the two magnetic centers. Hence this mechanism favors FM coupling. It turns out that similar as before the coupling constant is proportional to the fourth power of the hopping matrix element between the p- and the d-orbitals but this 90° superexchange mechanism is usually weaker than the 180° mechanism and both compete if the angle lies between 90° and 180° [168]. Detailed accounts and more specific rules on superexchange interactions can be found in the contributions of Goodenough and Kanamori [176, 177].

3.2.3. Double Exchange

In materials where the magnetic ion is simultaneously present in two different oxidation states (mixed valence), the double exchange[4] mechanism can be observed. Prominent examples of systems showing this type of exchange interaction are $La_{1-x}Sr_xMnO_3$ (LSMO) for x up to 0.175 or Fe_3O_4 [166, 167]. In LSMO the Mn ions coexist in two oxidation states namely Mn^{3+} and Mn^{4+} for which the double exchange mechanism can be explained with reference to Fig. 3.3(a). An octahedral crystal environment at the Mn ions splits the 5 d-states into three degenerate lower lying t_{2g}-states and two degenerate higher lying e_g-states. For Mn^{3+} the spins of all four d-electrons are aligned ferromagnetically throughout the t_{2g}- and e_g-states according to the first Hund's rule. Now the single e_g electron can hop to a neighboring Mn^{4+} site. This hopping process will be energetically favored when it arrives at the Mn^{4+} site with its spin parallel to the ones of the t_{2g} electrons already present at that site again due to the first Hund's rule. Therefore without spin flipping during the hopping, this process gives rise to an effective FM coupling of the magnetic sites as for AFM alignment the hopping will be suppressed. In addition to this magnetic coupling, the hopping electron also leads to metallic behavior of the material below the Curie temperature [166]. It should however be mentioned that the double exchange mechanism can also be understood in terms of the Alexander-Anderson model as indicated in Fig. 3.1 since the interaction of the d-states at the Fermi level gives rise to the formation of bonding and antibonding states [172, 174].

Based on a cluster model describing the hopping process again an effective Hamiltonian for the spin-spin interaction can be derived which only in lowest order $n = 1$ is of Heisenberg

[4]The name double exchange originates from the finding that this interaction doubles the amount of states leading to delocalization [175].

type and otherwise contains higher orders of the scalar product between the spins [167]:

$$H_{\mathrm{DE}}^{\mathrm{spin}} = -t \sum_{n=0}^{2S} J_n^{\mathrm{DE}}(S)(\mathbf{S}_1 \cdot \mathbf{S}_2)^n, \tag{3.24}$$

where 'DE' means 'double exchange', t is the hopping matrix element between the magnetic centers with different electronic configurations and S is again the absolute value of the localized magnetic moments (without the hopping electron). The coupling constant depends on the size of these moments. However the dominating bilinear term, which is of Heisenberg type, is always FM [167].

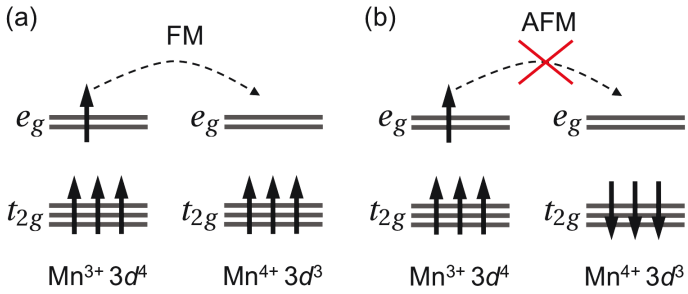

Figure 3.4.: Double exchange mechanism as a hopping process. The hopping of the e_g electron of a $3d^4$ ion to a $3d^3$ ion is only possible for a FM alignment (a) of the magnetic moments. For an AFM alignment (b) of the moments the hopping process is suppressed due to the fact that at the receiving ion the first Hund's rule would be violated (based on a figure in Ref. [166]).

3.2.4. RKKY Interaction

In f-metals the localized magnetic centers are embedded in a sea of conduction electrons which can also act such as to couple the moments of these centers [167]. This is a result of the magnetic polarization of the conduction electrons induced by the localized moments. The magnetization of the conduction electrons extends away from the magnetic center that caused it and can thereby reach another magnetic moment a distance R away [166]. Due to this mechanism the two distant centers are effectively magnetically coupled. This interaction was first considered for the coupling of nuclear spins and later on extended to FM metals [167]. It has been given the name RKKY interaction according to the names of the first investigators: Rudermann, Kittel, Kasuya and Yosida (RKKY) [166]. The RKKY interaction can be derived as a result of second order perturbation theory where the resulting effective Hamilto-

nian is again of Heisenberg type [167]:

$$H_{\mathrm{RKKY}}^{\mathrm{spin}} = -\frac{1}{2}\sum_{i,j} J_{ij}^{\mathrm{RKKY}} \mathbf{S}_i \cdot \mathbf{S}_j. \tag{3.25}$$

In an effective mass approximation the exchange coupling constant can be expressed (in atomic units) as [167]:

$$J_{ij}^{\mathrm{RKKY}} = \frac{J^2 k_{\mathrm{F}}^6}{E_{\mathrm{F}}} \frac{\Omega^2}{N^2 (2\pi)^3} F(2k_{\mathrm{F}} R_{ij}), \tag{3.26}$$

where J is the coupling constant between the localized spin and the spin of the conduction electrons, k_{F} is the Fermi wave vector, Ω is the volume of the crystal, N is the number of coupled localized spins within the crystal and the function $F(x)$ is given by:

$$F(x) = \frac{\sin x - x\cos x}{x^4}. \tag{3.27}$$

This function is plotted in Fig. 3.5 outlining that the RKKY coupling constant shows real space oscillatory behavior in sign and decays as $J_{ij}^{\mathrm{RKKY}}(R_{ij}) \propto \frac{\cos(2k_{\mathrm{F}}R_{ij})}{R_{ij}^3}$ for $R_{ij} \gg k_{\mathrm{F}}^{-1}$ which means that the interaction is of relatively long range [167]. The real space oscillations are a consequence of the sharp Fermi surface in reciprocal space. These spatial oscillations are of pronounced importance in layered structures made from alternating FM and nonmagnetic metal layers as the so-called GMR devices (see Subsection 4.2.1) since the thickness of the nonmagnetic spacer layer determines whether the coupling between the FM layers is FM or AFM [166]. Furthermore, the coupling constant decisively depends on the electron density of the conduction electrons n_{ce} over k_{F} as $J_{ij}^{\mathrm{RKKY}} \propto n_{\mathrm{ce}}^{\frac{4}{3}}$ [167].

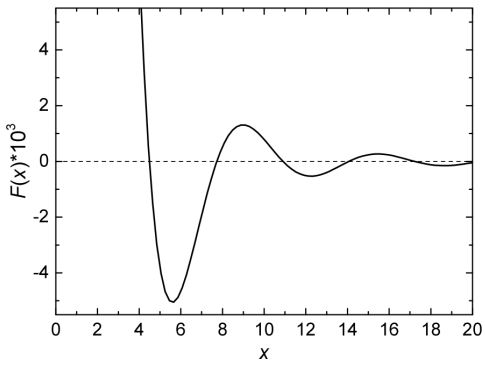

Figure 3.5.: Plot of the function of Equation (3.27) that determines the spatial oscillations of the exchange coupling constant J_{ij}^{RKKY}.

3.2.5. Higher Order Exchange

The classical Heisenberg model can be derived from the Hubbard model by a perturbation expansion in powers of $\frac{t^2}{U}$ for large U as a second order perturbation [2, 168]. The third order contribution is zero (without spin-orbit coupling) and from the fourth order perturbation two additional higher order exchange contributions result. The first is the so-called four-spin interaction (also known as ring-exchange) between spins at sites i, j, k and l [2]:

$$H_{\text{4-spin}}^{\text{spin}} = \sum_{i,j,k,l} K_{ijkl}[(\mathbf{S}_i \cdot \mathbf{S}_j)(\mathbf{S}_k \cdot \mathbf{S}_l) + (\mathbf{S}_j \cdot \mathbf{S}_k)(\mathbf{S}_l \cdot \mathbf{S}_i) - (\mathbf{S}_i \cdot \mathbf{S}_k)(\mathbf{S}_j \cdot \mathbf{S}_l)], \tag{3.28}$$

where the interaction parameter $K = \frac{5t^4}{U^3}$ for nearest neighbors.

The second higher order contribution is known as biquadratic exchange and takes the form [2]:

$$H_{\text{biquadratic}}^{\text{spin}} = \sum_{i,j} B_{ij}(\mathbf{S}_i \cdot \mathbf{S}_j)^2, \tag{3.29}$$

where the interaction parameter B_{ij} is again proportional to $\frac{t^4}{U^3}$ [166]. It can be of special relevance for superexchange and double exchange [166, 167]. In general both higher order terms scale as the fourth power of the magnetic moments and are therefore increasingly important for systems with large moments although they are small in most cases [2]. They can however play an important role when the first order Heisenberg exchange contribution becomes small due to competing effects which can cause special non-collinear magnetic textures at surfaces [4].

3.2.6. Magnetic Anisotropy and Antisymmetric Exchange

Besides the isotropic exchange contributions mentioned above, there are also anisotropic interactions which give rise to an orientation dependent energy contribution named magnetic anisotropy energy (MAE). This means that for the magnetic moments certain spatial directions are energetically preferable compared to others [2]. There are two effects contributing to the magnetic anisotropy the first of which is the classical dipole-dipole interaction of Equation (3.2) which is usually small and contributes mostly to the shape anisotropy [167]. The second contribution originates from SOC (see Equation (2.54)) which connects spin and orbital motion in the lattice potential leading to the so-called magneto-crystalline anisotropy (MCA) also called single-ion anisotropy [2]. According to second order perturbation theory with respect to SOC the uniaxial MCA over all sites i can be expressed as [2]:

$$H_{\text{MCA}}^{\text{spin}} = \sum_i K_{2,ix} S_{i,x}^2 + K_{2,iy} S_{i,y}^2 + K_{2,iz} S_{i,z}^2, \tag{3.30}$$

where the absolute value of the anisotropy constant K_2 is proportional to the square of the SOC strength. For cubic or octahedral environments higher order terms need to be considered. Remarkably, anisotropy energies are usually larger in low symmetry structures compared to high symmetry structures [166].

There is also a unidirectional magnetic interaction originating from SOC in first order which can be considered as a special type of antisymmetric exchange interaction and has become known as the Dzyaloshinskii-Moriya interaction [2]:

$$H_{\mathrm{DM}}^{\mathrm{spin}} = \frac{1}{2}\sum_{i,j} \mathbf{D}_{ij} \cdot (\mathbf{S}_i \times \mathbf{S}_j), \tag{3.31}$$

where 'DM' stands for 'Dzyaloshinskii-Moriya' and the Dzyaloshinskii-vector $\mathbf{D}_{ij}$ depends decisively on the symmetry of the crystal. It lies either parallel or perpendicular to the vector that connects the two spins and vanishes when an inversion center between the two magnetic centers exists [166]. From a mathematical perspective the Dzyaloshinskii-Moriya interaction of Equation (3.31) yields lowest energy when the two spins are at right angles with respect to each other and their vector product is antiparallel to $\mathbf{D}_{ij}$. Therefore, this interaction favors the canting of spins and competes with the Heisenberg exchange which tries to keep the moments parallel to maximize the scalar product in Equation (3.15). Hence depending on sign, symmetry properties and absolute value of $\mathbf{D}_{ij}$ collinear magnetic structures can become unstable due to the Dzyaloshinskii-Moriya interaction and are replaced by non-collinear magnetic structures of specific chirality ($\nearrow\nwarrow$ has different energy than $\nwarrow\nearrow$) [2]. One possible consequence of this interaction is the occurrence of weak ferromagnetism in antiferromagnets [166]. Furthermore, the Dzyaloshinskii-Moriya interaction can be of importance in multiferroic materials [2] and is one decisive ingredient for the formation of non-collinear magnetic structures at surfaces [3, 4].

4 Introduction to Molecular Spintronics

This chapter gives an overview of the research area of molecular spintronics (MS). After some preliminaries from molecular electronics (ME) with a special emphasize on the processes of physisorption and chemisorption, spintronics is introduced as an area of science in which the electron spin, or in a few cases the nuclear spin, is used as information carrying entity. The foundation of modern spintronics is the giant magnetoresistance (GMR) effect. Afterwards, a categorization of the spintronics research field is given in which the areas of molecular, organic and pure carbon based spintronics are outlined. Subsequently, the origin of organic and molecular spintronics is presented by referring to the first investigations in the respective field. In the following, an overview of the different developments in MS research till present is given. Finally, the novel development to tune surface magnetic exchange interactions by molecular adsorption is specially highlighted. This sets the stage for appealing questions referring to this new approach which mark the outline for the presentation of the results obtained within this thesis.

4.1. Preliminaries from Molecular Electronics

4.1.1. Short Overview of Molecular Electronics

The scientific field investigating the electrical and thermal transport properties of single molecules (or small assemblies of molecules) is known as molecular electronics (ME) [178] and is thereby distinguished from organic electronics which is concerned with thin film devices consisting of a large number of molecules. It is a highly interdisciplinary research area applying the so-called bottom-up approach to build electronic devices out of nanoscale components[1]. On the one hand the investigation of single molecules as active electronic device components can be motivated in terms of fundamental research aspects as it allows to study transport properties at the smallest possible scale entirely governed by quantum mechanics [178]. On the other hand from a technological point of view single molecules:

- are the smallest possible electronic units controllable with atomic precision,
- are inherently monodisperse: having always the same number of atoms, atomic and electronic structure,
- show specifically tunable electronic properties by chemical functionalization.

[1] In contrast the so-called top-down approach tries to miniaturize larger devices to microscopic dimensions.

The scientific starting point of ME dates back to the beginning of the 1970's where the first researchers began to study the transport through molecular monolayers by measuring the conductance of Langmuir-Blodgett films placed between metallic electrodes [179]. The observed exponential decay of the conductivity with increasing length of the molecule consolidated the basic quantum mechanical tunneling probability dependence on the barrier thickness and showed that these molecules exhibit a tunneling transport regime. Soon afterwards Aviram and Ratner suggested that a single molecule could in principle behave like a p-n junction in a semiconductor device [180]. The molecule they proposed (see Fig. 4.1) consists of an acceptor unit which has a high electron affinity and therefore prefers to take up charge, and a donor unit which has a low ionization potential and hence prefers to give up charge. Both units are separated by a barrier in order to avoid an interaction between them. The electronic asymmetry induced by the different groups is then analogous to a p-n junction and was predicted to lead to rectification behavior of the molecule when placed into an electronic circuit. However as outlined in Ref. [181] in order for the proposed molecular rectifier to work, resonant states extending over the entire molecule should be avoided for at least one of the bias polarities since otherwise the rectification could be quenched. Nevertheless, the idea of molecular rectification was later on confirmed in Ref. [182].

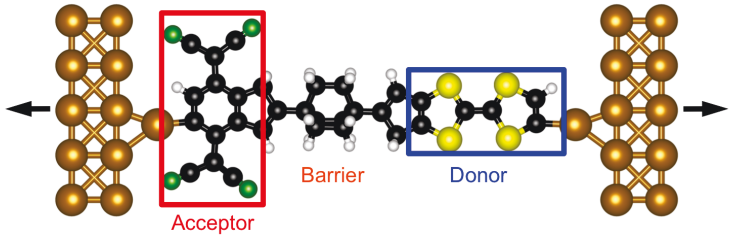

Figure 4.1.: A schematic representation of the rectifier molecule suggested by Aviram and Ratner [180] attached to two contacts. Due to the high electron affinity of the acceptor unit and the low ionization potential of the donor unit an electronic asymmetry is induced so that current is supposed to flow preferably from the left to the right side and not in the opposite direction. Both units of the molecule are isolated by a barrier between them to prevent interaction.

At the turn between the 1980's and 1990's the possibility of fabricating metallic atomic-sized contacts by either STM or the mechanically controllable break-junction (MCBJ) technique significantly advanced the field of nanoscience and paved the road for contacting individual molecules [178]. The first proposal of a transport experiment on a single molecule junction was then published in Ref. [183] where the authors investigated the conductance of a benzenedithiol molecule attached to gold contacts using a MCBJ. Even though the really first transport measurements on single molecules were carried out using STM [184–188],

the significant advance presented in Ref. [183] was to show a symmetric and at the same time stable contacting of a molecule that could in principle be used for integration into a larger circuit [178]. However it was debated based on arguments about the qualitative and quantitative agreement of measured and simulated conductance curves [189–191] whether in the experiment indeed a single molecule or a pair of molecules is the active device component between the contacts. Nevertheless these experimental results definitely stimulated the field. Later on conductance measurements on a single hydrogen molecule between Pt contacts were demonstrated [192].

At the turn to the 21st century new methods for single molecule contacting such as the nanopore technique and electromigration were introduced [178] and molecules were shown to be able to exhibit all the characteristics of microelectronic components such as wires, switches, rectifiers and storage units (see [193] for a review and references therein). The electromigration technique also allowed to add a gate electrode to the experimental setup so that specifically designed single-electron transistors based on a single C_{60} molecule could be realized [194]. Furthermore, also the fundamental physical effects of Coulomb blockade and Kondo effect could be demonstrated using this arrangement [26, 27]. Based on these scientific achievements also companies started to work on molecular based electronic devices, integrated them into larger electronic structures and built ultra-high density memories [178]. Although the potential of molecules for electronics was clearly demonstrated, one of the largest issues is still the stability of the manufactured devices.

In the meantime the field has developed beyond the investigation of pure charge transport and the inclusion of mechanical, optoelectronic, thermoelectric, spintronic and quantum interference functionalities is intensively studied (see Ref. [195] for a review). More detailed accounts on ME can be found in Refs. [193, 195–198] and a special account on single-molecule contacting can be found in Ref. [178]. Finally, it should be mentioned that these developments also pushed the theoretical description of transport in nanojunctions to new frontiers. They stimulated the development of the NEGF method briefly described in Subsection 2.3.5 (see for instance Refs. [153, 155–157, 159, 160, 190]) since the experimental techniques posed the need for a realistic description of non-equilibrium processes from first principles.

4.1.2. Physisorption and Chemisorption

When a molecule interacts with a (metallic) surface, two limiting cases in terms of interaction strength can be distinguished. In the first case, called physisorption, only a weak physical interaction occurs and no chemical bonds between the molecule and the surface are established. The energy gain due to the adsorption of the molecule expressed by the adsorption energy E_{ads} is then usually well below 1 eV for small molecules with less than 20 atoms. The

molecules are generally at a large distance from the surface (see Fig. 4.2(a)) and as a consequence of the weak interaction, the DOS on the molecular site consist of sharp features (see Fig. 4.2(b)) which resemble the discrete levels of the isolated molecule. In case of a magnetic surface the peaks in the DOS at the site of the molecule can become slightly spin split. However due to the presence of the surface screening effects occur which usually lead to minor energetic shifts of the electronic levels but can renormalize the gap between the HOMO and LUMO of the molecule. In this weak coupling limit energetic barriers for the charge injection into the molecule or the charge extraction out of the molecule are usually formed having a pronounced influence on the transport behavior [44, 195, 199].

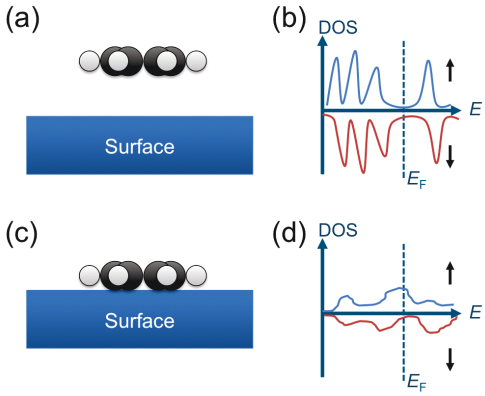

Figure 4.2.: In case of a physisorption type interaction of a molecule with a surface the molecule generally has a large distance to the surface (a). This weak interaction leads to a DOS on the site of the molecule characterized by sharp peaks (b) which in case of a magnetic system can be slightly spin split. When the molecule is chemisorbed on the surface, it is usually much more tightly bonded to the substrate (c) and the strong interaction consequently leads to broad bands in the DOS on the molecular site (d).

On the other hand the molecule can also interact more strongly with the substrate, a scenario called chemisorption. The adsorption energy is then usually larger than 1 eV for small molecules. In this case the molecule binds in general much more closely to the surface (see Fig. 4.2(c)) so that the distance of the molecular atoms to the ones of the surface is well below the sum of their van der Waals radii. Hence a chemical bond between the molecule and the surface is formed which means that suitably aligned and extended states of the molecule (for example π-states) mix with the states of the surface to form new molecule-metal hybrid states. Due to this hybridization process the hybrid molecule-surface system can exhibit states which do neither resemble orbitals of the isolated molecule nor of the isolated surface, i. e. the bonding of the molecule to the surface leads to the formation of a qualitatively new material [40].

The DOS on the site of the molecule now consists of broad peaks (bands) (see Fig. 4.2(d)) which extend over a large energy range of several eV. Hence the molecular part of this hybrid system becomes metallic in this case, i. e. also has finite DOS at E_F.

In view of the description of these different interaction mechanisms using *ab initio* DFT calculations especially the development to account for the vdW interaction as described in Subsection 2.2.4 turned out to be of great importance [98, 111, 200, 201]. This is particularly true for the weak interaction regimes of physisorption and weak chemisorption since there the bonding is decisively governed by the vdW contribution due to nonlocal correlation effects. In the following two examples will be given demonstrating which influences are important for physisorption and chemisorption type interactions.

In a systematic study in Ref. [98] concerning the adsorption of benzene (Bz), pyridine (Py) and pyrazine (Pz) on Cu(110) it was shown that the bonding character of these molecules to the surface is significantly different. Firstly, Py can be thought of as being made out of Bz by exchanging a CH bond by N. Furthermore, in Pz another CH group has been exchanged by N. This inclusion of heteroatoms (here N) into the molecular structure leads to an energetic lowering of the π-states when going from Bz to Pz. Since these π-states are important for the flat adsorption of the molecules, a markable influence on the adsorption behavior can be expected. The adsorption of the molecules has been investigated by using two different approaches, i. e. studying the system either with the PBE functional or additionally taking into account the D2 dispersion correction of Grimme [69]. It turns out that in both cases Bz is chemisorbed and is positioned close to the surface with a molecule-surface distance of 2.43 Å and 2.35 Å for pure PBE and for taking into account the D2 correction, respectively (see Fig. 4.3). On the contrary, Py 'becomes' chemisorbed due to the inclusion of D2 as pure PBE does not properly describe the bonding of the molecule to the surface. Finally, Pz is physisorbed in both cases but D2 reduces the molecule-surface distance by 0.4 Å. The important messages that can be derived from this study are that (i) the inclusion of dispersion corrections can be of great importance for weakly bonded systems and (ii) physisorption and chemisorption processes can be tuned by including specific heteroelements into the molecular structure, i. e. *the chemical structure of the molecule plays a crucial role.*

Figure 4.3.: The geometry of Bz, Py and Pz adsorbed on Cu(110) when treated with the PBE functional (left part) and including the D2 dispersion correction (right part). The figure was taken from Ref. [98]. Copyright (2009) by the American Physical Society.

A complementary study has been carried out in Ref. [202] where the adsorption of cyclooc-

tatetraene (COT) C_8H_8 on different surfaces has been studied by a combined approach using STM and DFT. On an Au(111) surface COT is found to be physisorbed with an adsorption energy of $E_{ads} = -0.162$ eV and a large molecule-surface distance of 2.86 Å. Due to the weak interaction the molecule preserves its non-planar shape of the gas phase. On Ag(100) however COT is chemisorbed with an adsorption energy of $E_{ads} = -1.604$ eV and a molecule-surface distance of 2.39 Å. Eventually, on Cu(100) the molecule is strongly chemisorbed with $E_{ads} = -2.636$ eV and a molecule-surface distance of 2.10 Å. In both chemisorbed cases the molecule lies flat on the surface. This investigation clearly showed that *also the reactivity of the metal surface determines the interaction strength.*

4.2. Origin and Categorization of Spintronics

4.2.1. The Giant Magnetoresistance Effect

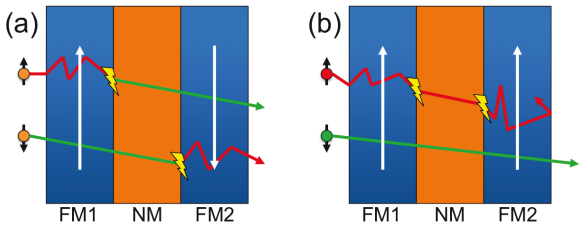

Figure 4.4.: Schematic representation of a spin-valve device showing the GMR effect out of two magnetic layers FM1 and FM2 sandwiching a non-magnetic layer (NM). The magnetic layers can be magnetized antiparallel (a) or parallel (b). A switching between the states can be realized by applying a magnetic field. In case of an antiparallel alignment of the magnetizations each spin is strongly scattered in one of the two magnetic layers. For parallel alignment one spin is scattered in both magnetic layers whereas the other spin can propagate easily through both layers yielding an effective shortcut and hence lower resistance than in the antiparallel case. For the resistance difference especially the spin-dependent interface scattering between a FM layer and the nonmagnetic layer is important [203] and these events were therefore specifically highlighted in the figure. (Based on a figure in Ref. [204].)

Spintronics deals with the ability to inject, manipulate, amplify and detect currents of different spin [18, 166] and therefore considers the spin degree of freedom as a possible information carrier for computing and storage. This modern field of science was initiated by the discovery of the giant magnetoresistance (GMR) effect for which A. Fert and P. Grünberg were awarded the physics Nobel Prize in 2007. The constructed devices eventually connected the fields of magnetism and microelectronics [1] in that the pioneering works on GMR demon-

strated for the first time that the magnetic properties of a device which are connected to the spin of the electron can significantly influence the resistance state of that device [5, 6].

The working principle of GMR can be explained with reference to Fig. 4.4. One considers a metallic layered system made up of two FM layers (for instance Fe or Co [1, 166]) with a non-magnetic spacer (for example Cr or Cu [1, 166]) in between, each layer having thicknesses of a few nm [6]. The resistance state can be analyzed by referring to the two-current model, i. e. assuming that the total current is given by the sum of the currents of spin up and spin down electrons. For a suitably chosen thickness of the spacer layer the interlayer magnetic exchange coupling between the FM layers is AFM (see Fig. 4.4(a)) [1]. In this configuration each of the spins experiences a strong scattering in one of the magnetic layers [205]. By applying a magnetic field the parallel alignment of the magnetizations of the FM layers can be induced (see Fig. 4.4(b)). In this case one of the spins is scattered heavily in both layers whereas electrons of the other spin direction can propagate easily through the system providing a conductance shortcut which gives this configuration a considerably lower resistance [204]. In Ref. [203] it is noted that especially the spin-dependent scattering at the interface between the FM and non-magnetic layers gives rise to the different resistance for both spins. It is this difference in resistance due to magnetization switching which is known as the GMR-effect.

The magnetoresistance (MR) ratio is defined as [1]:

$$\frac{\Delta R}{R} = \frac{R(H=0) - R(H_S)}{R(H_S)}, \tag{4.1}$$

where R is the resistivity of the device, H stands for the applied magnetic field and H_S is the saturation field which needs to be applied to achieve a FM alignment over all layers. For a suitable choice of materials MR ratios of up to 100% can be obtained for devices based on the GMR effect [166]. One should however note that Equation (4.1) is the optimistic definition for MR, in the pessimistic definition $R(H = 0)$ is used in the denominator which makes the obtained MR values smaller since the resistance at zero field is usually largest [166][2]. The size of the resistance change made the effect attractive for sensor applications and it was therefore quickly exploited in read heads of hard disks. More detailed accounts on the GMR effect can be found in Refs. [204, 205, 207, 208].

In the further development a related effect to GMR was studied by investigating layer systems in which the nonmagnetic metallic spacer was replaced by an insulating barrier. The resulting effect has become known as tunneling magnetoresistance (TMR) and can give rise to even higher MR ratios especially when using MgO barriers [14]. The TMR signal is strongly dependent on the spin polarization $P_{1/2}$ of the first/second magnetic layer which is expressed

[2] Also other definitions of the MR ratio can be found in the literature (see for instance Refs. [31, 43, 205, 206]).

by the Julliere formula [1, 8]:

$$\frac{\Delta R}{R} = \frac{R_{AP} - R_P}{R_P} = \frac{2P_1P_2}{1 - P_1P_2}, \tag{4.2}$$

where R_P (R_{AP}) is the resistance of the device for (anti)parallel alignment of the FM layer magnetizations. The mechanism of TMR can be explained with reference to the DOS since for parallel alignment there is large DOS at the Fermi energy for one spin channel in both magnetic layers. Hence states are available into that the conducting electron can tunnel which is not the case for antiparallel alignment [204].

4.2.2. Categorization of Spintronics

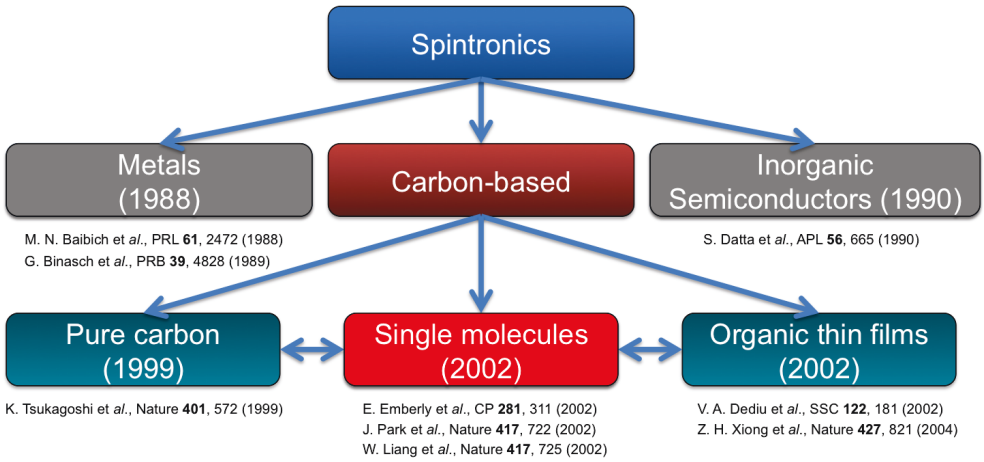

Figure 4.5.: Categorization of spintronics based on the materials used. The spintronics research field was initiated by the discovery of the GMR effect in devices based on metals at the end of the 1980's. Afterwards also the implementation of spintronics functionalities into semiconductors was put forward in the 1990's. The field of carbon-based spintronics can be further subdivided into investigations dealing with pure carbon systems, organic thin films and single molecules containing carbon which were all established at the turn to the 21st century. There are certain connections between these three subfields. This thesis is rooted in the field of single molecule spintronics. The publications mentioned below the fields denote the first investigations carried out in the respective area.

There are many ways to classify the area of spintronics. Here the subdivision will be made according to the materials in which the spintronic functionality is included and which are therefore the key ingredients of the devices (see Fig. 4.5). The whole research field was kicked off by the discovery of GMR in metallic layer systems described in Subsection 4.2.1 at the end of the 1980's. Soon afterwards an implementation of spintronics functionalities into semi-

conductors was put forward. Datta and Das suggested a spin field-effect transistor based on the Rashba effect in semiconductor heterostructures where the precession of spins injected from a magnetic contact can be controlled via an external gate voltage [16]. This allows to adjust the spin direction of the electrons reaching a second magnetic contact that acts as a spin analyzer. Reviews about semiconductor based spintronics can be found in Refs. [17, 209].

Also carbon-based systems were used to implement spintronics. This area allows for a further subdivision into investigations dealing with pure carbon systems, organic thin films and single carbon-based molecules as active device units exhibiting the spintronics functionality. The first study of spin transport in a pure carbon material was given in Ref. [210] where the contacting of multi-walled carbon nanotubes to magnetic Co contacts and spin-valve behavior of the resulting device was demonstrated. Spin injection and spin-valve behavior of organic thin film devices were proposed in Refs. [21] and [22] by placing a layer of 8-hydroxyquinoline aluminium (Alq_3) molecules between two LSMO electrodes or one LSMO and one Co electrode, respectively. This field is known as organic spintronics [211]. When investigating single molecules for their spintronics functionality, the field is termed molecular spintronics (MS) [18]. Already the studies of Park and coworkers [26] and Liang and coworkers [27] on the Kondo effect in single-molecule transistors mentioned in Subsection 4.1.1 fall in this category. However the first proposal for spin-dependent transport in molecules was given by Emberly and Kirczenow in Ref. [25] by investigating benzenedithiol attached to magnetic contacts in different device geometries.

It should be noted that the distinction between the three subfields of carbon-based spintronics is not very sharp and certain interconnections exist as indicated by the horizontal arrows between the fields in Fig. 4.5. In this sense fullerenes are pure carbon structures but can also be studied under the topic of MS when the spintronics functionality of single fullerenes is investigated. On the other hand MS can help to understand the interface properties of single molecules adsorbed on magnetic substrates which can be of relevance for the interface between magnetic contacts and the organic layer in organic spintronics. Because of these interconnections, contributions from all three areas will be included in the following description but a special emphasis will be put on single molecule spintronics investigations.

It remains however the question why spintronics in carbon-based systems should be favorable. As far as the spin transport through materials is concerned, carbon-based systems are preferable because of two main reasons: (i) low SOC as carbon is a light element (SOC scales as the second power of the atomic number $E_{SO} \propto Z^2$ [167]) and (ii) weak hyperfine interactions since the most abundant form of carbon ^{12}C (natural abundance 98.9%) has a nuclear spin quantum number of $I = 0$ [212]. There has been some debate which of the two mechanisms is actually responsible for the spin-relaxation in organic materials [213, 214] and the answer might even depend on the specific material used [18]. On the other hand when one is

not primarily interested in the spin transport through the material but more in view of creating storage units, carbon-based systems can be advantageous because of (i) the formation of atomic scale hybrid molecule-surface units [19] to achieve high densities and (ii) the possible chemical functionalization of magnetic surface properties due to the adsorption of carbon materials. The last point will be the main topic of this thesis. In addition, the implementation of spintronics into organic/molecular devices might offer the possibility to envision cheap ways of production [215].

4.2.3. Origin of Organic and Molecular Spintronics

The first proposal of room temperature spin injection into an organic material and an organic based magnetoresistance was published in Ref. [21]. In this investigation the authors studied the spin transport through a lateral device in which a several 100 nm thick film of the organic molecule sexithienyl (T_6) was placed between two LSMO electrodes. The authors found that the resistance of the device was strongly reduced (MR=30%) when a strong magnetic field of 3.4 kOe was applied. After switching off the field, the resistance partially increased again. The results were interpreted in view of the fact that LSMO is a double exchange material as outlined in Subsection 3.2.3. When the magnetic field is applied the magnetizations of the LSMO layers should become aligned and the fact that an MR signal is detected, was interpreted in the sense that the double exchange mechanism between the two LSMO electrodes takes place through the organic layer, i. e. the spin-polarized electrons are supposed to be injected from one contact and keep their spin information until they are injected into the second electrode. A parallel alignment of the spin of the injected electron with respect to the local LSMO magnetization is preferred on the basis of the double exchange mechanism.

Soon after this first investigation another experimental work was presented in which GMR was reported for an organic spin-valve (OSV) exhibiting an MR up to -40% at low temperatures [22]. The spin-valve was constructed with an LSMO bottom electrode (FM1) on top of which a thin film (several 100 nm thick) of the organic molecule Alq_3 was deposited. Finally, a Co top electrode (FM2) was put on the organic layer by evaporation (see Fig. 4.6(a)). The recorded spin-valve signature is schematically depicted in Fig. 4.6(b). The results were interpreted such as that from the FM electrodes spins are injected into the organic semiconductor which travel coherently to the second FM electrode where they are detected. When one starts from large negative fields the magnetizations in the FM layers are aligned and one then increases the field until the coercive field of the first electrode (here LSMO) H_c^1 is reached. The magnetization of this electrode switches and one obtains an antiparallel alignment with a lower resistance. When upon further increase of the field the coercive field of the second electrode (here Co) H_c^2 is reached, the device switches again to FM alignment with higher resis-

tance. The mechanism is supposed to work accordingly for decreasing the magnetic field. In addition, also a high-field MR was found that was supposed to be related to the MR in Ref. [21] and was further investigated in Ref. [216] where it was outlined to be due to LSMO. The further development of OSVs made it possible to demonstrate operation at room temperature and air-stability [217, 218].

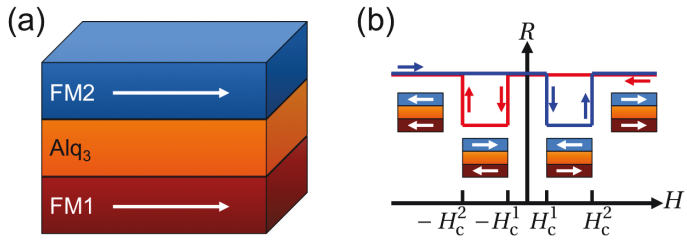

Figure 4.6.: Schematic picture of a vertical spin-valve device with an organic spacer as used in Ref. [22] (a). When the two ferromagnetic materials have different coercive fields H_c^1 and H_c^2 a characteristic resistance change with applied magnetic field H is typical for spin-valve behavior (b). In the initial state a parallel alignment of the magnetizations in the ferromagnetic layers is assumed. If one then increases the field (blue curve) the first layer will reverse its magnetization at H_c^1 giving rise to an antiparallel alignment which has a different resistance (here lower) than the parallel alignment. At H_c^2 also the harder magnetic layer reverses its magnetization which again gives rise to a parallel alignment and one switches back to the initial resistance state. When reducing the magnetic field the mechanism works accordingly (red curve).

The common message from the above studies was outlined to be that spin injection into an organic material as well as coherent spin transport through the organic material over more than 100 nm should be possible. The deduced spin diffusion lengths l_s, indicating the average distance over which the spin direction is maintained [206], were found to be of the order of several 10 to 100 nm [21, 22]. There was however intense debate about the spin injection and propagation in organic materials and hence about the mechanism of the obtained spin-valve behavior since tunneling through the layer seems unlikely considering its spatial extent. Another puzzling point was the negative sign of the MR since the resistance of the OSV was smaller for antiparallel alignment of the electrode magnetizations [22, 219]. One of the main problems is that the top electrodes were deposited by evaporation which together with pinholes in the organic layer could lead to inter-diffusion and metal inclusions in the organic layer [220]. Moreover it is well established that spin injection is suppressed when the conductivity of the FM electrode and the spacer is largely different (conductance mismatch) which might be avoided by using tunneling barriers at the interface or electrodes with lower conductivity [221].

Another controversial point is that due to the weak spin relaxation mechanisms of SOC and hyperfine interaction in carbon-based materials (see Subsection 4.2.2) long spin relaxation times τ_s are expected for organic materials [206, 222][3]. The relation connecting spin diffusion length and spin relaxation time is given by [37]:

$$\tau_s = \frac{e l_s^2}{k_B T \mu}, \tag{4.3}$$

where k_B is Boltzmann's constant, T is the temperature and μ is the drift mobility. However due to their very small mobilities (typically of the order of 10^{-8} to 10^{-14} $m^2V^{-1}s^{-1}$ [206]) when compared to pure carbon materials or inorganic semiconductors [206], short spin-diffusion lengths of only a few nanometers should be expected for organic materials [18] which have indeed been observed experimentally [34, 35, 37]. Finally, further measurements on OSVs showed neither MR signals nor indications for spin transport in the organic material [223] and also no Hanle precession signatures were observed which could proof the spin injection [224].

Besides the experimental investigations of the Kondo effect in single-molecule transistors already outlined in Subsection 4.1.1, the first investigation in MS can be assigned to the theoretical work of Emberly and Kirczenow in Ref. [25] which was motivated to be an extension of the results presented by Reed and coworkers [183] to magnetic contacts. There the authors investigated within a semiempirical tight-binding approach the transport properties of the device based on the Landauer formalism. They studied the contacting of the 1,4-benzenedithiolate molecule in nanojunctions made from magnetic contacts. In the break-junction geometry when the molecule is placed between Ni contacts, they proposed the observation of the spin-valve behavior. In addition, for an STM setup with a Ni tip the injection of a highly spin-polarized current into an Au substrate is predicted. Eventually, the spin-valve behavior in case of a Ni substrate is found to be even stronger than in the break-junction scenario. Later on also first-principles calculations suggested a molecular spin-valve effect for the benzenedithiol molecule [28]. Experimentally such an effect was found for Ni-octanethiol-Ni junctions manufactured by the nanopore technique but with variable sign of the MR [29]. Another early theoretical study in MS addressed the transport in a single-molecule magnet (SMM) on a metallic surface [30].

[3] The spin relaxation time indicates the average time over which an electron keeps its spin orientation [206].

4.3. Overview of Important Developments in Molecular Spintronics

4.3.1. Spectroscopic Investigations

The first evidence for induced magnetic order in a molecular monolayer due to adsorption on a FM surface was presented in Ref. [23] where manganese(III)-tetraphenylporphyrin chloride (MnTPPCl) on a Co substrate was studied by X-ray magnetic circular dichroism (XMCD). From the recorded spectra and deduced element-specific hysteresis curves the authors concluded that a net magnetization was induced on the Mn centers of the molecules which were ferromagnetically coupled to the Co surface magnetization via exchange interaction. In a similar study in Ref. [24] also an induced FM order in an Fe porphyrin layer on both Ni and Co substrates on Cu(100) was found by means of X-ray absorption spectroscopy (XAS) and XMCD. In addition, based on DFT calculations a hybridization of Fe and N as well as Co and N states was detected and consequently a 90° superexchange mechanism between the molecular Fe and the Co of the substrate over the N atoms of the ligand was suggested. Also in Ref. [225] FM coupling of MnPc to an underlying Co(001) substrate was found but in contrast to the aforementioned cases was assigned to a direct exchange coupling between Mn and Co. In addition, the authors stressed the decisive role of the central Mn ion for the interface spin polarization due to interface states and its impact on spintronic devices. On the other hand in Ref. [226] supramolecular control of the magnetic anisotropy in high-spin Fe arrays on a nonmagnetic metal surface was demonstrated using the same techniques. It was shown that the coordination of Fe atoms on a Cu(100) substrate by 1,4-benzenedicarboxylate molecules lead to a long-range ordered 2D system with an in-plane easy axis of magnetization. When oxygen molecules were dosed onto this structure a reorientation of the magnetization to out-of-plane was found demonstrating that the magnetic anisotropy on a surface can be tuned chemically. Moreover in Ref. [227] it has been demonstrated that additional axial ligands as NO and NH_3 can affect the spin state of molecular metal centers at surfaces and can also tune the magnetic coupling between the metal center and the substrate.

However new methods had to be developed to study spin injection into and spin diffusion through organic materials since the methods applied in inorganic spintronics rely on SOC which is exceptionally weak in organics [215]. Therefore a major progress was to apply the two-photon photoemission technique to measure the spin injection efficiency through an organic-ferromagnetic interface and the quasi-elastic spin-flip length in the organic material in Ref. [34]. In this method spin-polarized electrons are excited in the FM layer but only spin-polarized electrons from the surface of the organic film are photoemitted by the second photon pulse due to the short inelastic mean free path of the electrons. The authors found a

spin-injection efficiency of about 85% from Co into unoccupied states of CuPc. In addition, they proposed that quasi-elastic spin-flip processes are the microscopic mechanism that limits spin diffusion and report a quasi-elastic spin-flip length of about 12.6 nm and a spin diffusion length of about 7.5 nm. In a further study applying the same technique but adding a time-dependent information due to a real time pump-probe scheme of the photon pulses, the femtosecond spin dynamics at a Co/Alq_3 interface could be accessed [36]. It was found that due to chemisorption of the Alq_3 hybrid interface states are formed for which the lifetimes for spin up and spin down electrons differ by about a factor of two. It was consequently concluded that these states act as spin dependent hybrid interface traps which give rise to spin-filtering due to different confining potentials for the two spins. In Ref. [228] it was indicated that the hybrid interface states can be tailored by a chemical functionalization of the organic molecule and that thereby the spin polarization of the states can be tuned to exhibit even slightly larger values than the bare Co surface.

An alternative approach to address the spin diffusion in a fully functional OSV was reported by Drew and coworkers in Ref. [35] who investigated the spin diffusion length in a spin-valve out of LiF, Alq_3, TPD[4] as well as NiFe and FeCo FM electrodes by low-energy muon spin rotation. In the experiment muons were implanted into the organic layer of the spin-valve for which the depth was controlled by the implantation energy. When the muons decay in the sample, positrons are emitted predominantly along the direction of the muon-spin whose detection consequently yields information about the local spin polarization in the sample [166]. The authors found a spin diffusion length of about 10 nm at 90 K and reported a correlation between the temperature dependence of the MR signal and the spin diffusion length in that they found $l_s \approx 30$ nm and MR values of 0.2% at temperatures below 20 K. Later on it was proposed by using the same technique that the LiF layer on the NiFe contact allows to control the spin polarization of the extracted electrons and thereby the sign of the MR value compared to a device without LiF [229].

4.3.2. Transport Studies Through Very Thin Organic Layers

In order to gain further understanding about the working principles of OSVs and the spin-relaxation mechanisms in organic materials, transport studies through very thin organic layers, i. e. for layer thicknesses from a few molecules to about 30 nm, have been carried out. By investigating the transport properties of an organic nanowire spin-valve out of a ≈30 nm thin Alq_3 film placed between FM Ni and Co contacts, Pramanik and coworkers [37] could observe exceptionally long and relatively temperature independent spin relaxation times of ms up to s in the organic material. They obtained the spin relaxation time by first estimating

[4]TPD=N,N'-diphenyl-N-N'-bis(3-methylphenyl)-1,1'-biphenyl-4,4'-diamine

the spin diffusion length ($l_s \approx$4 nm at 50 K) analogously to the procedure in Ref. [22] by using the Julliere formula and subsequent evaluation of τ_s by making use of Equation (4.3) and the electron mobilities of Alq_3 reported in the literature. Furthermore, the authors identified the Elliot-Yafet mechanism as the main source of spin relaxation which was further confirmed later on [214].

A transport investigation through ultrathin organic layers has been presented in Ref. [38] where room-temperature TMR and spin-polarized tunneling through an organic barrier was demonstrated. The devices were made up of about 2 nm thin Alq_3 films placed between Co and NiFe FM electrodes including an additional 0.6 nm thin Al_2O_3 layer between Co and Alq_3. The characteristic spin-valve behavior with up to 7.5% MR at 4.2 K was demonstrated for a large bias range from −100 to +100 mV. The authors especially emphasized that the Al_2O_3 layer secures a large spin polarization of the tunneling current due to the suppression of interface states. Similarly, for rubrene based tunnel junctions an analogous improvement of the spin polarization of the tunneling current was found when an Al_2O_3 seed layer was placed between the Co contact and the organic layer in Ref. [39]. Even more importantly, this study revealed a large spin diffusion length for amorphous rubrene of l_s =13.3 nm by directly measuring the spin polarization of the tunneling current for various organic layer thicknesses into a superconducting Al electrode. The influence of the Al_2O_3 seed layer on the growth morphology of the rubrene layer has been in detail analyzed in Ref. [230]. It was found that the seed layer drastically affects the growth of the organic layer and hence the spin and charge injection. In addition also the top contact was found to be affected by the different growth mechanism of the rubrene layer due to alumina.

In Ref. [41] an alternative method to manufacture tunneling devices with ultrathin organic layers of 2 to 4 nm in thickness has been presented. During this nanoindentation technique a conductive atomic force microscopy tip was indented into an Alq_3 layer deposited on LSMO and the generated nanohole was subsequently filled with Co. Using this highly local probe experiment MR values of up to 300% were recorded which strongly decreased with increasing temperature and bias voltage. The authors especially outlined the role of the hybrid molecular-ferromagnetic interface and developed a model to demonstrate that the spin selective hybridization at the interface can ultimately give rise to an inversion of the effective spin polarization at the organic site. This was supposed to provide a possible explanation for the negative MR found in large-area OSVs [22]. Later on it was reported in a study using the same technique that nominally equivalent Co/CoPc interfaces can have opposite spin polarization depending on whether the bottom or top interface in an OSV was investigated [231].

4.3.3. Investigations of Single Molecule-Surface Hybrid Systems

The ultimate case in terms of downscaling of a molecular spintronic device and at the same time a direct model for the interface between an organic material and a FM surface is provided by studies on single molecules between (magnetic) leads and single molecules on substrates. In the beginning, spin-polarized transport studies on single molecule junctions were mainly theoretically motivated. In Ref. [31] the DFT-NEGF approach outlined in Subsection 2.3.5 was used to study MR in single molecule spin valves. Large MR values of up to 100% and 600% were predicted for the tunneling and the metallic limit of conduction for octanedithiol and tricenedithiol attached to Ni contacts, respectively. For benzenedithiol contacted by Ni leads a strongly bias dependent MR of up to 27% at low bias was proposed using the same method [32]. Moreover, in Ref. [232]the influence of surface states on the MR in such Ni-based spin valves was outlined to be especially important in an STM setup leading to a pronounced bias dependence of the MR ratio. Later on also the use of organic radicals as spin-filters was suggested applying the DFT-NEGF scheme [233].

The first experimental study demonstrating that the spin state of a single molecule on a FM surface can be read and visualized was presented in Ref. [33] by addressing individual CoPc molecules on Co nanoislands by SP-STM. The authors found different magnetic states of the molecular units readable by the STM tip which depended on the magnetization of the Co island underneath. Based on this a FM coupling between the Co magnetic moments of the molecule and the substrate was inferred which was supported by DFT calculations outlining that the coupling mechanism is at least partially determined by the 90° superexchange mechanism. Soon afterwards it was also demonstrated using STM that the magnetic anisotropy of a single FePc molecule could be switched from easy plane to easy axis due to adsorption on an oxidized Cu(110) surface [234] and later on that the spins of individual FePc molecules on Au(111) are coupled by the RKKY interaction [235].

An SP-STM study demonstrating spin- and energy-dependent tunneling through a single CoPc molecule on 2 monolayer (ML) Fe on a W(110) substrate with intramolecular spatial resolution was presented in Ref. [40]. The authors found a pronounced spin polarization on both the metal center as well as on the ligand of CoPc. The DFT calculations using the PBE functional showed a strong hybridization of molecular and substrate orbitals which could only be described when a dispersion correction (D2) accounting for the attractive vdW forces was included. These vdW forces brought the molecule 0.5 Å closer to the surface compared to the relaxed DFT geometry without dispersion correction. It was found that due to charge transfer the CoPc is nonmagnetic on the surface but the spin polarization arises due to spin-split hybrid states in specific energy intervals.

A subsequent theory driven study addressed the local spin polarization over organic-ferro-

magnetic units compared to the clean surface generalizing the previous results [19]. The spin polarization P is defined as:

$$P = \frac{n^{\uparrow} - n^{\downarrow}}{n^{\uparrow} + n^{\downarrow}}, \tag{4.4}$$

where $n^{\uparrow}$ and $n^{\downarrow}$ are the charge densities for spin up and spin down within a given energy interval. By studying Bz, the cyclopentadienyl radical and COT on 2 ML Fe/W(110) it was demonstrated that the spin polarization over these hybrid molecule-surface units is inverted with respect to the underlying substrate. The mechanism of this inversion can be understood with reference to Fig. 4.7(a). For the isolated molecule (upper left part in Fig. 4.7(a)) the electronic structure consists of sharp levels which have predominantly p_z character close to the Fermi energy. On the other hand the DOS of the substrate (lower left part in Fig. 4.7(a)) shows spin-split d-bands with minority states dominating close to E_F which gives rise to a negative spin polarization of the substrate. When now the two systems are brought together a hybridization takes place (right part in Fig. 4.7(a)) which leads to the formation of hybrid $p_z - d$ bands that are delocalized over molecule and substrate. Due to this bonding, the hybrid states with contributions on the molecular site are shifted up in energy for the spin up channel whereas they are shifted down in energy for the spin down channel. Because of this mechanism now the hybrid states above the molecule have larger weight in the spin up channel compared to the spin down channel and hence the spin polarization is inverted. That this is indeed a very general behavior was consolidated by SP-STM measurements on a large nonmagnetic molecule (H_2Pc) on the same surface demonstrating that also in this case the spin polarization is inverted over the entire molecule as depicted in Fig. 4.7(b).

This study underscored that nonmagnetic molecules can be used to pattern the spin polarization of a magnetic surface essentially on a molecular scale which might be useful for spintronic devices. In addition, the inversion of the spin polarization was suggested as a possible mechanism for the observed negative MR in OSVs [219] as for instance found in Ref. [22]. Subsequently, it was shown that this effect can also be tuned due to a chemical functionalization of the molecule as fluorination can lead to a spin polarization differing in sign below and above the Fermi energy [20]. Further studies revealed a reversible spin polarization due to the switchability of an azobenzene molecule on 1 ML Fe/W(110) from trans to cis configuration [236] and inversion of the spin polarization at an organic-antiferromagnetic interface for several molecules on 1 ML Mn/W(110) [237]. A detailed experimental characterization of CoPc on the FM 1 ML Co/Ir(111) surface in Ref. [238] applying SP-STM showed that the central Co ion has the same spin polarization as the substrate indicating FM coupling but that the polarization on the ligand is again inverted. This finding highlighted again the special role of the central metal ion at the molecular site.

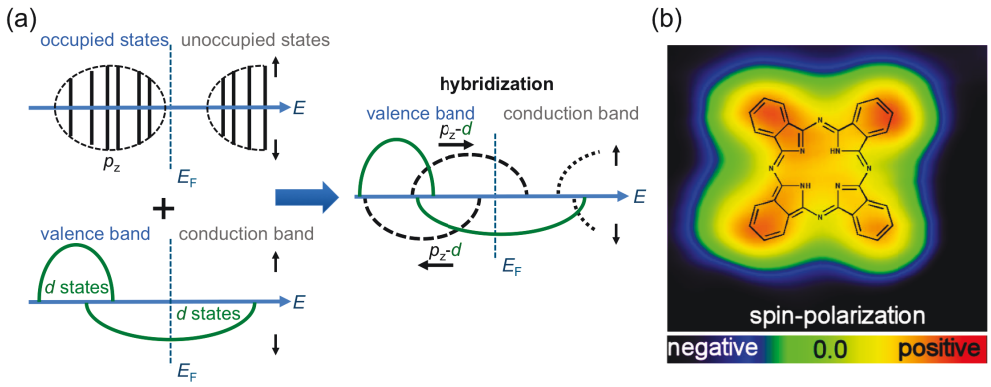

Figure 4.7.: Mechanism of the spin inversion for organic molecules containing π-electrons on magnetic surfaces. (a) The electronic structure of the isolated molecule consists of sharp states of p_z type close the Fermi energy (upper left part). The substrate shows spin split d-bands with minority spin states at E_F (lower left part). For the combined system the hybridization leads to the formation of hybrid $p_z - d$ bands having a large weight in the spin up channel at E_F (right part). (b) Inversion of the spin polarization above an H_2Pc molecule on 2 ML Fe/W(110) at a bias voltage of 0.05 V recorded by SP-STM. For (b): Taken from Ref. [19]. Copyright (2010) by the American Physical Society.

Also STM investigations were presented directly addressing the MR of single molecule junctions. GMR through a single CoPc molecule contacted to both a FM Co island on Cu(111) and a spin-polarized Co STM tip was reported in Ref. [43]. Besides a pronounced TMR signal ranging up to about 150% at negative bias, the authors found a sudden increase in conductance when they approached the tip close to the surface. This was interpreted as the CoPc molecule jumping into contact with the STM tip and thereby establishing a direct current path through the molecule. From the experimental data an MR ratio of about 60% was obtained which was close to the theoretical value of 65% determined from DFT-NEGF calculations. The mechanism of the GMR was outlined to be related to the spin selective hybridization between molecule and tip/substrate establishing a highly conductive electronic structure for parallel alignment of tip and surface magnetization. In Ref. [42] large MR values of -30% at -0.5 V and close to $+100\%$ at around 0 V were reported for single C_{60} molecules on a Cr(001) surface probed by a spin-polarized Fe coated W tip. The authors proposed that a spin-split hybrid state was responsible for the observed sign inversion of the TMR signal at different bias voltages.

Finally, also a combined experimental and theoretical study was presented showing that the $4f$-states of a single $NdPc_2$ molecule on Cu(100) can be accessed by STM [239]. The $4f$-orbitals were found close to the Fermi energy in contrast to other double-decker phthalocya-

nine molecules including late lanthanide ions which have the corresponding states at much lower energies. Hence a significant contribution of these states to the charge transport was reported and they were found to be highly spin-polarized carrying the magnetic moment of the molecule adsorbed on the surface. Based on these findings the possibility of electrical manipulation and detection of the spin state of such molecules was envisioned.

4.3.4. Spintronic Investigations Using Single-Molecule Magnets

So far an overview of investigations on nonmagnetic or paramagnetic molecules used for spintronic functionalities was given. In this subsection contributions to the field of MS using SMMs will be reviewed. SMMs are a class of molecules that show a magnetic hysteresis which is connected to the properties of the single molecule and not to a large assembly of magnetic centers as in bulk magnets [175]. The most prominent example is Mn_{12} acetate having a spin ground state of $S = 10$ [240]. The conditions that a molecule shows slow relaxation of magnetization below a certain temperature (blocking temperature) are determined by a large ground state spin and a large anisotropy barrier with easy axis magnetic anisotropy [175].

The electronic transport properties of an SMM on a metallic surface probed by STM were first investigated theoretically [30] as already mentioned in Subsection 4.2.3. A later combined experimental and theoretical study of Mn_{12} attached to Au electrodes revealed negative differential conductance and complete current suppression for specific bias windows which were explained by a spin blockade mechanism [241]. An overview article envisioning several possible device geometries and significantly advancing the field was published by Bogani and Wernsdorfer in Ref. [44]. The authors suggested devices in which an SMM is either probed by STM or could be incorporated into a transistor geometry. Spin-valve behavior might be realized through an SMM attached to one FM contact with another diamagnetic electrode or by placing a magnetic molecule with two switchable magnetic centers between nonmagnetic electrodes. Finally, also multidot devices were proposed in which magnetic molecules could bridge inorganic quantum dots or SMMs could be grafted onto a suspended carbon nanotube for which spin selective transport through the nanotube was expected due to the presence of the molecular magnet.

The latter scenario has been realized shortly afterwards by wiring a $TbPc_2$ derived SMM to a single-walled carbon nanotube and still maintaining the hysteretic behavior [242]. Interestingly, the coupled SMM-nanotube unit showed increased anisotropy and magnetic relaxation time compared to the pure crystalline compound. Using this coupling of the $TbPc_2$ derived SMM to the nanotube, a supramolecular spin valve without magnetic leads could be demonstrated operating at temperatures below 1 K [45]. In this experiment the authors reported that two SMMs couple slightly differently to the nanotube which lead to different coercive fields

so that the device can be switched between parallel and antiparallel alignment of the $TbPc_2$ magnetizations giving rise to MR values of up to 300%. Later on the real-space visualization of the spin-split LUMO of $TbPc_2$ on a FM Co layer on Ir(111) by SP-STM was reported [243].

It was also demonstrated that an Fe_4 based SMM can be wired to a gold surface without detrimentally altering its properties, i. e. the SMM-surface hybrid system still showed a hysteresis below 1 K [46]. This is a significant contribution since SMMs are often fragile systems and hence frequently loose their distinct hysteretic properties when grafted onto surfaces [244]. Even more importantly, it was shown afterwards that a ML of these Fe_4 based SMMs on Au(111) exhibited quantum tunneling of magnetization, i. e. a stepped hysteresis curve which is the most appealing feature connected to the quantum nature of these magnetic materials [47].

Instead of using the electron spin as information carrier which can be strongly coupled to the environment leading to short relaxation times, the nuclear spin could be used as it is usually much less affected by environmental influences. In Ref. [48] it was proposed that the nuclear spin state of an individual metal ion in an SMM could be read out electronically. The experiments were carried out on a $TbPc_2$ molecule placed between Au contacts through which the electronic transport was studied. For the $TbPc_2$ a strong hyperfine interaction couples the magnetic moment of Tb to its nuclear spin ($I = \frac{3}{2}$). Hence the ground state of this ion is split into four sub-states. When the charge flows through the ligand it is affected by the nuclear spin state and the signal indicating magnetization reversal of the Tb magnetic moment occurs at four different applied magnetic fields directly connected to the nuclear spin states. In addition, long relaxation times of the nuclear spin of the order of tens of seconds were found. Recently, even the switching between different nuclear spin states by electric fields was demonstrated for this system by making use of the hyperfine Stark effect [49].

4.3.5. Spin Crossover Molecules for Molecular Spintronics

There is another class of materials of particular interest for MS. These are the so-called spin crossover materials for which the spin ground state can be changed by applying external stimuli as light, temperature or pressure [245]. They show an entropy driven transition from a low-spin to high-spin state due to the external influence [18]. These compounds hence also attracted the interest of the MS community since they can obviously act as a spin switch. In Ref. [246] an electrostatic spin crossover effect was demonstrated for di-cobaltocene based molecules which was induced by switching the sign of the exchange coupling between two magnetic centers. The control of the spin state, i. e. the initialization of the crossover by electric fields is outlined to be particularly promising from the application point of view as it allows the incorporation into electronic circuits. In addition, the authors pointed out that the

crossover fields of about 1 V/nm should be readily achievable in devices.

Other groups have been investigating the crossover in cyanide-based bimetallic polymers showing a temperature induced low-spin to high-spin transition observed experimentally [247] as well as theoretically [248]. An explanation of the effect was given based on bond stretching and charge redistribution. It was also demonstrated that DFT+U combined with *ab initio* molecular dynamics is able to simulate the temperature and pressure driven spin crossover in bimetallic metal-organic frameworks [249].

Later on an electron-induced reversible switching of single spin crossover complexes was demonstrated by STM on a double layer of the molecules on Au(111) [250]. Only a switching of the molecules in the second layer was observed which was deduced from the observed electronic structure change and a Kondo resonance being absent for the low-spin state. In addition, a robust spin crossover was reported for a single Fe-phen molecule on CuN on Cu(100) using STM [251]. The CuN layer on the surface was necessary to decouple the spin crossover molecule from the Cu(100) substrate on which no switching between the spin states was found.

4.3.6. Organic Magnetoresistance

Also in nonmagnetic organic materials without magnetic electrodes attached to them a universal low field magnetoresistance was found known as organic magnetoresistance (OMAR) for which the hyperfine interaction plays a central role [18]. The first results of an increase in the current (and light) output of an Alq_3 based light emitting diode by applying a magnetic field were presented in Ref. [252]. The current increased by 3% when using a field of 300 mT. Subsequently, a MR of up to 10% for fields of the order of 10 mT at room temperature was reported for polyfluorene sandwich devices and outlined to be a bulk effect of the organic material [253]. It was also demonstrated that the MR can be tuned between positive and negative values by adjusting the injection process of the charge carriers [254] or applied voltage and temperature [255]. However it was noted in Ref. [256] that none of the standard models of MR at that time were able to explain the results. Later on, as a possible mechanism of OMAR bipolaron formation in the presence of the hyperfine fields of the hydrogen nuclei and the external magnetic field was suggested [257].

4.3.7. Spin and Chirality

Based on experimental findings using photoelectron spectroscopy it has also been suggested that chiral molecules (molecules which are not identical to their mirror image) can lead to spin selectivity. In Ref. [258] the electron transmission of photoelectrons through a self-assembled ML of double-stranded DNA on Au(111) was studied. A spin polarization of up

to 60% was observed for the electrons emitted from the sample by linearly polarized light at room temperature. The spin polarization was found to increase nearly linearly with the length of the double-stranded DNA and no polarization was found for single-stranded DNA. An explanation for the observed findings was suggested based on an effective Hamiltonian to be a combination of spin-dependent backscattering and spin-flip processes [259]. Later on it was also outlined that the contact geometry can have a strong influence on the spin polarization [260]. Alternatively, also the concept of electrically driven pure spin currents in DNA was put forward [261].

Very recently, a strong magneto-chiral dichroism was observed in a paramagnetic molecular helix [262]. This usually weak effect occurs in magnetized chiral systems and indicates an inequivalent absorption of unpolarized light for different magnetization directions. In this study a strong magneto-chiral dichroism was only found for a molecular helicoidal chain including Co^{2+} ions but was essentially absent for an isostructural system with Mn^{2+} ions. The authors suggested that the studied Co system could be a promising candidate to observe the 'inverse' magneto-chiral dichroism which would allow to induce a magnetization in a chiral system using non-polarized light.

After this brief historical overview of important developments in MS research it should however be mentioned that already a number of reviews on the field have been published (see for instance Refs. [18, 158, 206, 211, 220, 221]) and that also a special issue of the MRS Bulletin has been devoted to this topic [263–269] where more detailed accounts on the specific subfields can be found.

4.4. Tuning Surface Magnetic Exchange by Molecular Adsorption

In the studies considered up to this point only the magnetic properties of the molecular part of the hybrid molecular-ferromagnetic interfaces have been taken into account. This especially concerns the magnetic order within a molecular layer induced by a FM substrate (Subsection 4.3.1), the spin injection and propagation in the organic material (Subsections 4.3.1 and 4.3.2) and the interface spin polarization on the site of the molecule (Subsection 4.3.3). In order to understand and explain those findings, the change of the electronic and magnetic structure of the underlying magnetic substrate was considered to be less relevant. This is surely not a good approximation for strongly interacting molecule-surface systems, i. e. the molecular adsorption and the associated hybridization of the states will also modify the magnetic properties of the surface. This paradigm shift gave rise to the new development in MS

research to tune the surface magnetic exchange interaction and anisotropy by molecular adsorption as introduced by several studies in 2013.

The first indication that this might indeed be a fruitful direction to follow was presented in Ref. [50] where the magnetic properties of Co intercalated graphene on Ir(111) were studied by SP-STM and DFT. Based on a recorded hysteresis loop deduced from the percentage of the intercalated regions aligned with respect to an applied magnetic field, the system showed an out-of-plane magnetization with a large coercive field of over 4.5 T which is strongly enhanced compared to a clean Co/Ir(111) surface [270]. It was outlined that the enhanced coercive field of the intercalated system is due to an interface effect which turns the graphene/Co/Ir(111) system into a magnetically harder material. In contrast, a recent theoretical study using the LSDA functional found that graphene adsorption on Co/Ir(111) would lead to a reduction of the Curie temperature and a decrease of the MAE [271].

4.4.1. Inter-layer Magnetic Softening Effect

The next investigation presenting results in the direction to modify the surface magnetic exchange interaction by molecules showed the large device relevance of the effect as a spin-valve like MR in a structure with at first sight only one magnetic contact was found [51]. The authors investigated a vertical device consisting of a Co bottom electrode on which a layer of several 10 nm of zinc methyl phenalenyl (ZMP) molecules was deposited and finally a non-magnetic Cu top electrode was put on the structure (see Fig. 4.8(a)). When measuring the electric resistance response of this device with respect to an applied magnetic field, a MR of about 20% was found that was observable even close to room temperature. Due to several control devices in which also an ultrathin Al_2O_3 layer was placed between the bottom Co and the ZMP which resulted in no MR, the MR behavior was assigned to the Co-ZMP interface and consequently the observed effect was termed interface magnetoresistance (IMR). This means that a second magnet in the system is formed at the interface between Co and ZMP. According to an *ab initio* model the working principle of the IMR device is explained as follows (see Fig. 4.8(b)). For large (negative) magnetic fields the magnetization of the interface magnet and the bulk Co magnetization are aligned parallel representing the low resistance state. As the field is increased, the coercive field of the bulk Co bottom electrode is reached first ($H_c^1 \approx 38$ Oe) and hence the Co magnetization switches to antiparallel alignment associated with an increase in resistance. At larger fields also the hard interface magnet switches ($H_c^2 \approx 600$ Oe at 4.2 K and ≈ 100 Oe at 250 K) establishing again parallel alignment of the magnetizations and therefore the device switches back to the low resistance state.

The mechanism of the independent switching of the bulk Co magnetization with respect to the interface magnetization was outlined to be a consequence of the strong interaction of

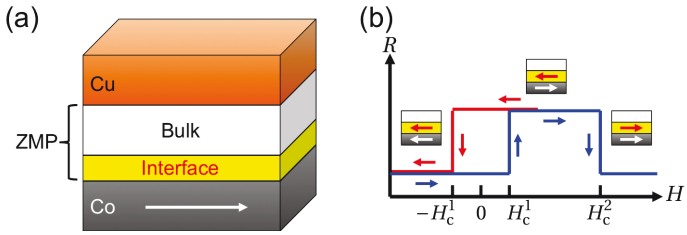

Figure 4.8.: Schematic representation of the device showing IMR [51] (a) made up of a bottom Co electrode, an interface region at the Co-ZMP boundary, the bulk part of the ZMP layer and a Cu top contact. Working principle of the IMR device (b): For large negative magnetic fields the bulk Co and the interface magnetization are aligned parallel leading to a low resistance state of the device. When the field is increased, the bulk Co layer switches at its coercive field H_c^1 giving rise to antiparallel alignment with higher resistance. At much larger fields also the hard interface magnetic layer reverses its magnetization at H_c^2 switching back to the low resistance state. Based on a figure in Ref. [51].

the first ZMP layer with the Co surface. The first ZMP molecule was found to be chemisorbed on the surface. This strong hybridization of the adsorbate with the uppermost Co atoms was outlined to magnetically decouple the first layer Co atoms below the molecule from the rest of the Co contact: *inter-layer magnetic softening* effect. This was quantified by the finding that the inter-layer magnetic exchange coupling constant $J_\perp$ between the first and second Co layer was reduced by 70% compared to a clean surface without molecules and even by 84% compared to the bulk coupling. Due to this decoupling the bulk magnetization was outlined to switch independently with respect to the interface magnetization.

A remarkable consequence of these findings is that the spin- and therefore the resistance-selectivity of the device is situated right at the interface between Co and ZMP. This means that in this case the spin transport through the bulk part of the organic material is not decisive to observe the MR behavior but rather the alignment of the magnets at the organic-ferromagnetic interface decides over the barrier for charge injection into the organic layer. In this way the controversial discussion of whether spin injection into and spin propagation through organic layers is possible, mentioned at the end of Subsection 4.2.3, is circumvented.

4.4.2. In-plane Magnetic Hardening Effect

Subsequently, an *ab initio* study was presented investigating the adsorption of 2,2-paracyclophane (PCP) on 1 ML Fe/W(110) elucidating the influence of the molecular adsorption on the magnetic exchange interaction between the surface Fe atoms in Ref. [52]. The relaxed molecule-surface geometry of this investigation in side and top view is shown in Fig. 4.9(a).

The study demonstrated that the magnetic exchange coupling constants J between the surface Fe atoms directly bound to the PCP molecule are strongly increased compared to the clean surface value. This strong enhancement of the in-plane exchange coupling between the Fe atoms of the first layer below the molecule was outlined to locally create a hard hybrid molecule-surface magnetic unit showing an enhanced barrier for magnetic switching: *in-plane magnetic hardening* effect. As a consequence, due to the molecular adsorption the hysteresis curve of the 1 ML Fe/W(110) surface was widened (see Fig. 4.9(b)), i. e. an increase of the coercive field $H_c^{1\,\mathrm{ML\,Fe/W(110)}}$ was observed, and also the simulated Curie temperature of the hybrid system was found to be significantly larger than the one of the clean surface.

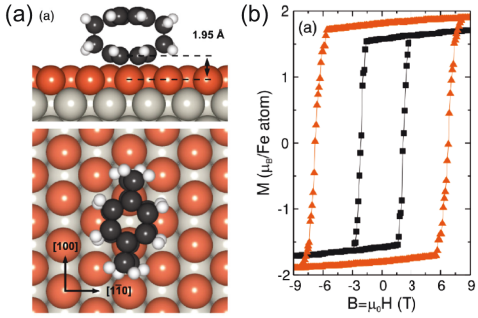

Figure 4.9.: Adsorption geometry of PCP on 1 ML Fe/W(110) in side view (upper part) and top view (lower part) (a) and opening of the hysteresis curve of the 1 ML Fe/W(110) system due to PCP adsorption (b). Figures taken from Ref. [52]. Copyright (2013) by the American Physical Society.

A direct experimental proof that carbon-based π-electron systems locally increase the magnetic exchange coupling was presented in Ref. [272]. There coronene molecules and graphene nanoflakes were studied on the magnetically non-collinear 1 ML Fe/Ir(111) surface by SP-STM experiments and DFT calculations. By recording magnetic field dependent SP-STM images of the coronene molecules and graphene nanoflakes on the surface it could be shown that these regions switch at a certain applied magnetic field. Hence locally collinear magnetic units were formed out of the 1 ML Fe/Ir(111) surface due to the adsorption of carbon-based π-systems. This is a remarkable point since the magnetically non-collinear structure of the 1 ML Fe/Ir(111) surface is established due to the delicate balance of different magnetic energy contributions, i. e. exchange, Dzyaloshinskii-Moriya and maybe also the four-spin interaction are of comparable energy scale in this case [4]. Since exchange favors collinear magnetic structures but the Dzyaloshinskii-Moriya interaction prefers perpendicularly aligned spins, a 'compromise' must be established which leads to the non-collinear magnetic structure. This magnetic structure has no net magnetic moment an does not respond to an external

magnetic field. However when the carbon-based π-electron systems were put onto the surface, they enhanced the exchange interaction due to the in-plane magnetic hardening and thereby establish it as the dominant magnetic energy scale leading to the local formation of collinear magnetic units. The authors also showed that the coercive field required to switch the collinear units was larger for the graphene nanoflakes compared to coronene (6.25 T compared to 1.25 T) since the strongly coupled magnetic units are larger in the first case. Finally, experimentally also a long-range coupling of the collinear units was observed which was mediated by the magnetically non-collinear clean surface regions.

Notably very recently, in other publications an opening of the hysteresis loop was also observed for alkanethiolate and C_{60} molecules on an ultrathin Co film on Au(111) [273, 274]. Moreover, a film of MnPc molecules on Co/Cu(100) showed an AFM order at room temperature which allowed to exchange bias the Co substrate at temperatures below 100 K [275]. Furthermore also a way to overcome the Stoner criterion of magnetism and turn Cu and Mn into FM materials at room temperature due to the adsorption of a layer of C_{60} molecules leading to a magnetic hardening mechanism was suggested in Ref. [276]. Moreover it was proposed that C_{60} adsorption could induce a magnetic reconstruction on a Ni(111) substrate [277].

4.4.3. Deduced Questions

When considering the in-plane magnetic hardening and inter-layer magnetic softening effects proposed above, immediately several questions arise:

- Can the in-plane magnetic hardening effect be tuned by a chemical functionalization of the adsorbed molecule?

  → Chapter 5

- What is the mechanism of the inter-layer magnetic softening effect?

  → Chapter 6

- What is the effect of extended, two-dimensional π-electron systems such as graphene onto the surface magnetic exchange interactions?

  → Chapter 7

- Can the concept be extended to form different magnetic units for logic operations using molecules with different molecular rings?

  → Chapter 8

- Is it possible to generalize the principle of molecular induced surface manipulation to other surface magnetic properties than exchange?

  → Chapter 9

These questions can be regarded as an outline for the results part of this thesis presented in the following. It is the objective of this thesis to provide some answers to these questions and to elucidate the richness of the approach for the discovery of new physical phenomena in surface magnetism.

Part II.

Results

5 Chemical Tuning of Magnetic Hardening

In this chapter the question whether the molecular induced in-plane magnetic hardening effect can be tuned by a chemical functionalization of the molecule is investigated. For this purpose a systematic approach is used where the influence of the four different molecules methyleneborane (CH_3B), ethene (C_2H_4), methyleneimine (CH_3N) and formaldehyde (CH_2O) on the magnetic exchange interactions of a 1 ML Fe/W(110) surface is studied. The electronic structure of the isolated molecules shows that the π-states are lowered in energy along the series from the B containing system methyleneborane to the O incorporating system formaldehyde. On the surface all molecules are chemisorbed and have similar stable adsorption positions with the π-bond situated between three surface Fe atoms. Only in case of methyleneborane the geometry is slightly different as the B atom occupies the hollow site between three Fe atoms.

When evaluating the magnetic exchange coupling constants for these systems within a nearest neighbor Heisenberg model, it turns out that most coupling constants are increased compared to the clean surface value. In particular the hardening of the coupling constants is especially strong when either C or B mediate the exchange coupling. Even more interestingly, a softening of the coupling constants is found when either elements of higher electronegativity as N and O or the B-C bond, due to the different adsorption geometry of methyleneborane, mediate the coupling. It is demonstrated that the geometrical distortions of the surface induced by the adsorption of the molecules cannot account for the change in the coupling constants, i. e. the observed changes of the coupling constants due to molecular adsorption are a consequence of the hybridization of states from the molecules and states of the substrate.

Finally, the implication of the modified exchange interactions between the surface Fe atoms for macroscopically observable quantities as the coercive field strength is estimated by evaluating a multi-scale Heisenberg Hamiltonian. The computed macroscopic hysteresis loops show that the coercive field of the 1 ML Fe/W(110) surface can be tuned selectively over a range of 2.2 T using the different adsorbates or by varying their concentration on the surface. These results demonstrate that it is indeed possible to chemically functionalize the surface magnetic exchange interactions leading to tailored magnetic hysteresis loops.

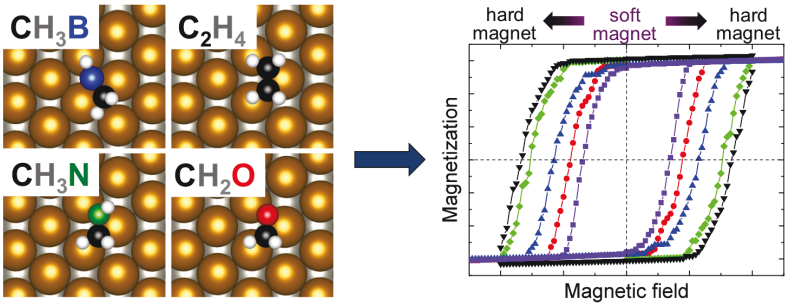

The investigations proposing an in-plane magnetic hardening of the surface magnetic exchange interactions by molecular or graphene adsorption outlined in Section 4.4 were dealing with π-electron adsorbates. In this chapter the magnetic hardening behavior will be investigated systematically by studying the effect of molecular π-electron systems containing heteroelements[1] on the change of the coupling constant J between magnetic surface atoms. The molecules are investigated on 1 ML Fe on a W(110) substrate since this surface is known to exhibit FM coupling within the Fe layer with in-plane magnetization [278] and is a well suited system for molecular spintronic examinations [52, 236]. Moreover, the initial proposal of molecular-induced in-plane magnetic hardening by PCP has been dealing with this substrate [52].[2]

5.1. Presentation of the Molecular Species

In order to gain understanding about the physical origin of in-plane magnetic hardening and possible in-plane magnetic softening induced by nonmagnetic organic molecules containing π-electrons, it is strongly appealing to systematically study the induced effects for the smallest π-electron systems possible. This means that one starts with a molecule containing only one π-bond, i. e. ethene (C_2H_4). The advantage of this starting point is also that in a simple fashion hetero-analogues can be derived by just exchanging one carbon atom by a specific heteroelement as B, N or O (see Fig. 5.1). As depicted in this figure, within each row the number of valence p-electrons as well as the electronegativity (according to the definition of Allred and Rochow [279]) increases from left to right. Hence these heteroatoms allow to tune the π-bond strength of the specific molecule. Moreover all structures are planar because of the sp^2-hybridization of the atoms contributing to the double bond.

Even more variability could be achieved when heteroelements from the third period, i. e. Si, P and S are taken into account (Al is not considered a valuable choice since metals do usually not form stable covalent bonds with C inside molecules). For these elements the change in electronegativity as shown in Fig. 5.1 is naturally less pronounced since the core potential is more effectively screened by the inner electrons in case of $3p$-elements compared to $2p$-elements. On the other hand the spatial extent of the p-states of these elements is considerably larger than for elements of the second row. This leads to spatially more extended π-states. Unfortunately, it turned out that these molecules are in general not stable on the 1 ML Fe/W(110) surface and only a metastable position could be found for each system. The results obtained for these metastable positions are presented in Appendix A in Subsection A.5.4.

[1] Heteroelements are elements other than C or H in organic compounds.

[2] Part of the results of this chapter have already been published in: R. Friedrich, V. Caciuc, N. S. Kiselev, N. Atodiresei, and S. Blügel, *'Chemically functionalized magnetic exchange interactions of hybrid organic-ferromagnetic metal interfaces'*, Physical Review B **91**, 115432 (2015).

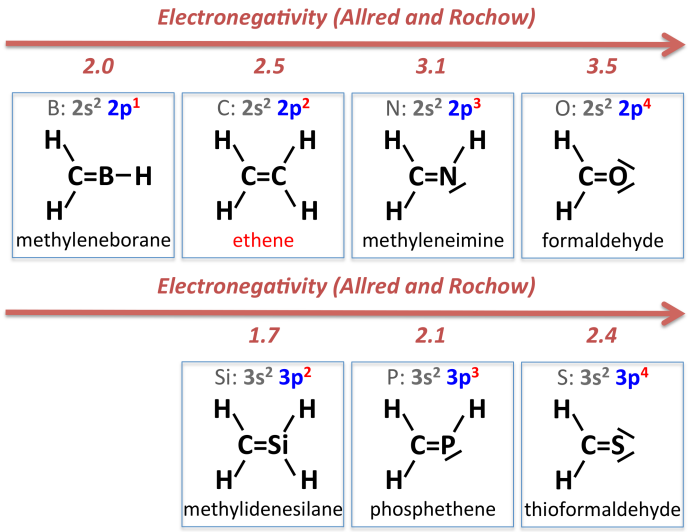

Figure 5.1.: Systematic presentation of the small π-electron systems studied. The given electronegativity value applies to carbon in case of ethene or to the heteroelement in all other cases and the values were taken from Ref. [279]. The tilted lines assigned to N, O, P and S stand for free electron pairs.

To depict even more clearly the change in the electronic structure between the different molecules, in Fig. 5.2(a) the calculated energy level spectra of these compounds are presented. Note that for this visualization the HOMO was aligned at the calculated respective ionization potential (IP)[3]. In addition, the bonding and antibonding π-states of each system are labeled by π and π^* respectively. As expected, the π- as well as the π^*-states are lowered in energy when going from methyleneborane to formaldehyde since the core potential of elements with higher atomic number is more attractive and therefore energetically lowers the states. In addition, also the spatial extent of the π-states is affected by the presence of the heteroelement as depicted by the isosurface plots of the charge density of those states in Fig. 5.2(b). In case of the bonding π-state, the charge density is polarized in the direction to the more electronegative element whereas for the antibonding π^*-state this trend is reversed. Considering this degree of variablity it seems reasonable to anticipate that these systems couple differently to the d-states of a metallic substrate and also alter the magnetic properties, i. e. the magnetic exchange coupling constants J between the surface atoms, to a different extent.

[3] In general those IPs calculated from the total energy difference between the neutral molecule and the cation with one electron less are in reasonable agreement with experiment as for ethene the calculated value of 10.42 eV is close to the accurate value of about 10.51 eV [280].

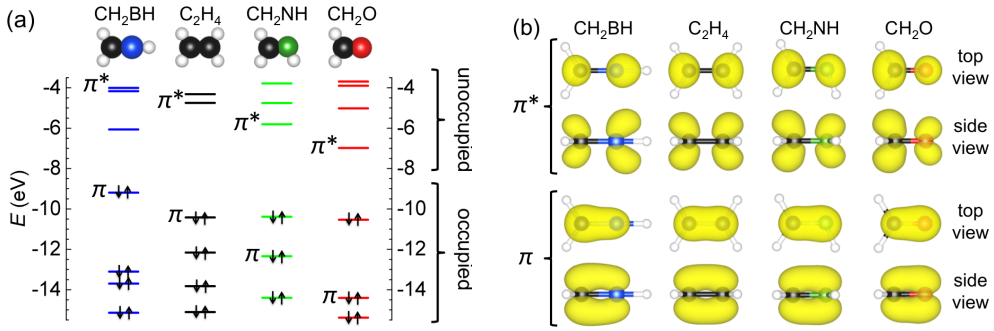

Figure 5.2.: Calculated energy levels of isolated methyleneborane, ethene, methyleneimine and formaldehyde (from left to right) (a). Note that the HOMO of each system was aligned at the calculated ionization potential (IP) which amount to 9.20 eV, 10.42 eV, 10.38 eV and 10.54 eV for CH_3B, C_2H_4, CH_3N and CH_2O, respectively. The bonding and antibonding π-states have been labeled π and π^*, respectively. The occupation of each state is indicated by arrows. Above the energy levels, the chemical formula and the atomic structure in a ball model of the respective molecule is given. Color code: white for H, black for C, blue for B, green for N and red for O. (b): Isosurface plots of the π- and π^*-states in top view and side view for each system. All plots were made for an isovalue of $1.01 \cdot 10^{-1}$ $e/\text{Å}^3$.

5.2. Adsorption Geometries and Structural Properties

The different investigated adsorption sites are depicted in Fig. 5.3 as illustrated for ethene. In case of the hollow site (Fig. 5.3(a)) the π-bond sits in a hollow position of the surface and connects four surface Fe atoms. Within the bridge and bridge35 structures (Figs. 5.3(b) and 5.3(c)) the π-bond of the molecule connects two Fe atoms which are next nearest neighbors and nearest neighbors, respectively. Furthermore, the molecule can be positioned directly on top of an Fe atom with the π-bond either pointing in the $[1\bar{1}0]$ (top position, Fig. 5.3(d)) or in the [001] direction (top90 position, Fig. 5.3(e)). Finally, the molecule can be placed into a threefold hollow atop site where the π-bond connects three Fe atoms (Fig. 5.3(f)).

During the structural optimization of the different adsorption positions for all molecules it turned out that only some of the considered sites represent local minima in the potential energy landscape but not all are stable. The ground state adsorption geometries for the different molecules adsorbed on the substrate are shown in Fig. 5.4. For ethene, methyleneimine and formaldehyde (see Figs. 5.4(b-d) and (f-h)) the atop site is favored with the hydrogens on the right pointing away from the surface. This also makes sense in view of the results presented in Ref. [52] since there two π-bonds of the lower benzene ring of PCP are positioned between three Fe atoms as the π-bond of ethene is here. In contrast, the most stable adsorp-

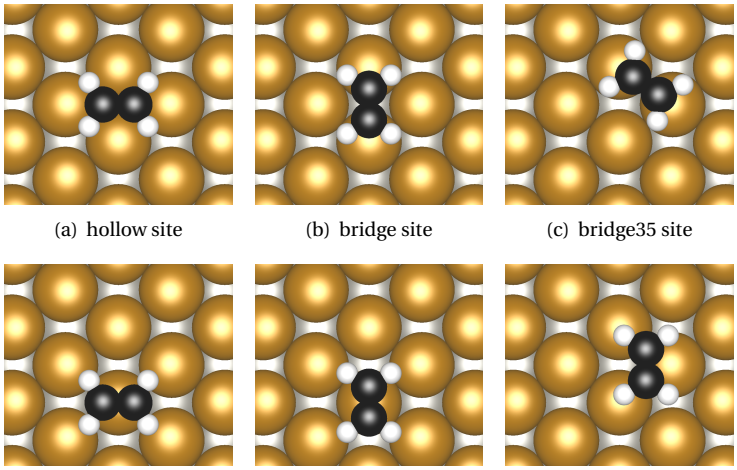

(a) hollow site (b) bridge site (c) bridge35 site

(d) top site (e) top90 site (f) atop site

Figure 5.3.: Investigated adsorption sites shown for the exemplary case of ethene. Color code of the surface atoms: gold for Fe and gray for W.

tion position for methyleneborane (see Figs. 5.4(a) and (e)) is characterized by the fact that the boron is positioned in the threefold hollow created by the surrounding Fe atoms. This finding can be rationalized by the general tendency of B to compensate for its lack of valence electrons (hypovalency) by the formation of additional bonds [281].

From the structural point of view the adsorption of the molecules modifies the surface geometry such that for ethene, methyleneimine and formaldehyde the distance between the three Fe atoms below the π-bond is reduced compared to the clean surface value (see Table 5.4)[4]. On the other hand for methyleneborane these three Fe atoms relax away from one another as a consequence of the presence of B. Moreover, in general the distance of the heteroatoms to the surface Fe atoms they are bound to is smaller than the respective C-Fe distance (see Table 5.1).

The corresponding adsorption energies for the stable geometries are listed in Table 5.1. The adsorption energy is defined as

$$E_{\mathrm{ads}} = -[E_{\mathrm{sys}} - (E_{\mathrm{surf}} + E_{\mathrm{mol}})], \tag{5.1}$$

where E_{sys} is the total energy of the combined molecule-surface system, E_{surf} stands for the total energy of the undistorted clean surface and E_{mol} represents the total energy of the isolated molecule. Thus the adsorption energy expresses the energy gained when the molecule

[4]The modified Fe-Fe distances will later on be discussed in detail in terms of the coupling constants evaluated for the molecular-induced surface geometries.

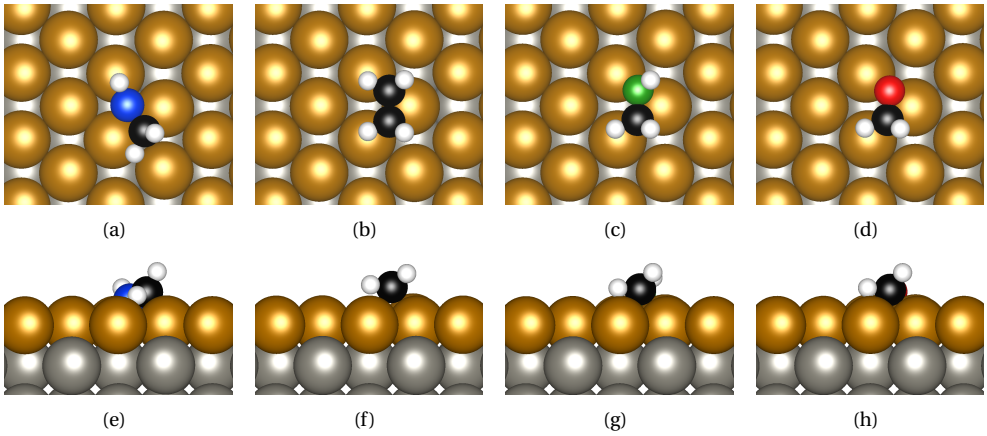

Figure 5.4.: Ground state geometries for methyleneborane, ethene, methyleneimine and formaldehyde on 1 ML Fe/W(110) in top view (a to d) and side view (e to h).

and the surface are brought together. A negative number for E_{ads} indicates a repulsive interaction of both systems. Here especially the very high adsorption energy of methyleneborane being larger by about a factor of two compared to all other systems is remarkable pointing again to a strong interaction with the surface due to the special reactivity of B induced by its lack of valence electrons. For the other molecules in the atop position the adsorption energy is about 2 eV smaller. Nevertheless, the most important point is that all adsorption energies are larger than 1 eV which for these small systems indicates a chemisorption of all molecules to the surface according to Subsection 4.1.2.

Table 5.1.: Calculated adsorption energies E_{ads} and molecule-surface distances for the ground state adsorption geometry of each molecule on 1 ML Fe/W(110) depicted in Fig. 5.4. The labeling of the Fe1, Fe2 and Fe3 atoms is presented in Fig. 5.5. 'h' stands for 'hetero'.

molecule/surface	E_{ads} (eV)	distances (Å)				
		C-Fe1	C-Fe3	h-Fe1	h-Fe2	h-Fe3
methyleneborane (CH_3B)	3.30	2.12	2.21	2.13	1.98	2.14
ethene (C_2H_4)	1.19	2.11	2.25	2.11	2.25	3.10
methyleneimine (CH_3N)	1.76	2.11	2.19	2.05	2.01	3.00
formaldehyde (CH_2O)	1.48	2.10	2.15	2.03	2.05	2.99

5.3. Magnetic Moments and Exchange Coupling Constants

In addition, all molecules have a pronounced influence on the magnetic moments of the surface Fe atoms. However, it is observed that only the three surface Fe atoms directly bound to the molecule are affected. This is also true in case of methyleneborane (CH_3B) where the distance between the Fe atom below the C atom in Fig. 5.4(a) and this C atom is 2.6 Å which is found to be too large to affect the Fe magnetic moment. Consequently, the impact of the molecules is confined to the three Fe atoms forming underneath them the threefold hollow labeled Fe1, Fe2 and Fe3 in Fig. 5.5. In addition, also the magnetic exchange coupling constants are assigned in the figure which are needed for the later discussion.

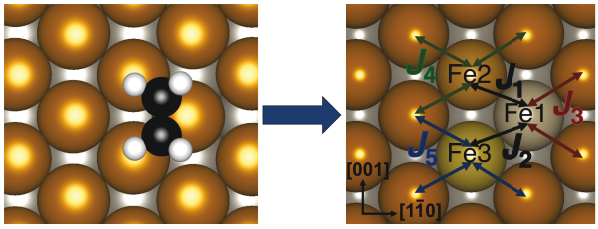

Figure 5.5.: The influence of the molecules onto the surface magnetic moments (here for the exemplary case of ethene) is confined to the three Fe atoms labeled Fe1, Fe2 and Fe3 directly bound to them. Also the magnetic exchange coupling constants needed for the nearest neighbor Heisenberg model are assigned in the right part of the figure.

More precisely, the magnetic moments of Fe1, Fe2 and Fe3 are listed for each system in Table 5.2. The general observation is that the moments of the Fe atoms close to the molecules are significantly reduced compared to the clean surface value of 2.5 μ_B. This finding is a consequence of the hybridization of the substrate d- and mainly the molecular p_z-states leading to a broadening of the DOS which effectively reduces the magnetic moments. Notably, the moment of the Fe2 atom, which is close to the heteroelement, increases from methyleneborane (CH_3B) to formaldehyde (CH_2O) towards the clean surface value. This behavior reveals that although the bond distances between the heteroatoms and the surface Fe are usually shorter than the Fe-C bond distances as mentioned in Section 5.2, the impact of those elements on the magnetic properties of the surface Fe decreases when going from B to O. This suggests a *local* element specific selectivity which is in line with the reduced spatial extent of the π-states for the molecules with heteroelements of larger electronegativity as depicted in Fig. 5.2. A similar but less pronounced trend is observed for the moment of the Fe1 atom whereas the moment of Fe3, which is close only to C, is practically the same for all hybrid molecule-surface systems.

Table 5.2.: Magnetic moments of the three Fe atoms close to the π-bonded molecules adsorbed on the 1 ML Fe/W(110) surface.

molecule/surface	magnetic moments (μ_B)		
	Fe1	Fe2	Fe3
clean surface	2.5	2.5	2.5
methyleneborane (CH_3B)	2.0	2.0	2.1
ethene (C_2H_4)	2.2	2.1	2.1
methyleneimine (CH_3N)	2.2	2.3	2.0
formaldehyde (CH_2O)	2.3	2.5	2.0

For the calculation of the coupling constants J one needs to consider that the magnetic moments of the Fe atoms close to the molecules, i. e. Fe1, Fe2 and Fe3, are modified and therefore also the coupling among them and to the neighboring clean surface Fe atoms as depicted in Fig. 5.5 is supposed to be changed. The exchange coupling between the magnetic moments of the Fe atoms is described by an effective nearest neighbor Heisenberg Hamiltonian:

$$H^{\text{spin}} = -\sum_{\langle i>j\rangle} J_{ij}\mathbf{m}_i\mathbf{m}_j, \tag{5.2}$$

where $\mathbf{m}_i$ and $\mathbf{m}_j$ stand for the magnetic moments of centers i and j respectively[5] and the notation $\langle\ldots\rangle$ denotes that only nearest neighbors are taken into account. According to this Hamiltonian and in the spirit of Ref. [170] the energy difference between the FM and a specific AFM alignment characterized by the flipped moments i with respect to their unflipped nearest neighbor moments j of the magnetic moments of surface Fe atoms can be expressed as:

$$E_{\text{FM}} - E_{\text{AFM}_{i,j}} = -2\sum_n N_n J_n m_{\{i\},n} m_{\{j\},n}, \tag{5.3}$$

where $m_{\{i\},n}$ and $m_{\{j\},n}$ are the absolute values of the magnetic moments of the coupled sorts of flipped $\{i\}$ and unflipped nearest neighbor $\{j\}$ Fe atoms and N_n denotes the number of equivalent neighbors of sort n. For example for the Fe2 atom in Fig. 5.5 there are three equivalent couplings J_4 to three clean surface neighbors ($N_4 = 3$) and another coupling J_1 to its Fe1 neighbor ($N_1 = 1$). The sum over all N_n is the number of all nearest neighbors for all centers for which the spin is flipped with respect to the neighbors, i. e. it denotes the number of nearest neighbor couplings 'activated' by the specific AFM alignment. From Equation (5.3) the different J parameters labeled in Fig. 5.5 can be obtained from *ab initio* by taking into account a suitably chosen set of AFM configurations and solving the resulting linear system of equations for the exchange coupling constants.

[5]The absolute value of the magnetic moments will later on be included in the coupling constants J_{ij} which are then expressed in terms of energy units.

Considering the case shown in Fig. 5.5, to obtain those AFM configurations one can flip the magnetic moment of each of the three influenced Fe atoms individually yielding three equations. In addition, there are three possibilities to flip the spins of pairs giving another three equations. Finally, one can flip the spin of all three Fe moments simultaneously ending up in one further equation. Those seven AFM configurations are schematically visualized in Fig. 5.6. So in total there are seven equations for in general five different coupling constants[6]. However, it can be shown that two of those seven equations are linearly dependent on the five others so that there are only five linearly independent equations. More explicitly, when flipping the moments of Fe2 and Fe3 simultaneously, this is according to the applied nearest neighbor Heisenberg model just the sum of the equations resulting from flipping the Fe2 and Fe3 moments individually. So this set of three equations is linearly dependent. Further, also the equations resulting from flipping the Fe1 moment, flipping Fe1 and Fe2 together, flipping Fe1 and Fe3 together and flipping all three at once yield a set of four linearly dependent equations. Hence one has to take care of the fact that when calculating the coupling constants always a set of independent equations needs to be selected. There are 12 possibilities to select 5 independent equations considering the underlying dependency within a set of three and of four of the seven equations. This reveals an opportunity to check the consistency of the results by calculating the coupling constants with various sets of equations.

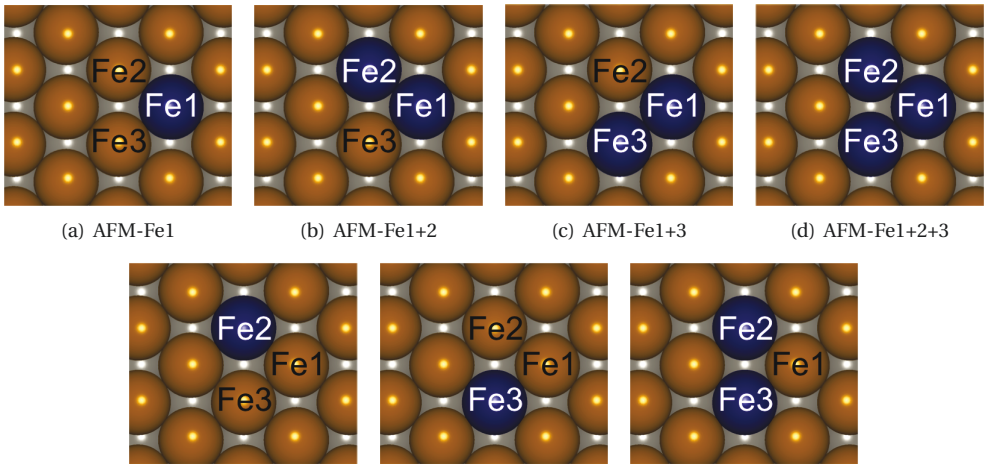

(a) AFM-Fe1 (b) AFM-Fe1+2 (c) AFM-Fe1+3 (d) AFM-Fe1+2+3

(e) AFM-Fe2 (f) AFM-Fe3 (g) AFM-Fe2+3

Figure 5.6.: The AFM configurations used to calculate the exchange coupling constants for the small π-electron systems on 1 ML Fe/W(110). The atoms for which the moment is flipped in the respective configuration are displayed in dark blue.

[6]For ethene adsorbed on the surface as presented in Fig. 5.4 there are only three different coupling constants since $J_1 = J_2$ and $J_4 = J_5$ due to symmetry.

In Table 5.3 and Fig. 5.7(a) the magnetic exchange coupling constants evaluated using the above procedure are presented for all investigated molecule-surface systems. The values have been obtained by averaging over the results deduced from taking into account different sets of equations[7]. As a reference, also the clean surface coupling constant of 35.3 meV is included in Fig. 5.7(a). In most of the cases one observes that the coupling constants of the hybrid molecule-surface systems are significantly increased compared to the clean surface value. This is especially pronounced in case of the ethene-surface system where $J_1 = J_2 = 59.9$ meV is about a factor two larger than the clean surface exchange coupling. Notably, when these coupling constants are expressed in meV/μ_B^2 instead of meV by dividing by the absolute values of the magnetic moments of the coupled centers, a value of 15.4 meV/μ_B^2 is obtained which is in good agreement with the value of 15.65 meV/μ_B^2 reported for PCP on the same surface [52]. Furthermore, also J_2, J_3 and J_4 of the methyleneimine- and formaldehyde-surface systems are enhanced to values between about 40 and 50 meV compared to the clean surface system.

Table 5.3.: Calculated magnetic exchange coupling constants J between the Fe atoms as labeled in Fig. 5.5 for the hybrid molecule-surface systems and the molecular-induced surface geometries.

molecule/surface	molecule/surface (meV)					induced geometry (meV)				
	J_1	J_2	J_3	J_4	J_5	J_1	J_2	J_3	J_4	J_5
clean surface	35.3	35.3	35.3	35.3	35.3	35.3	35.3	35.3	35.3	35.3
methyleneborane (CH_3B)	50.8	3.0	31.5	33.3	50.6	25.5	24.4	28.9	36.3	39.0
ethene (C_2H_4)	59.9	59.9	29.5	42.4	42.4	51.9	51.9	14.5	32.4	32.4
methyleneimine (CH_3N)	27.9	39.3	47.4	44.6	36.2	39.6	43.8	21.6	35.1	31.3
formaldehyde (CH_2O)	20.6	42.8	47.1	49.6	35.9	46.5	37.3	18.9	40.5	30.2

Interestingly, the value of J_1 systematically decreases along the series from ethene (C_2H_4) to formaldehyde (CH_2O) from 59.9 meV to 20.6 meV. However, for the methyleneborane-surface system $J_1 = 50.8$ meV is slightly smaller than it is in case of the ethene-surface system. This can be assigned to the different adsorption geometry displayed in Fig. 5.4(a) which shows that B is not positioned exactly between Fe1 and Fe2 as is the case for the other heteroatoms. Nevertheless, this decrease of J_1 from the C based to the O based system correlates with (i) an increase of the heteroatom electronegativity and (ii) the above mentioned reduction of the π-state extent along this series of molecules. Even more importantly, in case of the methyleneimine- and formaldehyde-surface systems J_1 is *smaller* than the clean surface value signifying a *softening* of the in-plane magnetic exchange coupling between Fe1 and Fe2 due to N and O. This finding demonstrates that it is indeed possible to *locally* tune the in-

[7] The error bar for the exchange coupling constants estimated from the results for the different sets of equations is of the order of 10 meV.

plane magnetic exchange interaction between surface atoms element-selectively due to suitably chosen adsorbates from hardening to softening.

The behavior of the methyleneborane-surface system is however qualitatively different from those of the other systems because of the different adsorption geometry. In this respect, the J_2 coupling is mediated by the B-C bond (see Fig. 5.4(a)) and is found to be drastically reduced to 3 meV compared to the clean surface coupling. This means that Fe1 and Fe3 are effectively magnetically decoupled due to the adsorption of methyleneborane. On the contrary, the J_5 coupling constant is strongly enhanced in this case which is a consequence of the fact that the B-C bond effectively 'pushes' Fe3 towards its left clean surface neighbors (see Fig. 5.4(a)) which consequently enhances their coupling strength.

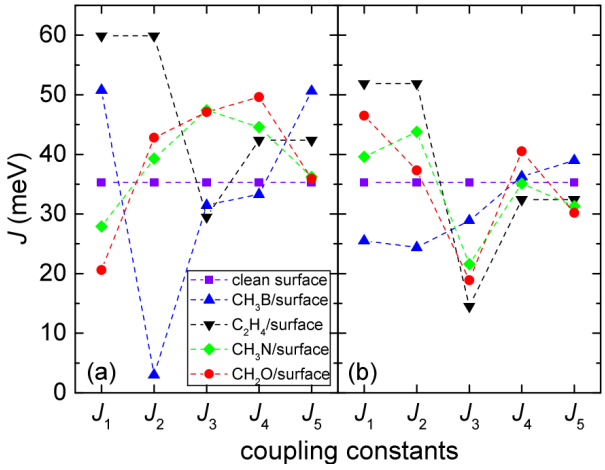

Figure 5.7.: Visualization of the magnetic exchange coupling constants calculated for the hybrid molecule-surface systems (a) and for the molecular-induced surface geometries (b).

Naturally, there arises the question after the mechanism of the molecular-induced in-plane magnetic hardening and softening of the exchange coupling constants outlined above. In Ref. [52] the hardening was suggested to be a consequence of the hybridization between the electronic states of the substrate and those of the molecule which is to be regarded as a molecule-surface hybridization effect. On the other hand, as already outlined in Section 5.2, the strong chemisorption interaction of the molecules with the substrate significantly distorts the surface geometry by modifying the Fe-Fe distances which is consequently also supposed to exert an influence on their magnetic coupling. This will be denoted as a geometrical influence. To clarify the contribution of the latter effect, the coupling constants have been recalculated for the molecular-induced surface geometries, i. e. the relaxed molecule-surface geometries but with the molecules removed from the system. For these geometries the mag-

netic moments of Fe1 to Fe3 deviate only by maximally 0.1 μ_B from the 2.5 μ_B clean surface moment.

These recalculated coupling constants of the molecular-induced geometries are included in Table 5.3 and are visualized in Fig. 5.7(b). One immediately realizes that these coupling constants do not reach the extremal values observed in case of the hybrid systems (see Fig. 5.7(a)) and in certain cases even show a *qualitatively* different behavior with respect to the clean surface coupling compared to the hybrid molecule-surface systems. In addition, they can be correlated with the modified Fe-Fe distances listed in Table 5.4. More specifically, the coupling constants J_1 and J_2 of the ethene-, methyleneimine- and formaldehyde induced geometries are all larger than the clean surface value but do not reproduce the values obtained for the hybrid systems. The general increase of these coupling constants is linked to the common characteristic of all three systems that due to the adsorption of the molecules the Fe1 atom is pulled closer to Fe2 and Fe3. Hence due to the reduced distance the $J_{1/2}$ couplings are slightly enhanced. On the contrary, J_3 is considerably reduced in all three cases which is associated to the fact that while the Fe1-Fe2 and Fe1-Fe3 distances are reduced, the distance of Fe1 to its clean surface neighbors on the right side (see Fig. 5.5) is enhanced to over 2.8 Å leading to weaker coupling. J_4 and J_5 are only weakly affected for the induced geometries as the corresponding distances are only slightly changed by the adsorption of the three molecules. In case of the methyleneborane-induced geometry the physical picture is again different. Here J_1 and J_2 are reduced compared to the clean surface value since the B adsorption pushes Fe1, Fe2 and Fe3 away from one another (see Fig. 5.4(a)) as already mentioned in Section 5.2 leading to a weakened coupling among them. However Fe3 is accordingly pushed closer to its clean surface neighbors which gives rise to a slight increase of J_5.

Table 5.4.: Fe-Fe distances for the small π-electron systems on 1 ML Fe/W(110). The clean surface (cs) Fe-Fe distance is 2.75 Å.

molecule/surface	distances (Å)				
	Fe1-Fe2	Fe1-Fe3	Fe1-cs	Fe2-cs	Fe3-cs
methyleneborane (CH_3B)	2.86	2.88	2.71	2.75	2.69
ethene (C_2H_4)	2.61	2.61	2.91	2.77	2.77
methyleneimine (CH_3N)	2.71	2.65	2.85	2.78	2.77
formaldehyde (CH_2O)	2.75	2.65	2.85	2.79	2.77

Nevertheless, the most important conclusion here is that the coupling constants for the induced geometries do not reproduce the changes observed for the hybrid molecule-surface systems. This is also demonstrated in Fig. A.3 in Appendix A which shows that only for the molecular-induced geometries a clear correlation between the size of J and the Fe-Fe distance exists since for the hybrid systems the molecule-surface hybridization effect is decisive.

5.4. Spin-polarized Projected Density of States

In Fig. 5.8(a) the spin-polarized projected DOS (SP-PDOS) of all d-states of Fe1 for the (undistorted) clean surface, the C_2H_4-surface system and the CH_2O-surface system are depicted. For clarity, only the results for two hybrid systems are displayed since the behavior of the other molecule-surface systems is qualitatively similar. The strong hybridization present for the molecule-surface systems is clearly visible and one observes a significant modification of the SP-PDOS compared to the one of the clean surface. This leads to the reduction of the magnetic moments of the surface atoms as reported in Table 5.2 since the hybridization reduces the occupation of the spin up channel and at the same time enhances the occupation of the spin down channel. These findings again point to a strong chemisorption of all molecules on the 1 ML Fe/W(110) surface.

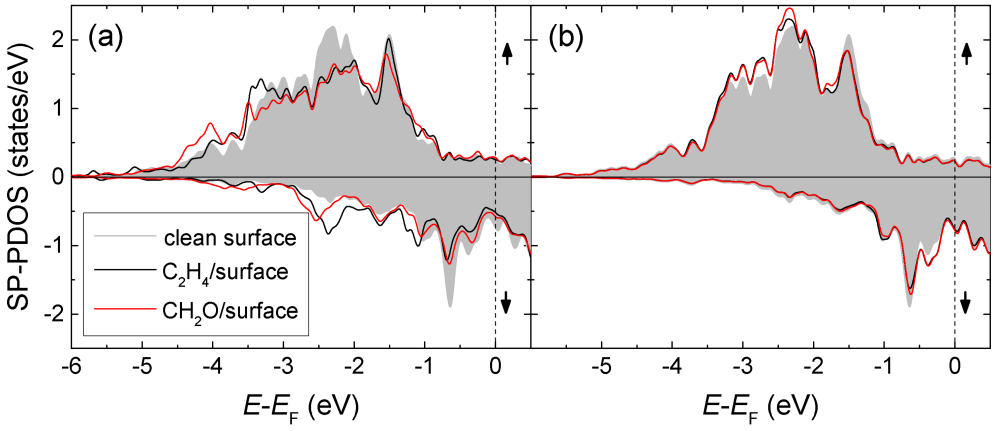

Figure 5.8.: SP-PDOS of the d-states of the Fe1 atom for (a) the hybrid molecule surface systems and (b) the molecular-induced surface geometries. For clarity, only the results for the clean undistorted surface, for the C_2H_4-surface system and for the CH_2O-surface system are shown as the results for the other hybrid systems are qualitatively similar. Note that the differences in the computed exchange coupling constants for the hybrid systems are assigned to the differences in the SP-PDOS in (a) and (b).

On the other hand, the SP-PDOS of the corresponding induced surface geometries shown in Fig. 5.8(b) exhibits only very small differences compared to the clean surface SP-PDOS. This again underscores that the hybridization of substrate states with states of the adsorbates significantly alters the electronic and magnetic properties of the surface Fe atoms bound to the molecules. It is however still important to note that the small differences observed in the SP-PDOS for the induced geometries compared to the (undistorted) clean surface account for

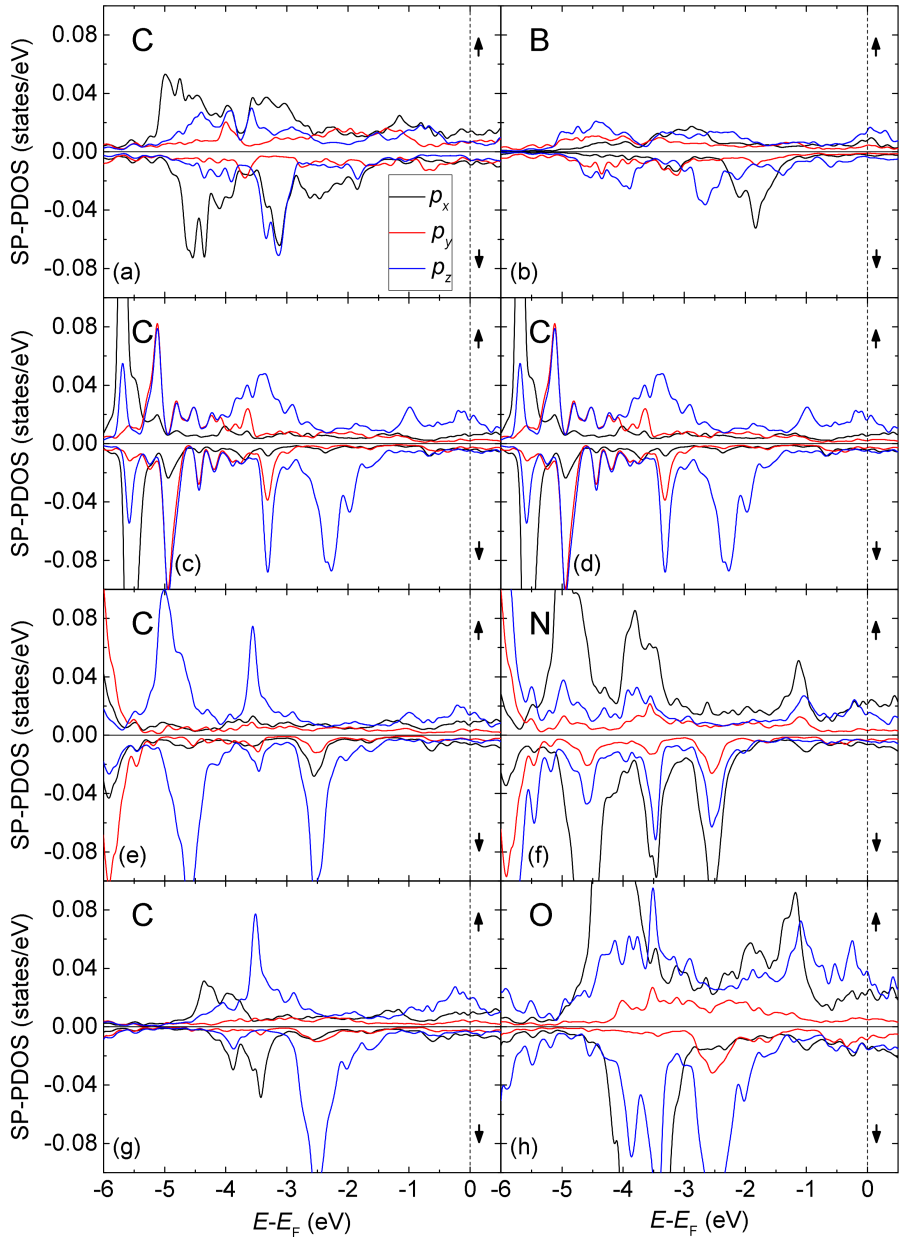

Figure 5.9.: SP-PDOS of the p-states on the molecular site of the hybrid systems for C and the respective heteroatom within methyleneborane (a), (b), ethene (c), (d), methyleneimine (e), (f) and formaldehyde (g), (h).

the modified coupling constants of Fig. 5.7(b) evaluated for these induced geometries. Thus, the decisive point here is that the molecule-surface hybridization is the key factor for the observed changes in the magnetic properties of the substrate and although for the induced geometries modifications are detectable, they do not account for the in-plane magnetic hardening and softening of the coupling constants found for the hybrid systems.

The SP-PDOS at the molecular site for the C and heteroatoms of each system is presented in Fig. 5.9. Generally, in all cases a strong hybridization of the states is observed which is due to the strong chemisorption of the molecules on the surface. In addition, one sees that in every case a finite DOS at the Fermi energy E_{F} exists which means that the whole molecule-surface hybrid system is metallic. Another general feature is that the peaks in the SP-PDOS reach higher values the more electronegative the element is which is a consequence of the additional valence electrons of atoms with higher atomic number. Remarkably, for the C SP-PDOS of the ethene-, methylenenimine- and formaldehyde-surface systems (see Fig. 5.9(c),(e),(g)) the hybridization close the Fermi energy is strongest in the p_z-channel indicating that the molecule-surface interaction is mainly driven by the p_z-d interaction with d-states from the substrate. However in the SP-PDOS of the N and O heteroatoms for the methyleneimine- and formaldehyde-surface systems also additional hybridization in the p_x- and p_y-channels is observed. This tendency is in line with the reduced heteroatom-surface distance compared to the C-surface distance noted in Section 5.2 meaning that when those atoms come closer to the surface also the in-plane p_x- and p_y-states can interact with the states of the substrate. The case of the methyleneborane-surface system is again different in the sense that all p-states of both C (see Fig. 5.9(a)) and B (see Fig. 5.9(b)) are strongly hybridized. This can be rationalized directly by referring to the side view of the adsorption geometry presented in Fig. 5.4(e) where the molecule 'sinks' into the surface giving rise to a favorable interaction of both out-of-plane p_z- as well as in-plane p_x- and p_y-states of C and B with the substrate.

5.5. Magnetic Anisotropy Energies

As a further step, also the magnetic anisotropy of the molecule-surface hybrid systems has been analyzed. The magnetic anisotropy establishes the connection between spatial directions and the directions in which the magnetic moments are pointing in that different spatial orientations of the magnetization due to the lattice potential lead to a different energy (see Subsection 3.2.6). Here it is addressed whether or not and to which extent the magnetization direction of the magnetic substrate is affected by the formation of the molecule-surface hybrid systems. This issue is of key importance since the magnetic stability of a system is connected to the anisotropy barrier opposing flipping of the magnetization.

The MCA energies have been calculated as the total energy differences between cases in

which all moments were aligned along the three high-symmetry directions, i. e. the [1$\bar{1}$0] and [001] in-plane (see Fig. 5.5) and the [110] out-of-plane direction, for all molecule-surface hybrid systems by including SOC into the calculations. Notably, the MCA energy is practically equivalent to the MAE for 1 ML Fe/W(110) since the shape anisotropy arising from magnetic dipole-dipole interactions is negligible in this case[8]. This justifies to denote the calculated energy differences as MAEs as done in Refs. [52, 283]. The obtained values are given in Table 5.5. In terms of consistency, the MAE of 2.7 meV obtained for the clean surface is in good agreement with the value of 2.8 meV obtained from full-potential linearized augmented plane wave calculations presented in Ref. [278]. It is found that for all systems the easy axis of magnetization lies along the in-plane [1$\bar{1}$0] direction which is the long axis of a c(2×2) surface unit cell. The energy of this configuration has consequently been set to zero and the energies for all other configurations are given with respect to this case. As a general feature, for the hybrid systems the MAE is reduced in the [001] direction whereas mainly the opposite is observed for the [110] direction. Interestingly, the calculated values indicate that the hard axis is changed from [001] to [110] due to molecular adsorption for the methyleneborane-, methyleneimine- and formaldehyde-surface systems which correlates with the magnetic softening of the coupling constant observed in these cases (see Fig. 5.7).

Table 5.5.: MAEs calculated for the small π-electron systems on 1 ML Fe/W(110).

molecule/surface	MAE (meV/atom)		
	[1$\bar{1}$0]	[001]	[110]
clean surface	0.0	2.7	2.3
methyleneborane (CH_3B)	0.0	2.3	3.1
ethene (C_2H_4)	0.0	2.1	2.1
methyleneimine (CH_3N)	0.0	1.9	2.4
formaldehyde (CH_2O)	0.0	2.2	3.0

5.6. Multi-scale Monte Carlo Simulations

To demonstrate the implication of the modified magnetic exchange coupling constants and MAEs for macroscopically observable quantities such as magnetic hysteresis loops at finite temperature and temperature dependence of the coercive field, Monte Carlo (MC) simulations[9] have been carried out [284]. For these simulations the evaluated coupling constants and the MAEs from Tables 5.3 and 5.5 have been utilized. The initial coverage density of the molecules in the MC simulations was twice the one used in the DFT calculations in order

[8] An estimate of the shape anisotropy based on the classical dipole-dipole interaction yields an energy contribution of about 0.03 meV per Fe atom [282].

[9] The MC simulations were performed by Nikolai S. Kiselev (PGI-1/Forschungszentrum Jülich).

to clearly show the influence of the modified coupling constants. Hence the unit cell consisted of 12 Fe atoms from which 3 were directly influenced by the molecules amounting to a coverage density of 1/4. The obtained hysteresis loops are presented in Fig. 5.10(a) which unequivocally depicts that the magnetization reversal process of the clean surface can be fine tuned by the adsorption of the different π-electron systems. The clean surface shows the narrowest hysteresis, i. e. has the smallest coercive field H_c[10] of about 1.5 T. This switching field is strongly enhanced (by about 2.2 T in Fig. 5.10(a)) for the hybrid ethene-surface system. The influence is however weaker in case of the methyleneimine adsorption and for the formaldehyde-surface system the coercive field is only slightly higher than that of the clean surface. Remarkably, for the methyleneborane-surface system the large values of the J_1 and J_5 coupling constants together with the very small J_2 coupling lead to the finding that for this system the corresponding coercive field fills the gap between the one of the methyleneimine- and the formaldehyde-surface systems. It is however important to realize that for the simulations all coupling constants need to be taken into account individually as the average coupling constant for each system will not lead to the same order as the evaluated coercive fields.

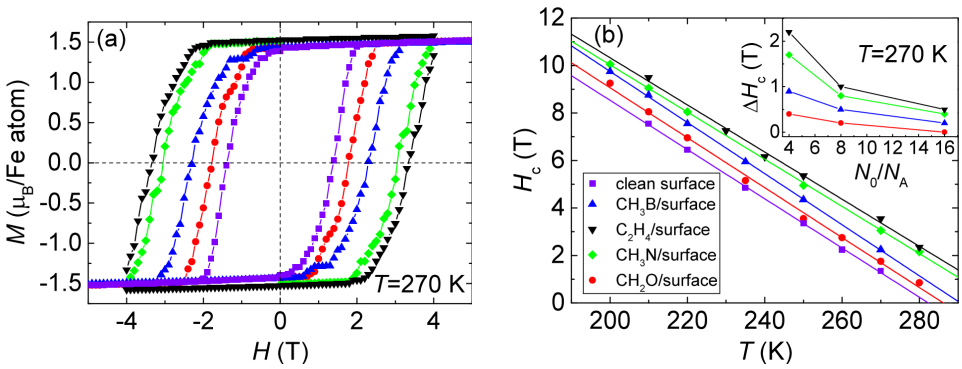

Figure 5.10.: Hysteresis curves (a) and temperature dependence of the coercive field strength (b) for the small π-electron systems on 1 ML Fe/W(110) simulated by MC calculations. The inset of (b) depicts a concentration dependence of the change of the coercive field strength ΔH_c of the respective molecule-surface system with respect to the clean surface. Note that the coverage density of the molecules increases from right to left. In every case the clean surface is the softest magnet with the smallest coercive field which is magnetically hardened by the deposition of the different molecules.

The temperature dependence of the coercive field strength in Fig. 5.10(b) shows a linear behavior over the investigated temperature range for all systems and reveals a similar trend

[10]The coercive field H_c is the absolute value of the external magnetic field that needs to be applied to achieve zero magnetization when the sample was magnetically saturated before the field is applied.

as the hysteresis loops in Fig. 5.10(a). The highest temperature-dependent coercive field is always observed for the ethene-surface system and the smallest increase compared to the clean surface is observed for the formaldehyde-surface system.

Most importantly, the tuning of the magnetic hysteresis loop due to the adsorption of the different molecules is essentially connected to the modified exchange coupling constants as they are strongly enhanced in most cases (see Fig. 5.7 and Table 5.3). On the contrary, the MAEs are mainly decreased for the hybrid systems with respect to the clean surface values. This is most clearly outlined in case of the ethene-surface system where (i) the reduction of the MAE is strongest and (ii) the largest enhancement of the coupling constants is observed for J_1 and J_2.

Notably, a second way to tune the coercive field strength is revealed when the concentration of the adsorbates on the surface is varied which is shown by the inset in Fig. 5.10(b). Here the total number of Fe atoms in the unit cell is denoted by N_0 whereas $N_A = 3$ stands for the number of Fe atoms modified by the molecules. Hence the coverage density of the molecules on the surface increases from right to left in the plot. As depicted by the inset, the coercive field can be selectively adjusted over a range of 2.2 T using the different adsorbates and varying their concentration on the surface. This finally demonstrates that the deposition of small π-electron systems incorporating heteroelements of different chemical reactivity gives rise to a chemical functionalization of the magnetic hysteresis curves.

Eventually, in the MC simulations in principle also the Curie temperature T_C of the systems could be evaluated and thereby the influence of the molecules onto this magnetic property could be studied. However close to T_C the spin fluctuations extend over large length scales which could consequently not be adequately described by only nearest neighbor coupling constants and therefore this magnetic property is not well described in the current model.

5.7. Conclusions

In the present chapter it was demonstrated that it is indeed possible to selectively tune the in-plane magnetic exchange coupling constants J of a FM substrate due to the chemical functionalization with a set of nonmagnetic π-bonded organic molecules. This study reveals that a hardening or softening of the in-plane coupling constants between the surface Fe atoms can be accomplished by taking into account molecules with heteroatoms of different electronegativity. The in-plane magnetic hardening of the coupling constant can be tuned by using either C or B. In-plane magnetic softening on the other hand is obtained by employing elements of large electronegativity as N or O or when a π-bond mediates the magnetic coupling as in case of the adsorption geometry of methyleneborane.

The role of the molecule-surface hybridization for the modification of the coupling con-

stants was analyzed in detail by comparing the evaluated coupling constants for the molecule-surface hybrid systems with those of the molecular-induced surface geometries. This investigation shows that also such molecular-induced surface distortions lead to a modification of the coupling constants but this geometrical contribution cannot account for the element selective behavior observed for the hybrid systems, i. e. the molecule-surface hybridization is the driving force for the in-plane magnetic hardening and softening of the coupling constants.

In addition, MC simulations based on a multi-scale Heisenberg Hamiltonian using the coupling constants and MAEs evaluated from *ab initio* showed that the different adsorbates lead to chemically functionalized magnetic hysteresis loops for which the coercive field can be tuned over a large range of 2.2 T. This functionalization observed over a large field range is essentially a consequence of the locally modified exchange coupling constants.

This study demonstrates that by choosing suitable organic π-bonded adsorbates, the exchange coupling of FM surfaces can be engineered essentially on the molecular scale due to the local creation of hard molecular based magnetic units. Remarkably, the most efficient molecule-surface interaction leading to the hardest magnetic units is observed for C based systems which can be further enhanced by increasing the number of C atoms in the adsorbate [272]. The additional degree of freedom regarding the modification of the surface magnetic exchange interactions outlined here is to couple the variation of the spatial extent of the π-system with the ability to appropriately chemically functionalize the molecule-surface systems. These results are expected to be of prototypical nature for any hybrid molecule-ferromagnetic surface system and therefore hold promise for further research in molecular spintronics.

6 Molecular Induced Skyhook Effect

This chapter is devoted to propose a general mechanism of the inter-layer magnetic softening effect first observed for ZMP on Co(111) [51]. For this purpose two molecular model systems namely dioxan ($C_4O_2H_8$) and dioxin ($C_4O_2H_4$) have been investigated on both 1 and 2 ML Fe/W(110) substrates. In case of dioxan all atoms are sp^3-hybridized so that only σ-bonds are formed, i. e. dioxan is a σ-system. In contrast, for dioxin the C atoms are sp^2-hybridized leading to the formation of π-bonds, i. e. dioxin contains in addition to the σ- also a π-system. Hence, although the molecules are similar according to the elements they include, their electronic properties are considerably different leading to a weak chemisorption of dioxan but a strong chemisorption of dioxin on the 1/2 ML Fe/W(110) surfaces. Consequently, dioxan has only a weak influence onto the magnetic moments of the surface Fe atoms it is bound to. Dioxin in the other hand strongly affects the surface Fe magnetic moments below the C-C bond.

Due to the adsorption of the two molecules both the in-plane exchange coupling constants within the first Fe-layer as well as the inter-layer coupling parameters between the first and the second Fe layer of the 2 ML Fe/W(110) substrate are modified. Consistently with the results of the previous chapter it is found that there is mainly a hardening of the in-plane exchange coupling constants. Interestingly, for the weakly chemisorbed dioxan system this is mainly due to the geometric distortions of the surface originating from the adsorption of the molecule. On the other hand, for the strongly chemisorbed dioxin molecule the molecule-surface hybridization plays again a crucial role.

As a key result, it is found that both molecules weaken the inter-layer exchange coupling considerably. This finding can be explained in terms of a different interaction of the peripheral hydrogen atoms with the surface with respect to the central part of the molecule. Whereas the hydrogens are repelled from the surface, the inner part of the molecules is strongly attracted to it leading to an induced geometric lift off of the first layer Fe atoms below the molecule with respect to the second layer. This molecular induced skyhook effect gives rise to the observed inter-layer magnetic softening and allows to selectively decouple hybrid molecule-surface magnetic units from the underlying substrate on a single molecular scale. In addition, the reduction of the inter-layer magnetic coupling is further enhanced due to a chemical (hybridization) contribution for the strongly chemisorbed dioxin-surface system.

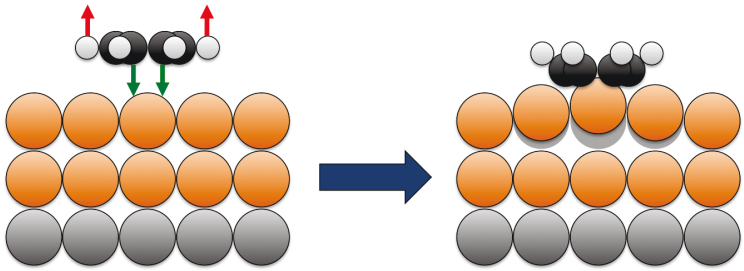

In view of the results presented in Section 4.4 and Chapter 5, only molecules with π-electrons have so far been investigated concerning their effect on the exchange interactions of magnetic substrates. It is therefore interesting to systematically investigate the impact of both a molecule with and without π-electrons on the surface magnetic exchange interactions. Moreover, by studying both molecules also on a 2 ML Fe/W(110) surface, their influence on the inter-layer exchange interaction between the two Fe layers can be outlined.[1]

6.1. Presentation of the Molecular Species

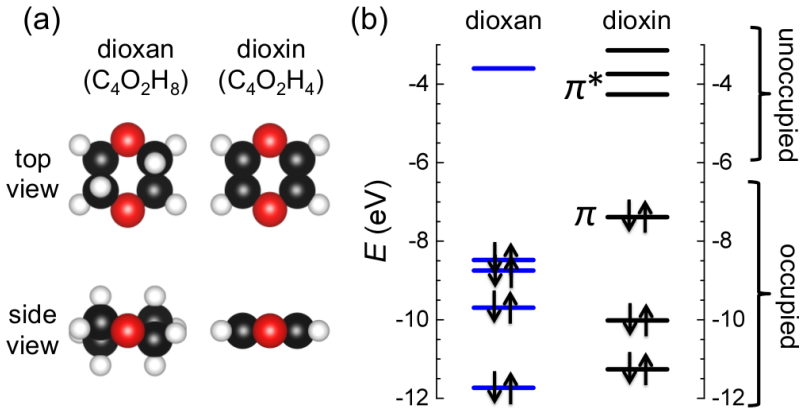

Figure 6.1.: Atomic structure of isolated dioxan and dioxin in top and side view (a) and calculated energy level diagram for both systems (b). In case of dioxin the bonding and antibonding π-states have been labeled π and π^*, respectively. The HOMO of each system was aligned at the calculated IP of 8.48 eV and 7.39 eV for dioxan and dioxin, respectively and the occupations of the levels are marked by arrows. Color code for atoms same as in Fig. 5.2.

This chapter is concerned with a comparative study of dioxan ($C_4O_2H_8$) and dioxin ($C_4O_2H_4$) on the two prototypical FM substrates of 1 and 2 ML Fe/W(110). Their structures in top and side view are presented in Fig. 6.1(a). Dioxan is a molecule with only single bonds (σ-system) since all C and O atoms are sp^3-hybridized and therefore it has a non-planar structure (see side view in Fig. 6.1(a)). Dioxin however incorporates also a π-electron system with double bonds between the carbon atoms due to the sp^2-hybridization of these atoms and consequently has a planar structure (see side view in Fig. 6.1(a)). Thus, although the sum formulas[2] of the two systems differ only by the number of H atoms, their structural properties are clearly different. Consequently, also the electronic structure is significantly different from one

[1] Part of the results of this chapter have already been published in: R. Friedrich, V. Caciuc, N. Atodiresei, and S. Blügel, *'Molecular induced skyhook effect for magnetic interlayer softening'*, Physical Review B **92**, 195407 (2015).

[2] The sum formula indicates the net amount of atoms of each element in a compound.

another which can be seen in the energy level diagrams depicted in Fig. 6.1(b). As expected, the σ-system dioxan has a large calculated HOMO-LUMO gap of about 4.87 eV. In contrast, the calculated gap of dioxin is considerably smaller (3.12 eV). This is due to the weaker overlap of the out-of-plane p_z-orbitals forming the π-states compared to the in-plane orbitals that form the σ-states. Therefore the HOMO of dioxin is a bonding π-state whereas the LUMO is an antibonding π^*-state. Taking into account these aspects, a different degree of interaction of both molecules with the 1 and 2 ML Fe/W(110) surfaces can be expected.

6.2. Adsorption Geometries and Structural Properties

To find the ground state of both molecules on the surfaces, four different adsorption sites were investigated which are displayed in Fig. 6.2 for the case of dioxin on 1 ML Fe/W(110). In the hollow site (Fig. 6.2(a)) four Fe atoms are effectively covered by the molecule which also holds for the hollow90 site (Fig. 6.2(b)) but there the molecule is rotated by 90° in the plane of the surface. For both the top (Fig. 6.2(c)) and the top90 (Fig. 6.2(d)) sites essentially only one surface Fe atom is covered by the molecule.

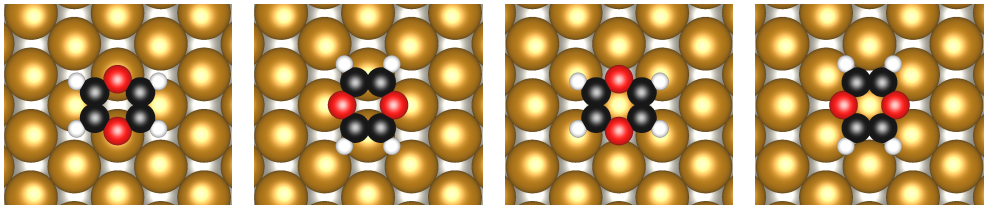

(a) hollow site (b) hollow90 site (c) top site (d) top90 site

Figure 6.2.: Investigated adsorption sites for dioxan and dioxin on 1 and 2 ML Fe/W(110) for the exemplary case of dioxin on 1 ML Fe/W(110). Color code of the surface atoms same as in Fig. 5.3.

When the structures are relaxed, it turns out that the most stable adsorption position for dioxan on both 1 and 2 ML Fe/W(110) is the hollow site whereas it is the hollow90 site in case of dioxin (see Fig. 6.3). A comparison of the adsorption energies for both molecules in their different adsorption positions is presented in Table 6.1 but in the following only the most stable (ground state) position for each system will be considered. From the values in Table 6.1 it becomes clear that the π-system dioxin interacts much more strongly with both surfaces than the σ-system dioxan, i. e. dioxan is weakly chemisorbed whereas dioxin is strongly chemisorbed[3]. This different interaction strength of the two molecule-surface systems is also

[3]The significant difference in the adsorption energy of about 1 eV for the chemisorbed dioxin on 1 compared to 2 ML Fe/W(110) will later on be referred to when discussing the SP-PDOS of the molecule-surface systems.

evident by comparing Figs. 6.3(c) and 6.3(d) showing that dioxin is much more tightly bound to the surface than dioxan.

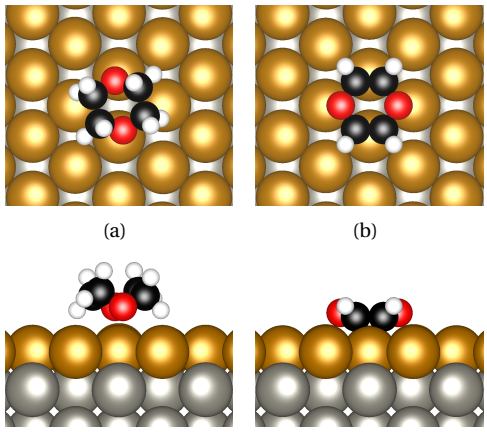

Figure 6.3.: Ground state geometries for dioxan and dioxin on 1 ML Fe/W(110) in top view (a), (b) and side view (c), (d), respectively. On 2 ML Fe/W(110) the stable structures are analogous.

Table 6.1.: Calculated adsorption energies E_{ads} for dioxan and dioxin on 1 and 2 ML Fe/W(110) for the different adsorption sites. The adsorption energy is defined as in Equation (5.1).

position	E_{ads} (eV)			
	1 ML Fe/W(110)		2 ML Fe/W(110)	
	dioxan	dioxin	dioxan	dioxin
hollow site	**1.10**	2.17	**1.12**	1.48
hollow90 site	1.09	**3.20**	0.84	**2.29**
top site	0.73	2.11	0.70	1.37
top90 site	0.78	1.43	0.69	0.76

To demonstrate this more explicitly, in Table 6.2 the distances between dioxan and the surface Fe1 and Fe2 atoms bound to the molecules (nomenclature as assigned in Fig. 6.4) are in general much larger than the corresponding distances for the dioxin-surface system. Only the O atoms of dioxan are close enough to the surface to give rise to a weak chemical bonding. For dioxin on the contrary, the whole molecular plane formed out of C and O atoms interacts strongly with the substrate. Notably, Fig. 6.3 also shows that the adsorption geometry of dioxin is more symmetric than the one of dioxan. The dioxan molecule is slightly twisted on the surface. However, the distortion from the symmetric case is so small that the magnetic moments of the surface Fe atoms still show the full symmetry with deviations only up

to 0.01 μ_B. Therefore also the magnetic exchange coupling constants were calculated as in the fully symmetric dioxin case as described below. One further remarkable point about the adsorption geometries is that the changes in the distances between the surface Fe atoms induced by the molecules are in general larger in the dioxan case (see Table 6.5). This is a consequence of the repulsive interaction between the molecular hydrogen atoms and the surface atoms as for dioxan four hydrogen atoms point towards the surface (see Fig. 6.3(c)). A more detailed discussion of the molecular-induced distortions of the surfaces will be given below in the context of the evaluated exchange coupling constants.

Table 6.2.: Calculated molecule-surface distances for dioxan and dioxin on 1 and 2 ML Fe/W(110). The nomenclature of the Fe atoms is in accordance with the labeling in Fig. 6.4.

molecule/surface	distances (Å)			
	C-Fe1	C-Fe2	O-Fe1	O-Fe2
dioxan/1 ML Fe/W(110)	3.26	3.35	2.27	3.58
dioxin/1 ML Fe/W(110)	2.04	2.66	3.01	2.12
dioxan/2 ML Fe/W(110)	3.31	3.43	2.31	3.64
dioxin/2 ML Fe/W(110)	2.04	2.59	3.07	2.15

6.3. Magnetic Moments and Exchange Coupling Constants

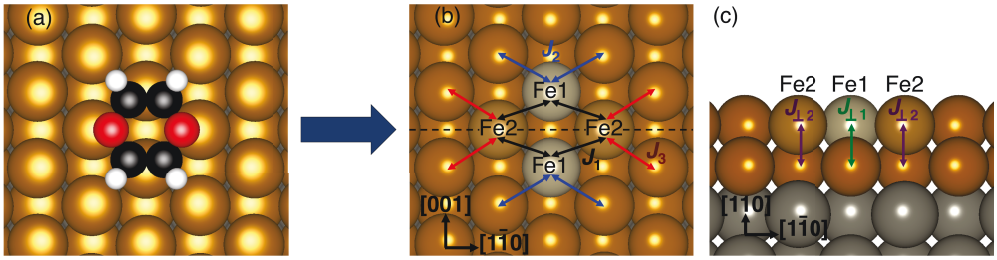

Figure 6.4.: The interaction of dioxan and dioxin with the 1 and 2 ML Fe/W(110) surfaces (here for the exemplary case of dioxin on 2 ML Fe/W(110)) (a) is confined to the four Fe atoms labeled Fe1 and Fe2 (b, c) directly bound to them. In addition, the in-plane and inter-layer magnetic exchange coupling constants modified by the adsorption of the molecules are assigned in (b) and (c), respectively. The side view in (c) depicts the surface cut along the dashed line in (b).

In all cases the magnetic moments of the surface Fe atoms are modified by the adsorption of the molecules. As labeled in Fig. 6.4 the influence of both molecules is confined to the four Fe atoms they are directly bound to. The moments for these Fe atoms are included in

Table 6.3. The influence of dioxan on the magnetic moments of Fe1 and Fe2 is rather weak as both values are close to the respective clean surface values of 2.5 μ_B and 2.8 μ_B for 1 and 2 ML Fe/W(110), respectively. This is due to the weak interaction of dioxan with those surfaces. However for the dioxin-surface system Fe1, positioned below the C-C bond of the molecule, is strongly influenced and its magnetic moment is reduced to 1.2 μ_B for 1 ML Fe/W(110) and to 1.9 μ_B for 2 ML Fe/W(110) whereas the magnetic moment of Fe2 below the molecular O is practically unaffected. This once again points to a strong hybridization between the states of Fe1 and dioxin which will be further discussed below when referring to the SP-PDOS.

Table 6.3.: Magnetic moments of the Fe atoms bound to dioxan and dioxin on 1 and 2 ML Fe/W(110). The second layer clean surface Fe moment of 2 ML Fe/W(110) is 2.2 μ_B.

molecule/surface	magnetic moments (μ_B)	
	Fe1	Fe2
1 ML Fe/W(110)	2.5	2.5
dioxan/1 ML Fe/W(110)	2.5	2.3
dioxin/1 ML Fe/W(110)	1.2	2.5
2 ML Fe/W(110)	2.8	2.8
dioxan/2 ML Fe/W(110)	2.9	2.8
dioxin/2 ML Fe/W(110)	1.9	2.9

The most important point is now to elucidate the impact of both molecules on the magnetic exchange coupling constants between the surface atoms. Analogously to the treatment in Chapter 5 the exchange coupling between the magnetic moments of the surface Fe atoms is described by an effective nearest neighbor Heisenberg Hamiltonian:

$$H^{\text{spin}} = -\sum_{\langle i>j\rangle} J_{ij}\mathbf{m}_i\mathbf{m}_j, \tag{6.1}$$

where $\mathbf{m}_i$ and $\mathbf{m}_j$ stand for the magnetic moments at sites i and j, respectively. From this ansatz a coupled system of equations can be obtained to determine the in-plane and inter-layer exchange coupling parameters J assigned in Fig. 6.4. To determine the coupling constants AFM configurations with (i) a single Fe1 spin reversed (Fig. 6.5(a)), (ii) a single Fe2 spin reversed (Fig. 6.5(b)), (iii) one pair of Fe1 and Fe2 spins reversed together (Fig. 6.5(c)), (iv) both Fe1 spins reversed (Fig. 6.5(d)), (v) both Fe2 spins reversed (Fig. 6.5(e)) and (vi) all four Fe1 and Fe2 spins reversed (Fig. 6.5(f)) have been taken into account for the molecules on the 1 ML Fe/W(110) surface.

For 2 ML Fe/W(110) there are in-plane couplings within the first layer, inter-layer couplings from first to second layer (sl) Fe atoms and in-plane couplings within the second layer (see Fig. 6.4). The in-plane coupling within the second Fe layer is unaffected according to the assumption that only first layer Fe atoms are influenced by the molecules. Hence the exchange

coupling parameter between the Fe atoms of the second layer is the one calculated for the clean surface (21.3 meV) [4] . Thus there are five modified exchange coupling constants in this case according to Fig. 6.4. To evaluate these parameters, the same AFM configurations as in the 1 ML Fe/W(110) case have been chosen and in addition: (vii) one configuration with the spin of the Fe atom below the center of the molecule within the second layer aligned antiferromagnetically (Fig. 6.5(g)), (viii) one configuration with all four nearest neighbors of this central Fe atom within the second layer aligned antiferromagnetically (Fig. 6.5(h)), (ix) another configuration with the spin of this central Fe atom and one nearest neighbor within the second layer aligned antiferromagnetically (Fig. 6.5(i)) and (x) a configuration with only the spin of one nearest neighbor Fe atom of the central Fe atom within the second layer aligned antiferromagnetically (Fig. 6.5(j)). The coupling constants have finally been evaluated in analogy to Chapter 5 for various sets of equations taking into account the linear dependency within subsets of the equations and averaging over the results obtained from different equation sets.

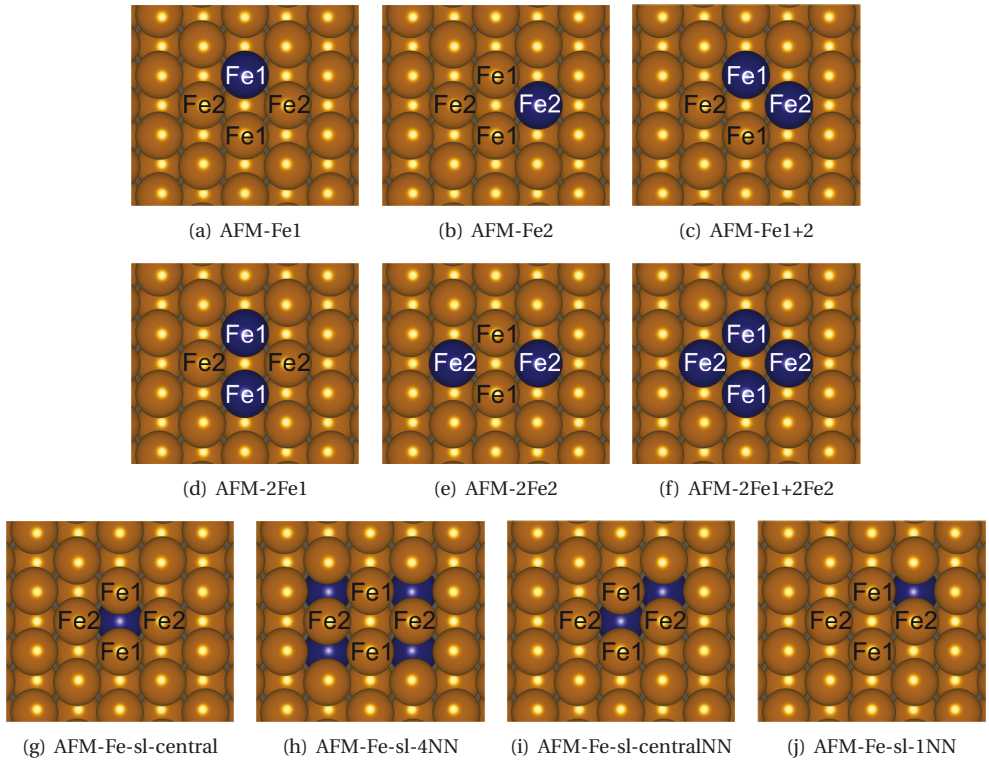

Figure 6.5.: The AFM configurations used to calculate the exchange coupling constants for dioxan and dioxin on 1 and 2 ML Fe/W(110). The atoms whose magnetic moments are flipped in the respective configuration are displayed in dark blue.

[4]The first and second layer clean surface Fe atoms are treated as different sorts according to Equation (5.3).

The exchange coupling constants calculated using this procedure are listed in Table 6.4, the in-plane coupling constants are visualized in Fig. 6.6 and the inter-layer coupling constants are depicted in Fig. 6.7. First, the modifications observed for the in-plane exchange coupling constants will be discussed. The important point to note here is that especially for dioxin the adsorption geometry is such that no single atoms of the molecule mediate the exchange coupling via superexchange between surface Fe atoms as it was the case in Chapter 5 (compare for instance Fig. 5.4 and Fig. 6.3). The adsorption position of dioxin is such that the C-O bond is positioned above the connection between Fe1 and Fe2. This makes the behavior of the in-plane exchange coupling constants more complicated since according to Chapter 5 carbon leads to an in-plane hardening of the coupling constants whereas oxygen gives rise to a softening. Hence an interplay of both effects is observed in the present cases.

More specifically, the J_1 coupling between Fe1 and Fe2 is slightly smaller than the clean surface value of 35.3 meV for both the σ-system dioxan and the π-system dioxin on 1 ML Fe/W(110) pointing to a softening of the exchange coupling. On the contrary, J_2 and J_3 standing for the interaction of Fe1 and Fe2 with their clean surface neighbors are larger than the clean surface value for the dioxan-surface system whereas for the dioxin-surface system J_2 is slightly softened. This could be partially assigned to the finding that the Fe1 surface atoms below the C-C bond of dioxin have a magnetic moment significantly smaller than that of a clean surface atom (see Fig. 6.4 and Table 6.3). The behavior of the in-plane coupling constants for the molecules adsorbed on 2 ML Fe/W(110) is similar although it can be observed that the size of the induced changes is in general larger than on the 1 ML Fe/W(110) surface. Nevertheless, the J_1 coupling constant is slightly larger than the clean surface value of 21.3 meV for both molecule-surface systems in case of 2 ML Fe/W(110).

Table 6.4.: Calculated magnetic exchange coupling constants J between the Fe atoms as labeled in Fig. 6.4 for the hybrid molecule-surface systems and the molecular-induced surface geometries.

molecule/surface	molecule/surface (meV)					induced geometry (meV)				
	J_1	J_2	J_3	$J_{\perp 1}$	$J_{\perp 2}$	J_1	J_2	J_3	$J_{\perp 1}$	$J_{\perp 2}$
1 ML Fe/W(110)	35.3	35.3	35.3	-	-	35.3	35.3	35.3	-	-
dioxan/1 ML Fe	24.8	41.2	41.4	-	-	22.4	34.8	38.5	-	-
dioxin/1 ML Fe	28.8	32.0	48.2	-	-	26.5	33.6	34.6	-	-
2 ML Fe/W(110)	21.3	21.3	21.3	126.1	126.1	21.3	21.3	21.3	126.1	126.1
dioxan/2 ML Fe	23.2	45.8	70.2	112.4	83.7	12.1	44.3	63.1	111.4	92.2
dioxin/2 ML Fe	23.6	10.9	70.0	63.1	78.6	26.2	33.0	42.4	104.4	100.7

As already discussed in Chapter 5, the in-plane magnetic hardening and softening induced by nonmagnetic organic molecules are due to the combination of (i) an adsorbate-substrate hybridization and (ii) a geometrical contribution originating from the distortion of the sur-

face induced by the adsorption of the molecules. The second mechanism is related to a re-hybridization of the d-states of the surface atoms which also has an impact on the coupling constants. To investigate the role of this geometrical effect also in the present case, the coupling constants have been recalculated for the relaxed molecule-surface geometries but with the molecules removed, i. e. for the molecular-induced surface geometries. The results are included in Table 6.4 and Fig. 6.6. In case of the dioxan-induced surface geometries for both 1 and 2ML Fe/W(110) the coupling constants (Figs. 6.6(a, c)) follow the J's of the hybrid systems and deviate from them only by a few meV. Therefore one can conclude that for the σ-system dioxan the modification of the coupling constants is mainly determined by the geometrical effect. Oppositely, for the dioxin-induced surface geometries the coupling constants show a qualitatively different behavior compared to the ones calculated for the hybrid systems. Especially the J_3 coupling constant of the induced geometries is much smaller than the corresponding coupling constant of the hybrid systems. This again underlines that for strongly chemisorbed π-systems such as dioxin the molecule-surface hybridization plays a crucial role leading to a considerably stronger change of the magnetic interactions than observed when only accounting for the geometrical effect.

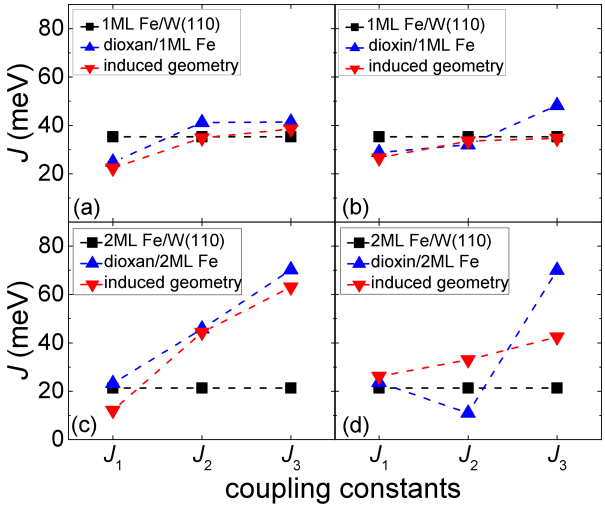

Figure 6.6.: Visualization of the in-plane magnetic exchange coupling constants calculated for dioxan and dioxin on 1 ML Fe/W(110) (a, b) and on 2 ML Fe/W(110) (c, d), respectively. In addition, the calculated coupling constants of the molecular-induced surface geometries are also included. Figure taken from Ref. [285]. Copyright (2015) by the American Physical Society.

As in Chapter 5 the modification of the coupling constants for the induced geometries can be correlated with the changed distances between the surface Fe atoms compared to the

undistorted clean surface. These modified distances are included in Table 6.5. In general, as noted in Section 6.2, the surface distortions induced by the dioxan adsorption are larger than for the dioxin adsorption. Hence also the range of the modified coupling constants for the dioxan-induced surface geometries are larger than for the corresponding dioxin-induced surface geometries (see Fig. 6.6). More explicitly, dioxan distorts the surfaces such that Fe1 and Fe2 are pushed away from one another leading to the smaller J_1 coupling on both surfaces compared to the respective clean surface value. As a consequence, the Fe2-cs distance is reduced and gives rise to an increase of the J_3 coupling. For the dioxin-induced geometry on 1 ML Fe/W/(110) the Fe1-Fe2 distance becomes also slightly increased leading to the weakening of J_1. On 2 ML Fe/W/(110) this distance is however smaller for the dioxin-induced geometry than the clean surface distance leading to an increase of J_1.

Table 6.5.: Fe-Fe distances for dioxan and dioxin on 1 and 2 ML Fe/W(110). The in-plane clean surface (cs) Fe-Fe distance is 2.75 Å. The clean surface distance from the first to the second layer (sl) is 2.35 Å.

molecule/surface	distances (Å)				
	Fe1-Fe2	Fe1-cs	Fe2-cs	Fe1-sl	Fe2-sl
dioxan/1 ML Fe/W(110)	2.87	2.77	2.65	-	-
dioxin/1 ML Fe/W(110)	2.78	2.74	2.74	-	-
dioxan/2 ML Fe/W(110)	2.88	2.76	2.66	2.40	2.33
dioxin/2 ML Fe/W(110)	2.74	2.71	2.79	2.35	2.41

Even more intriguing is the influence of the σ-system dioxan and the π-system dioxin onto the inter-layer exchange coupling constants $J_{\perp 1,2}$ describing the exchange coupling between the two Fe layers of 2 ML Fe/W(110) (see Fig. 6.4(c)). The values of these inter-layer coupling constants included in Table 6.4 and visualized in Fig. 6.7 show that both molecules locally induce a inter-layer magnetic softening, i. e. they reduce the inter-layer coupling strength with respect to the clean surface value of 126.1 meV. More precisely, $J_{\perp 1,2}$ are reduced to 112.4 and 83.7 meV in case of the dioxan-surface system and even more strongly to 63.1 and 78.6 meV for the dioxin-surface system.

Naturally, there arises the question after the mechanism of this inter-layer magnetic softening effect induced by the two nonmagnetic organic molecules, i. e. whether it is a hybridization effect or whether it is induced by the modified surface geometry due to molecular adsorption. For this purpose the calculated exchange coupling constants of the molecular-induced surface geometries are also included in Table 6.4 and Fig. 6.7. The coupling constants of the dioxan-induced geometry (see Fig. 6.7(a)) are very close to the values of the hybrid molecule-surface system, i. e. they deviate by less than 10 meV from the values of the hybrid system. Hence the inter-layer magnetic softening for the weakly chemisorbed molecular system is mainly geometrically driven. This is qualitatively different from the findings

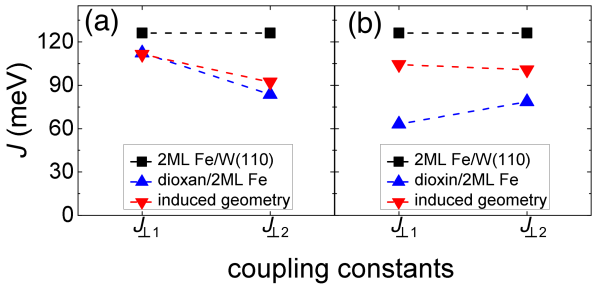

Figure 6.7.: Visualization of the inter-layer magnetic exchange coupling constants calculated for dioxan (a) and dioxin (b) on 2 ML Fe/W(110). In addition, the calculated coupling constants for the molecular-induced surface geometries are also included. Figure taken from Ref. [285]. Copyright (2015) by the American Physical Society.

in Ref. [52] and Chapter 5 where the in-plane magnetic hardening was outlined to be mainly a hybridization driven effect. On the other hand, for the strongly chemisorbed dioxin one observes that the coupling constants of the induced geometry are not as drastically reduced compared to the clean surface value as in case of the hybrid system (see Fig. 6.7(b)). This therefore points to an additional chemical contribution to the inter-layer softening, i. e. the molecule-substrate hybridization further weakens the exchange coupling between the Fe layers for a strongly chemisorbed molecule.

In particular, these results demonstrate that the reduction of the inter-layer magnetic exchange coupling is associated with the increased distance between the first-layer Fe atoms below the molecular oxygen and the second-layer Fe atoms. More precisely, for the dioxan-surface system the inter-layer distance of Fe1 to the second layer is increased to 2.40 Å compared to the clean surface distance of 2.35 Å (see Table 6.5). In case of the dioxin-surface system the distance of Fe2 to the clean surface is increased to 2.41 Å. To clearly depict the general mechanism of this lifting of the Fe atoms locally below the molecule for both weakly and strongly chemisorbed systems, in Fig. 6.8 a schematic representation of this *molecular induced skyhook effect* is given. The different parts of the molecule interact qualitatively differently with the substrate, i. e. whereas the peripheral hydrogen atoms are repelled from the surface, the central part is attracted to chemically interact with the states of the surface atoms (see Fig. 6.8(a)). This leads to an adsorption induced change of the surface geometry as indicated in Fig. 6.8(b) where the surface Fe atoms below the molecule are geometrically detached from the Fe atoms of the second layer. This increased distance leads to a rehybridization of the surface d-states giving rise to the inter-layer magnetic softening effect. More specifically related to the studied systems, the H-Fe distance for the dioxin-surface system is 2.43 Å whereas the C-Fe and O-Fe bond-lenghts are 2.04 Å and 2.15 Å, respectively (see Table 6.2). In addition, for the weakly chemisorbed dioxan the molecule-surface interaction is mainly governed

by dative-like bonds[5] from the free electron pairs in oxygen sp^3-orbitals to the surface Fe atoms which in the end also gives rise to a locally increased distance between the Fe layers. Taking into account this general mechanism, the present results also provide an explanation for the inter-layer magnetic softening calculated for ZMP molecules on a Co(111) substrate which was outlined to be a key ingredient for the observation of the IMR response reported in Ref. [51] briefly described in Section 4.4.

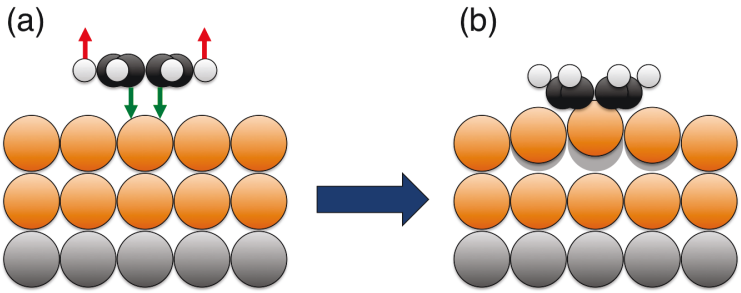

Figure 6.8.: Mechanism of the inter-layer magnetic softening due to the molecular induced skyhook effect. The different parts of the molecule interact differently with the substrate (a): whereas the H atoms are repelled from the substrate, the central part of the molecule is attracted to chemically interact with the surface atoms. This results in a geometric detaching of the first layer Fe atoms below the molecule with respect to the Fe atoms of the second layer leading to a decrease of the inter-layer exchange coupling (b).

6.4. Spin-polarized Projected Density of States

The different interaction mechanisms for the dioxan- and dioxin-surface systems and the resulting effect on the magnetic properties of the substrate atoms are also evident from analyzing the SP-PDOS of all d-states of the surface Fe atoms depicted in Fig. 6.9. In case of the weakly interacting dioxan system on both 1 and 2 ML Fe/W(110) (see Figs. 6.9(a), (c)) the SP-PDOS of Fe1 and Fe2 shows only small differences to the one of a clean surface Fe atom of the respective surface. Hence only a small degree of molecule-surface hybridization can be detected in this case signifying the weak chemisorption type bonding of dioxan to both surfaces. On the other hand, the SP-PDOS of especially the Fe1 atom is strongly changed compared to the clean surface reference for the dioxin molecule on both substrates (see Figs. 6.9(b), (d)). This confirms the strong chemisorption type bonding of dioxin to both surfaces as outlined before. When inspecting the SP-PDOS of Fe1 positioned below the C-C

[5]A dative bond is a bond in which the electrons are provided by only one of the two bonding atoms [286].

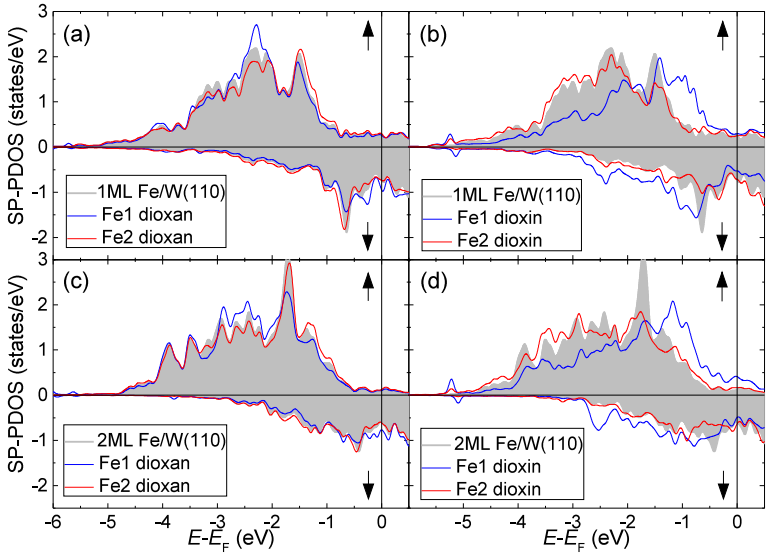

Figure 6.9.: SP-PDOS of the Fe1 and Fe2 d-states for dioxan and dioxin on 1 ML Fe/W(110) (a), (b) and on 2 ML Fe/W(110) (c), (d), respectively. As a reference, also the SP-PDOS of a clean surface Fe atom of the respective surface is given as gray shaded area.

bond of dioxin (see Fig. 6.3(b)) more closely, one observes that the spin up DOS is effectively shifted to higher energies whereas the spin down DOS is shifted to lower energies with respect to the clean surface. This energetic reordering of the d-state occupation of Fe1 is therefore responsible for the strongly reduced moment of 1.2 μ_B and 1.9 μ_B of this center compared to the clean surface values of 2.5 μ_B and 2.8 μ_B (see Table 6.3) for dioxin on 1 and 2 ML Fe/W(110), respectively. By comparing Figs. 6.9(b) and (d) also the possible reason for the much larger adsorption energy of dioxin on 1 ML Fe/W(110) compared to 2 ML Fe/W(110) (3.20 eV compared to 2.29 eV) can be outlined. Since the DOS around the Fermi energy is larger in case of 1 ML Fe/W(110), the energy gain due to the formation of bonding states close to E_F in the hybrid system is also expected to be larger in this case leading to a higher adsorption energy.

The different degree of hybridization in the two molecule-surface systems can also be detected when inspecting the SP-PDOS of the p-states of C and O for dioxan and dioxin on 1 and 2 ML Fe/W(110) in Figs. 6.10 and 6.11. When first focussing on the 1 ML Fe/W(110) case, the hybridization of the C and O p-states is much stronger for the dioxin-surface system (see Figs. 6.10(b), (d)) compared to the dioxan-surface system (see Figs. 6.10(a), (c)). More precisely, the states of the chemisorbed system are strongly broadened in the depicted energy interval and spread over a large energy-range of several eV. In the dioxan case essentially no hybridization is detected for C (see Fig. 6.10(a)) and only a weak interaction can be identified for O (see Fig. 6.10(c)). This underlines that the bonding of dioxan to the substrate takes place

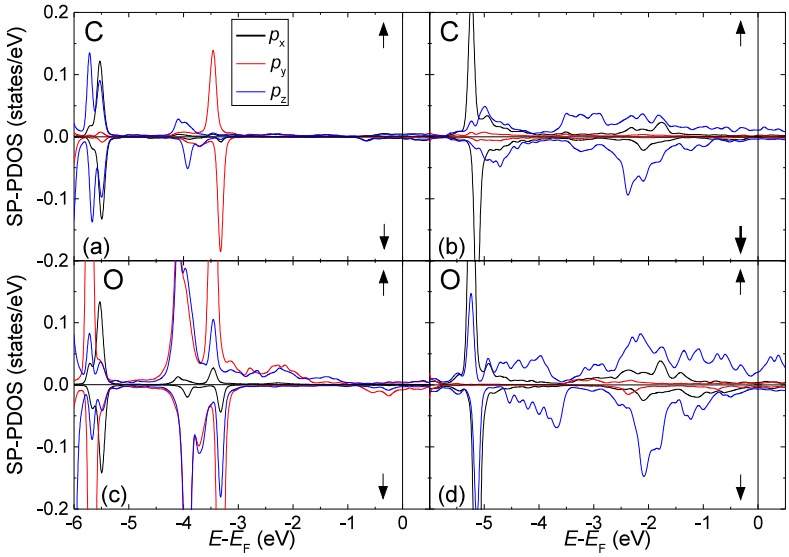

Figure 6.10.: SP-PDOS of the p-states of C and O for dioxan (a), (c) and dioxin (b), (d) on 1 ML Fe/W(110), respectively.

mainly through the O atoms. However the SP-PDOS consists predominantly of sharp peaks corresponding to the molecular orbitals of the free dioxan molecule. Notably, the SP-PDOS of the dioxan p-states on 2 ML Fe/W(110) in Fig. 6.11 shows an analogous behavior. One important finding is that for the chemisorbed dioxin molecule on both surfaces the p_z-states hybridize most strongly with the states of the substrate showing that these out-of-plane states forming the π-states of the free dioxin molecule are decisive to mediate the bonding to the surface. Figures of the SP-PDOS for the molecular-induced geometries can be found in Appendix A in Subsection A.6.1 and show as in Chapter 5 that for the dioxin-induced geometry the changes with respect to the clean surface SP-PDOS are considerably smaller than for the hybrid system. On the other hand, for the weakly chemisorbed dioxan molecule the changes in the SP-PDOS are mainly geometrically driven which is in line with the finding that in this case also the modifications of the exchange coupling constants are mainly due to the geometrical effect.

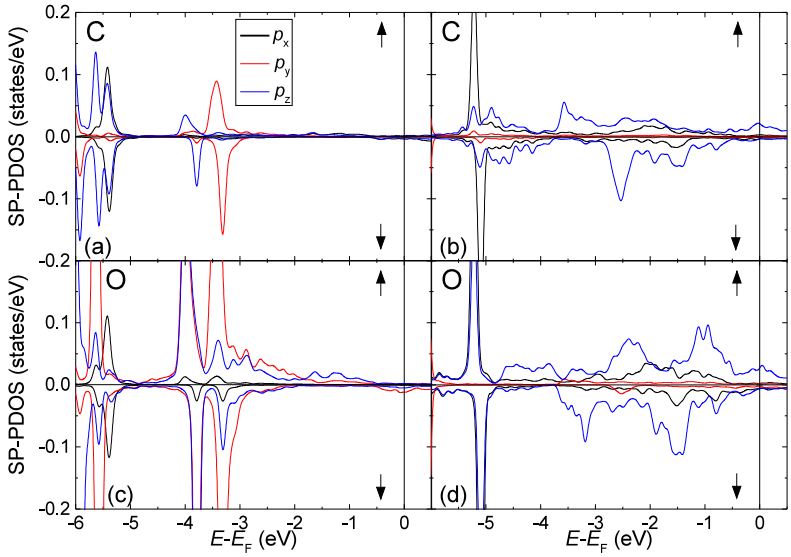

Figure 6.11.: SP-PDOS of the p-states of C and O for dioxan (a), (c) and dioxin (b), (d) on 2 ML Fe/W(110), respectively.

6.5. Conclusions

In summary, this study showed how prototypical weakly and strongly chemisorbed organic molecules as dioxan and dioxin adsorbed on 1 and 2 ML Fe/W(110) locally modify the in-plane and inter-layer exchange coupling strength between the surface Fe atoms below the molecules. On both substrates the in-plane exchange coupling constants can be strongly increased or decreased compared to the respective clean surface values. These modifications are mainly driven by the molecular-induced surface distortions for the weakly interacting dioxan-surface system whereas for the strongly interacting dioxin-surface system the hybridization between molecule and substrate leads to further qualitative changes.

Most importantly, on 2 ML Fe/W(110) both the weakly and the strongly chemisorbed molecule lead to a inter-layer magnetic softening effect, i. e. to a locally reduced magnetic exchange coupling between the first layer Fe atoms below the molecules and the second layer Fe atoms. More specifically, for the weakly chemisorbed dioxan the decrease of the inter-layer exchange coupling is due to a molecular induced skyhook effect: As a consequence of the repulsive interaction between the peripheral H atoms of the molecule and the surface on the one hand and the strongly attractive interaction between the central molecular atoms and the surface on the other hand, the Fe atoms below the molecule are locally detached from the second

layer Fe atoms. The associated rehybridization of the Fe d-states gives rise to the inter-layer magnetic softening. For the strongly chemisorbed dioxin in addition to this geometrical contribution also the molecule-surface hybridization further enhances the local decrease of the inter-layer exchange coupling signalizing an additional chemical influence for strongly chemisorbed molecules.

These results can be of special importance for spintronic devices in which different magnetic layers must be switched with respect to each other to obtain sizable MR effects. For instance this mechanism was outlined to give a possible explanation of the molecular induced IMR for ZMP molecules on a Co(111) substrate in Ref. [51] (see Section 4.4). Conclusively, the results presented in this chapter present role model scenarios how weakly and strongly chemisorbed molecules can be utilized to create magnetically hard and/or soft exchange interactions with a lateral resolution down to the molecular scale.

7 Magnetic Exchange Below 2D Materials

In the preceding chapters only finite size molecular systems primarily containing π-electrons had been investigated for their influence on the magnetic exchange interactions of a FM substrate. Consequently, there arises the question after the role played by extended, i. e. two-dimensional (2D) π-electron systems regarding their influence on the exchange interactions of an underlying substrate. To investigate this issue, the prototypical 2D materials graphene (Gr) and hexagonal boron nitride (hBN) have been investigated on the representative FM Co(111) substrate. The ground state adsorption position of both systems is such that one C/N atom is positioned on top of Co and the second C/B atom sits in an hcp hollow site of the surface for Gr/hBN, respectively. The adsorption energy per unit cell of both 2D materials is about 0.5 eV indicating that they are chemisorbed on the Co(111) substrate which is especially confirmed by the broad features found in the SP-PDOS. As regarding the magnetic moments of the surface Co atoms, the influence of the 2D materials is confined to the first Co layer leading to a hybridization driven reduction of the magnetic moments by about 0.1 μ_B.

When considering the magnetic exchange interactions between the surface Co atoms, both 2D materials lead to a strong in-plane magnetic hardening of the exchange coupling constants between the Co atoms within the first layer with respect to the clean surface (cs). This hardening effect is most pronounced for Gr since in this case the hybridization of the states from the substrate with the states of the 2D material is most efficient. On the other hand, the inter-layer magnetic exchange between the first and the second Co layer is found to be unaffected by the 2D materials which is in contrast to the results outlined in Chapter 6 that finite size molecular systems lead to a inter-layer magnetic softening, i. e., a reduction of the inter-layer exchange coupling constants. The reason for this comes from the fact that the molecular induced skyhook effect responsible for the inter-layer softening below molecules is not present for 2D materials.

The exchange coupling constants calculated for the surface geometries induced by the 2D materials show that the in-plane magnetic hardening is a hybridization effect driven by the interaction of p_z-states of the 2D materials and d-states of the surface. Finally, the SP-PDOS shows that although both 2D materials are nonmagnetic on the surface, within a given energy interval a net spin polarization can arise which is predicted to be measurable experimentally.

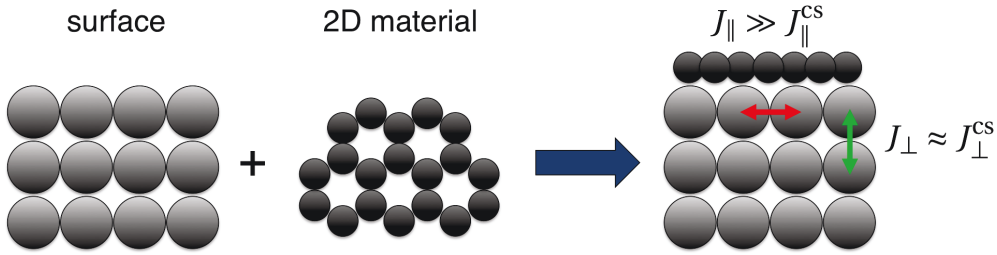

After the last two chapters dealing with individual molecules on 1 and 2 ML Fe/W(110), now 2D structures adsorbed on a Co(111) surface will be investigated. In Chapter 5 it was explicitly shown that especially the π-electrons of the organic molecules adsorbed on the surface are of crucial importance to significantly modify the in-plane magnetic exchange coupling constants of the FM surface. In addition, Chapter 6 demonstrated that finite-size molecules lead to a inter-layer magnetic softening via the molecular-induced skyhook effect. It is thus an obvious question, whether 2D structures containing extended π-states, i. e. Gr and a ML of hBN, do have a similar effect on the magnetic properties of the substrate. Therefore this chapter deals with a comparative study of both systems adsorbed on a Co(111) surface being the same substrate as used in the devices showing the IMR behavior in Ref. [51].[1]

7.1. Presentation of the 2D Materials

The atomic structures of isolated Gr and hBN are displayed in Figs. 7.1(a) and (b), respectively. Both are made up of a honeycomb lattice with two atoms per primitive unit cell (red parallelogram marked in Figs. 7.1(a), (b) for both systems). Gr is usually referred to as being a 'zero-gap insulator' with linear dispersion at the band crossings at the K and K$'$ points of the 2D BZ, a property of the energy dispersion known as Dirac cone [287]. However, accurate electronic structure calculations taking into account SOC showed that Gr has an intrinsic gap of about 24 μeV [288]. On the other hand, an atomically thin film of hBN is an insulating material with a band gap of 5.5 eV [289] compared to bulk hBN which has a gap of 6.0 eV [290]. Notably, both systems can be manufactured experimentally using a micromechanical cleavage technique as introduced by Novoselov and coworkers [291]. Especially Gr has been the subject of many fundamental investigations among which are the exploration of the 'electric field effect in atomically thin carbon films' [292], the study of a 'two-dimensional gas of massless Dirac fermions' [293], the observation of quantum Hall effect and Berry phase [294], the prediction of quantum spin Hall effect [295], the proposal of 'graphite and graphene as perfect spin filters' [296] and many other physical properties which have been in detail reviewed in Refs. [287, 297].

The calculated band structures of the isolated 2D materials are visualized in Figs. 7.1(c) and (d) for Gr and hBN, respectively. Both band structures agree well with the results of previous calculations in Refs. [298, 299]. The associated PDOS of both systems given in Figs. 7.1(e) and (f) clearly shows the van-Hove-singularities [300] in the electronic structure. As expected, the Gr band structure depicts a linear band crossing (Dirac point) marked by a red circle at the K-

[1] Part of the results of this chapter have already been published in: R. Friedrich, V. Caciuc, N. Atodiresei, and S. Blügel, *'Exchange interactions of magnetic surfaces below two-dimensional materials'*, Physical Review B Rapid Communication **93**, 220406(R) (2016).

point of the 2D BZ at the Fermi energy. On the other hand, hBN shows insulating properties with a large calculated band gap of about 4.5 eV. This reduced value compared to the experimental band gap of 5.5 eV [289] is due to the band gap problem of DFT [57]. Consequently, the electronic properties of these two systems are considerably different when compared to each other. However in both cases the highest occupied (valence) and lowest unoccupied (conduction) bands have bonding π- and antibonding π^*-character, respectively which are hence expected to be most important for the interaction with a substrate. It is therefore the purpose of this chapter to outline how these electronically different materials interact with a Co(111) substrate and modify its magnetic properties.

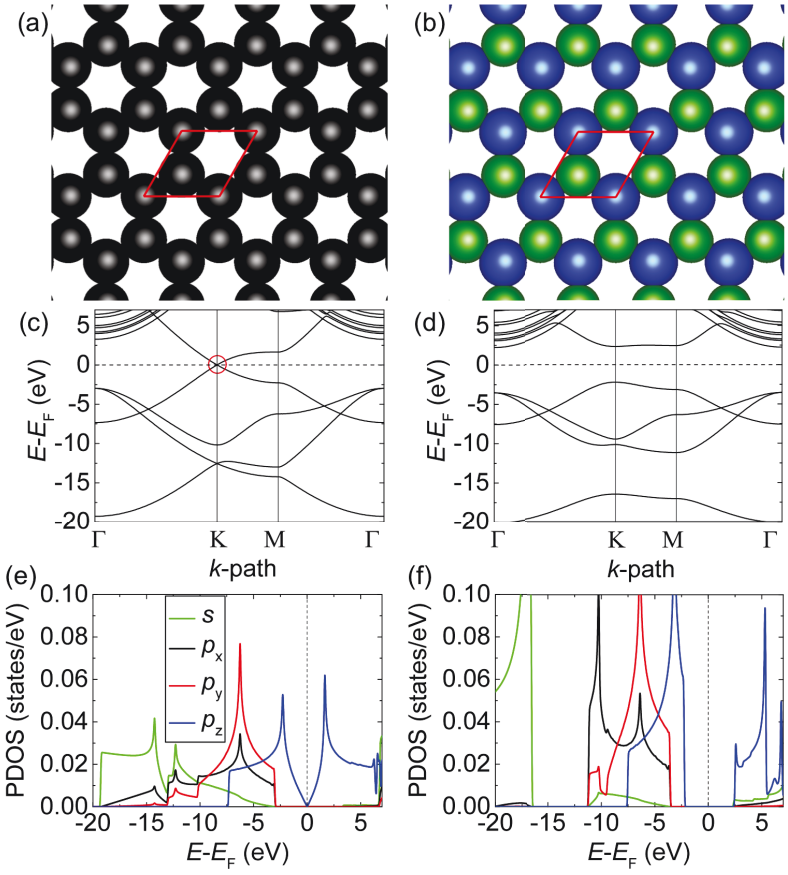

Figure 7.1.: Atomic structure, band structure and PDOS of isolated Gr (a), (c), (e) and hBN (b), (d), (f), respectively. The unit cell of each structure containing two atoms is marked by the red parallelogram. The linear band crossing at the K-point (Dirac cone) for Gr is marked by a red circle. Color code for atoms same as in Fig. 5.2.

7.2. Adsorption Geometries and Structural Properties

For the 2D materials commensurate on the underlying Co(111) substrate the in-plane unit cell consists of one Co atom per layer and two C atoms for Gr or one B and one N for hBN. There are three possibilities to place the two adsorbate atoms into high symmetry positions in the unit cell so that the overall honeycomb structure is obtained. These possibilities are visualized for Gr and hBN in Figs. 7.2(a)-(c) and Figs. 7.3(a)-(c), respectively. More precisely, for the exemplary case of Gr the first possibility is to place one C atom on top of Co and the other C atom into the fcc position of the underlying lattice (top-fcc geometry in Fig. 7.2(a)). The two carbon atoms can then also be shifted by one third along the face diagonal of the in-plane unit cell so that both atoms occupy the fcc and hcp sites yielding the fcc-hcp geometry (see Fig. 7.2(b)). Finally, the two atoms can be shifted once more by one third along the face diagonal leading to the top-hcp geometry (see Fig. 7.2(c)). However since for hBN B and N are different atomic species, one has to take into account that for all three cases both atoms can be interchanged which results in three further geometries as the fcc and hcp sites are not equivalent. These additional possibilities are not shown here but have been taken into account during the calculations. As displayed in Figs. 7.2(d) and 7.2(e) for Gr and in Figs. 7.3(d) and 7.3(e) for hBN also two further adsorption geometries can be constructed where either the sixfold carbon ring sits in a bridge position or it is slightly distorted away from the top position (atop geometry), respectively.

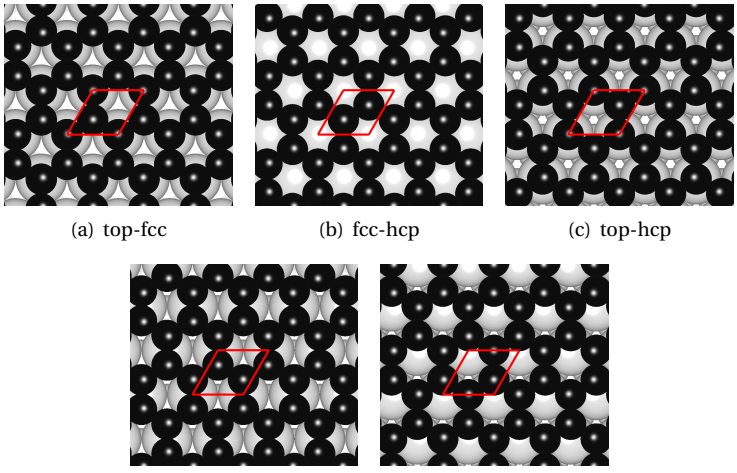

(a) top-fcc (b) fcc-hcp (c) top-hcp

(d) bridge (e) atop

Figure 7.2.: Investigated adsorption positions for Gr on the Co(111) surface. The unit cell of the systems is marked by the red parallelogram. Color code of the surface atoms: light gray for Co.

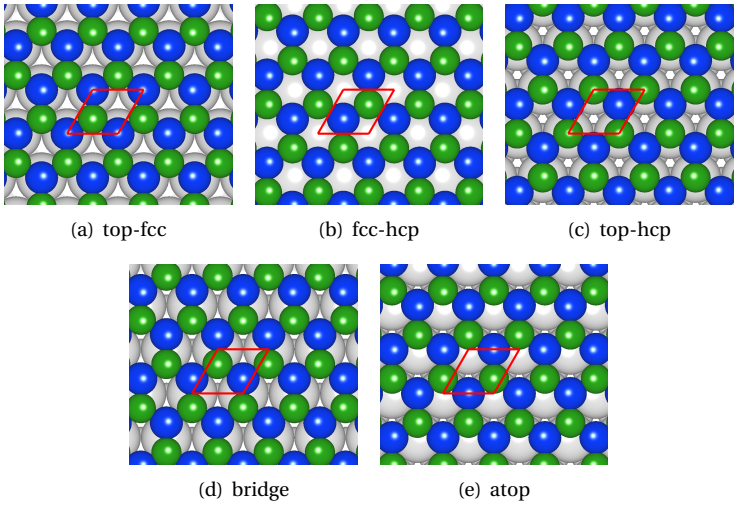

(a) top-fcc (b) fcc-hcp (c) top-hcp

(d) bridge (e) atop

Figure 7.3.: Investigated adsorption positions for hBN on the Co(111) surface. The unit cell of the systems is marked by the red parallelogram.

The structural relaxation of these systems indicates that the lowest energy is obtained for the top-hcp geometry for both 2D materials adsorbed on the surface as indicated by the comparison of the adsorption energies for all positions presented in Table 7.1. Clearly the top-hcp adsorption geometry is favored by at least 0.1 eV for both systems. Notably, the bridge and atop positions move to the top-hcp position during the relaxation in case of Gr which is the reason for the identical adsorption energy in all three cases. However, the adsorption energies obtained from further test calculations using the PBE+U functional are 0.2 to 0.3 eV smaller than for rev-vdW-DF2+U which points to the fact that nonlocal correlation effects contribute in a significant way to the bonding between surface and 2D material for both systems. Hence from the adsorption energies it is suggested that both 2D materials bind to the surface via a weak chemisorption type bonding mechanism as already suggested in Ref. [301] for Gr on Co(111). In the following only the results obtained for the ground state top-hcp adsorption geometry will be discussed further. This means that for Gr (hBN) the most stable configuration is associated with one C (N) atom sitting on top of Co and the other C (B) atom sitting between three Co atoms consistent with the results presented in Ref. [301].

For both systems the honeycomb lattices adsorb practically flat on the surface (see Fig. 7.4): For Gr both C atoms are 2.09 Å (top position) and 2.06 Å (hcp position) above the surface. In case of hBN the B atom is about 0.1 Å closer to the surface than the N atom (2.04 Å compared to 2.15 Å). A more detailed analysis of the adsorption geometries is provided by the calculated interatomic distances reported in Table 7.2. Firstly, the in-plane Co-Co distance of 2.51 Å is not modified by the adsorption of the 2D materials due to the commensurate stacking of

Table 7.1.: Calculated adsorption energies per unit cell E_{ads} for Gr and hBN on the Co(111) surface for the different adsorption geometries considered in this study. The adsorption energy is defined analogously as in Equation (5.1) where in the present case E_{mol} has to be substituted by E_{2D} which stands for the total energy of the respective freestanding 2D material. For hBN the results of the geometries with the N and B atoms interchanged within the unit cell are listed in the last five rows of the table. Note that the bridge and atop positions move to the top-hcp position during the relaxation in case of Gr.

position	E_{ads} (eV)	
	Gr	hBN
top-fcc	0.311	0.151
fcc-hcp	−0.010	0.078
top-hcp	**0.468**	**0.420**
bridge	0.468	0.400
atop	0.468	0.400
top-fcc-interchanged		0.315
fcc-hcp-interchanged		0.155
top-hcp-interchanged		−0.009
bridge-interchanged		0.368
atop-interchanged		0.267

the lattices. On the other hand, Gr and hBN lead to a very small increase of the inter-layer distance by 0.03 Å and 0.01 Å between the first (Co1) and second (Co2) Co layer, respectively which is however considerably smaller than the increased inter-layer distance below finite-size molecules outlined in Chapter 6 (see Fig. 7.5 for a labeling of the Co layers). The tabulated distances between the atoms of the 2D materials and Co1 show again that both systems bind closely to the surface supporting the above mentioned chemisorption mechanism.

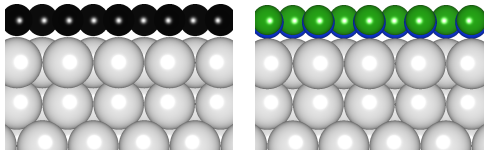

(a) (b)

Figure 7.4.: Side view of the relaxed top-hcp geometry for Gr (a) and hBN (b) adsorbed on the Co(111) surface.

Table 7.2.: Calculated distances for Gr and hBN on the Co(111) surface in top-hcp geometry. C_{top} and C_{hcp} stand for the C atoms of Gr adsorbed in the top site and hcp site, respectively. The nomenclature of the Co atoms is in accordance with the labeling in Fig. 7.5.

system/surface	distances (Å)		
	Co1-Co2	C_{top} (N)-Co1	C_{hcp} (B)-Co1
clean surface	2.45	-	-
Gr	2.48	2.09	2.52
hBN	2.46	2.15	2.50

7.3. Magnetic Moments and Exchange Coupling Constants

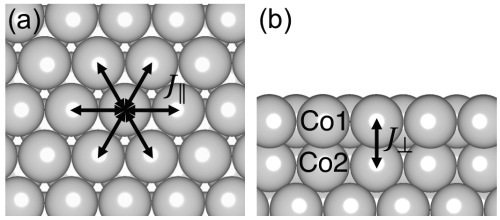

Figure 7.5.: The interaction of the 2D materials with the Co(111) surface is confined to the first layer Co atom labeled Co1. Also the in-plane magnetic exchange coupling constant $J_\parallel$ within the first Co layer (a) and the inter-layer exchange coupling constant $J_\perp$ between the first and second layer (Co2) Co atoms (b) are assigned.

The adsorption of Gr and hBN also has an impact on the magnetic moments of the surface Co atoms which are presented in Table 7.3. In analogy to the results outlined in Chapters 5 and 6, the moment of the surface Co1 atom directly bound to the respective extended π-system is considerably reduced from the clean surface value of 1.95 μ_B to about 1.8 μ_B due to the 2D material-substrate hybridization. On the other hand, the moment of the Co2 atom is practically unaffected signalizing that the influence of the 2D adsorbate is confined to the first surface layer. Remarkably, the moment of the second layer is already close to the calculated bulk value of 1.86 μ_B.

Table 7.3.: Magnetic moments in μ_B and evaluated exchange coupling constants in meV for the hybrid Gr-/hBN-surface systems and the surface geometries induced by the 2D materials on the Co(111) surface.

system/surface	magnetic moments		with 2D material		induced geometry	
	Co1	Co2	$J_\parallel$	$J_\perp$	$J_\parallel$	$J_\perp$
clean surface	1.95	1.87	32.0	62.2	32.0	62.2
Gr	1.81	1.87	85.0	61.6	32.8	56.4
hBN	1.83	1.88	68.2	62.8	31.1	59.8

Now the procedure of how to evaluate the in-plane and inter-layer magnetic exchange coupling constants between the Co atoms of the surface will be explained. The exchange coupling between the magnetic moments of the Co atoms is as outlined in detail in Chapters 5 and 6 described by an effective nearest neighbor Heisenberg Hamiltonian:

$$H^{\text{spin}} = -\sum_{\langle i>j\rangle} J_{ij}\mathbf{m}_i\mathbf{m}_j, \tag{7.1}$$

where $\mathbf{m}_i$ and $\mathbf{m}_j$ stand for the magnetic moments of centers i and j, respectively. As depicted in Fig. 7.5 there are two different types of coupling constants that are supposed to be modified by the adsorption of the extended π-electron systems, namely the in-plane exchange coupling constant $J_\parallel$ between the Co1 atoms of the first surface layer and the inter-layer exchange coupling parameter $J_\perp$ between the first and second Co layer. The inter-layer exchange coupling constant can be calculated directly from the energy difference between the FM state and the AFM state resulting when reversing the spin of the Co1 atom with respect to all lower layers in the unit cell:

$$-6J_\perp m_{\text{Co1}} m_{\text{Co2}} = E_{\text{FM}} - E_{\text{AFM-Co1}}, \tag{7.2}$$

which results in:

$$J_\perp = \frac{E_{\text{FM}} - E_{\text{AFM-Co1}}}{-6m_{\text{Co1}} m_{\text{Co2}}}, \tag{7.3}$$

where m_{Co1} and m_{Co2} stand for the magnetic moments of Co1 and Co2 respectively and $E_{\text{AFM-Co1}}$ is the total energy calculated for the configuration with the moment of the Co1 atom reversed with respect to the other layers.

In order to calculate the in-plane exchange parameter $J_\parallel$ a 2×2 unit cell needs to constructed to create a row-wise AFM alignment of the first layer moments (see Fig. 7.6 for a visualization of this configuration). Since in this configuration the flipped moments are also antiparallel to their nearest neighbor moments within the Co2 layer below, one obtains the following equation that incorporates a contribution from $J_\perp$ which is already known from Equation (7.3):

$$-16J_\parallel m_{\text{Co1}}^{\text{AFM}} m_{\text{Co1}} - 12J_\perp m_{\text{Co1}}^{\text{AFM}} m_{\text{Co2}} = E_{\text{FM}}^{2\times2} - E_{\text{AFM-Co1}}^{2\times2}, \tag{7.4}$$

leading to:

$$J_{\parallel} = \frac{(E_{\mathrm{FM}}^{2\times2} - E_{\mathrm{AFM\text{-}Co1}}^{2\times2}) + 12J_{\perp}m_{\mathrm{Co1}}^{\mathrm{AFM}}m_{\mathrm{Co2}}}{-16m_{\mathrm{Co1}}^{\mathrm{AFM}}m_{\mathrm{Co1}}}, \tag{7.5}$$

where $m_{\mathrm{Co1}}^{\mathrm{AFM}}$ is the moment of a Co1 atom whose spin is flipped, whereas m_{Co1} is the moment of the unflipped Co1 atoms. $E_{\mathrm{FM}}^{2\times2}$ and $E_{\mathrm{AFM\text{-}Co1}}^{2\times2}$ are the total energies of the 2×2 cells in the FM state and in the row-wise AFM configuration, respectively[2].

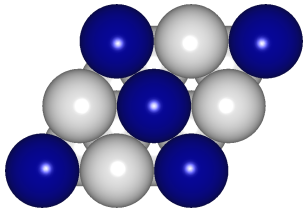

Figure 7.6.: 2×2 surface unit cell allowing to calculate a row-wise AFM alignment of the first layer moments. The atoms marked in dark blue indicate the flipped moments.

The calculated exchange coupling parameters as obtained by using the above mentioned relations are included in Table 7.3. It should first be noted that the calculated exchange coupling constant for bulk fcc Co[3] is J_{bulk} = 24.4 meV (8.0 meV/μ_{B}^2) being in good agreement with the values of 27.64 meV and 8.54 meV/μ_{B}^2 presented in Refs. [302] and [51], respectively[4]. For both 2D materials a strong increase of the in-plane exchange coupling constant $J_{\parallel}$ from the clean surface value of 32.0 meV to 85.0 meV and 68.2 meV is observed for Gr and hBN adsorbed on the Co(111) surface, respectively. This behavior is qualitatively similar to the case of a Co ML intercalated between Gr and an Ir(111) substrate where in the regions for which Gr is chemisorbed also a strong in-plane magnetic hardening of the coupling constants is observed [50, 303].

As previous experimental as well as theoretical investigations in Refs. [50–52, 272, 283, 304] have shown, the immediate consequence of the enhanced in-plane exchange coupling constants is a magnetic hardening of the hysteresis curve, i. e., it leads to an increase of the coercive field strength of the systems. More precisely, this magnetic hardening was clearly evidenced by the experimentally measured opening of the hysteresis loop for the Gr/Co/Ir(111) structure [50] compared to the bare Co/Ir(111) system [270]. Importantly, a similar behavior

[2] In order to obtain the coupling constants in terms of energy units one has to multiply the values obtained from Equations (7.3) and (7.5) with the absolute values of the coupled magnetic moments.

[3] Using this bulk coupling constant the mean-field Curie temperature $T_{\mathrm{C}}^{\mathrm{MF}}$ can be evaluated via $k_{\mathrm{B}}T_{\mathrm{C}}^{\mathrm{MF}} = J_0/3$[302], where in this case $J_0 = 12J_{\mathrm{bulk}}$ is an effective exchange parameter[171] and k_{B} is the Boltzmann constant. The obtained value $T_{\mathrm{C}}^{\mathrm{MF}}$ = 1132 K is in good agreement with the previously obtained values of 1280 K and 1200 K [302] especially when taking into account that only nearest neighbor couplings were considered.

[4] Note that in the present case the coupling constant is defined as twice the value compared to Ref. [302].

was observed for the Gr/Fe/Ir(111) system [304] as well as for an Fe/Ir(111) substrate when coronene molecules and Gr nanoflakes were adsorbed on top [272]. Also the formation of the magnetically hard interface layer found in Ref. [51] for ZMP on Co(111) revealed a strong in-plane magnetic hardening. In the present work the hybrid 2D material-surface structures were also treated within an alternative approach using the PBE functional for both the structural optimization and the calculations of the AFM configurations[5]. The results for the structural and magnetic properties obtained from these calculations are included in Appendix A in Tables A.5 and A.6, respectively. In this case no in-plane magnetic hardening of the coupling constants is observed in contrast to the experimental results outlined above. Based on these findings the results obtained by using the PBE+U functional for the magnetic properties presented in Table 7.3 are considered as more reliable and it is concluded that the in-plane magnetic hardening effect should also be experimentally measurable for Gr and hBN on the Co(111) substrate.

In order to study the contribution of the structural changes induced by the 2D material adsorption on the Co(111) surface with respect to the modification of the magnetic exchange coupling constants, the Js have been recalculated for the induced geometries, i. e. for the relaxed hybrid structures but with the 2D materials removed. The obtained exchange coupling constants for these induced geometries are included in Table 7.3. From these values it can hence be concluded that without Gr or hBN the same surface structure does not show a significant in-plane magnetic hardening of the $J_{\parallel}$ coupling constant as the obtained deviations of 0.9 meV from the undistorted clean surface value are within the error bar for the present evaluation of the coupling constants. This finding consequently demonstrates that the 2D material-substrate hybridization is the key factor to achieve a sizable increase of $J_{\parallel}$ analogously as it was found in Chapters 5 and 6.

Remarkably, the calculated inter-layer exchange coupling constants $J_{\perp}$ in Table 7.3 are neither significantly enhanced nor reduced compared to the clean surface inter-layer coupling of 62.2 meV. Importantly, this result is qualitatively different from the results presented in Chapter 6 and Ref. [51] where a inter-layer magnetic softening of the exchange coupling was found for the first layer magnetic atoms below dioxan/dioxin and ZMP, respectively. In Chapter 6 the mechanism of this inter-layer magnetic softening was ascribed to the molecular induced skyhook effect, i. e. due to the repulsion of the peripheral molecular hydrogens from the surface but the attraction of the central molecular part to the surface, the Co/Fe atoms under the molecules are slightly detached from the second layer. This mechanism which is present for finite-size molecular π-systems can obviously not emerge for the 2D materials on the Co(111) substrate since they have no peripheral hydrogens that could be repelled from the surface

[5]Within this approach the top-fcc geometry is found to be more stable by 6 meV compared to the top-hcp geometry for Gr on Co(111).

leading to the skyhook effect. The finding of the essentially unaffected inter-layer coupling of the Co(111) substrate due to 2D material adsorption hence nicely outlines the difference between finite-size molecular and extended π-systems and complements the results reported in Chapter 6.

7.4. Spin-polarized Projected Density of States

As already outlined in Chapters 5 and 6, the increase of the in-plane coupling constants induced by π-electron systems adsorbed on a FM surface is caused by the hybridization especially between out-of-plane d-states of the substrate and p_z-states of the adsorbates which in the present case are the 2D materials. This contribution is denoted as a hybridization effect. The strong 2D material-substrate hybridization can be clearly seen when analyzing the SP-PDOS for the d-states of Co1 (see Fig. 7.7) and for the p-states of Gr and hBN (see Fig. 7.8). More specifically, the SP-PDOS of Co1 for the hybrid systems in Fig. 7.7(a) is strongly changed compared to the clean surface SP-PDOS. On the other hand, the SP-PDOS of Co2 in Fig. 7.7(b) is considerably less modified by the adsorption of the 2D materials underlining that the extended π-systems Gr and hBN essentially only influence the first Co layer. Conclusively, this indicates a significant hybridization of the first layer Co d-states predominantly with the p_z-states of the 2D material as revealed in Fig. 7.8. The SP-PDOS of the p_x- and p_y-states shows essentially no hybridization close to the Fermi energy. This illustrates that the p_z-d hybridization is the dominant mechanism for the in-plane magnetic hardening of the exchange coupling constants.

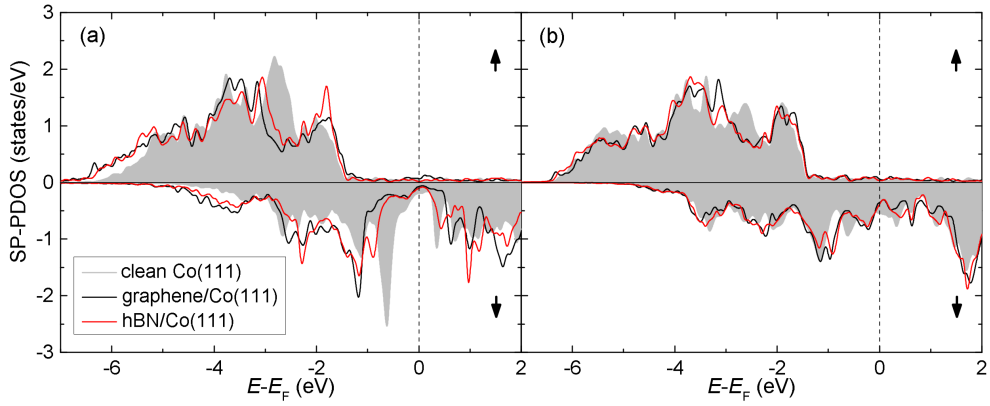

Figure 7.7.: SP-PDOS of the d-states of the Co1 (a) and Co2 (b) atom for Gr and hBN adsorbed on the Co(111) surface. As a reference also the SP-PDOS of a respective clean surface Co atom is included in each figure as gray shaded area.

Another important point when analyzing the SP-PDOS in Fig. 7.8 is that the extended π-systems Gr and hBN acquire no net magnetic moments on Co(111). However, as revealed in Fig. 7.8, they show a net spin polarization within given energy intervals around the Fermi energy. This behavior was also demonstrated for different molecules containing π-electrons on magnetic surfaces in Refs. [19, 40]. It is responsible for the inversion of the spin polarization above the molecules with respect to the clean FM surface as outlined in Subsection 4.3.3. This inversion of the spin polarization can also be seen in Fig. 7.8 for the 2D materials close to the Fermi energy since at this energy the largest weight of the states can be found in the spin up channel. Hence it can be predicted that these magnetic features should be experimentally accessible by for instance SP-STM.

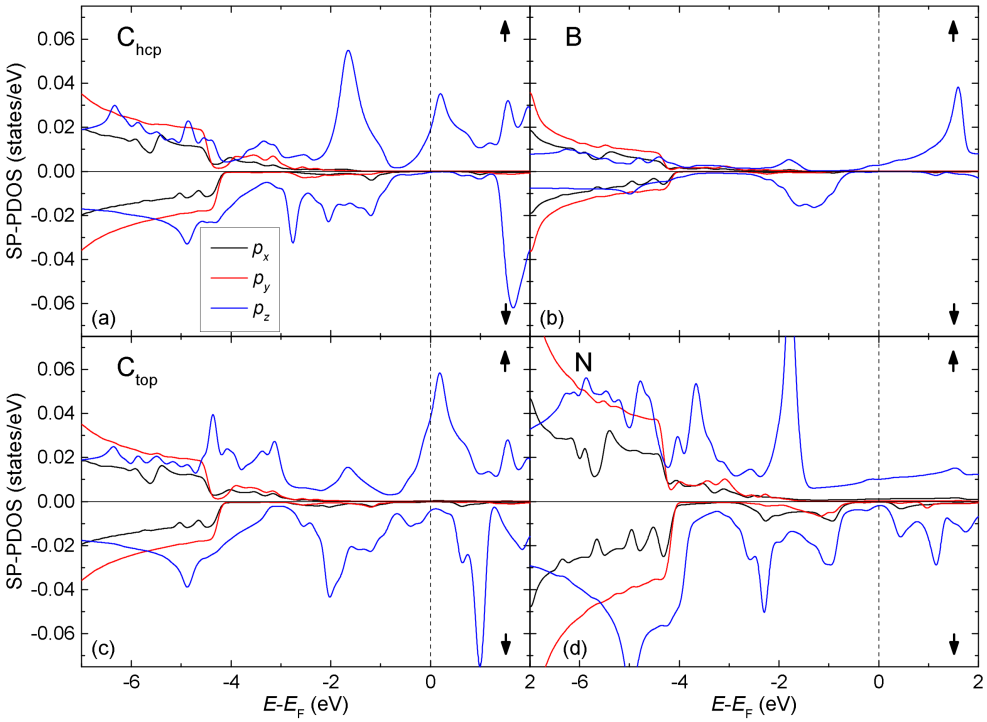

Figure 7.8.: SP-PDOS of the p-states for the C_{hcp}/B (a), (b) and C_{top}/N (c), (d) atoms for Gr and hBN on Co(111), respectively.

7.5. Conclusions

The results presented in this chapter show that the adsorption of 2D materials containing π-electrons such as Gr and hBN on a FM Co(111) surface gives rise to an in-plane enhance-

ment of the magnetic exchange interactions within the first surface layer. More specifically, the hybrid 2D material-Co(111) systems have strongly increased in-plane exchange coupling constants between the Co atoms within the first layer compared to the clean Co(111) surface. An analysis of the SP-PDOS at the site of the substrate and at the site of the 2D materials shows that the driving mechanism of this in-plane magnetic hardening of the exchange coupling constants is the hybridization between p_z-states of the 2D material and d-states of the surface Co atoms. This behavior is qualitatively similar to the experimentally [50] as well as theoretically [303] found in-plane magnetic hardening for the Gr/Co/Ir(111) system.

On the contrary, the calculated inter-layer magnetic exchange coupling constants between the first and second Co layer showed no significant magnetic hardening or softening. This is in contrast to the inter-layer magnetic softening found for finite-size molecules adsorbed on magnetic surfaces in Ref. [51] and Chapter 6. The reason for this qualitatively different behavior of finite-size and extended π-electron systems comes from the fact that the molecular-induced skyhook effect outlined to be responsible for the inter-layer magnetic softening in Chapter 6 does not occur for the extended π-electron systems as no peripheral hydrogen atoms terminate these 2D materials. In this sense the present findings complement the results of the previous chapter and suggest that extended π-electron systems can be utilized to preserve the magnetic properties of a substrate as also Gr-passivation was already suggested as a way to prevent oxidation of Ni electrodes [305].

Conclusively, the results of this chapter clearly highlight the potential of extended (2D) π-electron systems to modify or preserve the magnetic properties of a FM substrate. This knowledge can hence be of importance to distinctly control the magnetic properties and spin-injection processes at Gr/hBN-electrode interfaces within spintronic devices.

8 Formation of Different Magnetic Units

In this chapter the question whether different intramolecular magnetic units can be formed below a single molecule is addressed. For this purpose the 2,4,6-triphenyl-1,3,5-triazine (TPT) molecule, which consists of two types of chemically different rings, was studied on the 2 ML Fe/W(110) surface by a combined theoretical and experimental [306] approach. When investigating the adsorption geometry of TPT on the substrate it is found that the molecule is chemisorbed and that the ground state adsorption position is chiral, i. e. the structure is different from its mirror image. This is an interesting finding since it means that out of two non-chiral components, the surface and the TPT molecule, a chiral structure is formed upon molecular adsorption. This behavior can be rationalized by (i) the low compatibility of the molecular (D_{3h}) and surface (C_{2v}) symmetries and (ii) the general tendency of cyclic molecular structures to adsorb with the rings positioned over hollow sites of the substrate. As a consequence of this symmetry breaking effect, the four rings of the TPT form four structurally different units with the substrate underneath. Moreover the molecular induced skyhook effect, i. e. the molecular induced detaching of the first layer Fe atoms below the molecule from the second layer introduced in Chapter 6, is found to be more pronounced below the phenyl rings as compared to the central triazine-like ring.

The simulated STM images indicate that especially at small bias voltages the structural asymmetry gives rise to an electronic asymmetry among all four units as the different molecular lobes appear distinctly different in both the spin averaged and the spin polarized images. Eventually, this gives rise to an inversion of the spin polarization above the molecule with respect to the surface, i. e. positive (reddish) above the molecule vs. negative (blueish) above the surface, which varies on an intramolecular length scale between the different units. This asymmetry in the electronic and magnetic properties is also found in the experimentally recorded STM images [306] and on a qualitative level agrees well with the simulated data.

Finally, it is found that also the magnetic units formed below the molecular rings are different with respect to their magnetic exchange coupling among each other and to the clean surface. This shows that the asymmetry of the hybrid molecule-surface structure carries over to the electronic and magnetic properties and that indeed different magnetic units could be formed below a single molecule. Ultimately, the different switching behavior of magnetic units within a single molecule-surface system might possibly be used for molecular based spin logic devices.

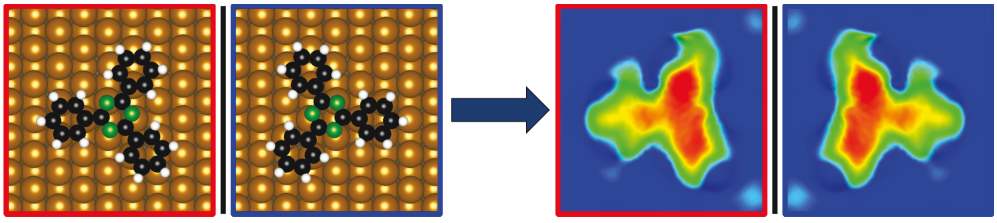

In the preceding chapters the magnetic exchange coupling was analyzed in detail by calculating the coupling constants between the individual magnetic centers. However as shown in Ref. [52] and Chapter 6, below molecular rings strongly exchange coupled magnetic units can be formed on magnetic surfaces. In this chapter the idea is to generalize the previous concepts and to consider the adsorption of a molecule with different rings so that one can expect that different magnetic (sub-)units are formed which are supposed to show a different switching behavior in an applied magnetic field. Considering the formation of the different magnetic units, in this chapter the exchange coupling constants are calculated for those magnetic units formed by the adsorption of the molecule. Hence these coupling constants are directly related to the energy difference between the FM state and the state with the moment of the respective unit flipped.

8.1. Presentation of the TPT Molecule

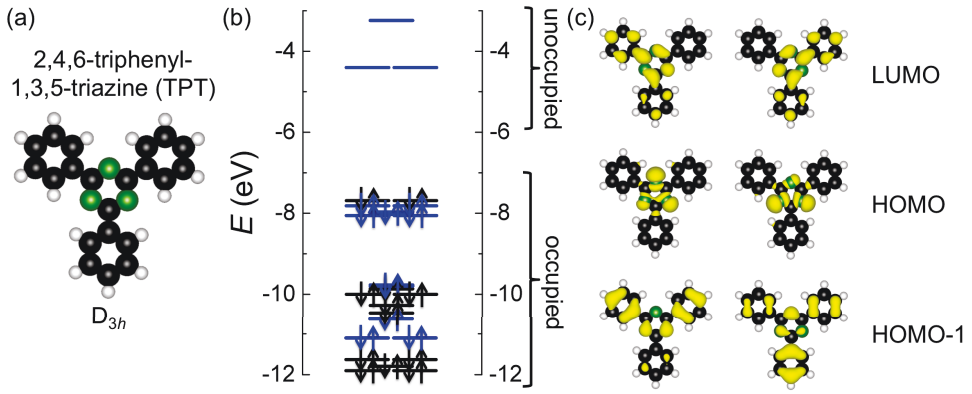

Figure 8.1.: Atomic structure (a), calculated energy level diagram (b) and charge density of the HOMO−1, HOMO and LUMO states (c) for TPT in the gas phase. As indicated in (a), the molecular structure has a D_{3h} point group symmetry. In the energy level diagram the molecular π-states are marked in blue whereas the σ-states are marked in black. The occupation of the states is indicated by arrows. Note that again the HOMO was aligned at the calculated IP of 7.69 eV. For the twofold degenerate HOMO−1, HOMO and LUMO states the depicted isosurface plots represent one possible basis of the 2D orbital space at the respective energy. The isosurface plots were made for an isovalue of $1.35 \cdot 10^{-2}$ $e/\text{Å}^3$. Color code for atoms same as in Fig. 5.2.

In this chapter the adsorption of the TPT molecule ($C_{21}N_3H_{15}$) on the 2 ML Fe/W(110) surface is investigated. The atomic structure of the molecule in the gas phase is depicted in Fig. 8.1(a).

Clearly, the flat molecular structure is made up of three peripheral phenyl rings which are attached to a central triazine-like ring. As indicated below the structure, the molecule has a D_{3h} point group symmetry. Since this group contains 2D irreducible representations [55] it is already clear from the symmetry point of view that among the electronic states twofold degenerate energy levels will be present. The energy level diagram in Fig. 8.1(b) shows that most of the molecular orbitals around the HOMO-LUMO gap are π-states (see for instance the isosurface plots of the charge density of the HOMO-1 and LUMO states presented in Fig. 8.1(c)) which are marked in blue whereas the σ-states are marked in black. An exception to this rule is the twofold degenerate HOMO state which is a molecular orbital with a density distribution in the plane of the molecule, i. e. a σ-state. As indicated in the middle of Fig. 8.1(c) it is derived from the free electron pairs at the nitrogens of the central triazine-like ring.

These findings show that TPT is made up of two types of rings which are chemically and consequently electronically different. Together with the element specific change of the coupling constants presented in Chapter 5, this raises the expectation that due to the adsorption of the molecule on a magnetic surface (at least) two different magnetic units can be formed that interact via the exchange coupling between them and show a different magnetic switching behavior.

8.2. Adsorption Geometries and Structural Properties

The investigated adsorption positions for TPT on the 2 ML Fe/W(110) surface are depicted in Fig. 8.2. As indicated for example in Refs. [19, 52, 202] and Chapter 6, the adsorption of cyclic molecules onto (magnetic) surfaces is driven by the fact that the center of the molecular ring is in favor of occupying a hollow site of the surface. Therefore the guideline for the construction of the adsorption positions was to place as many rings of the TPT as possible over hollow site positions. In the hollow site geometry (Fig. 8.2(a)) the central triazine-like ring is positioned over the hollow site formed by four surface Fe atoms. In the N-top site (Fig. 8.2(b)) the N atoms of the central ring are on top of surface Fe atoms. For the hollow90 site (Fig. 8.2(c)) the TPT molecule was rotated clockwise by 90° with respect to the hollow site. When this arrangement is shifted along the [001]-direction the atop site results (Fig. 8.2(d)). Remarkably, all these adsorption positions are symmetric with respect to a mirror plane either along the $[1\bar{1}0]$- or the [001]-direction.

In addition, using STM measurements showing atomic resolution on both the surface as well as the TPT molecule, the adsorption position could be determined experimentally as depicted in Fig. 8.2(e)[1] [306]. The derived adsorption geometry used as another starting point for the structural relaxation is given in Fig. 8.2(f).

[1] The STM measurements were performed by Volkmar Heß (PGI-6, Forschungszentrum Jülich) [306].

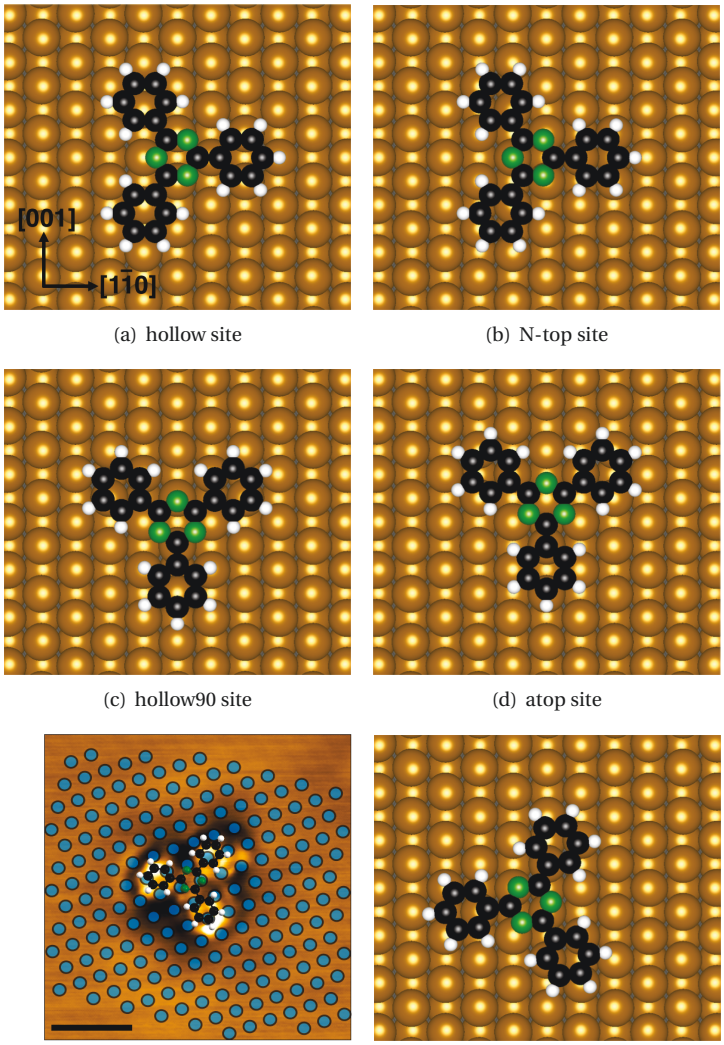

(a) hollow site (b) N-top site

(c) hollow90 site (d) atop site

(e) experimental (f) chiral site

Figure 8.2.: Investigated adsorption sites for TPT on 2 ML Fe/W(110). The image in (e) derived from STM results was provided by Volkmar Heß (PGI-6, Forschungszentrum Jülich) [306]. In this image the atomic positions of the surface layer are denoted by blue circles and the black bar indicates a length of 1 nm. Color code of the surface atoms same as in Fig. 5.3.

An investigation of the stability of the different adsorption sites has been performed with a slab containing a reduced number of layers, i. e. consisting of two Fe layers and one W layer with the TPT adsorbed on top of the uppermost Fe layer. For this study the molecular

coordinates and the uppermost Fe layer were relaxed. The adsorption energies calculated for the relaxed adsorption positions presented in Table 8.1 corroborate the experimentally suggested chiral adsorption geometry as having the largest binding energy to the surface[2]. For this most stable geometry the relaxation was then continued after adding four more W layers to the slab and following the procedure described in Section A.8. The final relaxed ground state structure is presented in Figs. 8.3(a) and (b) in top and side view, respectively.

Table 8.1.: Calculated adsorption energies E_{ads} for TPT on 2 ML Fe/W(110) for the different adsorption sites. The adsorption energy is defined as in Equation 5.1.

position	E_{ads} (eV)
chiral site	**3.90**
hollow site	3.82
atop site	3.63
N-top site	3.55
hollow90 site	3.19

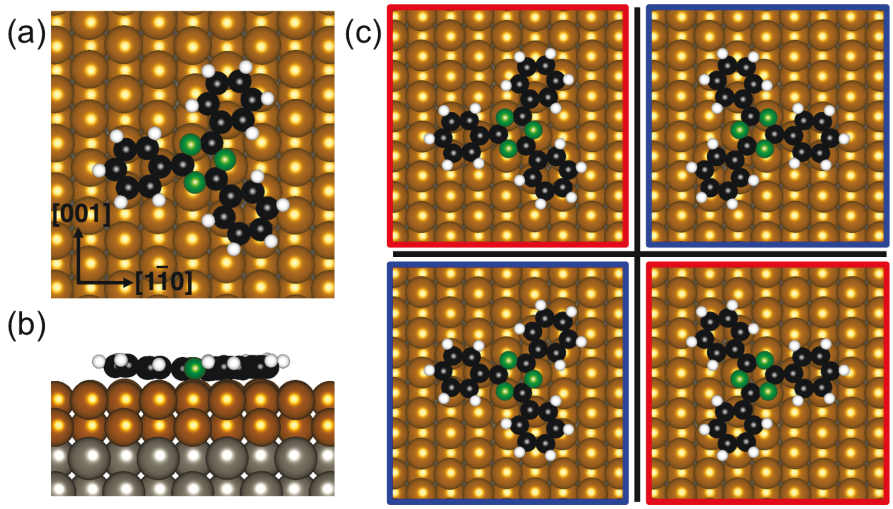

Figure 8.3.: Ground state geometry for TPT on 2 ML Fe/W(110) in top view (a) and side view (b), respectively. In (c) the mirror images of the structure along horizontal and vertical mirror planes are displayed. Only the pairs surrounded by either a red- or blue-frame can be overlaid by a 180° rotation, i. e. they are identical. When comparing red-framed and blue-framed structures it turns out that these geometries are different enantiomers that cannot be superimposed onto one another.

[2]The small energy difference between the experimentally suggested geometry and the hollow site in Table 8.1 can be understood when comparing Fig. 8.2(a) and Fig. 8.3(a) since the optimized adsorption position can be thought of as being derived from the hollow site by mirroring the molecule with respect to a vertical mirror plane and slightly distorting the position of the upper and lower phenyl rings.

The interesting characteristic of this ground state adsorption geometry is that it is completely asymmetric, i. e. the structure lacks any symmetry (besides identity). This leads to the finding that when mirror images of this structure are constructed by mirroring with respect to horizontal and vertical mirror planes positioned perpendicular to the surface plane as done in Fig. 8.3(c), four structures are obtained which are not all identical[3]. The two red-framed structures in Fig. 8.3(c) are identical as they can be transformed into one another by a 180° rotation. The same holds when comparing the two blue-framed structures. However when comparing red-framed with blue-framed structures those are not identical as they cannot be overlayed by any rotation, i. e. these mirror images are not identical. A structure which is not identical to it's mirror image is chiral and the two non-identical mirror images are called enantiomers [281].

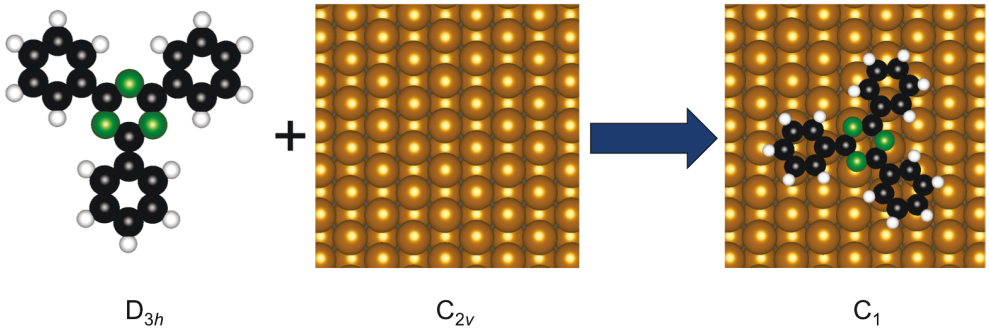

Figure 8.4.: Symmetry analysis for the TPT adsorption on 2 ML Fe/W(110). The isolated TPT molecule has D_{3h} symmetry, the clean surface has C_{2v} symmetry and the resulting adsorption geometry belongs to the C_1 point group, i. e. it lacks of any symmetry except of identity.

In terms of symmetry, the present scenario is analyzed in Fig. 8.4. The isolated TPT molecule has D_{3h} symmetry, the clean 2 ML Fe/W(110) surface belongs to the C_{2v} point group and when combining these two symmetric objects, the ground state adsorption geometry is asymmetric belonging to the C_1 point group. From the symmetry point of view the necessary and sufficient condition for chirality is that the object supposed to be chiral has no mirroring symmetry element, i. e. it has no mirror plane, inversion center or inversion axis (S_2-axis) [281]. Hence an object which is completely asymmetric as the detected adsorption geometry of TPT on the 2 ML Fe/W(110) surface fulfills those conditions and is therefore chiral. Conclusively, in the present case a chiral structure is formed out of two non-chiral components[4]. It should

[3] All four structures are seen in the STM measurements of Volkmar Heß (PGI-6, Forschungszentrum Jülich) [306].

[4] However it should be noted that no significant enantioselectivity of the TPT adsorption on the magnetic surface was found, i. e. the two enantiomers could not be distinguished. More precisely, no significant difference

however be noted that the adsorption induced 'chiralization' of molecule-surface systems has already been studied for other systems (see e. g. Ref. [307] for a review).

To further characterize the bonding of the TPT molecule to the surface, in Table 8.2 an overview of the molecule-surface bond distances between the molecular C/N atoms and the surface Fe atoms is given. All three N atoms of the central triazine-like ring and all C atoms of the phenyl rings that sit directly on top of surface Fe atoms are very tightly bonded between 2.0 Å to 2.1 Å to the surface Fe atoms. This picture is further supported by the side view in Fig. 8.3(b) which shows that the whole molecular plane is close to the surface as also revealed by the additional bond distances in Table 8.2. Together with the large adsorption energy presented in Table 8.1 these findings give a clear indication for a chemisorption of the TPT onto the 2 ML Fe/W(110) surface. When comparing the different molecular rings in Fig. 8.3(a), the central triazine-like ring is most closely bound to the surface, whereas the phenyl ring aligned along the $[1\bar{1}0]$ direction is farthest away from the surface being about 0.1 Å higher than the triazine-like ring. Considering the other two phenyl rings the upper one covering four surface Fe atoms is slightly closer to the surface than the lower one covering only three surface Fe atoms.

Table 8.2.: Overview of the molecule-surface distances between the molecular C/N atoms and the surface Fe atoms for TPT on 2 ML Fe/W(110).

distance range (Å)	number of bonds
2.0-2.1 (Fe-N)	3
2.0-2.1 (Fe-C)	4
2.1-2.2 (Fe-C)	5
2.2-2.5 (Fe-C)	13

Regarding the distortions induced on the 2 ML Fe/W(110) surface by the adsorption of the TPT molecule, the general behavior of the in-plane distances within the uppermost Fe layer is that the surface Fe atoms below the phenyl rings come closer together by about 0.1 Å-0.2 Å. However the three Fe atoms below the central triazine-like ring get farther apart from one another by about 0.15 Å as compared to the clean surface nearest neighbor Fe-Fe distance of 2.75 Å. Concerning the inter-layer Fe-Fe distances, all Fe atoms of the first layer below the molecule are detached from the lower Fe layer (see Table 8.3), i. e. they show the molecular induced skyhook effect introduced in Chapter 6 which can be seen directly when closely inspecting the side view in Fig. 8.3(b). There it is also clearly visible that the peripheral hydrogen atoms of the TPT are tilted away from the surface. More specifically, this molecular induced lift off of the first layer enhances the inter-layer Fe-Fe distance up to 2.48 Å compared to the clean surface reference of 2.35 Å. On average the largest detachment is observed for the Fe

has so far been detected in the STM data and during a calculation taking account SOC the energy difference between the enantiomers was found to be smaller than 1 meV.

atoms below the phenyl ring aligned along the $[1\bar{1}0]$ direction and the smallest effect is observed for the surface Fe atoms below the central triazine-like ring. For the other two phenyl rings the lift off is stronger for the Fe atoms below the upper ring covering four Fe atoms (see Fig. 8.8(b)).

Table 8.3.: Overview of the inter-layer Fe-Fe distances for TPT on 2 ML Fe/W(110). The clean surface inter-layer Fe-Fe distance is 2.35 Å.

distance range (Å)	number of bonds
2.35-2.40	4
2.40-2.45	17
2.45-2.49	5

8.3. Simulated STM Images and Spin-polarized Projected Density of States

In Fig. 8.5 an overview of the simulated STM topography images in Tersoff-Hamann approximation is presented. According to Section 2.3.5 the constant current mode of STM measures isosurfaces of the charge density integrated over the specific energy interval given by the bias voltage. In the *ab initio* calculations the charge density was therefore integrated over the respective energy window relative to the Fermi energy and a suitable isovalue was chosen for the subsequent visualization. For negative bias voltages the occupied states of the hybrid molecule-surface system within the bias window below the Fermi energy are probed whereas for positive bias the unoccupied states above the Fermi level are accessed.

The spin averaged STM images in the top row in Fig. 8.5 indicate that for large bias voltages the TPT structure appears essentially symmetric on the surface whereas for small bias voltages (± 0.1 V) clearly a difference between the different rings, as revealed by the asymmetric (chiral) adsorption geometry, can be detected. This indicates that the induced asymmetry in the electronic structure is confined to a rather small energy interval close to the Fermi level. Notably, the brightness of the different rings in the -0.1 V topography image follows the height distribution of those rings above the surface (see Section 8.2) as the least brightest spot is associated with the central triazine-like ring that is most tightly bound to the surface whereas the brightest spot corresponds to the phenyl ring aligned along the $[1\bar{1}0]$-direction having the largest distance to the surface.

In case of the images corresponding to the spin up and spin down channel visualized in the second and third row in Fig. 8.5 the molecular structure is much more clearly detectable in the up channel rather than in the down channel. One important point is that for the clean surface close to the Fermi level the minority (spin down) states dominate. Therefore the spin

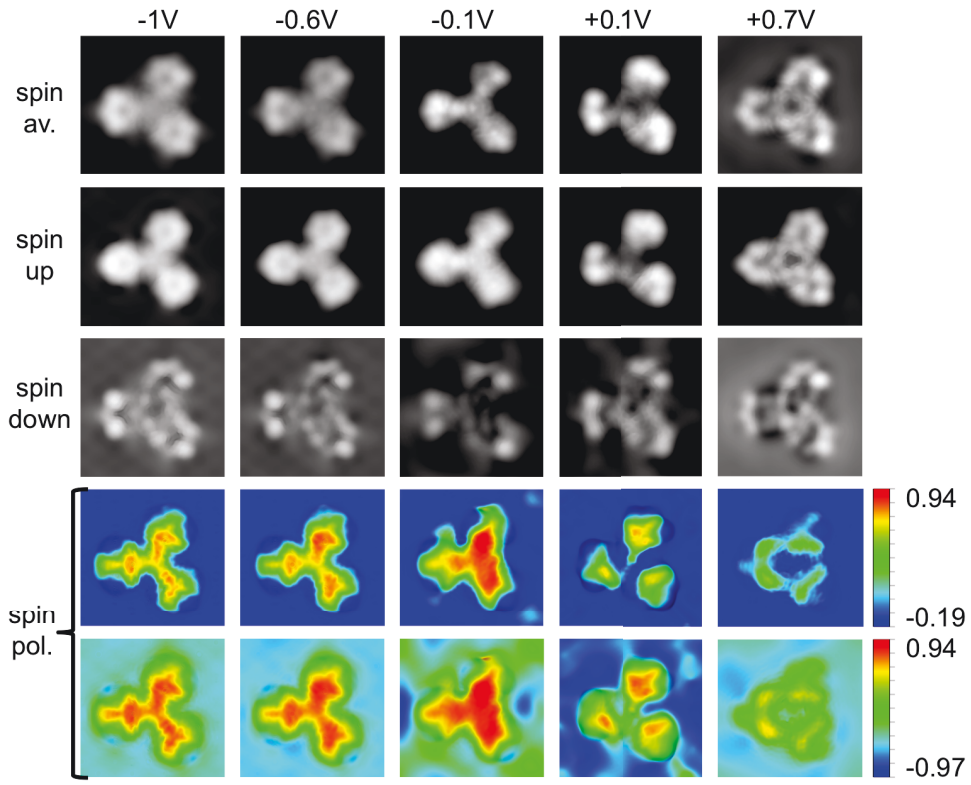

Figure 8.5.: Overview of the simulated STM topography images for TPT on 2 ML Fe/W(110) at different bias voltages. In the first row the spin averaged topography images are presented. In the second and third rows the images for the spin up and spin down channel are given, respectively. The last two rows show the calculated spin polarization according to Equation (4.4) at the different bias voltages for two different ranges of the polarization scale. The spin averaged, spin up and spin down images at -1 V, -0.6 V and +0.7 V are displayed for an isovalue of $3.37 \cdot 10^{-5}$ $e/\text{Å}^3$, at -0.1 V for $3.37 \cdot 10^{-6}$ $e/\text{Å}^3$ and at +0.1 V for $2.02 \cdot 10^{-6}$ $e/\text{Å}^3$. All images for the spin polarizations were made for an isovalue of $6.75 \cdot 10^{-6}$ $e/\text{Å}^3$ colored with the degree of spin polarization at each point. The scale bars to the right of the last two rows indicate the respective range of spin polarization. The orientation of the TPT molecule on the surface is in every case the same as in Fig. 8.3(a).

polarization of the surface close to the Fermi energy according to Equation (4.4) is negative. However when the simulated spin polarization at the different bias voltages in the fourth row in Fig. 8.5 is considered, clearly it is mostly positive above the molecule, i. e. it is inverted in agreement with the results presented in Ref. [19] for which the general mechanism based on the $p_z - d$-hybridization was briefly explained in Section 4.3.3. The largest (positive) spin

polarization is observed at −0.1 V and the effect of the inversion above the molecule becomes weaker for larger bias voltages. When the range of the scale bar between maximum and minimum of the spin polarization is changed as in the last row in Fig. 8.5 it shows that also the (negative) spin polarization of the substrate varies over a wide range in the different energy intervals.

In Fig. 8.6 a comparison of the experimentally measured[5] topography images at ±0.1 V and the calculated spin polarizations with the simulated results is shown. Considering first the topography images in Fig. 8.6(a), it can be seen that on a qualitative level for both bias voltages the simulated images agree nicely with the measured ones. The simulation correctly reproduces the topography of the different lobes[6] and the relation of their brightness seen in the experiment. However for larger bias voltages the comparison of measured and simulated images is complicated by tip states present in the experiment [306, 308] but not explicitly included in the calculation. For this and the second reason that the asymmetric structure of the hybrid molecule-surface system is most clearly seen close to the Fermi level, the analysis focuses onto the two small bias voltages.

The comparison of the spin polarizations in Fig. 8.6(b) again indicates a good qualitative agreement between theory and experiment in that for both biases the polarization above the molecule is inverted with respect to the substrate[7]. In addition, the simulation correctly reproduces the smaller degree of positive spin polarization above the TPT at +0.1 V as compared to −0.1 V for which above two molecular rings very strong positive spin polarization is detected. However the relative degree of the spin polarization among the lobes is slightly different between experiment and theory. This might again be due to the electronic structure of the tip included in the measurements but not the simulations according to the Tersoff-Hamann approximation. Nevertheless the most important point is that in both the experimental as well as the theoretical results a pronounced difference in the spin polarization among the lobes is found which is particularly obvious at −0.1 V. This means that the structural asymmetry outlined in Section 8.2 carries over not only to the electronic (see Fig. 8.6(a)) but also to the magnetic properties of the system. Hence a strongly energy- as well as site-dependent spin polarization is observed which varies on an intramolecular length scale.

An overview of the SP-PDOS for the individual molecular rings, the whole molecular part of the hybrid system and for the d-states of selected surface Fe atoms positioned directly below C or N is depicted in Fig. 8.7. The molecular parts named triazine, phenyl1, phenyl2

[5] The STM measurements were performed by Volkmar Heß (PGI-6, Forschungszentrum Jülich) [306].

[6] The terms 'lobe' and 'ring' are treated as synonyms in this chapter.

[7] A direct comparison of the recorded and simulated images for the spin up and spin down channel was not possible since the spin polarization of the tip was found to be significantly below 100% which does not affect the deduced spin polarization but renders a comparison with the theoretical data for spin up and spin down difficult.

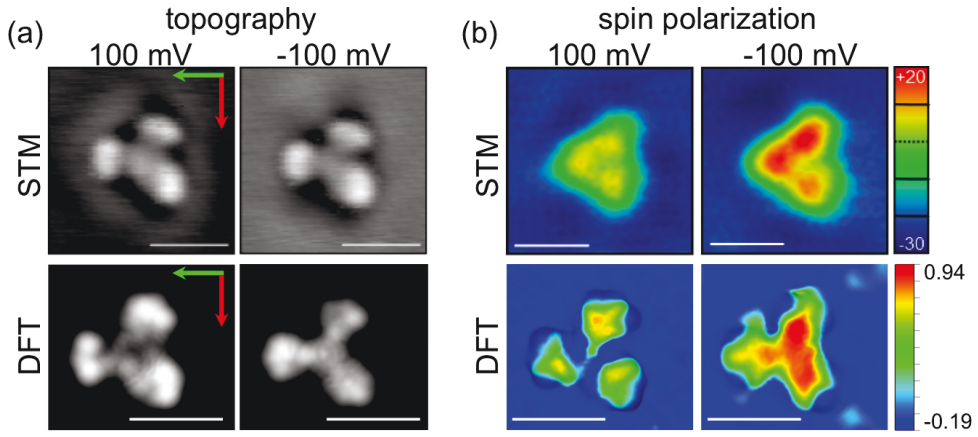

Figure 8.6.: Comparison of the simulated and measured STM topography images at −0.1 V and +0.1 V (a) and for the spin polarizations at these bias voltages (b) for TPT on 2 ML Fe/W(110). The white scale bar in all images corresponds to 1 nm and the green and red arrows stand for the $[1\bar{1}0]$- and [001]-directions, respectively. The scale bar for the experimental spin polarization indicates the height differences (in pm) obtained when subtracting the data for the spin up and spin down channels. It should be noted that the experiment is sensitive to the spin polarization of the combined tip-sample system whereas the simulated images show the spin polarization of the hybrid molecule-surface system only. The experimental images were provided by Volkmar Heß (PGI-6, Forschungszentrum Jülich) [306].

and phenyl3 correspond to the molecular rings positioned above the units 1, 2, 3 and 4 labeled in Fig. 8.8, respectively. The dashed lines in Fig. 8.7 indicate the bias ranges relative to the Fermi energy for which the simulated STM images in Fig. 8.5 were generated. All diagrams clearly show the strong hybridization of the TPT states with the states of the substrate as the molecular DOS consists of broad features corroborating the chemisorption type bonding of TPT to the surface remarked in Section 8.2. The finite DOS at the Fermi energy on the site of the molecule underlines that a hybrid metallic molecule-surface system is formed due to the molecular adsorption. For the molecular SP-PDOS in addition to the total DOS the contribution of the σ- and π-states is given underscoring that the molecular derived electronic structure close to the Fermi energy is dominated by π-states. It is these states which are predominantly measured by STM since the σ-states have smaller weight and due to their distribution within the molecular plane also decay faster as compared to the π-states in the direction perpendicular to the surface.

With respect to these π-states for all molecular rings the positive spin polarization close to E_F is clearly visible in Figs. 8.7(a)-(d) which is consequently also seen in the summed SP-PDOS in Fig. 8.7(e). In contrast, as underscored in Fig. 8.7(f), the spin polarization of the surface Fe

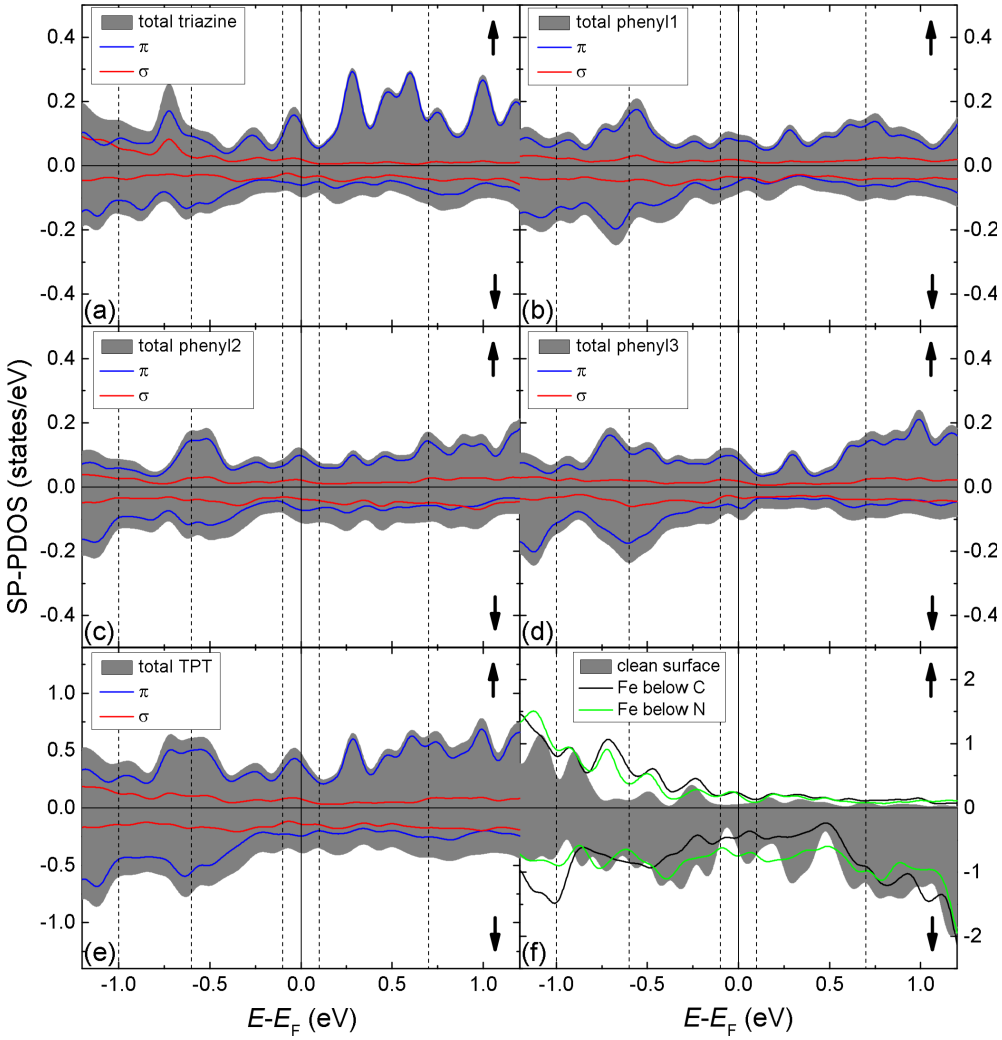

Figure 8.7.: SP-PDOS of the individual molecular rings (a)-(d), total molecular SP-PDOS (e) and *d*-states of surface Fe atoms positioned below a C or N atom (f) for TPT on 2 ML Fe/W(110). As a reference, in (f) also the SP-PDOS of a clean surface Fe atom is given as gray shaded area. The dashed lines indicate the bias voltages for which the images in Fig 8.5 were simulated. Triazine, phenyl1, phenyl2 and phenyl3 correspond to the molecular rings positioned above the units 1, 2, 3 and 4 labeled in Fig. 8.8, respectively. For the visualization of the Fe *d* SP-PDOS below the molecule in (f) the right Fe atom of unit 4 and the upper Fe atom of unit 1 assigned in Fig. 8.8 have been chosen.

atoms especially below the molecule is dominated by minority spin states at E_F, i. e. it is negative as can also be seen for the clean surface regions in the last two rows of Fig. 8.5. The SP-PDOS of the Fe d-states displayed over a larger energy region can be found in the Appendix A in Fig. A.10 signifying the strong hybridization between molecule and substrate over the whole energy range of the d-bands. It should however be noted that the DOS visualized in Fig. 8.7 is not directly comparable to the LDOS measured by STM since the tip is positioned at least several Å above the molecule and the SP-PDOS shown is obtained from the states within the PAW spheres centered at the atomic cores[8].

8.4. Magnetic Moments and Exchange Coupling Constants

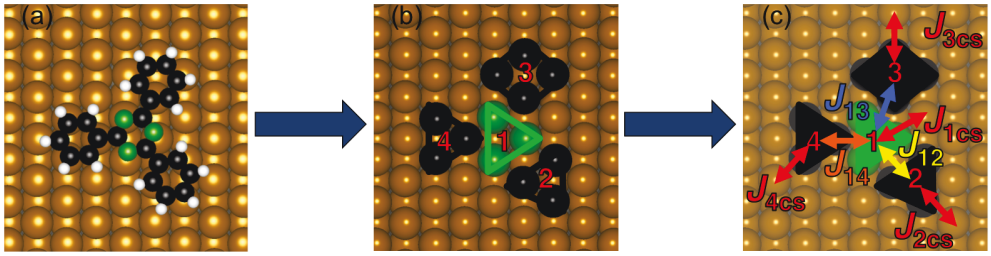

Figure 8.8.: The interaction of TPT with the 2 ML Fe/W(110) surface (a) is confined to the thirteen Fe atoms directly bound to it (b). Below the different rings of the molecule magnetic units are formed which are labeled as 1 to 4. To calculate the magnetic exchange coupling constants for the different units, the couplings between the units and from each unit to the clean surface need to be considered as assigned in (c).

Analogously as in Chapters 5 and 6, the influence of the TPT adsorption onto the surface is confined to the thirteen first layer Fe atoms to which it is directly bound to as indicated in Fig. 8.8(b). An overview of the magnetic moments of these influenced Fe atoms is given in Table 8.4 showing the common behavior known from the previous chapters that all Fe moments are considerably reduced compared to the clean surface value of 2.9 μ_B due to the strong molecule-surface hybridization. In addition, it can be remarked that in analogy to the results presented in Chapter 5 the moments of the Fe atoms directly below N are less reduced by about 0.1 μ_B to 0.2 μ_B compared to the Fe atoms below C.

In Ref. [52] it was outlined that below the lower molecular ring of PCP on 1 ML Fe/W(110) a strongly exchange coupled hybrid molecule-surface magnetic unit is formed. In generalizing this idea it can be concluded that the TPT molecule leaves an imprint of four magnetic units

[8]The radius of the PAW sphere (core radius) is typically in the range of 0.5 Å to 1.5 Å.

Table 8.4.: Overview of the magnetic moments of the surface Fe atoms directly bound to TPT on 2 ML Fe/W(110). The clean surface first and second layer Fe moments are 2.9 μ_B and 2.3 μ_B, respectively.

moment range (μ_B)	number of moments
2.4-2.5	2
2.5-2.6	6
2.6-2.7	4
2.7-2.8	1

on the surface formed below the different molecular rings which are labeled in Fig. 8.8(b). In contrast to the previous chapters where the exchange coupling constants have been evaluated between the individual magnetic centers, the target is now to evaluate the coupling constants between these *units* by generalizing the procedure used in Chapters 5, 6 and 7. Therefore a generalized nearest neighbor Heisenberg Hamiltonian is used:

$$H_{\text{units}}^{\text{spin}} = -\sum_{\langle i>j\rangle} J_{ij}\mathbf{m}_i\mathbf{m}_j, \tag{8.1}$$

where $\mathbf{m}_i$ and $\mathbf{m}_j$ stand for the magnetic moments of units i and j, respectively. Accordingly, the energy difference between FM and AFM alignment of the moments of specific magnetic units can be expressed as:

$$E_{\text{FM}} - E_{\text{AFM}} = -2\sum_{\langle i>j\rangle} J_{ij}m_i m_j, \tag{8.2}$$

where m_i and m_j are the absolute values of the moments of the magnetic units i and j. By taking into account a suitably chosen set of AFM configurations where the moments of selected molecular-induced magnetic units are flipped, the coupling constants between the units can be obtained from the resulting coupled system of equations.

As depicted in Fig. 8.8(c) in the present case there are couplings between the individual molecular-induced magnetic units, i. e. J_{12}, J_{13} and J_{14}, and each of these units is also coupled to an unaffected clean surface unit via J_{1cs}, J_{2cs}, J_{3cs} and J_{4cs}. The respective clean surface unit to which each molecular-induced unit is coupled to, is made up of the nearest neighbor first and second layer clean surface Fe atoms of each molecular-induced unit. The magnetic moments of all these units are summarized in Table 8.5. The moment of unit 3 is about 2.5 μ_B larger than the ones of the other molecular-induced units since it incorporates 4 instead of 3 surface Fe atoms. The clean surface unit to which the molecular-induced unit 1 is coupled to (cs1) consists of 8 nearest neighbor Fe atoms (3 in the first layer + 5 from the second layer). Accordingly, cs2 is made up of 10 (5 + 5), cs3 of 14 (7 + 7) and cs4 of 10 (5 + 5) nearest neighbor Fe atoms. For this reason the magnetic moment of unit cs3 is the largest.

Table 8.5.: Magnetic moments of the magnetic units used to evaluate the exchange coupling constants for TPT on 2 ML Fe/W(110). cs$n$ is the clean surface unit the molecular-induced unit n is coupled to, $n = 1,2,3,4$.

magnetic unit	1	2	3	4	cs1	cs2	cs3	cs4
magnetic moment (μ_B)	8.1	7.7	10.4	7.6	20.2	25.8	36.3	25.9

The AFM configurations used to evaluate the seven coupling constants are schematically presented in Fig. 8.9. Four equations are obtained from switching the moment of each of the four molecular-induced units individually (Figs. 8.9(a)-8.9(d)). Another three equations result from switching the moments of unit 1 and one other molecular-induced unit[9] (Figs. 8.9(e)-8.9(g)). Finally, an additional equation is gained when the moments of all four molecular-induced units are flipped at once (Figs. 8.9(h)). The coupling constants have been eventually evaluated similar as in Chapters 5 and 6 by solving the algebraic system for various sets of equations and averaging over the results obtained from the different sets. However, it should be noted that the equations for the AFM-unit1, AFM-unit1+2, AFM-unit1+3, AFM-unit1+4 and AFM-unit1+2+3+4 configurations form a linearly dependent set.

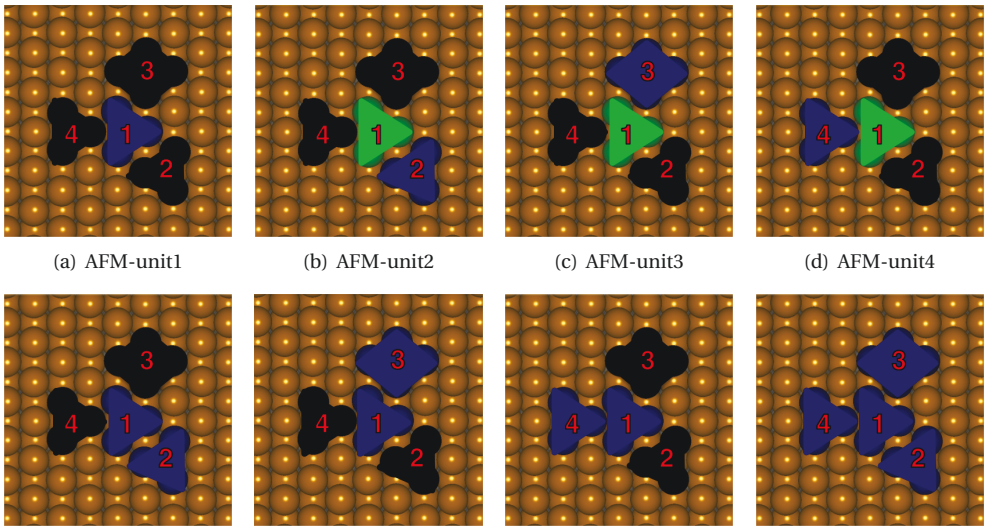

(a) AFM-unit1 (b) AFM-unit2 (c) AFM-unit3 (d) AFM-unit4

(e) AFM-unit1+2 (f) AFM-unit1+3 (g) AFM-unit1+4 (h) AFM-unit1+2+3+4

Figure 8.9.: The AFM configurations used to calculate the exchange coupling constants between the magnetic units for TPT on 2 ML Fe/W(110). The units for which the moment is flipped in the respective configuration are displayed in dark blue.

[9] Switching the moments of two units below the phenyl rings together does not result in any new information since according to the applied nearest neighbor Heisenberg model they are not coupled.

The coupling constants obtained from using this procedure are listed in Table 8.6 in the first row as total values and below normalized to the number of Fe-Fe bonds between the coupled units. The first row indicates that units 1 and 4 are much more strongly magnetically coupled than units 1 and 2 or 1 and 3 as J_{14} is more than a factor of two larger than J_{12} and J_{13}. By comparing Fig. 8.8(a) and (b) it can be seen that this is partially due to the fact that the molecular rings above units 1 and 4 are most suitably positioned to mediate the coupling between the units as compared to the other inter-unit couplings. In addition, the coupling between units 1 and 3 is only mediated by one nearest neighbor (Fe-Fe) bond whereas between units 1 and 2 as well as 1 and 4 it is mediated by two nearest neighbor bonds (see Fig. 8.8(b)). The total exchange coupling values of the individual units to the clean surface are much larger than the coupling between the molecular-induced units since the coupling is mediated by more nearest neighbors, i. e. bonds, as described above. Nevertheless, when comparing the different values of the exchange couplings to the clean surface it is immediately clear that all four units are different in their coupling to the clean surface. The large value of the J_{3cs} coupling is mainly due to the fact that unit 3 consists of four surface Fe atoms in contrast to the other molecular-induced units which incorporate three surface Fe atoms.

When the J values are normalized to the number of Fe-Fe bonds between the magnetic units as done in the second row in Table 8.6, the strong J_{14} coupling especially compared to J_{12} becomes even more evident. Comparing these values to the exchange couplings between the molecular-induced magnetic units and the clean surface shows that the former are in general smaller. Only J_{3cs} is 2 meV smaller than J_{14} due to the fact that, as a consequence of the molecular adsorption, the atoms of unit 3 are pulled together particularly increasing their distance to the neighboring clean surface atoms.

Table 8.6.: Calculated exchange coupling constants as total values and normalized with respect to the number of Fe-Fe bonds between the respective units for TPT on 2 ML Fe/W(110) as assigned in Fig. 8.8(c).

	coupling constant (meV)						
	J_{12}	J_{13}	J_{14}	J_{1cs}	J_{2cs}	J_{3cs}	J_{4cs}
J	51	44	121	594	695	828	644
J/bond	26	44	61	74	70	59	64

Moreover, the coupling constants of each molecular-induced unit to all other units can be added to give a direct measure of the energy scale for flipping the magnetic moment of the respective unit relative to all other (nearest neighbor) units. These values are presented in Table 8.7 again in the first row as total values and in the second row normalized to the number of Fe-Fe bonds over which each unit is coupled to other units. As a reference also the coupling constant evaluated from flipping the moment of a single Fe atom of the clean surface

is given[10]. Clearly, the energy scale to flip the moments of the molecular-induced magnetic units is larger than that required to flip the moment of a single clean surface Fe atom which is a consequence of the fact that these units are formed out of more than one surface Fe atom. When normalized to the number of Fe-Fe bonds (see values in the second row in Table 8.7) the coupling of all units is slightly weaker as compared to the coupling of a single Fe moment to the clean surface indicating a small softening of the coupling to the clean surface due to the formation of the molecular-induced units.

Even more importantly, the coupling constants of all molecular-induced magnetic units in the first row of Table 8.7 are considerably different with respect to each other as they deviate from one another by up to 17%. This demonstrates that the adsorption of the TPT leads to the formation of four different (molecular-induced) magnetic units which are clearly distinguished with respect to their magnetic exchange coupling behavior. However it should be noted that these values are not meant be directly transformed into switching fields describing the magnetization reversal process since the switching will not take place by a direct flipping of the moments of these different units. Nevertheless, the presented values of the exchange coupling constants for each molecular-induced unit still point to the inequivalence of the magnetic units formed below the molecular rings.

Table 8.7.: Calculated coupling constants of each molecular-induced magnetic unit as total values and normalized with respect to the number of Fe-Fe bonds to all other units it is coupled to for TPT on 2 ML Fe/W(110). As a reference the coupling constant for a single clean surface Fe atom $J_{1\mathrm{Fecs}}$ is also given.

	coupling constant (meV)				
	$J_{1\mathrm{Fecs}}$	J_{unit1}	J_{unit2}	J_{unit3}	J_{unit4}
J_{unit}	403	811	746	872	765
J_{unit}/bond	67	62	62	58	64

8.5. Conclusions

In this chapter the adsorption of TPT onto the 2 ML Fe/W(110) surface was investigated. It was found that the TPT molecule adsorbs in a chiral adsorption geometry on this surface, i. e. the adsorption geometry is different from its mirror image, as consistently revealed by STM measurements and DFT calculations. This is especially interesting as both the individual TPT molecule as well as the clean surface are non-chiral, i. e. due to the adsorption of TPT a chiral object is formed out of two non-chiral components. This chirality expresses itself as an

[10] According to Equation (8.2) this value is just half the energy difference between the FM state of the clean surface and the state with the single Fe moment flipped.

asymmetric geometry in which all *units* formed out of the molecular rings and the underlying surface atoms are structurally and chemically different.

The simulated STM images indicate that the impact of the structural asymmetry onto the electronic properties of the hybrid molecule-surface system is confined to a small energy window around the Fermi energy. A comparison with the experimentally recorded STM images shows that the calculation is able to qualitatively correctly reproduce the observed shapes and relative intensities of the different molecular parts on the substrate. Moreover an inversion of the spin polarization above the molecule with respect to the surface over a large bias range of several eV around the Fermi energy was found in agreement with the general spin polarization inversion mechanism outlined for non-magnetic organic molecules on magnetic surfaces [19]. Even more importantly, the structural asymmetry was found to give rise to a variation of the spin polarization among the different molecular rings indicating a modulation of the spin polarization on an intramolecular length scale.

Furthermore, due to the structure of the TPT being made up of different molecular rings, magnetic units are formed out of these rings and the surface Fe atoms positioned below them. It is found that again due to the structural asymmetry of the hybrid molecule-surface system, those units show a different behavior with respect to their magnetic exchange coupling. When taking all these findings together they show that the structural asymmetric (chiral) system formed due to the adsorption of TPT onto the 2 ML Fe/W(110) surface causes an associated asymmetry in the electronic and magnetic properties. This might offer the possibility to create magnetic units below a molecule made up of different rings for which a certain unit could switch depending on the magnetic state of the other units ultimately leading to molecular based spin logic devices. In this respect the present results can be regarded as a step towards this direction establishing the concept of (magnetically) distinct units *within* a single molecule-surface hybrid structure.

9 Molecular Tuning of the Rashba Effect

In this chapter the question whether the idea of modifying surface magnetic properties by adsorption of molecules can also be extended to spin-orbit related effects is explored. The Rashba effect as a widely investigated spin-orbit phenomenon was selected for this case study. The $BiAg_2$/Ag(111) surface alloy and two molecules of opposite electronic character, NH_3 with a free electron pair (electronegative) and BH_3 with an empty p_z-orbital (electropositive), were chosen as materials specific examples to examine this issue. NH_3 shows a weak physisorption type bonding to the surface, which results in an increase of the outward buckling of the Bi surface atom out of the first layer. BH_3 on the other hand binds considerably closer to the surface so that a hybridization of the p_z-states of the Bi and B atoms gives rise to a weak chemisorption of the molecule. This chemisorption causes a strong inward relaxation of the Bi. Consequently, the surface states of the $BiAg_2$/Ag(111) surface alloy originating from Bi s- and p-states and forming one occupied and one unoccupied Rashba split surface state are significantly modified.

More precisely, NH_3 enhances the Rashba splitting of the occupied surface state by an amount that is comparable to the total Rashba splitting of the well-known Au(111) surface state, whereas the unoccupied Rashba-split surface state is only weakly modified. The investigation of the molecular-induced surface geometry reveals the enhancement of the splitting of this occupied surface state to be a consequence of the surface geometry change induced upon molecular adsorption. BH_3 on the contrary moves the occupied Rashba-split state into the bulk Ag band structure and causes an asymmetry of the unoccupied Rashba-split surface state along different $\mathbf{k}$*-directions ($\mathbf{k}_1$ and $\mathbf{k}_2$), i. e. it creates an anisotropy of the splitting in k-space. Moreover, the BH_3 adsorption is found to induce a spin splitting of a further unoccupied surface state, which is not Rashba-split in case of the clean surface. This induced splitting is confined to and varies in size between specific* $\mathbf{k}$*-directions and is related to the in-plane potential gradients caused by the BH_3-surface bonding. Hence, oppositely to the NH_3 case, these modifications of the surface states are outlined to mainly arise from the chemisorption of the BH_3 onto the surface.*

Finally, the spin polarization of the surface states is only slightly modified by the adsorption of NH_3 where the quantization axis is mainly kept in the plane of the surface in line with the Rashba model. On the contrary, in the BH_3 case the in-plane potential gradient caused by the molecular adsorption is so large as to induce a dominant out-of-plane spin polarization. Hence the original idea to generalize the molecular induced tuning to other surface magnetic effects than exchange turns out to be indeed promising and offers valuable new research prospects.

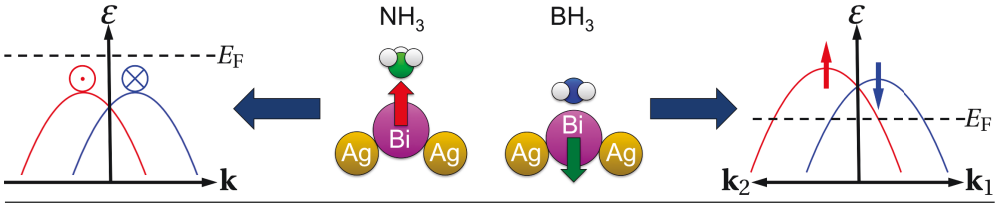

In the preceding chapters the influence of the molecular adsorption onto surface magnetic exchange interactions has been analyzed in detail. This chapter is concerned with generalizing the idea of the molecular-induced tuning to other surface magnetic properties than magnetic exchange coupling. The Rashba effect at the $BiAg_2$/Ag(111) surface alloy has been selected to investigate this issue. Before outlining the obtained results, a short introduction to the Rashba effect will be presented.

Introduction to the Rashba Effect

The original study on the Rashba effect goes back to the early contributions of Rashba [309] and later on of Bychkov and Rashba [310, 311] on the lifted spectral degeneracy in a 2D electron gas (2DEG). The effect can be rationalized based on a simple model for the 2DEG [312] as it can for instance be found in epitaxially grown III-V quantum-well heterostructures [313]. A schematic picture of such a heterostructure is depicted in Fig. 9.1. Due to the potential well in the strained $In_{0.77}Ga_{0.23}As$ layer a 2DEG is formed for which the electrons can be provided by an n^+ doped layer within the InP [313].

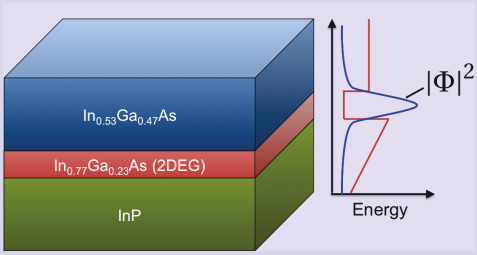

Figure 9.1.: Schematic representation of a III-V quantum-well heterostructure. The 2DEG forms due to a localization of the electron density ($|\Phi|^2$) within the potential well of the strained $In_{0.77}Ga_{0.23}As$ layer (based on a figure in Ref. [312]).

If one now works within a single-particle approach without an applied magnetic field and neglecting the electronic correlations, one obtains a simple kinetic energy Hamiltonian:

$$H_K = \frac{p^2}{2m^*}, \tag{9.1}$$

where m^* stands for the effective mass of the considered electrons. The eigenenergies are then naturally given by $\varepsilon(\mathbf{k}) = \frac{\hbar^2}{2m^*}\mathbf{k}^2$ with the eigenfunctions being plane waves. Due to space and time inversion symmetry each eigenvalue $\varepsilon_{\uparrow\downarrow}(\mathbf{k})$ is so far twofold degenerate for spin up and spin down electrons: $\varepsilon_\uparrow(\mathbf{k}) = \varepsilon_\downarrow(\mathbf{k})$ [312] meaning that the parabolic energy dispersions for the two electron spins lie on top of one another.

If now the potential in which the electrons move is inversion asymmetric as for instance in the above heterojunction, the spin-degeneracy is lifted and only the Kramer's degeneracy $\varepsilon_\uparrow(\mathbf{k}) = \varepsilon_\downarrow(-\mathbf{k})$, which is due to time inversion symmetry, remains. This can be understood when the effective potential $v_s(\mathbf{r})$ at the interface is expanded in a Taylor series which in lowest order yields [312]:

$$v_s(\mathbf{r}) \approx v_{s0} - e\mathbf{E}\cdot\mathbf{r} \tag{9.2}$$

showing that the inversion asymmetry at the interface is associated with an electric field $\mathbf{E} = -\frac{1}{e}\nabla v_s$. This electric field in the global reference frame transforms into a magnetic field $\mathbf{B}$ in the local frame of the electron [167]:

$$\mathbf{B} = -\frac{\hbar}{m^* c^2}\mathbf{k}\times\mathbf{E}. \tag{9.3}$$

The so-called Bychkov-Rashba Hamiltonian describing the interaction of this magnetic field with the magnetic moment of the electron is then given by [310, 311, 314]:

$$H_R = \alpha_R(|\mathbf{E}|)\vec{\sigma}\cdot(\mathbf{k}\times\hat{\mathbf{e}}), \tag{9.4}$$

where $\alpha_R = \alpha_R(|\mathbf{E}|) = \frac{\mu_B\hbar}{m^* c^2}|\mathbf{E}|$ is the material specific Rashba parameter, $\vec{\sigma}$ is the vector of Pauli matrices and $\hat{\mathbf{e}}$ is the direction of $\mathbf{E}$. This Hamiltonian does then give rise to the spin-splitting in the structure inversion asymmetric potential known as the Rashba effect [309–312].

More specifically, a 2DEG in the (x,y)-plane with an electric field in the z-direction $\hat{\mathbf{e}} = (0,0,1)$ can be considered for which the total Hamiltonian can be expressed as [312]:

$$H = H_K + H_R = \frac{\mathbf{p}_\parallel^2}{2m^*} + \frac{\alpha_R}{\hbar}(\vec{\sigma}\times\mathbf{p}_\parallel)_{|z} = \frac{\mathbf{p}_\parallel^2}{2m^*} + \frac{\alpha_R}{\hbar}(\sigma_x p_y - \sigma_y p_x), \tag{9.5}$$

where $\mathbf{p}_\parallel = (p_x, p_y, 0)$ is the momentum in the (x,y)-plane. The eigenfunctions of this Hamiltonian can be written as the product of a plane-wave and a 2D spinor [312]:

$$\phi_{\uparrow\downarrow\mathbf{k}_\parallel}(\mathbf{r}_\parallel) = \frac{e^{i\mathbf{k}_\parallel\cdot\mathbf{r}_\parallel}}{2\pi}\frac{1}{\sqrt{2}}\begin{pmatrix} ie^{-i\varphi/2} \\ \pm e^{i\varphi/2}\end{pmatrix}, \tag{9.6}$$

where $\mathbf{r}_\parallel = (x,y,0)$ and $\mathbf{k}_\parallel = (k_x, k_y, 0) = k_\parallel(\cos\varphi, \sin\varphi, 0)$ are real-space and reciprocal space vectors in the (x,y)-plane, respectively. Finally, the eigenvalues are expressed as

[312]:

$$\varepsilon_{\uparrow\downarrow}(\mathbf{k}_\parallel) = \frac{\hbar^2}{2m^*}\mathbf{k}_\parallel^2 + \alpha_R(\vec{\sigma}\times\mathbf{k}_\parallel) = \frac{\hbar^2}{2m^*}\mathbf{k}_\parallel^2 \pm \alpha_R|\mathbf{k}_\parallel| = \frac{\hbar^2}{2m^*}(\mathbf{k}_\parallel \pm k_{SO})^2 - \Delta_{SO}, \tag{9.7}$$

where the shift of the energy curves from the origin is $k_{SO} = m^*\alpha_R/\hbar^2$, the spin-orbit lowering is given by $\Delta_{SO} = m^*\alpha_R^2/(2\hbar^2)$ and the '+' applies to the spin up (↑) solution whereas the '−' applies to the spin down (↓) solution defined with respect to a local spin quantization axis. This solution shows that the energy dispersion is characterized by two shifted parabolas in $k_\parallel$-space (see Fig. 9.2) - one for each spin -, meaning that besides for $k_\parallel = 0$ ($\bar{\Gamma}$) the spin degeneracy is indeed lifted. The energetic spin-splitting is linear in $k_\parallel$: $\varepsilon_\uparrow(\mathbf{k}_\parallel) - \varepsilon_\downarrow(\mathbf{k}_\parallel) = 2\alpha_R k_\parallel$. Moreover the Rashba energy is defined as the energy difference between the extremum of the parabolas and the value at $\bar{\Gamma}$, i. e. $E_R = \hbar^2 k_{SO}^2/2m^*$ [315]. It can further be shown that the spin quantization axis is always in the plane of the 2DEG and perpendicular to $\mathbf{k}_\parallel$ which eventually means that ↑-states turn into ↓-states if one transforms $\mathbf{k}_\parallel$ to $-\mathbf{k}_\parallel$ (Kramer's degeneracy) [312]. The continuous change of the spin direction is indicated at the top of the parabolas in Fig. 9.2(b). Remarkably, on the basis of the Rashba effect a spin field effect transistor was suggested by Datta and Das [16] as an external gate voltage in addition to the interface field could be used to adjust the spin direction with which electrons are injected into a FM contact after propagating in the gate.

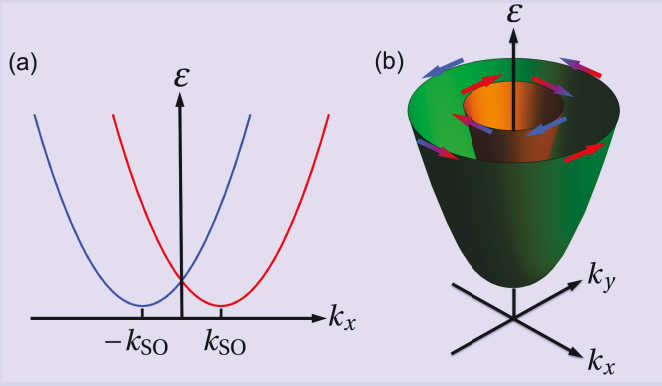

Figure 9.2.: The energy dispersion for the electrons of the 2DEG according to Equation (9.7) along the k_y axis (a) and in perspective view over the 2D k-space (b).

Nevertheless the above mentioned model provides a slightly oversimplified picture of the behavior of real materials. In principle, a microscopic theory is required since SOC is

at the origin of the Rashba effect [312]. In this framework, *ab initio* methods are of special importance as they can treat the electronic structure caused by the inversion asymmetric potential from first principles. It turned out that the size of the spin-splitting in the inversion asymmetric potential depends essentially on the asymmetry of the wave function close to the nuclei [316] which was revealed when studying Rashba split surface states.

A surface state can be regarded as a special representative of a 2DEG as it is localized in the surface region. In addition, a surface always breaks the inversion symmetry so that a gradient of the effective potential at the surface exists which results in a Rashba type term in the Hamiltonian. From a simple free electron model one would however only expect a Rashba splitting in energy of the order of μeV being unobservable experimentally [312]. However in 1996 a spin splitting of the surface state of a Au(111) surface brought about by SOC was observed which was of the order of 0.1 eV ($k_{SO} \approx 0.012$ Å^{-1}) [317]. In contrast, for other surfaces as Ag(111) or Cu(111) no splitting was found which could neither be explained by the difference in SOC strength nor by the potential gradients at the surface [312]. At first it turned out that the majority contribution leading to the splitting of the Au(111) surface state comes from the surface layer with a strong localization in the core region [316]. Therefrom it could be concluded that what really matters is the asymmetry of the surface state wave function in this core region. One way to quantify this asymmetry of the wave function is to analyze the l character of the surface state, i. e. how much polarized for instance a p-surface state is by a d contribution [312]. The interpretation of this is that the potential gradient distorts the surface state wave function and thereby polarizes it with other l contributions. If one now looks at the ratio of the l to the $l \pm 1$ contribution of the surface states one finds that this $p-d$ ratio is 9.5 for Ag(111) compared to 3.3 for Au(111) signalizing that the Au(111) p surface state is much more asymmetric, i. e. polarized by the d contribution [316]. This gives a physical and at the same time very useful explanation for the stronger Rashba-splitting at Au(111).

Based on the aforementioned findings there is ongoing research to find new surfaces with enhanced Rashba splittings and preferable properties for spintronic applications. For the low index surfaces of Bi large Rashba splittings of $k_{SO} \geq 0.04$ Å^{-1} have been reported by a combined experimental and theoretical study [318]. For the Lu(0001) surface a Rashba splitting of $k_{SO} \approx 0.011$ Å^{-1}/0.043 Å^{-1} was proposed theoretically at the $\overline{\Gamma}$ and $\overline{\mathrm{M}}$ points of the surface BZ, respectively [316]. Even at the magnetic Gd(0001) surface a Rashba effect has been found which could be tuned by oxidation [319]. According to the explanation that the Rashba splitting is determined by the asymmetry of the surface state wave function, surfaces with an enhanced Rashba splitting could be synthesized due to a surface alloying technique [315, 320] which could even be detected using STS [321].

The surface alloys of $PbAg_2$/Ag(111) and $BiAg_2$/Ag(111) showed a 'giant' spin splitting of $k_{SO} = 0.11$ Å^{-1} and $k_{SO} = 0.13$ Å^{-1}, respectively [315, 320] which was well reproduced by a theoretical investigation using a full-potential method [314]. Furthermore the Rashba splitting of $k_{SO} = 0.038$ Å^{-1} of an Ir(111) surface was reported to be stable under Gr in air [322] and a Rashba splitting in Gr was observed due to the hybridization with an Au layer on top of Ni(111) [323]. For the molecular systems C_{60}, iron octaethylporphyrin (FeOEP) and 3, 4, 9, 10-perylene-tetracarboxylic acid (PTCDA) angle resolved photoemission spectroscopy (ARPES) measurements indicated chemical inertness of the Rashba splitting at the $BiAg_2$/Ag(111) surface due to a weak molecule-surface interaction [324].

9.1. Presentation of the Molecular Species

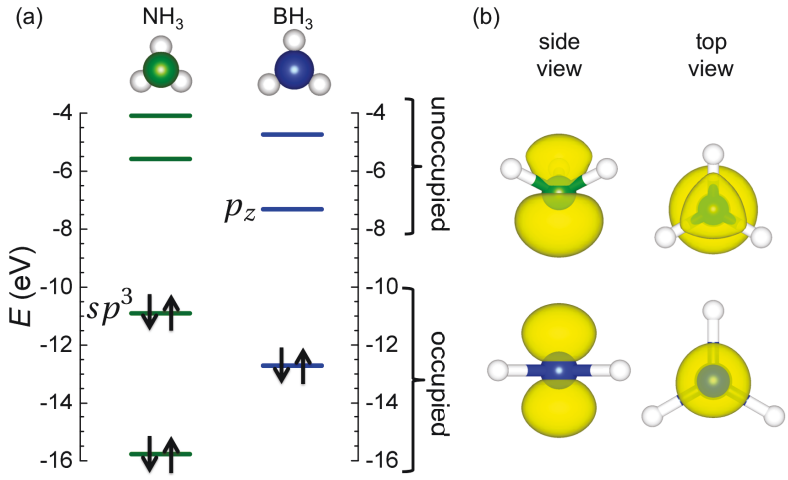

Figure 9.3.: Energy level diagram (a) and isosurface plots of the charge density of the HOMO/LUMO for NH_3/BH_3 in side and top view (b). The HOMO of NH_3 is a free electron pair in an sp^3-like orbital (upper part in (b)) and the LUMO of BH_3 is an empty p_z-like state (lower part in (b)). The occupation of the states is marked by arrows. Note that the HOMO of each molecule is aligned at the calculated IP of 10.91 eV and 12.71 eV for NH_3 and BH_3, respectively. The isosurface plots were made for an isovalue of $2.02 \cdot 10^{-1}$ e/Å^3. Color code for atoms same as in Fig. 5.2.

To investigate the adjustability of the Rashba effect, two molecules with opposite electronic character have been chosen. The ammonia molecule (NH_3) has a non-planar geometry because, as the energy level diagram in Fig. 9.3(a) shows, the HOMO is a free electron pair in an sp^3-like state at the nitrogen (see top row in Fig. 9.3(b)) which electronically repels the other N-H bonds leading to a pyramidal structure. For molecules containing nitrogen it is known

that this lone pair plays an important role in determining the bonding to a surface [325]. On the other hand in case of the borane molecule (BH_3) the structure is planar since here the LUMO is an empty p_z-like state (see Fig. 9.3(a) and second row in (b)) with symmetric density distribution on both sides of the plane formed by the B and H atoms. Due to this hypovalency (lack of valence electrons) of the borane it has a strong tendency to form diborane (B_2H_6) [281]. Based on this opposite electronic character of the two molecules a considerable difference in their interaction with surfaces is to be expected which will be investigated in this chapter for the adsorption on the $BiAg_2$/Ag(111) surface alloy.

9.2. Presentation of the Clean Surface Alloy

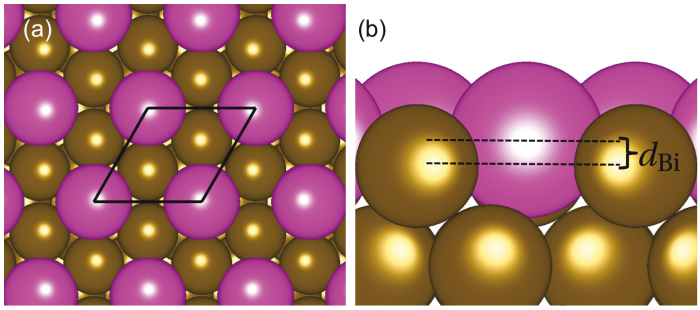

Figure 9.4.: Top (a) and side (b) view of the clean $BiAg_2$/Ag(111) surface alloy. The in-plane $(\sqrt{3} \times \sqrt{3})R30°$ surface unit cell is marked by the black parallelogram in (a). In (b) the outward buckling of the Bi out of the surface is labeled by d_{Bi}. Color code of the surface atoms: magenta for Bi and brown for Ag.

In the long-range ordered $BiAg_2$/Ag(111) surface alloy one third of the Ag atoms of the uppermost layer are replaced by Bi (see Fig. 9.4(a)) which can be experimentally achieved by Bi deposition onto a Ag(111) surface under ultrahigh vacuum conditions [315]. This surface alloying considerably alters the hybridization of the electronic states at the surface and hence gives rise to a new surface electronic structure compared to clean Ag(111). Remarkably, the larger size of the Bi atom with respect to the Ag surface atoms leads to an outward buckling of the Bi out of the surface denoted by d_{Bi} (see Fig. 9.4(b)). Due to this outward buckling the polarization of the Bi derived surface states is quite strong and leads to a larger ('giant' [315]) Rashba splitting compared to a Bi(111) surface [314].

In view of the later study of the adsorption of NH_3 and BH_3 on the $BiAg_2$/Ag(111) surface, the band structure of the clean surface has been calculated with different approaches for which the results are summarized in Fig. 9.5. Furthermore, in Table 9.1 the Bi bucklings and the Rashba splittings are listed for the different methods and in Table 9.2 the effective

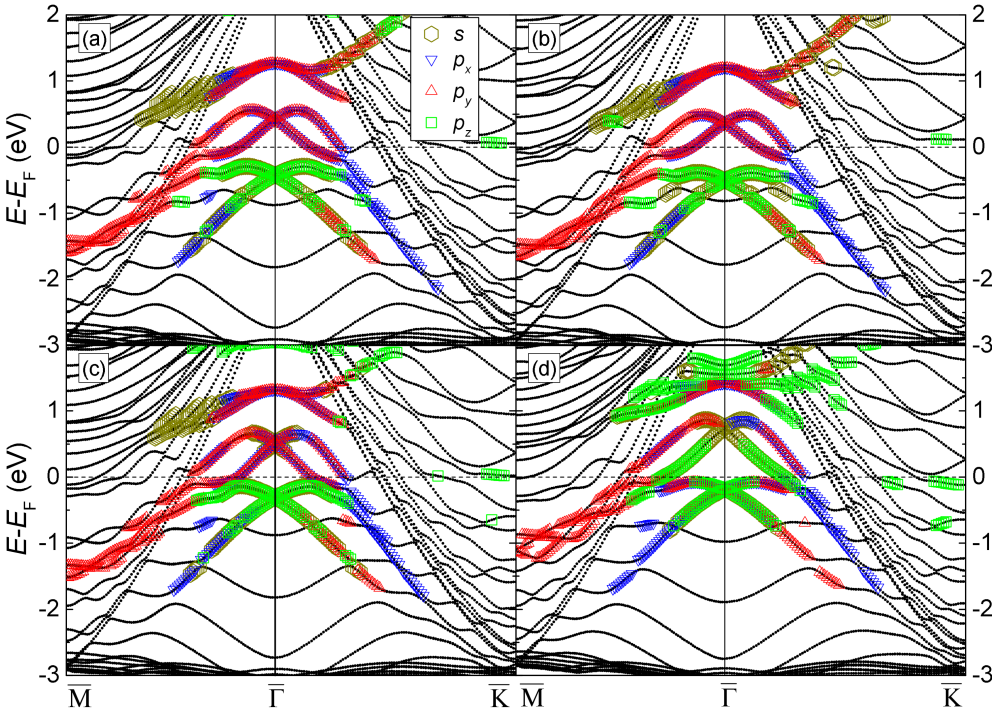

Figure 9.5.: Comparison of the band structures calculated for the clean $BiAg_2$/Ag(111) surface alloy using different functionals: (a) band structure calculated with PBE including SOC for a geometry optimized with PBE without SOC, (b) band structure calculated with PBE including SOC for a geometry optimized with rev-vdW-DF2 without SOC, (c) band structure calculated with PBE including SOC for a geometry optimized with PBE with SOC and (d) band structure calculated with PBE including SOC for a geometry optimized with rev-vdW-DF2 with SOC. In each case the s-, p_x-, p_y- and p_z-orbital contributions (of at least 0.08 e in the PAW spheres) of states mainly located at the surface are plotted on top of the band structure.

masses and Rashba parameters as obtained from a quadratic fit of the respective surface states in the band structure are given together with the Rashba energies. In the first case (Fig. 9.5(a)) the structural relaxation was performed within a non spin-polarized PBE calculation. Afterwards a self-consistent density was calculated for this relaxed geometry with PBE including SOC (PBE+SOC). Using this density the band structure was then calculated along the $\overline{M} \rightarrow \overline{\Gamma} \rightarrow \overline{K}$ path of the surface BZ within the PBE+SOC framework[1]. In the second approach (Fig. 9.5(b)) essentially the same procedure was applied but in this case the relaxation was done using the rev-vdW-DF2 functional. The third case (Fig. 9.5(c)) is distinct from the

[1]Notably, it was found that the band structure calculated with PBE+SOC shows only very small differences whether a self-consistent density of a PBE+SOC or a pure PBE calculation was used.

first in that SOC has already been included during the structural relaxation with PBE+SOC. In the last case (Fig. 9.5(d)) SOC was used together with rev-vdW-DF2 during the relaxation (rev-vdW-DF2+SOC). As can be seen from Fig. 9.5 all approaches yield at first sight band structures with qualitatively similar properties in agreement with experimental [315] and previous theoretical results [314]. There are two Rashba split surface states for which the lower one is occupied and has mainly s, p_z-character whereas the upper one is in the unoccupied region of the band structure being mainly derived from p_x- and p_y-states of the surface layer atoms. In all cases the Rashba splitting in k-space ($2k_{SO}$) is larger for the occupied state.

Table 9.1.: Calculated Bi buckling d_{Bi} and Rashba splittings $k_{SO}^{occ/unocc}$ for the clean $BiAg_2$/Ag(111) surface alloy using different methods.

method		d_{Bi}	k_{SO}^{occ}	k_{SO}^{unocc}
relaxation	band structure	(Å)	(Å^{-1})	(Å^{-1})
PBE	PBE+SOC	0.64	0.10	0.08
rev-vdW-DF2	PBE+SOC	0.61	0.09	0.08
PBE+SOC	PBE+SOC	0.75	0.12	0.08
rev-vdW-DF2+SOC	PBE+SOC	0.96	0.10	0.07

More specifically, the PBE relaxation for the band structure in Fig. 9.5(a) leads to an outward buckling of the Bi by $d_{Bi} = 0.64$ Å giving rise to Rashba splittings of $k_{SO}^{occ} = 0.10$ Å^{-1} and $k_{SO}^{unocc} = 0.08$ Å^{-1} for the occupied and unoccupied surface states, respectively. When the rev-vdW-DF2 is used during the relaxation, the outward buckling is diminished to $d_{Bi} = 0.61$ Å reducing the first splitting to $k_{SO}^{occ} = 0.09$ Å^{-1} but yielding the same $k_{SO}^{unocc} = 0.08$ Å^{-1}. This is an expected behavior since the vdW interaction is attractive in most cases. Including SOC during the relaxation with PBE slightly enhances the outward buckling in the third case to $d_{Bi} = 0.75$ Å which is associated with an increase of k_{SO}^{occ} to 0.12 Å^{-1} but again does not affect the k_{SO}^{unocc} amounting to 0.08 Å^{-1}. These results are in good agreement with the experimentally determined splitting of $k_{SO}^{occ} = 0.13$ Å^{-1} using ARPES [315] and previous theoretical investigations yielding $k_{SO}^{occ} = 0.13$ Å^{-1} and $d_{Bi} = 0.85$ Å [314]. In the theoretical work [314] it was also outlined that the inclusion of SOC during the relaxation has only a small influence on the geometry, i. e. on the outward buckling of the Bi, in agreement with the present finding that in the third approach during the relaxation the outward buckling is only increased by 0.11 Å compared to the first case.

However when SOC is included during the relaxation with rev-vdW-DF2 in the fourth approach the outward buckling strongly increases to $d_{Bi} = 0.96$ Å which marks an enhancement by 0.35 Å (57%) compared to the relaxation without SOC in the second approach. The resulting Rashba splittings are however not increased as strongly and amount to $k_{SO}^{occ} = 0.10$ Å^{-1} and $k_{SO}^{unocc} = 0.07$ Å^{-1}. In addition, also the orbital character of the two Rashba split surface

states especially close to $\overline{\Gamma}$ is qualitatively different in this case, i. e. no significant *s* character is found for the occupied state whereas the unoccupied state has mainly *s* character. This physically unexpected behavior hints to the finding that rev-vdW-DF2 is not suited to be used together with SOC. This conclusion is further supported by the fact that rev-vdW-DF2 has been constructed for spin unpolarized systems and only very recently a spin dependent version of the vdW-DF has emerged [106]. Therefore rev-vdW-DF2 was not used in conjunction with SOC in the further calculations as the results obtained by this approach are regarded as unphysical.

When one however analyses the results obtained with the other three approaches one finds the correlation that a stronger outward buckling of the Bi leads to an increased Rashba splitting of the occupied surface state $k_{\mathrm{SO}}^{\mathrm{occ}}$ but leaves the splitting of the unoccupied state $k_{\mathrm{SO}}^{\mathrm{unocc}}$ unaffected. This is also consistent with the pronounced increase of the associated Rashba parameter $\alpha_{\mathrm{R}}^{\mathrm{occ}}$ whereas $\alpha_{\mathrm{R}}^{\mathrm{unocc}}$ remains merely constant in Table 9.2. Consequently, also the Rashba energy $E_{\mathrm{R}}^{\mathrm{occ}}$ increases from the second over the first to the third case with $E_{\mathrm{R}}^{\mathrm{unocc}}$ showing only minor changes[2]. This correlation will be of special importance for the results obtained for NH_3 and BH_3 adsorbed on the surface.

Table 9.2.: Effective masses $m^{*,\mathrm{occ}}$ and $m^{*,\mathrm{unocc}}$, Rashba parameters $\alpha_{\mathrm{R}}^{\mathrm{occ}}$ and $\alpha_{\mathrm{R}}^{\mathrm{unocc}}$ and Rashba energies $E_{\mathrm{R}}^{\mathrm{occ}}$ and $E_{\mathrm{R}}^{\mathrm{unocc}}$ of the two Rashba split surface states for the $BiAg_2$/Ag(111) surface alloy. The effective masses and Rashba parameters were deduced from a quadratic fit of the respective surface states in the band structure whereas the Rashba energies are directly accessible from the band structures.

method		$m^{*,\mathrm{occ}}$	$m^{*,\mathrm{unocc}}$	$\alpha_{\mathrm{R}}^{\mathrm{occ}}$	$\alpha_{\mathrm{R}}^{\mathrm{unocc}}$	$E_{\mathrm{R}}^{\mathrm{occ}}$	$E_{\mathrm{R}}^{\mathrm{unocc}}$
relaxation	band structure	(m_e)	(m_e)	(eVÅ)	(eVÅ)	(eV)	(eV)
PBE	PBE+SOC	−0.25	−0.16	−3.00	−3.89	−0.13	−0.13
rev-vdW-DF2	PBE+SOC	−0.28	−0.17	−2.49	−3.71	−0.11	−0.12
PBE+SOC	PBE+SOC	−0.22	−0.14	−4.16	−4.27	−0.18	−0.14
rev-vdW-DF2+SOC	PBE+SOC	−0.36	−0.13	−2.11	−3.99	−0.10	−0.11

Furthermore also the spin polarization of the states in the band structure calculated with the second approach has been analyzed as depicted in Fig. 9.6. In Fig. 9.6(a) the in-plane spin polarization is visualized on top of the band structure meaning that the spin quantization axis was chosen perpendicular to both the surface normal and the respective in-plane $\mathbf{k}_{\parallel}$ direction. In general a large in-plane spin polarization reaching values up to about 70% for the occupied states directly accessible by spin polarized ARPES is observed and the results are in good agreement with Ref. [314]. More precisely, for the occupied surface state around $\overline{\Gamma}$ the two shifted energy parabolas show opposite spin polarization consistent with the Rashba

[2]Notably, regarding the values listed in the last row of Table 9.2, the different qualitative behavior of the fourth approach becomes once more evident.

model. However the physical picture is a bit more complicated in case of the unoccupied Rashba split surface state where the spin polarization is in general small around $\overline{\Gamma}$ and even changes sign at small k away from $\overline{\Gamma}$ in both directions. At higher momentum the strong in-plane spin polarization of the upper branch of these states is reestablished. More specifically, as already noted in Ref. [314] the surface state at about 1 eV above the Fermi level is split by higher order terms in k also giving rise to a sizable spin polarization away from $\overline{\Gamma}$. The first and second unoccupied surface states were outlined to be coupled to $m_j = \pm\frac{1}{2}$ and $m_j = \pm\frac{3}{2}$ states due to atomic-like SOC, respectively [314].

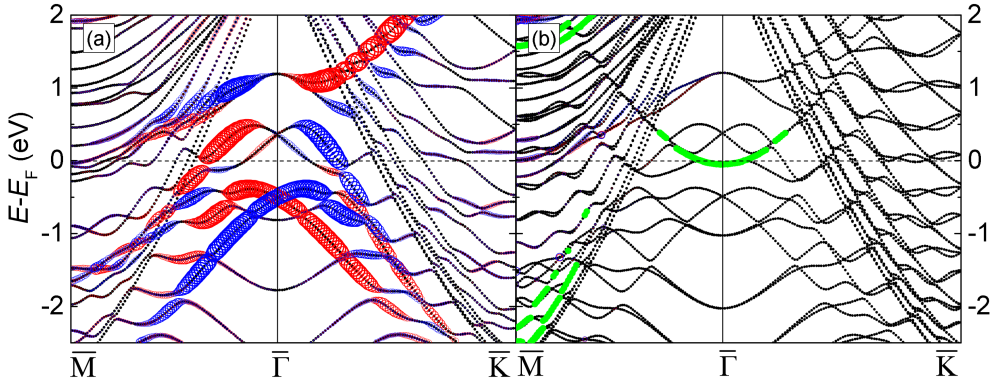

Figure 9.6.: In-plane (a) and out-of-plane (b) spin polarizations of the clean $BiAg_2$/Ag(111) surface alloy. Positive (negative) spin polarization larger than 2% is indicated in red (blue) and the size of the symbols indicates the degree of spin polarization. In (a) the spin quantization axis is chosen perpendicular to both the surface normal and the respective in-plane $\mathbf{k}_\parallel$ direction. In (b) states predominantly localized at the clean Ag side of the asymmetric slab (at least 0.1 e in the PAW spheres) are marked in green.

In Refs. [315, 326] it was noted that the surface alloying with Bi also gives rise to an in-plane gradient in the surface potential which on the one hand was outlined to significantly contribute to the large Rashba splitting and on the other hand to generate an out-of-plane spin polarization in the direction normal to the surface. In Fig. 9.6(b) the out-of-plane spin polarization is depicted for an asymmetric ten-layer slab which was made up of a clean Ag(111) surface on one side and the $BiAg_2$/Ag(111) surface alloy on the other side. This alternative geometry was used in order to check the position and splitting of the surface states with respect to the structure of the slab. Firstly, the surface state band structure is practically identical to the results obtained in case of the symmetric slab and the Ag(111) surface state around $\overline{\Gamma}$ is marked in green whose shape and energetic position is in good agreement with Ref. [314]. Notably, no out-of-plane spin polarization is observed along the $\overline{\Gamma}\overline{\mathrm{K}}$ direction which is a consequence of the fact that the second surface layer shows mirror symmetry with respect to this

direction and that the state is localized at the surface. Hence no (in-plane) potential gradients perpendicular to this direction exist and therefore no out-of-plane spin polarization is observed. However in case of the $\overline{\Gamma M}$ direction this symmetry argument does not hold and consequently a finite out-of-plane polarization of a few percent is observed.

9.3. Adsorption Geometries and Structural Properties

When investigating the adsorption of NH_3 and BH_3 on the $BiAg_2$/Ag(111) surface alloy it turned out that the PBE functional does not properly bind the NH_3 molecule to the surface as the structural relaxation resulted in geometries with H atoms pointing towards the surface in discrepancy with the findings outlined in Chapters 6, 8 and Appendix B. Therefore the rev-vdW-DF2 functional was used in a non-spin polarized calculation to relax the molecule-surface systems. A ML coverage of the molecules was modeled by adsorbing one NH_3 or BH_3 molecule into the $(\sqrt{3} \times \sqrt{3})R30°$ in-plane surface unit cell. The four initial adsorption geometries are depicted in Fig. 9.7 for the exemplary case of NH_3. The molecular N can either be put on top of a Ag or Bi atom (Ag-top and Bi-top sites in Fig. 9.7(a) and 9.7(b), respectively), into a bridge site between two Ag atoms (see Fig. 9.7(c)) or in a hollow site between two Ag and one Bi atom (see Fig. 9.7(d).).

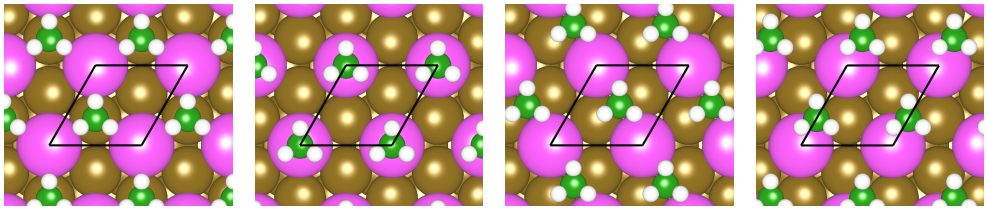

(a) Ag-top site (b) Bi-top site (c) bridge site (d) hollow site

Figure 9.7.: Investigated adsorption sites for NH_3 and BH_3 on the $BiAg_2$/Ag(111) surface alloy for the exemplary case of NH_3. The unit cell of each structure is marked by the black parallelogram.

In the ground state geometry of NH_3 on the surface the N atom adsorbs in an fcc hollow site whereas for BH_3 the B adsorbs in an hcp hollow site as can be seen in the relaxed structures depicted in Fig. 9.8. The bridge sites are not stable and the molecules move into their respective hollow site when the relaxation is started from this position. The adsorption energies for the different stable adsorption positions are given in Table 9.3. From these values it becomes clear that both molecules are rather weakly bonded to the surface which is especially true for NH_3 for which the largest adsorption energy of 0.23 eV points to a physisorption type bonding mechanism. The slightly higher values in case of BH_3 ranging up to 0.50 eV hint to a

chemical contribution to the binding, i. e. weak chemisorption of this molecule. This picture of a qualitatively different local bonding of the two molecular species to the surface is further supported by the side views presented in Fig. 9.8(c) and (d) where the significantly larger distance of NH_3 to the surface compared to BH_3 (2.83 Å vs. 2.03 Å) can be clearly seen. More specifically, the molecule-surface distances included in Table 9.4 outline that the N center of NH_3 is at least 0.6 Å farther away from the surface Bi/Ag atoms than the B center of BH_3. As a side remark, the distances of the H atoms to the surface are at least 3.21 Å for NH_3 and 2.39 Å for BH_3. These observations are in line with the previous finding that the $BiAg_2$/Ag(111) surface alloy is relatively inert concerning molecular adsorption [324].

Table 9.3.: Calculated adsorption energies E_{ads} for NH_3 and BH_3 adsorbed on the $BiAg_2$/Ag(111) surface alloy for the different stable adsorption sites. The adsorption energy is defined as in Equation 5.1.

position	E_{ads} (eV)	
	NH_3	BH_3
hollow site	**0.23**	**0.50**
Ag-top site	0.20	0.35
Bi-top site	0.10	0.43

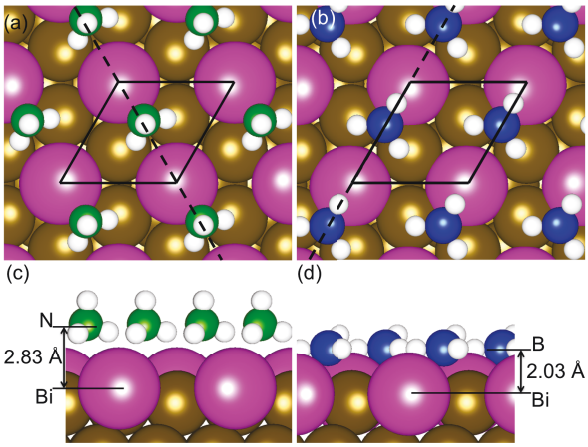

Figure 9.8.: Ground state geometries for NH_3 and BH_3 on the $BiAg_2$/Ag(111) surface alloy in top view (a, b) and side view (c, d), respectively. The unit cell of each structure is marked by the black parallelogram in the respective top view. The dashed lines in (a) and (b) indicate the cuts along which the charge density difference plots in Fig. 9.10 and the visualization of the surface states in Fig. 9.15 were made.

An especially important influence that both molecules exert onto the surface is the structural change of the surface geometry they induce, i. e. how they modify the outward buckling

of the Bi out of the first surface layer as presented in Table 9.4. Due to the interaction of NH_3 with the surface, the Bi is pulled out of the surface to $d_{Bi}^{NH_3}$ = 0.67 Å which compared to the clean surface buckling of 0.61 Å marks a ≈10% enhancement. On the contrary, the BH_3 adsorption leads to a strong ≈40% inward relaxation of the Bi to $d_{Bi}^{BH_3}$ = 0.37 Å. In view of the correlation between the size of the Rashba splitting of the occupied surface state and the degree of the outward buckling of the Bi mentioned in Section 9.2, these results raise the expectation that the Rashba splitting of the $BiAg_2$/Ag(111) surface alloy can indeed be tuned by the adsorption of the two molecular species NH_3 and BH_3.

Table 9.4.: Outward buckling of the Bi d_{Bi} and molecule-surface distances for NH_3 and BH_3 on the $BiAg_2$/Ag(111) surface alloy.

system/surface	distances (Å)		
	d_{Bi}	N/B-Bi	N/B-Ag
clean surface	0.61	-	-
NH_3	0.67	3.46	3.85
BH_3	0.37	2.85	2.86

9.4. Charge Density Difference and Electrostatic Potential

The bonding of the two molecules to the $BiAg_2$/Ag(111) surface can be further characterized when looking at the electronic properties. In Fig. 9.9(a) the integrated total charge density (of the valence electrons) is displayed for the two hybrid systems and the clean $BiAg_2$/Ag(111) surface alloy. The vertical lines indicate the positions of the second layer Ag, first layer Bi and the molecular B and N atoms. Here the slight outward relaxation of the surface Bi in the NH_3 case and the inward relaxation in the BH_3 case can be clearly seen since the position of the second layer Ag atoms differs by less than 10 mÅ in all three cases. Obviously, the N center of NH_3 is much farther away from the surface than the B center of BH_3 in their respective systems. Most remarkably, in the NH_3 case the charge density between the molecule and the surface nearly goes to zero at around 30.5 Å with respect to the scale given along the abscissa of the diagram. This indicates that practically no bonding between the two systems takes place which is in line with the proposed physisorption of this molecule on the surface outlined in Section 9.3. In the BH_3 case however the situation is different since here a significant charge density is found between molecule and surface at around 30 Å. This is indicative of overlapping charge density distributions derived from the surface and the molecule and therefore clearly points to a molecule-surface bonding (chemisorption) in this system. Notably, also

the height of the first surface layer charge density peak at around 28.5 Å varies between the systems. This is a direct consequence of the different Bi buckling with respect to the two first layer Ag atoms.

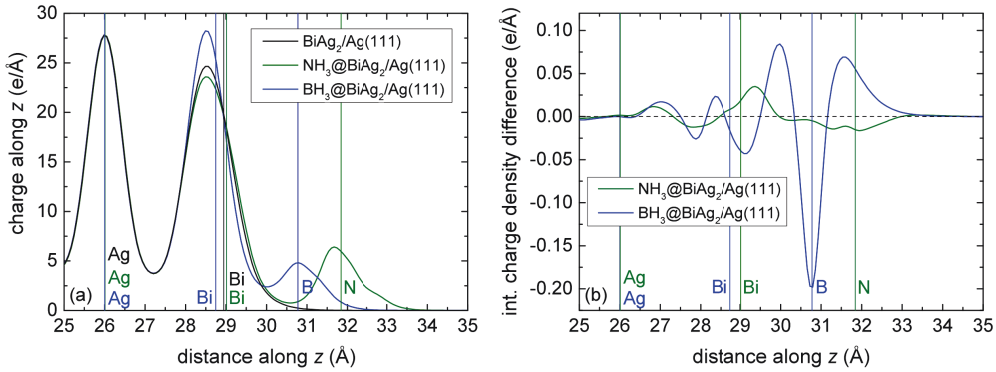

Figure 9.9.: Integrated total charge density (a) and charge density difference (b) of the valence electrons displayed along the z direction perpendicular to the surface for NH_3 and BH_3 on $BiAg_2/Ag(111)$. The lines in the figures indicate the positions of the respective second layer Ag, first layer Bi, B and N centers along z. As a reference in (a) also the integrated total charge density for the clean $BiAg_2/Ag(111)$ surface is shown. For clarity the positions of the first layer Ag atoms are not indicated.

Further inside can be gained when the charge density difference $n_{\text{diff}}(\mathbf{r})$ is considered which is defined as:

$$n_{\text{diff}}(\mathbf{r}) = n_{\text{sys}}(\mathbf{r}) - (n^{\text{SCF}}_{\text{surf}}(\mathbf{r}) + n^{\text{SCF}}_{\text{mol}}(\mathbf{r})), \tag{9.8}$$

where $n_{\text{sys}}(\mathbf{r})$ is the charge density of the hybrid system, $n^{\text{SCF}}_{\text{surf}}(\mathbf{r})$ stands for the charge density of the isolated surface and $n^{\text{SCF}}_{\text{mol}}(\mathbf{r})$ represents the charge density of the isolated molecule. The charge densities of the two latter systems were obtained by removing the respective coordinates of the other system from the hybrid geometry and performing a single self-consistent field (SCF) calculation. The obtained charge density differences on the (110) and (100) planes[3] (each marked by dashed lines in Fig. 9.8) for the NH_3 an BH_3 based hybrid systems, respectively, are presented in Fig. 9.10. Clearly, the charge reorganization in the hybrid system is much stronger in the BH_3 case as compared to the NH_3 case. The small charge redistribution in the NH_3 based system once more indicates physisorption. On the other hand, as shown in Fig. 9.10(b), in the BH_3 based hybrid system there is a strong charge accumulation close to the molecular B center in the shape of a p_z-like orbital. In Section 9.1 it was stated that essentially this p_z-state at the B forms the LUMO of the isolated BH_3 molecule. The charge accumulation in this state within the hybrid system nicely reflects the tendency of B to form additional bonds using this orbital. However it is noted that no significant net charge accu-

[3] These planes are defined with respect to the basis vectors of the surface unit cell.

mulation at the BH_3 site is found according to the charges within the PAW spheres around the atomic centers and when integrating the charge density difference over the molecular part.

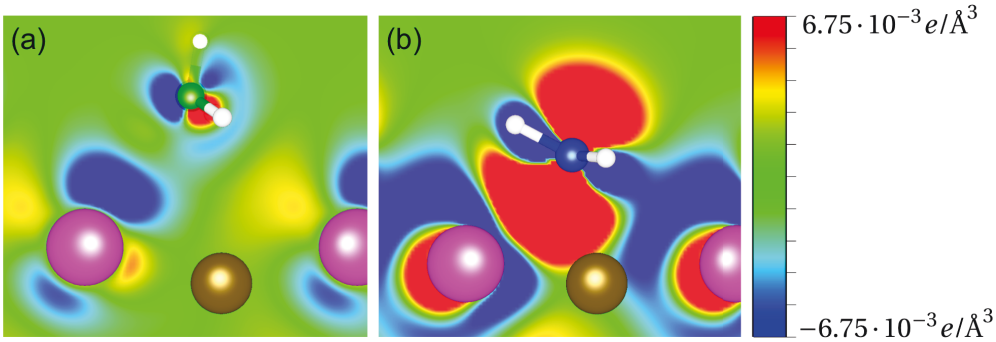

Figure 9.10.: Charge density difference on the (110) and (100) planes marked as dashed lines in Fig. 9.8 for NH_3 (a) and BH_3 (b) on the $BiAg_2$/Ag(111) surface alloy, respectively.

When integrating $n_{\text{diff}}(\mathbf{r})$ over the plane of the surface ((x,y)-plane) and displaying it along the z-axis an even more explicit information about the net charge accumulation and depletion along the surface normal is revealed as presented in Fig. 9.9(b). There the considerably stronger charge redistribution for the BH_3 based hybrid system with respect to the NH_3 based hybrid system is ultimately proven. Precisely at the position of the B a strong reduction of the electron density is observed whereas above and below a pronounced gain of electronic charge is observed reflecting the p_z shape seen in Fig. 9.10(b). This means that large parts of the in-plane charge within the plane formed out of B and the attached H atoms is moved into a region perpendicular to this plane. This is favorable since the bonding of the B derived p_z-state with states of the surface allows for a better delocalization of the electrons. In addition, in the region directly above the Bi at around 29 Å a net charge loss is observed in the BH_3 case whereas in the NH_3 case a net charge gain is observed at around 29.5 Å. This means, with respect to the clean surface, the BH_3 adsorption pulls charge out of the surface region increasing the surface/interface dipole whereas the NH_3 pushes the charge into the surface reducing the dipole.

These findings are in line with the observed work function change due to the molecular adsorption as depicted in Fig. 9.11. In Fig. 9.11(a) the electrostatic potential (potential of the ions plus the Hartree potential) of each system approaches an asymptotic value for large z-distances above the surface which was aligned at the calculated work function by setting the Fermi energy of each system to zero. In Fig. 9.11(a) clearly the clean surface work function of 4.1 eV[4] is reduced in the NH_3 based hybrid system to 3.2 eV whereas it is enhanced to 5.0 eV in case of the BH_3 based hybrid system. In Fig. 9.11(b) the electrostatic potentials of

[4]This value of the clean surface work function is in reasonable agreement with the experimental value of 4.5-4.6 eV given in Ref. [327].

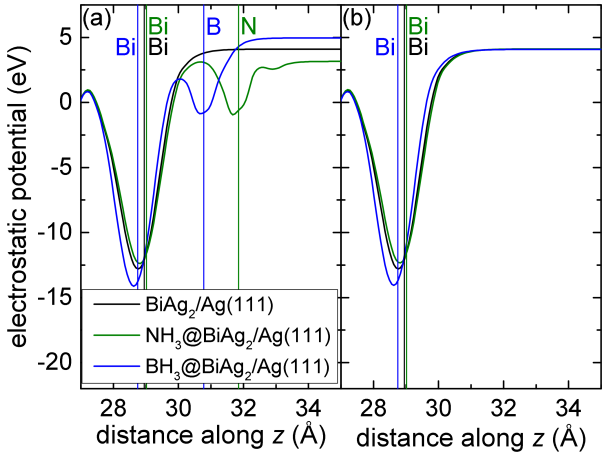

Figure 9.11.: Electrostatic potentials of the hybrid molecule-surface systems (a) and the molecular-induced geometries (b) for NH_3 and BH_3 on the $BiAg_2$/Ag(111) surface alloy. The vertical lines in the figures indicate the positions of the respective first layer Bi, B and N centers along z. As a reference in (a) and (b) also the electrostatic potential of the clean $BiAg_2$/Ag(111) surface alloy is included. Note that in each case the asymptotic value of the potential for large z-distances represents the calculated work function. For clarity in both diagrams the positions of the first layer Ag atoms are not indicated.

the respective molecular-induced geometries are plotted, i. e. for the surface structures of the hybrid molecule-surface systems but with the molecules removed. In this case the difference in the work function between the different induced surface geometries is only of the order of 10 meV outlining that the change of the work function in the hybrid systems is a hybridization driven effect due to the interaction of the molecular states with the states of the surface and not a structural one.

9.5. Band structures and Rashba-split Surface States

Now the band structures calculated for the molecule-surface hybrid systems will be considered. Since the rev-vdW-DF2 functional was applied during the relaxation of the hybrid systems, the band structures were obtained according to the second approach outlined in Section 9.2 for the clean $BiAg_2$/Ag(111) surface, i. e. for the relaxed geometry a self-consistent density was calculated with PBE+SOC and subsequently the band structure was evaluated with PBE+SOC using this density. The most important point to realize at the beginning is that due to the adsorption of both molecules the hexagonal symmetry of the surface is broken. When the surface BZ is visualized on top of the respective structure as done in Fig. 9.12 it can be seen that the equivalence of all the six $\overline{\Gamma M}$ as well as all the six $\overline{\Gamma K}$ directions, present in

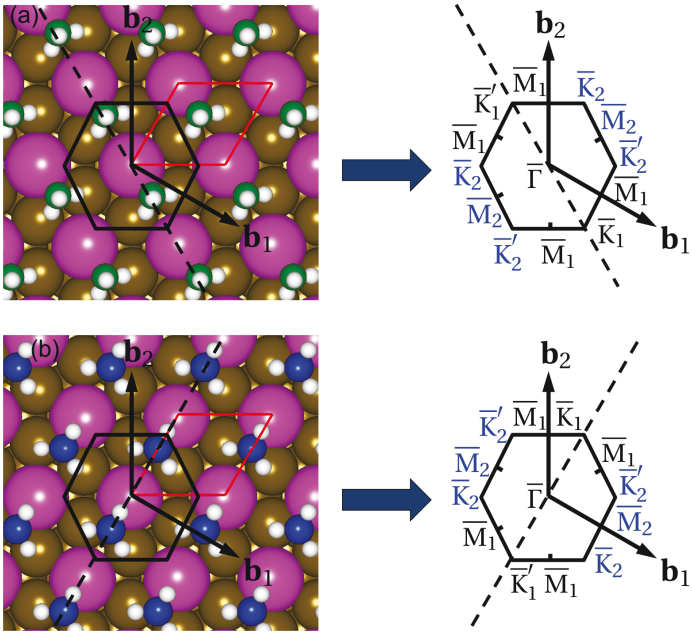

Figure 9.12.: Surface Brillouin zones and high-symmetry points for NH_3 (a) and BH_3 (b) on the $BiAg_2$/Ag(111) surface alloy. Note that the real space unit cell is marked in red and that the dashed line indicates the direction along which the NH_3 and BH_3 molecules are aligned, respectively. $\mathbf{b}_1$ and $\mathbf{b}_2$ indicate the reciprocal lattice vectors.

case of the clean surface alloy, is lifted. In both cases the molecules lie along a specific $\overline{\Gamma K}_1$ direction which is also a mirror symmetry element with respect to the first surface layer. The other corners of the surface BZ along which the molecule is not aligned are indicated as $\overline{K}_2$. Similarly, in case of the $\overline{M}$ points the four points close to the $\overline{\Gamma K}_1$ direction are denoted as $\overline{M}_1$ whereas the others are labeled as $\overline{M}_2$. The additional primes among the $\overline{K}$ points indicate their inequivalence with respect to the translational symmetry in k-space. Moreover it should be noted that due to the Kramer's degeneracy opposite directions in k-space have opposite spin polarization. Hence for each system the band structure is plotted along four directions, namely $\overline{\Gamma M}_1$, $\overline{\Gamma K}_1$, $\overline{\Gamma M}_2$ and $\overline{\Gamma K}_2$.

The obtained band structures of the hybrid systems are summarized in Fig. 9.13 with the Rashba splittings listed in Table 9.5 and the deduced Rashba energies and Rashba parameters given in Tables 9.6 and 9.7, respectively. The effective masses obtained from a quadratic fit of the surface states in the band structure can be found in Appendix A in Table A.7. In case of the NH_3 based hybrid system (see Figs. 9.13(a) and (b) as well as Table 9.5) the influence of the molecular adsorption onto the band structure is rather small meaning that the

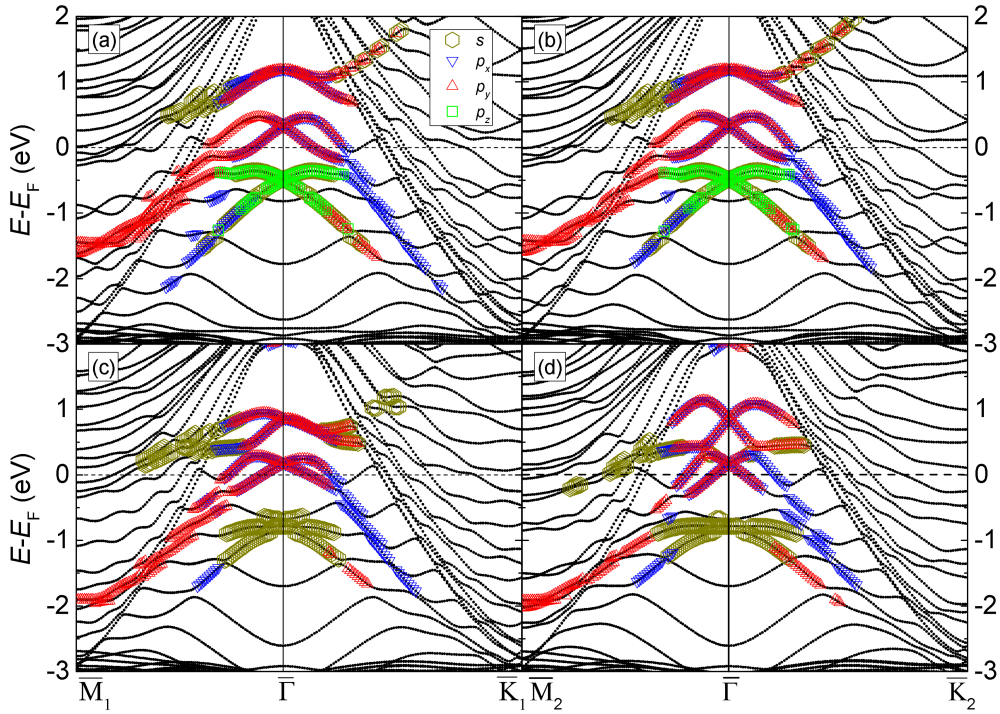

Figure 9.13.: Band structures calculated for the hybrid molecule-surface systems: (a) band structure for NH_3 on the $BiAg_2$/Ag(111) surface alloy along the $\overline{\Gamma M}_1$ and $\overline{\Gamma K}_1$ directions, (b) band structure for NH_3 on the $BiAg_2$/Ag(111) surface alloy along the $\overline{\Gamma M}_2$ and $\overline{\Gamma K}_2$ directions, (c) band structure for BH_3 on the $BiAg_2$/Ag(111) surface alloy along the $\overline{\Gamma M}_1$ and $\overline{\Gamma K}_1$ directions and (d) band structure for BH_3 on the $BiAg_2$/Ag(111) surface alloy along the $\overline{\Gamma M}_2$ and $\overline{\Gamma K}_2$ directions. In each case the s-, p_x-, p_y- and p_z-orbital contributions (of at least 0.08 e in the PAW spheres) of states mainly located at the surface are plotted on top of the band structure.

equivalence of the different **k**-directions is only 'slightly' modified. Nevertheless the Rashba splitting of the occupied surface state is indeed increased compared to the clean surface value of $k_{SO}^{cs,occ} = 0.09$ Å^{-1} to $k_{SO}^{NH_3,occ} = 0.10$ Å^{-1} in all **k**-directions as expected from the increased outward buckling of the Bi due to NH_3 adsorption as pointed out in Section 9.3. This is consistently supported by the increased Rashba energies of $E_R^{NH_3,occ} = -0.13$ eV and the Rashba parameters of $\alpha_R^{NH_3,occ} = -2.54$ to -2.90 eVÅ as compared to the clean surface values of $E_R^{cs,occ} = -0.11$ eV and $\alpha_R^{cs,occ} = -2.49$ eVÅ (see Tables 9.6 and 9.7). Remarkably, this enhancement of the Rashba splitting is as large as the whole Rashba splitting of the Au(111) surface state ($k_{SO}^{Au(111)} \approx 0.01$ Å^{-1}) [317]. In terms of the orbital contributions of this (s, p_z) type state, the increase of the splitting can be traced back to a stronger polarization by $p_{(x,y)}$ and some

p_z character making the corresponding surface state more asymmetric. More specifically, the angular momentum contributions over the three first layer surface atoms to this state at $\overline{\Gamma}$ in case of the clean surface are: s: 47.6%, p_x: 7.7%, p_y: 7.7% and p_z: 20.2%[5], whereas for the NH_3 based hybrid system the distribution is: s: 41.1%, p_x: 9.3%, p_y: 9.3% and p_z: 20.9%. The splitting of the unoccupied Rashba split surface state becomes slightly anisotropic in k-space in that $k_{SO}^{NH_3,unocc} = 0.09\,\text{Å}^{-1}$ in the $\overline{\Gamma M}_2$ direction whereas it remains at the clean surface value of $0.08\,\text{Å}^{-1}$ in all other directions. Consistently a small variation of both the associated Rashba energies and the Rashba parameters is found. Notably, no significant change of the orbital contributions at $\overline{\Gamma}$ with respect to the clean surface is detected.

Table 9.5.: Spin splittings in k-space of the occupied k_{SO}^{occ} and unoccupied $k_{SO}^{unocc}/k_{SO}^{unocc,2}$ Rashba split surface states for NH_3 and BH_3 on the $BiAg_2$/Ag(111) surface alloy as well as for the respective molecular-induced geometries.

system/surf.	k_{SO}^{occ} (Å^{-1})				k_{SO}^{unocc} (Å^{-1})				$k_{SO}^{unocc,2}$ (Å^{-1})			
	$\overline{\Gamma M}_1$	$\overline{\Gamma K}_1$	$\overline{\Gamma M}_2$	$\overline{\Gamma K}_2$	$\overline{\Gamma M}_1$	$\overline{\Gamma K}_1$	$\overline{\Gamma M}_2$	$\overline{\Gamma K}_2$	$\overline{\Gamma M}_1$	$\overline{\Gamma K}_1$	$\overline{\Gamma M}_2$	$\overline{\Gamma K}_2$
clean surf.	0.09	0.09	0.09	0.09	0.08	0.08	0.08	0.08	-	-	-	-
NH_3	0.10	0.10	0.10	0.10	0.08	0.08	0.09	0.08	-	-	-	-
BH_3	-	-	-	-	0.09	0.08	0.07	0.08	0.07	-	0.09	0.09
NH_3 induced	0.10	0.10	0.10	0.10	0.08	0.08	0.08	0.08	-	-	-	-
BH_3 induced	-	-	-	-	0.07	0.07	0.08	0.08	0.02	-	0.04	0.04

In the BH_3 case (see Figs. 9.13(c) and (d) as well as Table 9.5) it seems at first sight that the Rashba splitting of the occupied surface state disappears due to the molecular adsorption in all **k**-directions. However the BH_3 modifies the character of this surface state such that it becomes a surface resonance being pushed into the bulk Ag band structure[6]. This is consistent with the finding that the state extends now over all layers of the slab and is not any more localized at the surface. This leads to an interaction of the states from the upper and the lower surface of the slab which hence gives rise to a small energetic splitting of the state around $\overline{\Gamma}$. Notably, as can be seen in Fig. 9.13(c) and (d) the p_z character of the state is greatly removed meaning that the states have almost pure s-character close to $\overline{\Gamma}$. More precisely, the orbital contributions of the highest occupied state are: s: 67.3%, p_x: 2.9%, p_y: 7.7% and p_z: 7.7%.

Even more importantly, for the unoccupied surface state the Rashba splitting is still present but it becomes anisotropic and amounts to $k_{SO}^{BH_3,unocc} = 0.09/0.07\,\text{Å}^{-1}$ along $\overline{\Gamma M}_1/\overline{\Gamma M}_2$ whereas it persists at $0.08\,\text{Å}^{-1}$ along the $\overline{\Gamma K}_1$ and $\overline{\Gamma K}_2$ directions. Moreover, whereas in case of the clean

[5]The remaining contributions to the surface state arise from a small d-character.

[6]Due to the finite amount of layers (10) in the slab the bulk Ag band structure does not fully develop and one should therefore be aware of the fact that for the real system more bulk bands will appear in the energy region of the surface resonance.

Table 9.6.: Rashba energies E_R^{occ}, E_R^{unocc} and $E_R^{unocc,2}$ of the Rashba split surface states for NH_3 and BH_3 on the $BiAg_2$/Ag(111) surface alloy as well as for the respective molecular-induced geometries.

system/surf.	E_R^{occ} (eV) $\overline{\Gamma M}_1/\overline{\Gamma K}_1/\overline{\Gamma M}_2/\overline{\Gamma K}_2$	E_R^{unocc} (eV) $\overline{\Gamma M}_1/\overline{\Gamma K}_1/\overline{\Gamma M}_2/\overline{\Gamma K}_2$	$E_R^{unocc,2}$ (eV) $\overline{\Gamma M}_1/\overline{\Gamma K}_1/\overline{\Gamma M}_2/\overline{\Gamma K}_2$
clean surf.	−0.11/−0.11/−0.11/−0.11	−0.12/−0.12/−0.12/−0.12	-/-/-/-
NH_3	−0.13/−0.13/−0.13/−0.13	−0.12/−0.11/−0.14/−0.13	-/-/-/-
BH_3	-/-/-/-	−0.11/−0.07/−0.14/−0.14	−0.09/-/−0.28/−0.23
NH_3 induced	−0.14/−0.14/−0.14/−0.14	−0.13/−0.13/−0.13/−0.13	-/-/-/-
BH_3 induced	-/-/-/-	−0.07/−0.06/−0.10/−0.09	−0.01/-/−0.05/−0.04

surface the orbital contributions at $\overline{\Gamma}$ to this state are: s: 9.5%, p_x: 24.2%, p_y: 24.2% and p_z: 5.3%, they are modified to: s: 11.4%, p_x: 21.7%, p_y: 21.1% and p_z: 7.6%. Consequently, the associated Rashba energy (−0.07 eV) and Rashba parameter (−2.31 eVÅ) are especially small along $\overline{\Gamma K}_1$ whereas an enhancement to −0.14 eV/−0.14 eV and −5.93 eVÅ/−5.08 eVÅ is observed along $\overline{\Gamma M}_2/\overline{\Gamma K}_2$. Therefore the maximum of the parabola of this surface state varies on an energy scale of 0.07 eV over the different **k**-directions.

Table 9.7.: Rashba parameters α_R^{occ}, α_R^{unocc} and $\alpha_R^{unocc,2}$ of the Rashba split surface states for NH_3 and BH_3 on the $BiAg_2$/Ag(111) surface alloy as well as for the respective molecular-induced geometries.

system/surf.	α_R^{occ} (eVÅ) $\overline{\Gamma M}_1/\overline{\Gamma K}_1/\overline{\Gamma M}_2/\overline{\Gamma K}_2$	α_R^{unocc} (eVÅ) $\overline{\Gamma M}_1/\overline{\Gamma K}_1/\overline{\Gamma M}_2/\overline{\Gamma K}_2$	$\alpha_R^{unocc,2}$ (eVÅ) $\overline{\Gamma M}_1/\overline{\Gamma K}_1/\overline{\Gamma M}_2/\overline{\Gamma K}_2$
clean surf.	−2.49/−2.49/−2.49/−2.49	−3.71/−3.71/−3.71/−3.71	-/-/-/-
NH_3	−2.63/−2.54/−2.90/−2.76	−3.21/−3.81/−3.92/−4.51	-/-/-/-
BH_3	-/-/-/-	−3.65/−2.31/−5.93/−5.08	−2.43/-/−6.24/−4.29
NH_3 induced	−3.18/−3.05/−3.14/−3.05	−3.81/−4.36/−3.72/−4.29	-/-/-/-
BH_3 induced	-/-/-/-	−2.21/−2.24/−3.05/−3.21	−0.90/-/−1.91/−1.79

Strikingly, the $p_{(x,y)}$ derived state above the unoccupied Rashba split surface state discussed previously shows now also a Rashba-like splitting which is however only present in the $\overline{\Gamma M}_1$, $\overline{\Gamma M}_2$ and $\overline{\Gamma K}_2$ directions but not along $\overline{\Gamma K}_1$. The induced splitting ranging from $k_{SO}^{BH_3,unocc,2}$ = 0.07 to 0.09 Å^{-1} is comparable to the splitting of the aforementioned unoccupied Rashba split surface state and the associated Rashba energies and Rashba parameters of this new split surface state are very large along the $\overline{\Gamma M}_2$ and $\overline{\Gamma K}_2$ directions amounting to −0.28 eV and −0.23 eV as well as −6.24 eVÅ and −4.29 eVÅ, respectively. A partial rationalization of this can be given by analyzing the orbital contributions of this state at $\overline{\Gamma}$ which for the clean surface amount to:

s: 0%, p_x: 32.6%, p_y: 32.6% and p_z: 0%. These are changed to s: 4.5%, p_x: 35.8%, p_y: 20.8% and p_z: 3.3%, indicating a polarization of the state by s- and p_z-character at the expense of the p_y-character due to the BH_3 adsorption. Conclusively, a new SOC split surface state is induced in selected **k**-directions as a consequence of the formation of the hybrid system. These remarkable findings concerning the unoccupied states might be experimentally accessible via transport measurements, inverse ARPES or two-photon photoemission spectroscopy (2PPES) [312, 328, 329].

It is now interesting to investigate whether the observed changes in the band structure due to molecular adsorption are caused by the interaction of the molecules with the surface or to which extent the geometry change induced by the molecular adsorption is responsible for the recorded modifications. For this purpose the latter geometrical influence exerted onto the surface by the molecules has been investigated by recalculating the band structure for the geometries of the hybrid systems but with the molecules removed, i. e. the band structure was calculated for the molecular-induced surface geometries (see Fig. 9.14). In case of the NH_3-induced geometry Figs. 9.14(a) and (b) show that the band structure is very similar to the case when the molecule is actually present (see Figs. 9.13(a) and (b)) and that even the orbital contributions of the surface states are analogous. More precisely, the orbital contributions of the occupied Rashba state at $\overline{\Gamma}$ are: s: 40.0%, p_x: 9.9%, p_y: 9.9% and p_z: 19.9% confirming the geometrical origin of the increased polarization of the state by mainly p_x- and p_y-character. This is in line with the weak physisorption interaction mechanism detected for NH_3 on the surface and shows that the change of the band structure is largely geometrically driven which implies a rehybridization of electronic states in the molecular-induced surface geometry.

The splitting of the occupied surface state amounts to $k_{\mathrm{SO}}^{\mathrm{NH_3-induced,occ}} = 0.10$ Å^{-1} in all **k**-directions which is the same as for the hybrid system reflecting the correlation with the outward buckling of the Bi. Notably, also the Rashba energies and Rashba parameters show enhanced values compared to the clean surface band structure. However the splitting of the unoccupied state largely recovers now the isotropy in k-space, i. e. $k_{\mathrm{SO}}^{\mathrm{NH_3-induced,unocc}} = 0.08$ Å^{-1} in all directions which also coincides with the clean surface value. Analogously the influence onto the orbital contributions is found to be minor. This leads to the conclusion that the small anisotropy in the splitting of the unoccupied state for the hybrid system is due to the charge rearrangement at the interface caused by the weakly bonded NH_3 which is indicated in the charge density difference plot in Fig. 9.10(a).

When the band structures of the BH_3-induced geometry in Figs. 9.14(c) and (d) are compared to the ones in Figs. 9.13(c) and (d), it becomes clear that the occupied Rashba split surface state of the clean surface is not recovered in this molecular-induced surface geometry. The orbital contributions also confirm that the highest occupied state at $\overline{\Gamma}$ is basically a pure s-state: s: 89.7%, p_x: 0.7%, p_y: 0.7% and p_z: 5.9%. In addition this state extends over

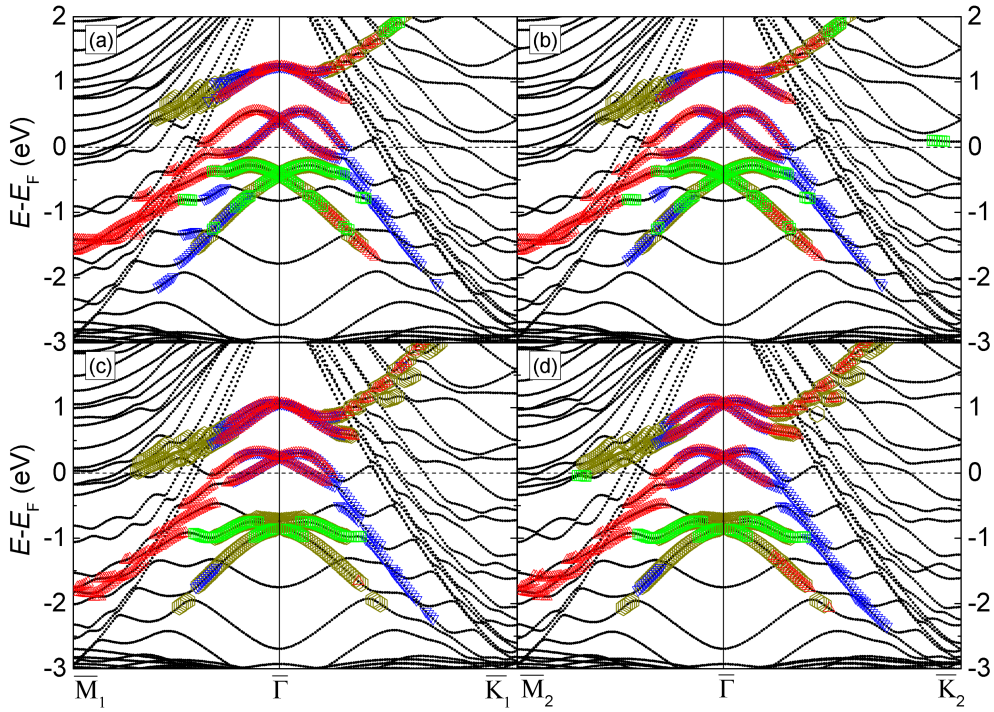

Figure 9.14.: Band structures calculated for the molecular-induced surface geometries: (a) band structure for the NH_3-induced geometry along the $\overline{\Gamma M}_1$ and $\overline{\Gamma K}_1$ directions, (b) band structure for the NH_3-induced geometry along the $\overline{\Gamma M}_2$ and $\overline{\Gamma K}_2$ directions, (c) band structure for the BH_3-induced geometry along the $\overline{\Gamma M}_1$ and $\overline{\Gamma K}_1$ directions and (d) band structure for the BH_3-induced geometry along the $\overline{\Gamma M}_2$ and $\overline{\Gamma K}_2$ directions. In each case the *s*-, p_x-, p_y- and p_z-orbital contributions (of at least 0.08 *e* in the PAW spheres) of states mainly located at the surface are plotted on top of the band structure.

the whole slab. This means that in the present case the BH_3 adsorption leads to such a strong inward relaxation that the Rashba splitting is shifted into the bulk Ag band structure, i. e. the geometrical effect plays a crucial role. However it can be seen that compared to the band structure of the hybrid system in Figs. 9.13(c) and (d) some p_z admixture especially close to $\overline{\Gamma}$ can be detected for the lower occupied state. This indicates that the band structure of this induced geometry in this energy region partially recovers the orbital polarization of the surface state compared to the hybrid system.

On the other hand, the unoccupied Rashba split surface state again shows an anisotropy with especially small splittings, Rashba energies and Rashba parameters along $\overline{\Gamma M}_1$ and $\overline{\Gamma K}_1$. However in this molecular-induced geometry the isotropy of this state in the different **k**-directions is largely recovered and only between the directions indexed by 1 and indexed

by 2 a significant difference is observed. The orbital contributions also indicate only small changes compared to the clean surface. This means that the strong anisotropy found in the band structure of the hybrid system in Figs. 9.13(c) and (d) originates predominantly from the hybridization between the molecule and the surface which is also indicated in the charge density difference plot in Fig. 9.10(b). A similar behavior is observed for the newly induced split unoccupied surface state above the aforementioned unoccupied surface state, i. e. it still shows a splitting in the same selected **k**-directions as for the hybrid system but the values of the associated parameters are greatly reduced as indicated in Tables. 9.5, 9.6 and 9.7. As regarding the orbital contributions the pure $p_{(x,y)}$ character of the state is reestablished: s: 0%, p_x: 32.1%, p_y: 31.5% and p_z: 0%. Conclusively, this analysis shows that the modification of the surface geometries due to the molecular adsorption has already a detectable influence on the band structures but that especially in case of BH_3 the hybridization contribution associated with the weak chemisorption of the molecule cannot be neglected.

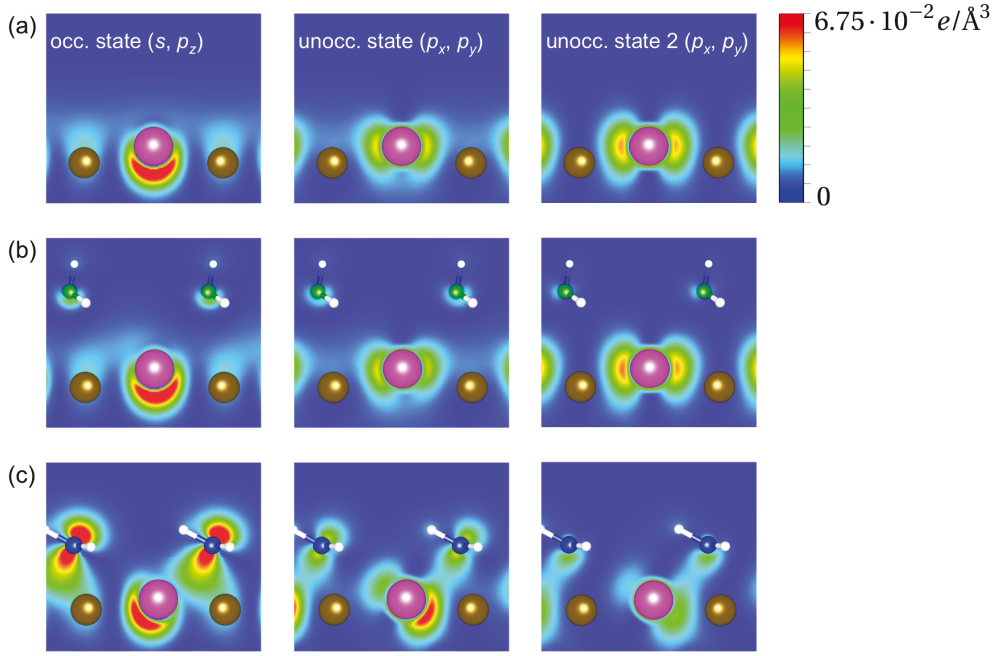

Figure 9.15.: Visualization of the charge density of the surface states at $\overline{\Gamma}$ for the clean $BiAg_2$/Ag(111) surface alloy (a) and for NH_3 (b) as well as BH_3 (c) on the (110) and (100) planes marked as dashed lines in Fig. 9.8, respectively.

This chemical influence of the BH_3 can be directly visualized when plotting the charge density of the individual surface states on the planes marked as dashed lines in Fig. 9.8 for each system as done in Fig. 9.15. In Fig. 9.15(a) for the clean surface the s, p_z like nature of the

occupied Rashba split surface state as well as the $p_{(x,y)}$ like character of the two unoccupied surface states at $\overline{\Gamma}$ can be clearly identified. For the NH_3-based hybrid system (Fig. 9.15(b)) these surface states are only slightly distorted and practically no orbital contribution at the molecular site is visible. On the contrary, in case of the BH_3-based hybrid system (Fig. 9.15(c)) the molecule clearly couples to the Bi-derived surface states, i. e. it binds to the surface states. This bonding effect is strongest in case of the occupied surface state since the orbital contribution at the molecular site in the first image in Fig. 9.15(c) is clearly largest compared to the other two. This indicates that the strong coupling of the molecule to this state contributes to the shift of this state into the bulk Ag bands as seen in the band structures above.

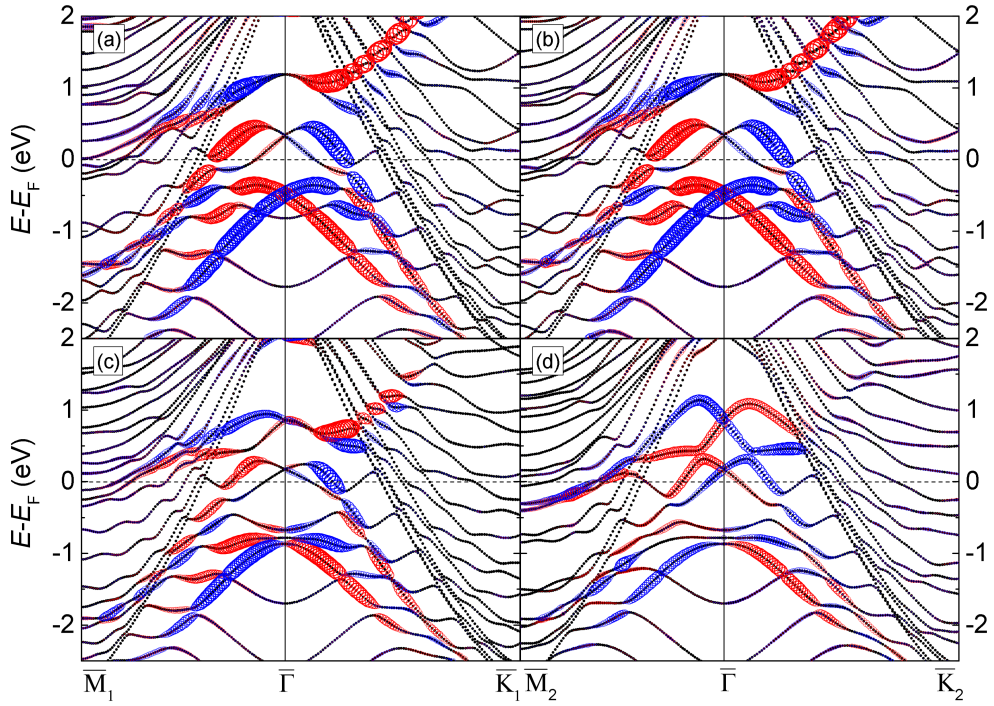

Figure 9.16.: In-plane spin polarizations visualized on top of the band structures for the hybrid molecule-surface systems: (a) for NH_3 on the $BiAg_2$/Ag(111) surface alloy along the $\overline{\Gamma M}_1$ and $\overline{\Gamma K}_1$ directions, (b) for NH_3 on the $BiAg_2$/Ag(111) surface alloy along the $\overline{\Gamma M}_2$ and $\overline{\Gamma K}_2$ directions, (c) for BH_3 on the $BiAg_2$/Ag(111) surface alloy along the $\overline{\Gamma M}_1$ and $\overline{\Gamma K}_1$ directions and (d) for BH_3 on the $BiAg_2$/Ag(111) surface alloy along the $\overline{\Gamma M}_2$ and $\overline{\Gamma K}_2$ directions. Positive (negative) spin polarization larger than 2% is indicated in red (blue) and the size of the symbols indicates the degree of spin polarization. The spin quantization axis is chosen perpendicular to both the surface normal and the respective in-plane $\mathbf{k}_\parallel$ direction.

In terms of a spintronics viewpoint especially the influence of the molecules onto the spin polarization of the Rashba spin-split states is of interest. In Fig. 9.16 the in-plane spin polarization of each electronic state is plotted on top of the band structure. For the NH_3-based hybrid system (see Figs.9.16(a) and (b)) the differences between the different **k**-directions and to the clean surface spin polarization are small. Compared to the clean $BiAg_2$/Ag(111) surface only a small reduction of the maximum in-plane spin polarization from about 70% to about 65% for the occupied states is observed. However in the BH_3-based hybrid system clearly the anisotropy of the states in the different **k**-directions also leads to an associated anisotropic spin polarization. More specifically, in general the in-plane spin polarization is reduced compared to the clean surface case and the maximum spin polarizations of the occupied states reach about 60% (predominantly along $\overline{\Gamma K}_1$) and 50% in Figs. 9.16(c) and (d), respectively.

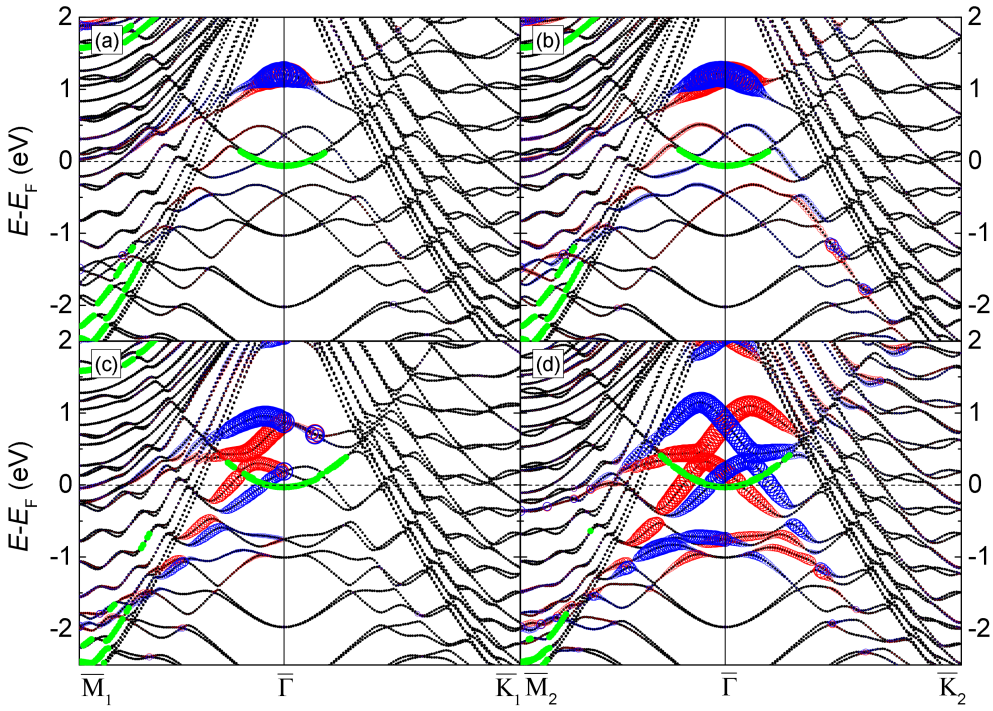

Figure 9.17.: Out-of-plane spin polarizations visualized on top of the band structures for the hybrid molecule-surface systems: (a) for NH_3 on the $BiAg_2$/Ag(111) surface alloy along the $\overline{\Gamma M}_1$ and $\overline{\Gamma K}_1$ directions, (b) for NH_3 on the $BiAg_2$/Ag(111) surface alloy along the $\overline{\Gamma M}_2$ and $\overline{\Gamma K}_2$ directions, (c) for BH_3 on the $BiAg_2$/Ag(111) surface alloy along the $\overline{\Gamma M}_1$ and $\overline{\Gamma K}_1$ directions and (d) for BH_3 on the $BiAg_2$/Ag(111) surface alloy along the $\overline{\Gamma M}_2$ and $\overline{\Gamma K}_2$ directions. Positive (negative) spin polarization larger than 2% is indicated in red (blue) and the size of the symbols indicates the degree of spin polarization. States predominantly localized at the clean Ag side of the asymmetric slab (at least 0.1 *e* in the PAW spheres) are marked in green.

On the other hand the out-of-plane spin polarization of the states is visualized in Fig. 9.17. Again a ten-layer asymmetric slab with a clean Ag surface on one side and the $BiAg_2$/Ag(111) surface alloy on the other side was chosen for this calculation in order to check the results with respect to the slab geometry. The Ag surface state is marked again in green. It is once more found that the energetic positions and splittings of the surface states are insensitive with respect to the type of the slab. When inspecting Fig. 9.17(a) as in case of the clean surface practically no out-of-plane spin-polarization is found in the $\overline{\Gamma K}_1$ direction which is a consequence of the fact that the NH_3 molecule lies along this direction representing a mirror symmetry element with respect to the surface layer. Hence no in-plane potential gradients perpendicular to this direction can occur and hence no out-of-plane spin polarization is observed along $\overline{\Gamma K}_1$. However in the other three **k**-directions this argument does not hold and therefore finite potential gradients are induced by the NH_3 adsorption which lead to visible out-of-plane spin polarization contributions reaching up to about 20% for the occupied states in Fig. 9.17(b).

Even more drastic is the situation for the BH_3-based hybrid system in Figs. 9.17(c) and (d). Again the band structure along $\overline{\Gamma K}_1$ shows no sizable polarization since this direction is a mirror symmetry element of the surface layer. However for the other **k**-directions strong spin polarizations reaching up to about 50% and 70% in case of the occupied states in Figs. 9.17(c) and (d), respectively, are observed. This means that the in-plane potential gradients induced by the BH_3 adsorption onto the $BiAg_2$/Ag(111) surface alloy are large enough to induce out-of-plane spin polarizations even exceeding the corresponding in-plane contributions. At the same time these large in-plane potential gradients could give an explanation for the observed strong spin splitting of the unoccupied surface state originally not showing a Rashba-like splitting in case of the clean surface. As outlined in Refs. [315, 326] both in-plane and out-of-plane potential gradients are important to obtain large spin splittings. Hence the creation of the new spin split surface state in case of the BH_3-$BiAg_2$/Ag(111) hybrid system can be thought of as being associated with the in-plane potential variations induced by the molecular adsorption.

9.6. Conclusions

To summarize, in this chapter the adsorption of NH_3 and BH_3 on the $BiAg_2$/Ag(111) surface alloy was investigated. The opposite electronic character of NH_3 having a free electron pair and BH_3 exhibiting an empty p_z-orbital gives rise to different interaction schemes of both molecules with the $BiAg_2$/Ag(111) surface alloy especially affecting the Rashba split surface states. On the one hand NH_3 is physisorbed on the surface. Consequently, the outward buckling of the Bi out of the surface is slightly enhanced. BH_3 on the contrary interacts more strongly with the surface, i. e. a hybridization of the surface Bi p_z-states with the p_z-states

of the molecular B leads to a weak chemisorption type bonding. Due to this chemisorption process a strong inward relaxation of the Bi is caused.

As a result of the molecular adsorption, the Rashba split surface states of the $BiAg_2$/Ag(111) surface alloy being derived from Bi *s*- and *p*-states are strongly affected. NH_3 increases the Rashba splitting of the occupied surface state by an amount equivalent to the Rashba splitting of the Au(111) surface state while the unoccupied split surface state is less affected. An analysis of the band structure of the molecular-induced surface geometry showed that the increase of the splitting of the occupied state is geometrically driven. The chemisorption of the BH_3 on the other hand leads to a shift of the occupied Rashba state into the bulk Ag band structure and at the same time induces a significant anisotropy of the unoccupied split surface state in different **k**-directions leading to a varying height of the parabola maximum in *k*-space. Even more importantly, the BH_3 adsorption leads to a spin splitting of another unoccupied surface state not showing a Rashba-like splitting in case of the clean surface, i. e. BH_3 induces a SOC based spin splitting in selected **k**-directions. These influences are found to be largely caused by the chemical bonding of the BH_3 to the surface since the band structure of the molecular-induced geometry showed only much less significant changes with respect to the clean surface.

In addition, when analyzing the surface state spin polarization, it was found that NH_3 only slightly affects the in-plane spin polarization inducing small out-of-plane contributions. On the contrary, BH_3 significantly reduces the in-plane spin polarization and due to the generation of in-plane potential gradients it creates out-of-plane spin polarization contributions even exceeding the in-plane ones. Hence it can be finally concluded that the results of this chapter unambiguously show that the adsorption of the prototypical NH_3 and BH_3 molecules allows to tune the characteristics of Rashba split surface states over a wide range. This work therefore opens the way to a systematic and sizable design of surface Rashba systems which can be controlled on a molecular scale. This might give ample possibilities for the discovery of new physical phenomena. Ultimately, it can be proposed that the initial idea to extend the molecular-induced tuning of surface properties to other surface magnetic effects than magnetic exchange coupling is indeed fruitful and has the potential to initiate further research in the field of surface magnetism.

10 Summary and Outlook

Research in the field of spintronics is of fundamental scientific interest as well as of considerable practical relevance as it aims to initiate innovations in data storage and processing using the spin degree of freedom of the electron. It was tried to incorporate the spintronic functionality onto several materials platforms among which molecular spintronics, i. e. to store and transmit the spin information using single molecular based magnetic units, is one of the most promising approaches.

In this thesis hybrid interfaces of metallic surfaces and molecules or 2D materials have been investigated for their suitability and application in spintronics by *ab initio* methods. The work originated from the new approach introduced in 2013 to tune surface magnetic exchange interactions by molecular adsorption. The main goals of this thesis were on the one hand to bring fundamental understanding to the observed effects and on the other hand to investigate the introduced approach for its relevance and generality in the field of surface magnetism.

The first systematic investigation concerned the in-plane magnetic hardening effect observed for carbon-based adsorbates, i. e. the molecular induced increase of the in-plane surface magnetic exchange interaction between the atoms directly bound by the adsorbed molecule. Naturally, the question arose whether this effect could be tuned by a chemical functionalization of the molecular part of the system. This issue was investigated using a set of small π-bonded organic molecules, namely methyleneborane (CH_3B), ethene (C_2H_4), methyleneimine (CH_3N) and formaldehyde (CH_2O), adsorbed on the prototypical ferromagnetic 1 ML Fe/W(110) surface. It was found that the molecules allow to locally and also element specifically tune the magnetic exchange interaction between individual surface Fe atoms. More precisely, C and B were found to strongly increase the exchange strength of the clean surface whereas, importantly, a small weakening was found for N which was even more pronounced in case of O. Interestingly, due to a special adsorption geometry of CH_3B it was discovered that a B-C bond leads to an even stronger softening of the in-plane exchange coupling between the surface Fe atoms it is bound to. Hence these results showed that due to an element specific influence the modification of the exchange coupling can be tuned from in-plane hardening to in-plane softening. Regarding the mechanism of the observed modifications it was found that the main influence leading to the change of the in-plane exchange coupling comes from the hybridization between states of the molecules and states of the surface whereas the distortions induced on the surface by the molecular adsorption have less impact. In addition it could be demonstrated by Monte Carlo simulations that the modified couplings lead to a tuning of macroscopically observable hysteresis curves by selectively influencing the coercive field of the system over a wide range. Hence it could be showcased that indeed a chemical functionalization of the surface magnetization reversal process is possible.

The complementary phenomenon represented by the magnetic inter-layer softening effect, i. e. the weakening of the inter-layer exchange interaction of a magnetic surface upon molecular adsorption, was also studied in detail. The physical origin of this phenomenon was investigated systematically. For this purpose two prototypical weakly and strongly chemisorbed molecules, namely dioxan and dioxin, had been chosen to be adsorbed on the 1 and 2 ML Fe/W(110) surfaces. As expected from the weak molecule-surface interaction, for the weakly chemisorbed dioxan system the change of the coupling constants was found to be mainly geometrically driven. On the contrary, in case of dioxin influences arising from the hybridization of the molecule with the surface led to additional qualitative changes. Eventually, the general mechanism of the magnetic inter-layer softening could be back traced to the so-called molecular induced skyhook effect, i. e. the detachment of the first layer magnetic atoms locally below the molecule from the second surface layer. The origin of this skyhook comes from the different interaction of the various molecular parts with the surface: whereas the central part of the molecule containing C and O is attracted to the surface, the peripheral H atoms are repelled from it leading to the skyhook effect.

A direct validation of the outlined mechanism was provided by studying the influence of 2D materials as Gr and hBN complementary to the finite-size molecular systems. When adsorbed on a Co(111) surface both 2D materials are on the one hand found to give rise to the well-known in-plane magnetic hardening effect between the Co moments of the first surface layer. This is once more found to be a hybridization effect between the d-states of the surface and predominantly the p_z-states of the adsorbates. On the other hand the inter-layer exchange coupling was found not to be affected signifying the distinct role of finite-size molecular adsorbates leading to the skyhook effect. When seen from a different perspective, 2D materials can be considered so as to protect the magnetic inter-layer properties of a substrate.

Regarding the finding that due to the in-plane magnetic hardening strongly exchange coupled magnetic units can be formed below molecules containing submolecular cyclic structures, the question arose whether this concept could be generalized to incorporate different magnetic units into a single molecule-surface hybrid system when using a molecule being made up of various rings. In this respect the TPT molecule, consisting of a central triazine-like ring surrounded by three peripheral phenyl rings, was studied on the 2 ML Fe/W(110) surface. Consistent with experimental findings based on STM results obtained within a collaboration with scientists from PGI-6/Forschungszentrum Jülich [306] the TPT was found to adsorb in a chiral adsorption position onto the surface meaning that in this case a chiral object was formed out of two non-chiral components. This asymmetric position gave rise to structural differences between all four molecular rings and carried over to the electronic properties as indicated by both experimental and simulated STM topography images. Moreover also the magnetic properties reflected the inequality of the molecule-based lobes by exhibiting a site

dependent spin polarization which consequently varied on an intramolecular length scale. The theoretical analysis also showed the distinctiveness of the magnetic units formed out of each molecular ring and the surface Fe atoms directly bound to it, i. e. significant differences in the energy scale for magnetic switching were found among the units. These findings hence suggest that indeed multiple intramolecular magnetic units can be formed within a single molecule-surface hybrid system. Eventually, a scenario could be envisioned in which certain intramolecular units might switch depending on the magnetic state of other units pointing to the possibility of realizing molecular based spin logic devices.

Finally, the question emerged whether the whole initial approach might be even more far reaching, i. e. whether the concept of molecular induced tuning of surface magnetic properties could be generalized beyond the exchange interaction between surface atoms. To investigate this issue the molecular adjustability of the Rashba effect at the $BiAg_2$/Ag(111) surface alloy was chosen to be studied by the adsorption of ammonia (NH_3) and borane (BH_3). The interaction strength was found to be different for the two adsorbates, i. e. NH_3 was physisorbed whereas BH_3 was weakly chemisorbed and both did indeed have an impact onto the surface Rashba states. NH_3 was found to slightly pull the Bi out of the surface which hence enhanced the spin splitting of the occupied surface state but leaving the unoccupied state practically unchanged. The bonding of the BH_3 to the surface however pushed the occupied Rashba split state into the bulk Ag band structure. On the other hand it induced in-plane potential gradients and an asymmetry leading to a modulation of the Rashba splitting of the unoccupied surface state in reciprocal space, i. e. the splitting is tuned selectively in different **k**-directions. Even more importantly, a previously non Rashba split surface state became split on the same order of magnitude as the other split states due to the presence of the BH_3. Eventually, the analysis of the surface state spin polarization showed that NH_3 nearly completely maintained the spin polarization in the plane of the surface inducing only tiny in-plane potential gradients which led to minor out-of-plane spin contributions. The larger in-plane potential gradients in the BH_3 case however led to strong out-of-plane spin polarization components even exceeding the in-plane ones over large parts of the band structure. This showcased that molecular adsorbates can be used to selectively tune the spin polarization direction of surface Rashba systems. Ultimately, this reveals the prospect to tune spin currents obtained from spin split surface states by molecular adsorption.

Hence based on the results outlined in this thesis it can be concluded that the approach to use molecular-metallic interfaces as a tool to design surface magnetic properties for molecular spintronics has just begun to uncover all its possibilities and can offer the potential to drive the field of surface magnetism to new frontiers. In this respect for instance the tuning of magnetic interactions favoring noncollinear magnetic structures could be of great interest. One could possibly study the influence of the molecular adsorption onto the Dzyaloshinskii-

Moriya interaction favoring a perpendicular alignment of spins. That this might indeed be possible is indicated by the fact that the Dzyaloshinskii-Moriya interaction is a consequence of SOC as is the case for the Rashba effect for which the adjustability has been confirmed in this thesis. Hence it could be very interesting to see whether it would be possible to *locally* induce a competition of the magnetic energy scales related to exchange and the Dzyaloshinskii-Moriya interaction. This could allow to locally create a non-collinear magnetic structure below a single molecule.

From a more application oriented perspective it could be envisioned that molecules which react to an external stimulus as an electric field by e. g. a conformational change are promising to investigate. When adsorbed on a magnetic surface the externally induced structural change could also lead to a change of the in-plane and inter-layer magnetic hardening or softening induced by these molecules. This might offer the prospect to electronically write a magnetic information encoded in the magnetic units formed by the hybrid molecule-surface systems. One should however be aware of the fact that in most cases where a sizable molecular-induced hardening or softening of the surface magnetic exchange interactions was found, the molecules were chemisorbed on the surfaces which might suppress the conformational change. It could therefore be especially promising to study larger molecular systems for which one part interacts with the surface and the other part is susceptible to the external stimulus. This scheme could allow to propagate the conformational change from the susceptible part over an intramolecular connection to the other part forming the magnetic unit with the substrate and consequently to write the magnetic information.

Part III.

Appendix

A Computational Details

A.1. The Vienna *Ab Initio* Simulation Package

The Vienna *ab initio* simulation package (VASP) program [330–332] is a state-of-the-art tool to perform *ab initio* electronic structure calculations and quantum-mechanical molecular dynamics simulations at the atomic scale. It is capable of carrying out DFT calculations based on the KS equations as well as computations using HF theory or hybrid-functionals. In addition, also Green's function based methods and many-body perturbation theory approaches are implemented [333].

The basis set is made up of plane waves into which the KS orbitals, the electron density and the local potential are expanded. For the description of the electron-ion interactions ultrasoft PPs or the PAW method are used. Within a self-consistent calculation efficient iterative matrix diagonalization algorithms as the residual minimization method with direct inversion of the iterative subspace (RMM-DIIS) or blocked Davidson methods are employed to obtain the eigenvalues and eigenfunctions of the KS Hamiltonian (in case of a DFT calculation). These are used in conjunction with sophisticated density mixing schemes of Broyden or Pulay to obtain a self-consistent charge density [331, 332]. In general the finite-temperature variant of DFT is applied in which the free energy of the electron system is the variational quantity [330].

A.2. The Spin Polarized Relativistic Tight-binding Korringa-Kohn-Rostoker Program

The spin-polarized relativistic tight-binding KKR (SPR-TB-KKR) package [334] is an electronic structure program based on the KKR formalism introduced in Subsection 2.3.4. It is capable of calculating the band structure and electronic properties of 2D as well as three-dimensional (3D) systems by applying the screened (tight binding) KKR formalism of Zeller and coworkers [149]. In addition, it also allows to treat 0-dimensional impurities in a 2D or 3D host structure by correctly solving the Dyson equation for the associated embedding problem. Furthermore the program can perform spin-polarized relativistic calculations, treat alloys and non-collinear magnetic structures and allows to deal with relativistic transport phenomena and the LSDA+U approach [334]. It also provides an effective implementation for the calculation of the (energy-dependent) exchange coupling constant $J(E)$ according to Equation (3.17) [171].

A.3. Visualization for Electronic and STructural Analysis

The Visualization for Electronic and STructural Analysis (VESTA) program is a software for the visualization of 3D crystallographic structures and electronic structure data [335]. Besides the display of structures it is capable of superimposing structural models, visualizing volumetric data and crystal faces. It can also model electron and nuclear densities as well as integrate those densities by Voronoi tessellation. A surface coloring method for isosurface plots is provided enabling the illustration of additional physical data at each point. A more detailed description of its functionalities is given in Ref. [335] and references therein.

This program has been used in the present thesis to display and analyze atomic structures of molecules, surfaces and hybrid molecule-surface systems. It was also used to visualize isosurfaces and 2D contour maps of (partial) charge densities and to depict calculated STM topography, spin up and spin down images as well as deduced spin polarizations above hybrid molecule-surface systems. In addition, it also aided to visualize AFM configurations.

A.4. Common Computational Details

The spin-polarized electronic structure calculations performed to obtain the results presented in Chapters 5, 6, 7, 8, 9, Subsection A.5.4, Appendix B and the VASP results in Appendix C were carried out in the framework of DFT [73, 74] using the VASP program [330–332]. In addition, PAW datasets [142] as constructed for the exchange-correlation functional of PBE [92] were employed. Throughout all calculations a plane wave cutoff of 500 eV was used. All structures were relaxed until the forces were smaller than 1 meV/Å in Chapters 5, 6, 7 and Subsection A.5.4 and smaller than 10 meV/Å in Chapters 8, 9 and Appendix B. For the relaxations in Chapters 5, 6, 8, Subsection A.5.4 and Appendix B only the Γ-point was taken into account. Nevertheless, for the calculation of the SP-PDOS and the AFM configurations to obtain the exchange coupling constants in Chapters 5, 6 and Subsection A.5.4 as well as for the MAEs in Chapter 5 a k-point set of $4 \times 5 \times 1$ was used. Due to the large size of the supercell[1] used in the calculations, the Brillouin zone was sampled only at the Γ-point for the evaluation of the SP-PDOS and the AFM configurations in Chapter 8 and Appendix B. Moreover in Chapters 5, 6, 7, 8, 9 for the asymmetric slabs, Subsection A.5.4 and Appendix B a dipole correction was applied in the direction perpendicular to the surface to correct for the interface dipole resulting from the adsorption of the molecules and 2D materials [336, 337].

[1] The size of the supercell was 22.4 Å×22.2 Å×33.1 Å in Chapter 8 and in Appendix B both vectors in the plane of the surface making up the unit cell had a length of 22.6 Å with a 60° angle between them and the height of the cell was 33.1 Å.

A.5. Small π-electron Systems on 1 ML Fe/W(110)

In the calculations the supercell consisted of one Fe layer and six W layers each represented by a 3×4 in-plane surface unit cell out of 24 Fe or W atoms. The molecules were adsorbed on top of the Fe layer on one side of the slab. The vacuum distance along the direction perpendicular to the surface plane to the following supercell was set to about 16 Å. The lateral distance between molecules in neighboring unit cells amounted to at least about 10 Å minimizing the lateral interaction between adjacent molecules. During the geometry optimization the upper three W layers, the Fe layer and the molecular coordinates were allowed to relax.

For the multi-scale MC simulations[2] the Hamiltonian consisted of a nearest neighbor Heisenberg exchange term ($H_{\mathrm{ex}}^{\mathrm{spin}}$), uniaxial anisotropy ($H_{\mathrm{MAE}}^{\mathrm{spin}}$) and the Zeeman term ($H_{\mathrm{Z}}^{\mathrm{spin}}$):

$$H = H_{\mathrm{ex}}^{\mathrm{spin}} + H_{\mathrm{MAE}}^{\mathrm{spin}} + H_{\mathrm{Z}}^{\mathrm{spin}} = -\sum_{\langle i>j\rangle} J_{ij}\mathbf{M}_i\mathbf{M}_j - K\sum_i (M_i^x)^2 - \mathbf{H}\sum_i \mathbf{M}_i, \tag{A.1}$$

where $\mathbf{M}_i = \mathbf{m}_i/\mu_{\mathrm{B}}$ represents the normalized magnetic moment for the ith Fe atom, $J_{ij} = J(i,j)$ and $i = 1,2,3,4$ stands for the site-dependent type of iron atom: Fe1, Fe2, Fe3 and clean surface Fe, respectively (see Fig. 5.5). $\mathbf{H}$ is the applied external magnetic field and K denotes the magneto-crystalline anisotropy parameter. The specific values for K, $J(1,2) = J_1$, $J(1,3) = J_2$, $J(1,4) = J_3$, $J(2,4) = J_4$ and $J(3,4) = J_5$ were obtained from Tables 5.3 and 5.5. In case of a clean surface all Fe atoms are of type 4. In addition, a regular distribution of the molecules over the surface was assumed.

In the actual simulations a 2D regular lattice with periodic boundary conditions was used. The lattice extension was slightly adapted to fit the boundary conditions for every coverage density of the adsorbates. The simulated domain consisted on average of about 90×90 spins. A combined sampling algorithm was used to enhance the efficiency of the simulations [284]. It incorporates a set of trial steps for each MC step. In the simulations three uniform trial steps and an additional small trial step are used, for further details see Ref. [284]. The simulations for annealing and magnetization reversal were carried out using 10^4 MC steps for the relaxation of the system and 10^5 MC steps for statistical sampling for each temperature and applied magnetic field, respectively. The temperature dependence of the coercive field strength and the magnetization curves were obtained from an averaging process over about 100 independent runs.

However in the simulations no defects were taken into account which are supposed to reduce the switching fields. Therefore the computed coercive fields should be taken as an upper bound but the trends observed for the simulations of different systems are still supposed to be valid. A detailed analysis of the influence of defects requires more accurate and complex

[2] The MC simulations were performed by Nikolai S. Kiselev (PGI-1/Forschungszentrum Jülich).

models which is beyond the scope of this work. Hence the MC simulations should be taken as to yield qualitative information about the magnetization process of the hybrid molecule-surface systems.

For the calculation of the clean surface energy-dependent exchange coupling constants using the Lichtenstein formula the SPR-TB-KKR program was employed [334]. During the all-electron calculations the LDA and the Perdew and Wang 1991 (PW91) [338] exchange-correlation functionals were applied. The angular momentum cutoff was set to $l_{max} = 3$ and 30×30×1 k-points were used to sample the surface BZ. The unit cell included six W layers and one Fe layer each represented by a p(1x1) surface unit cell relaxed with the VASP program using the approach described above.

A.5.1. Convergence Tests

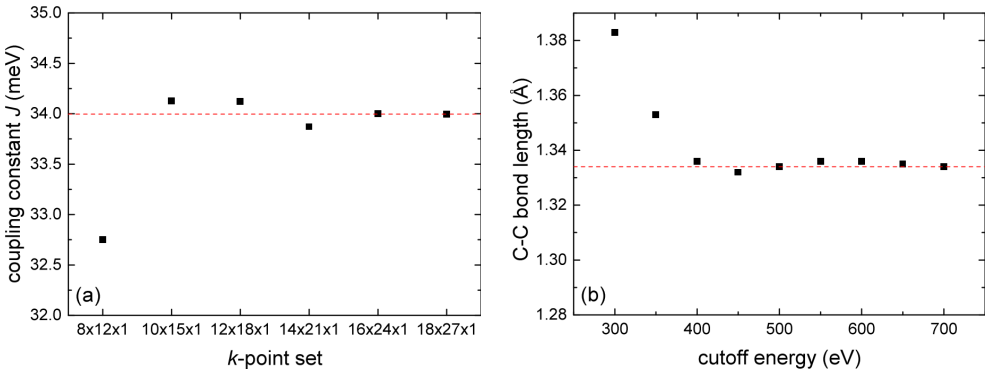

Figure A.1.: Convergence investigation of the clean surface magnetic exchange coupling constant of 1 ML Fe/W(110) with respect to the k-point set (a) and of the C-C bond length in ethene with respect to the energy cutoff (b). The red dashed line in both graphs corresponds to the value calculated with the largest number of k-points or highest energy cutoff, respectively.

A convergence investigation of the clean surface magnetic exchange coupling constant with respect to the number of k-points was carried out for a 1×1 surface unit cell of the 1 ML Fe/W(110) surface. The results of this investigation visualized in Fig. A.1(a) show that for a set of 12×18×1 k-points the coupling constant is essentially converged. This reveals that for the 3×4 surface unit cell used in the calculations with the molecules on the surface, a k-point set of $4 \times 5 \times 1$ yields reliable results. Also a convergence investigation with respect to the energy cutoff was performed. As the hardest PPs (PAW datasets) used in the calculations are associated with the elements from the second period of the periodic table, the C-C bond-length of ethene was investigated for convergence with respect to the energy cutoff. The results shown in Fig. A.1(b) outline that the bond-length is converged for an energy cutoff of 500 eV.

A.5.2. Energy-dependent exchange coupling constant of 1 ML Fe/W(110)

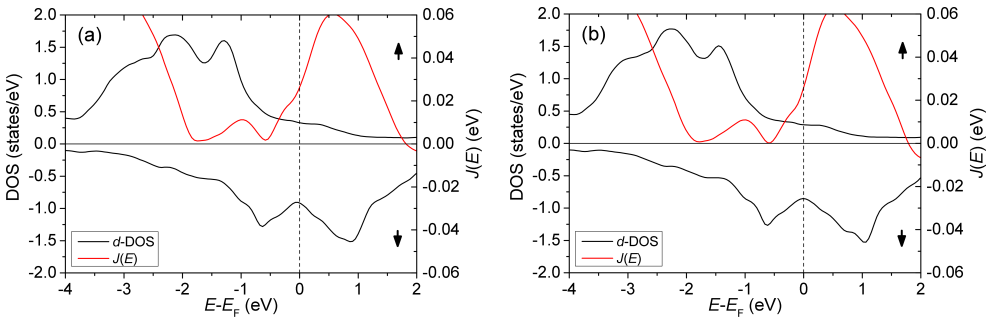

Figure A.2.: Energy-dependent exchange coupling constant and d-DOS of 1 ML Fe/W(110) calculated using the Lichtenstein formula with LDA (a) and the PW91 functional (b).

The energy-dependent exchange coupling constant of the clean 1 ML Fe/W(110) surface calculated using the Lichtenstein formula (Equation (3.17)) is depicted in Fig. A.2 together with the respective d-DOS for calculations using LDA and the PW91 functional. The value at the Fermi energy of 25.8 meV for both functionals is in reasonable agreement with the value of 35.3 meV presented in Chapter 5 taking into account the different methods and the restriction to nearest neighbor interactions in the latter case.

A.5.3. Distance Dependence of the Exchange Coupling Constants

The data of Tables 5.3 and 5.4 can be used to plot the calculated magnetic exchange coupling constants with respect to the Fe-Fe distance between the coupled centers as done in Fig. A.3. In case of the molecular-induced surface geometries (see Fig. A.3(a)) there is clearly a correlation such that for larger Fe-Fe distance the strength of the coupling decreases. On the other hand, for the hybrid molecule-surface systems (Fig. A.3(b)) the correlation is at least much less significant highlighting that in these cases the hybridization influence plays a crucial role. However it should be noted that even in Fig. A.3(a) the coupling constant does not decrease perfectly monotonically with distance which is a consequence of the fact that the surface distortions lead to a complex rehybridization of the surface Fe states.

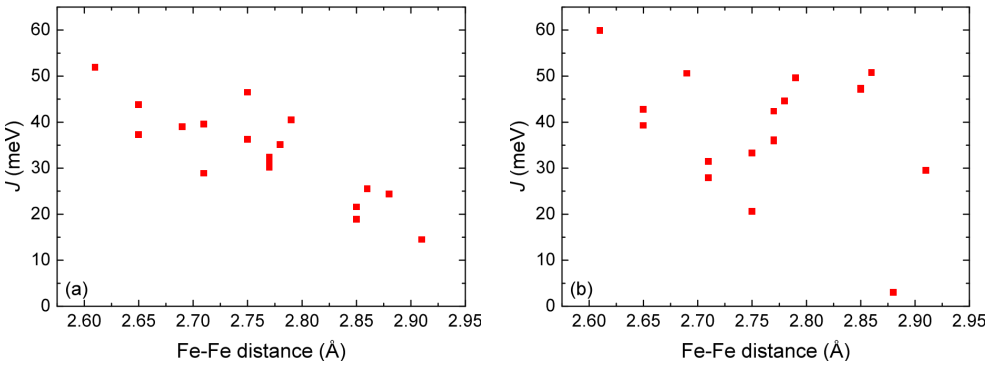

Figure A.3.: Distance dependence of the calculated magnetic exchange coupling constants for the molecular-induced surface geometries (a) and for the hybrid molecule-surface systems (b) for 1 ML Fe/W(110).

A.5.4. Small π-electron Systems with Third Period Elements on 1 ML Fe/W(110)

To complete the consideration of small organic molecules containing only one π-bond on 1 ML Fe/W(110), the adsorption of methylidenesilane (CH_4Si), phosphethene (CH_3P) and thioformaldehyde (CH_2S) (see Fig. A.4(a)) on this magnetic surface has been investigated. A representation of the electronic (KS) states of the isolated molecules is given in Fig. A.4(b). Note that again the HOMO of each molecule is aligned at the calculated IP. As in case of the molecules containing elements from the second period, both the π- and π^*-states are lowered in energy when going from CH_4Si to CH_2S. However since the heteroelements in this case are from the third period of the periodic table, their valence states are much more extended which at first leads to a larger bonding distance between carbon and the specific heteroelement. This then causes a less strong hybridization and reduced level splitting between bonding and antibonding (π-) states compared to the cases considered in Chapter 5 (see Fig. 5.2(a)).

As next step, a geometry optimization of the molecule-surface systems in the different adsorption sites depicted in Fig. 5.3 has been performed. It turned out that the molecular structures are not stable on the surface but dissociate for most positions during the relaxation. Nevertheless, the atop site is still a local minimum of the potential energy landscape. Therefore the properties of this local minimum will be considered further. A top and side view of these calculated metastable structures are depicted in Fig. A.5 and the adsorption energies are included in Table A.1. As the large adsorption energies indicate, all three systems are strongly chemisorbed on the surface. The molecule-surface distances included in Table A.1 show that the heteroatom is on average farther away from the surface atoms than the carbon atom due

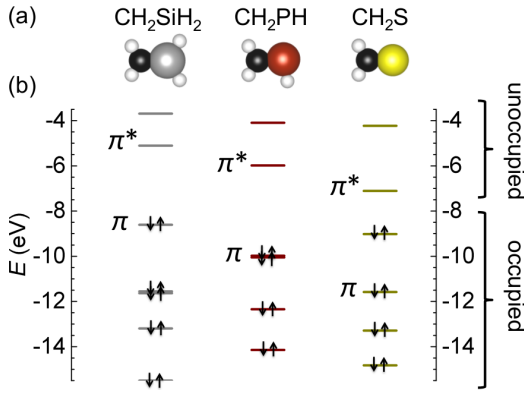

Figure A.4.: Atomic structure of methylidenesilane (CH_4Si), phosphethene (CH_3P) and thioformaldehyde (CH_2S) (from left to right) (a). Calculated energy levels of the isolated molecules (b). Note that the HOMO of each system was aligned at the calculated IP of 8.61 eV, 9.98 eV and 9.02 eV for CH_4Si, CH_3P and CH_2S, respectively. The bonding and antibonding π-states have been labeled π and π^*, respectively. The occupation of each state is indicated by arrows. Color code: white for H, black for C, gray for Si, dark red for P and yellow for S.

to the larger extent of their valence states compared to C. Especially the distance between carbon and Fe1 is small in all cases which indicates that this surface atom is strongly influenced by the molecules. The other distances of carbon to Fe3 and the distances of the heteroelement to Fe1 and Fe2 are larger although the h-Fe2 distance is quite small considering the increased spatial extent of the valence states of the elements from the third period.

Table A.1.: Calculated adsorption energies E_{ads} and molecule-surface distances for the metastable atop adsorption site of each molecule on 1 ML Fe/W(110) depicted in Fig. A.5. The adsorption energy is defined as in Equation (5.1). The labeling of the Fe1, Fe2 and Fe3 atoms is presented in Fig. 5.5. 'h' stands for 'hetero'.

molecule/surface	E_{ads} (eV)	distances (Å)				
		C-Fe1	C-Fe3	h-Fe1	h-Fe2	h-Fe3
methylidenesilane (CH_4Si)	3.24	2.08	2.26	2.38	2.31	3.48
phosphethene (CH_3P)	2.67	2.08	2.37	2.34	2.22	3.39
thioformaldehyde (CH_2S)	3.06	2.01	2.40	2.39	2.25	3.57

The strong interaction of the molecules with the surface manifests itself as in Chapter 5 by a strong influence on the magnetic moments of the Fe atoms. Essentially the three Fe atoms below the molecules (see Fig. 5.5) are affected whereas the other Fe atoms can be considered as clean surface atoms. The calculated magnetic moments of the three influenced Fe atoms are listed in Table A.2. Here the moments of Fe1 and Fe3 are nearly constant when going from

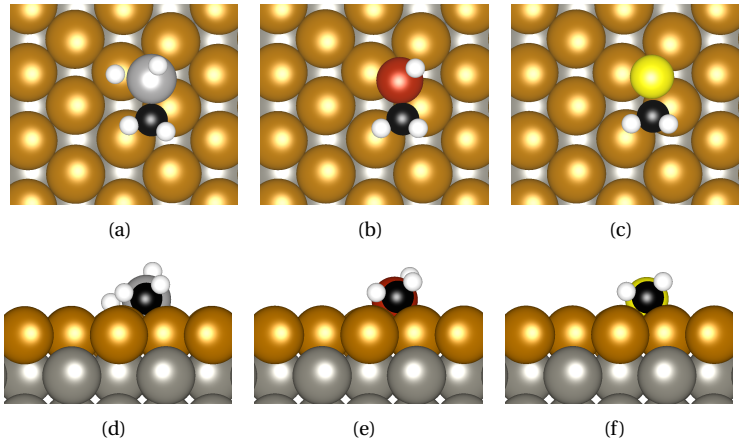

Figure A.5.: Optimized metastable structures for methylidenesilane (CH_4Si) ((a), (d)), phosphethene (CH_3P) ((b), (e)) and thioformaldehyde (CH_2S) ((c), (f)) on 1 ML Fe/W(110) in top view and side view, respectively.

one hybrid system to the other although Fe1 is more strongly influenced when compared to the clean surface moment of 2.5 μ_B. For Fe2 again the moment increases when going from methylidenesilane to thioformaldehyde in a similar way as in Chapter 5 when going from methyleneborane to formaldehyde. This indicates again a selectivity along the period due to the varying spatial extent of the π-states of the molecules.

Table A.2.: Magnetic moments of the three Fe atoms close to the π-bonded molecules with third period elements adsorbed on the 1 ML Fe/W(110) surface.

molecule/surface	magnetic moments (μ_B)		
	Fe1	Fe2	Fe3
clean surface	2.5	2.5	2.5
methylidenesilane (CH_4Si)	1.9	1.3	2.4
phosphethene (CH_3P)	1.9	1.7	2.4
thioformaldehyde (CH_2S)	2.0	1.8	2.4

The in-plane magnetic exchange coupling constants have been calculated in the same way as in Chapter 5 and the results for the hybrid molecule-surface systems and the molecular-induced surface geometries are included in Table A.3 and Fig. A.6. In case of all three hybrid systems the J_1 coupling that is mediated by the heteroatom is much smaller than the clean surface coupling of 35.3 meV with the strongest softening in case of methylidenesilane. This hints to the fact that the large extent of the states at the heteroatoms efficiently decouples the surface Fe1 and Fe2 atoms. On the other hand, J_2 which is related to the coupling over carbon

is once again strongly enhanced in all cases. Notably, the other coupling constants J_3 to J_5 are also mainly enhanced compared to the clean surface value.

Table A.3.: Calculated in-plane magnetic exchange coupling constants J between the Fe atoms as labeled in Fig. 5.5 for the hybrid molecule-surface systems and the molecular-induced surface geometries.

molecule/surface	molecule/surface (meV)					induced geometry (meV)				
	J_1	J_2	J_3	J_4	J_5	J_1	J_2	J_3	J_4	J_5
clean surface	35.3	35.3	35.3	35.3	35.3	35.3	35.3	35.3	35.3	35.3
methylidenesilane (CH_4Si)	0.5	44.8	49.2	28.4	42.7	13.9	49.6	28.1	36.0	34.3
phosphethene (CH_3P)	4.3	57.6	41.8	50.2	42.1	13.6	40.5	30.7	39.4	33.1
thioformaldehyde (CH_2S)	4.1	48.7	37.7	42.7	41.1	21.4	45.3	24.1	37.6	33.6

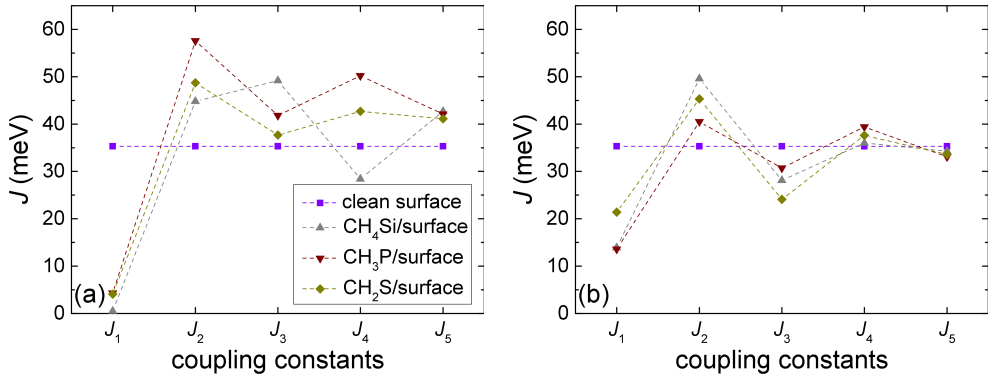

Figure A.6.: Visualization of the in-plane magnetic exchange coupling constants calculated for the hybrid molecule-surface systems (a) and for the molecular-induced surface geometries (b).

Again it is interesting to investigate which influence the distortions induced by the molecular adsorption on the surface exert on the coupling constants, i. e. how the coupling constants are modified by this geometrical effect. The calculated exchange coupling constants for the molecular-induced geometries are included in Table A.3 and Fig. A.6(b). As in Chapter 5 for the molecules with elements from the second period, these exchange coupling constants do not deviate as much from the clean surface value as in case of the hybrid systems. Nevertheless J_1 is also much smaller than the clean surface value which is a consequence of the increased distance between Fe1 and Fe2 (see Table A.4) due to the surface relaxation induced by the respective heteroatom. Also in case of the other coupling constants, their deviation from the clean surface value can be traced back to the induced surface distortions listed in

Table A.4. More precisely, the increase in J_2 comes from the reduced distance between Fe1 and Fe3 with the shortest Fe-Fe bond length in the methylidenesilane case which hence leads to the largest coupling constant. J_3 is slightly decreased due to the distance increase between Fe1 and its clean surface neighbors. Finally, J_4 and J_5 are not any more strongly affected since the corresponding distances are not significantly changed. Consequently, the same statement as in Chapter 5 holds, i. e. the change of the distances between the surface atoms induced by the molecular adsorption has an influence on the size of the coupling constants but when the molecules are present and hybridize with the states of the surface, the resulting coupling constants are even more strongly and in part also qualitatively differently changed.

Table A.4.: Fe-Fe distances for the small π-electron systems with third period elements on 1 ML Fe/W(110). The clean surface (cs) Fe-Fe distance is 2.75 Å.

molecule/surface	distances (Å)				
	Fe1-Fe2	Fe1-Fe3	Fe1-cs	Fe2-cs	Fe3-cs
methylidenesilane (CH_4Si)	2.92	2.60	2.72	2.68	2.81
phosphethene (CH_3P)	2.97	2.65	2.72	2.66	2.80
thioformaldehyde (CH_2S)	2.86	2.63	2.78	2.70	2.79

This picture is also further supported when the SP-PDOS of all d-states of Fe1 for the methylidenesilane-surface system and the thioformaldehyde-surface system is compared to the SP-PDOS of the clean surface as depicted in Fig. A.7. Clearly, the SP-PDOS of the clean surface is altered strongly due to the hybridization with the states of the molecules. As for the small π-electron systems in Chapter 5, the change of the SP-PDOS is much less pronounced in case of the molecular-induced surface geometries (see Fig. A.7(b)).

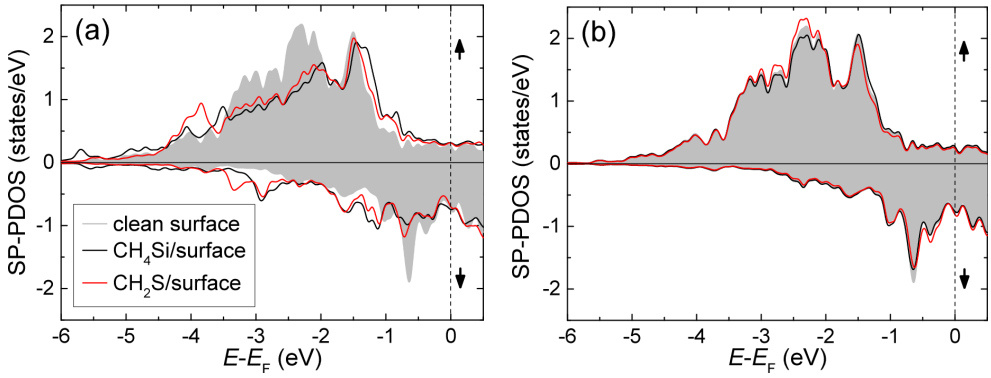

Figure A.7.: SP-PDOS of the d-states of the Fe1 atom for (a) the hybrid molecule surface systems and (b) the molecular-induced surface geometries for the small π-electron systems with third period elements on 1 ML Fe/W(110). For clarity, only the SP-PDOS for the clean surface, the CH_4Si-surface system and the CH_2S-surface system are shown as the results of the other system are qualitatively similar.

A.6. Dioxan and Dioxin on 1 and 2 ML Fe/W(110)

The unit cell consisted of one Fe layer and six W layers (1 ML Fe/W(110)) or two Fe layers and five W layers (2 ML Fe/W(110)) each represented by a 3×4 in-plane surface unit cell out of 24 Fe or W atoms. The molecules were adsorbed on top of the uppermost Fe layer. The vacuum distance perpendicular to the surface plane to the next periodic image was about 16 Å. The lateral distance between molecules in neighboring unit cells was at least 8 Å. During the geometry optimization the upper three W layers for 1 ML Fe/W(110) or the upper two W layers for 2 ML Fe/W(110), the Fe layers and the molecular coordinates were allowed to relax. To properly account for weak molecule-surface interactions, the dispersion correction DFT-D3 of Grimme and coworkers according to Ref. [109] was used.

A.6.1. SP-PDOS for the Molecular-induced Geometries

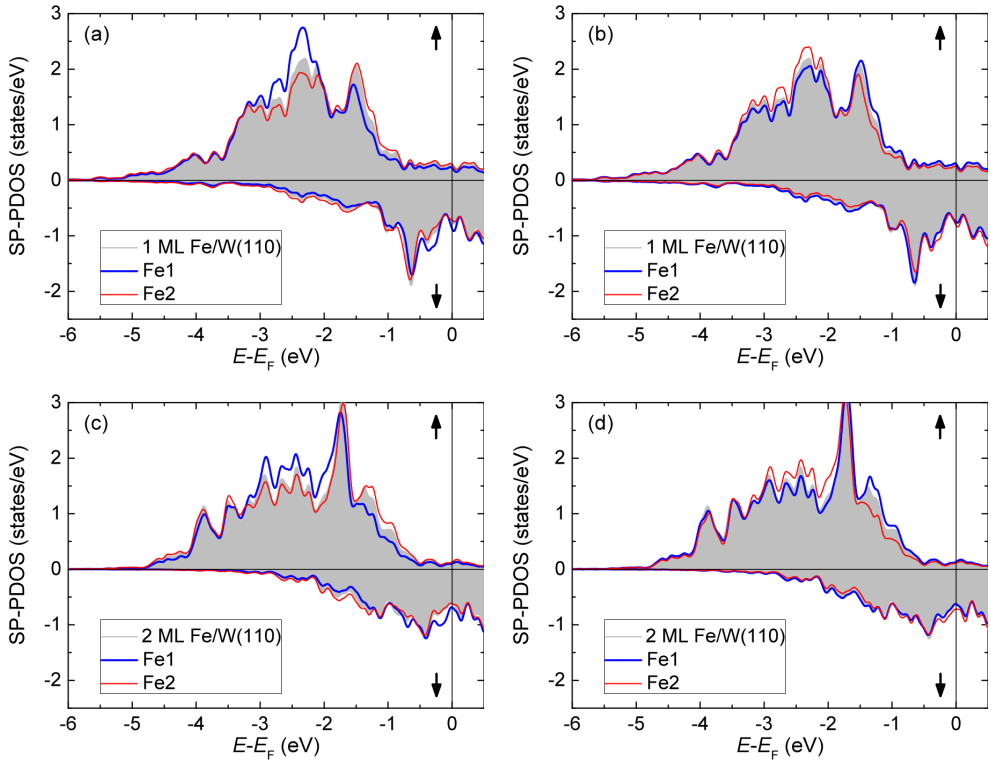

Figure A.8.: SP-PDOS of all d-states of Fe1 and Fe2 for the molecular-induced geometries of dioxan (a), (c) and dioxin (b), (d) on 1 and 2 ML Fe/W(110), respectively. As a reference, also the SP-PDOS of a clean surface Fe atom of the respective surface is given as gray shaded area.

A.7. Gr and hBN on Co(111)

For each calculation a k-point set of 32×32×1 k-points was applied since the inter-layer exchange coupling constant is converged for this sampling of the BZ as outlined in Fig. A.9. As Co was proposed to exhibit strong correlation effects [339], the DFT+U formalism [340] has been applied for the d-states of Co in the rotational invariant form [341] with an effective Hubbard-like interaction parameter U_{eff} = 3 eV consistent with previous calculations [51, 339]. The use of the DFT+U formalism is also supported by the finding that this scheme allows to reproduce the experimental spin polarization of Co-surfaces according to SP-STM measurements [50, 342].

The unit cell of the slab incorporated seven Co layers in fcc stacking each represented by a 1×1 in-plane unit cell containing one Co atom. Gr and hBN were adsorbed on one side of the slab with 2 atoms per unit cell by adapting the lattice constants of the surface and the 2D materials, i. e. making them commensurate, which has been a common procedure in previous investigations [296, 298, 343, 344] as it reduces the computational effort considerably. More precisely, in the present calculations the lattice constant of Gr and hBN has been adapted to the in-plane lattice constant of Co(111) using the experimental value of 3.545 Å of fcc-Co [345]. This adaptation of the lattice constants is justified by the observation that the Gr lattice constant of 2.46 Å [346] is very close to the 2.507 Å in-plane lattice constant of the Co(111) surface unit cell [345]. In case of hBN the mismatch to the surface is even smaller when taking into account its bulk in-plane lattice constant of 2.504 Å measured via X-ray diffraction [347][3].

The vacuum distance perpendicular to the surface plane to the following supercell was set to about 18 Å to avoid interaction between the periodic images. For the structural relaxation the rev-vdW-DF2+U functional was used to take into account non-local correlation effects (vdW interaction, see Subsection 2.2.4). During the geometry optimization the upper four Co layers and the coordinates of the 2D materials were allowed to relax. The magnetic exchange coupling constants were determined from the total energy differences between FM and AFM configurations for which PBE+U yields reliable results.

A.7.1. Convergence Test

A convergence investigation of the clean surface inter-layer magnetic exchange coupling constant with respect to the number of k-points has been carried out for a 1×1 surface unit cell of the Co(111) surface. The results of this investigation visualized in Fig. A.9 show that for a set of 32×32×1 k-points the coupling constant is essentially converged.

[3] The calculated lattice constants for Gr are 2.477 Å using the rev-vdW-DF2 functional [99–103] and 2.479 Å using PBE. For hBN the calculated lattice constants are 2.523 Å (rev-vdW-DF2) and 2.525 Å (PBE) which are close to previous calculations that estimated 2.51 Å [299, 348]. The calculated in-plane lattice constants of Co(111) are 2.492 Å using the rev-vdW-DF2+U functional and 2.519 Å using PBE+U.

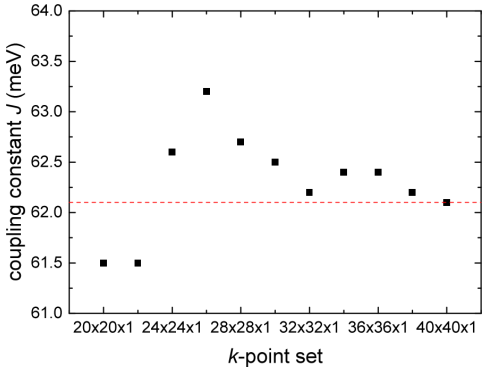

Figure A.9.: Convergence investigation of the clean surface inter-layer exchange coupling constant of the Co(111) surface with respect to the k-point set. The red dashed line corresponds to the value calculated with the largest number of k-points.

A.7.2. Results Obtained with the PBE Functional

Table A.5.: Adsorption energies per unit cell E_{ads} and distances for Gr and hBN on the Co(111) surface in top-fcc and top-hcp geometry using PBE, respectively. C_{top} and C_{fcc} stand for the C atoms of Gr adsorbed in the top site and fcc site, respectively. The nomenclature of the Co atoms is in accordance with the labeling in Fig. 7.5. The adsorption energy is defined analogously as in Equation (5.1) where in the present case E_{mol} has to be substituted by E_{2D} which stands for the total energy of the respective freestanding 2D material.

system/surface	E_{ads} (eV)	distances (Å)		
		Co1-Co2	C_{top} (N)-Co1	C_{fcc} (B)-Co1
clean surface	-	2.44	-	-
Gr	0.04	2.43	2.15	2.58
hBN	0.08	2.43	2.18	2.52

Table A.6.: Magnetic moments in μ_B and evaluated exchange coupling constants in meV for the hybrid Gr- and hBN-surface systems and the surface geometries induced by the 2D materials on the Co(111) surface using the PBE functional.

system/surface	magnetic moments		with 2D material		induced geometry	
	Co1	Co2	$J_\parallel$	$J_\perp$	$J_\parallel$	$J_\perp$
clean surface	1.75	1.68	35.0	63.5	35.0	63.5
Gr	1.57	1.66	34.0	48.7	35.8	63.1
hBN	1.60	1.68	25.9	58.9	38.5	64.3

A.8. TPT on 2 ML Fe/W(110)

The unit cell consisted of two Fe layers and five W layers each represented by a 5×7 in-plane surface unit cell out of 70 Fe or W atoms. The TPT molecule was adsorbed on top of the Fe layers. The vacuum distance perpendicular to the surface plane to the next periodic image was about 18 Å. The lateral distance between molecules in neighboring unit cells was at least 10 Å. During the geometry optimization the upper two W layers, the Fe layers and the molecular coordinates were allowed to relax.

A.8.1. SP-PDOS of the Fe d-states for TPT on 2 ML Fe/W(110)

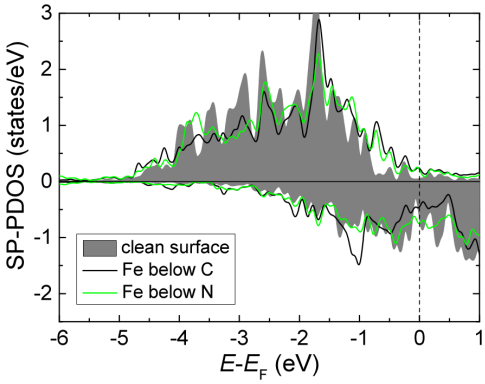

Figure A.10.: SP-PDOS of all d-states of Fe atoms below N and C for TPT on 2 ML Fe/W(110). As a reference, also the SP-PDOS of a clean surface Fe atom is given as gray shaded area.

A.9. Ammonia (NH_3) and Borane (BH_3) on $BiAg_2$/Ag(111)

For each calculation a k-point set of 15×15×1 k-points was used. In the unit cell each layer was represented by a $(\sqrt{3}\times\sqrt{3})R30°$ in-plane surface unit cell out of 3 Ag atoms or 2 Ag and 1 Bi atom for the first and last layer. The slab was made up of ten layers. The molecules were adsorbed on both sides of the slab. The vacuum distance perpendicular to the surface plane to the following supercell was set to about 15.5 Å for the clean surface and resulted in at least 7.6 Å for the hybrid systems[4]. The distance between molecules in neighboring unit cells was

[4] A test calculation with an increased vacuum distance of about 14 Å for the hybrid systems showed only a negligible difference in the obtained results.

about 5.1 Å. During the geometrical relaxation the upper and lower four layers on both sides of the slab and the molecular coordinates were allowed to relax whereas the two layers in the center of the slab were held fixed. The structures were relaxed in a spin-unpolarized calculation using the rev-vdW-DF2 functional [99–103]. The band structures were subsequently calculated for these relaxed geometries using the PBE functional and taking into account SOC since reliable band structures for the $BiAg_2$/Ag(111) surface alloy have already previously been obtained for this functional [314].

A.9.1. Convergence Tests

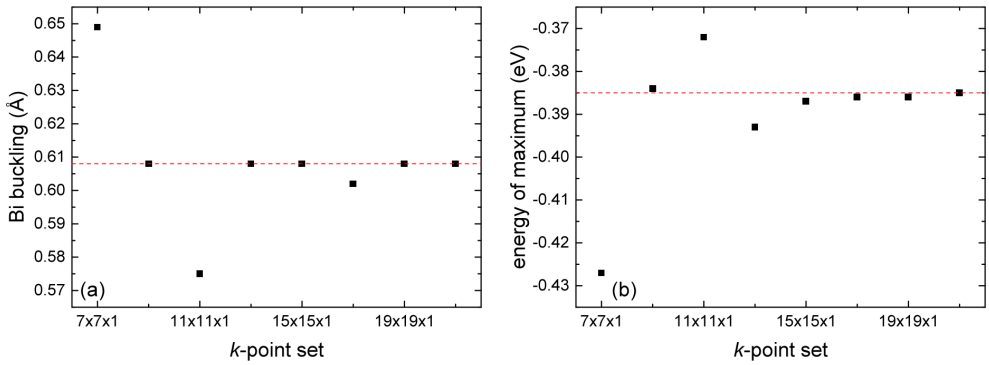

Figure A.11.: Convergence investigation of the clean surface Bi buckling out of the first layer (a) and the energetic position of the maximum of the occupied Rashba split surface state (b) of the $BiAg_2$/Ag(111) surface alloy with respect to the k-point set. The red dashed line in both graphs corresponds to the value calculated with the largest number of k-points.

A convergence investigation of the clean surface Bi buckling out of the first surface layer was carried out with respect to the number of k-points for the $(\sqrt{3}\times\sqrt{3})R30°$ in-plane surface unit cell of the $BiAg_2$/Ag(111) surface alloy (see Fig. A.11(a)). The buckling is clearly converged for a set of 15×15 k-points on a scale relevant for the observed changes in the hybrid systems. Also the energetic position of the parabola maximum of the occupied Rashba split surface state is converged for this k-point set as indicated in Fig. A.11(b).

A.9.2. Effective masses of the surface states for NH_3 and BH_3 on $BiAg_2$/Ag(111)

Table A.7.: Effective masses $m^{*,\mathrm{occ}}$, $m^{*,\mathrm{unocc}}$ and $m^{*,\mathrm{unocc,2}}$ of the Rashba split surface states for NH_3 and BH_3 on the $BiAg_2$/Ag(111) surface alloy as well as for the respective molecular-induced geometries. The effective masses were deduced from a quadratic fit of the respective surface states in the band structure.

system/surf.	$m^{*,\mathrm{occ}}$ (m_e) $\overline{\Gamma\mathrm{M}}_1/\overline{\Gamma\mathrm{K}}_1/\overline{\Gamma\mathrm{M}}_2/\overline{\Gamma\mathrm{K}}_2$	$m^{*,\mathrm{unocc}}$ (m_e) $\overline{\Gamma\mathrm{M}}_1/\overline{\Gamma\mathrm{K}}_1/\overline{\Gamma\mathrm{M}}_2/\overline{\Gamma\mathrm{K}}_2$	$m^{*,\mathrm{unocc,2}}$ (m_e) $\overline{\Gamma\mathrm{M}}_1/\overline{\Gamma\mathrm{K}}_1/\overline{\Gamma\mathrm{M}}_2/\overline{\Gamma\mathrm{K}}_2$
clean surf.	−0.28/−0.28/−0.28/−0.28	−0.17/−0.17/−0.17/−0.17	-/-/-/-
NH_3	−0.29/−0.30/−0.26/−0.28	−0.19/−0.16/−0.18/−0.15	-/-/-/-
BH_3	-/-/-/-	−0.19/−0.23/−0.09/−0.12	−0.22/-/−0.11/−0.16
NH_3 induced	−0.24/−0.25/−0.24/−0.25	−0.16/−0.14/−0.16/−0.14	-/-/-/-
BH_3 induced	-/-/-/-	−0.24/−0.24/−0.20/−0.19	−0.17/-/−0.16/−0.17

A.10. TPT on 2 ML Co/Cu(111)

The unit cell consisted of two fcc-stacked Co layers on top of five fcc-stacked Cu layers each represented by a 8×8 in-plane surface unit cell out of 64 Co or Cu atoms. The TPT molecule was adsorbed on top of the Co layers. The vacuum distance perpendicular to the surface plane to the next periodic image was about 18 Å. The lateral distance between molecules in neighboring unit cells was at least 8.8 Å. During the geometry optimization the upper Cu layer, the Co layers and the molecular coordinates were allowed to relax.

A.11. Graphene on 1 ML Fe/Co on Cu(111)

The spin-polarized electronic structure calculations within the DFT-based KKR formalism were carried out using the SPR-TB-KKR program [334]. During the all-electron calculations the LDA exchange-correlation functional was applied. The angular momentum cutoff was set to $l_{\max} = 3$ and 32×32×1 k-points were used to sample the surface BZ. The systems were also treated with the VASP program using the same k-point set. In case of the DFT+U calculations [340] the rotational invariant formulation [341] was applied using an effective Hubbard-like interaction parameter of $U_{\mathrm{eff}} = 3$ eV for the d-states of Co.

The unit cell included 17 fcc-stacked Cu layers, one fcc-stacked Fe or Co layer and one Gr layer adsorbed on each side of the slab. Due to the small in-plane lattice mismatch between the (111) surface of fcc Cu and Gr (agreement of the lattice constants is about 96% [346, 349])

Gr was treated commensurate on the substrate using the experimental lattice constant of bulk fcc Cu of 3.615 Å [349]. Hence the in-plane unit cell included one atom per metallic layer and two C atoms for Gr. The distance between Gr and the first surface layer was set to 2.09 Å. In the VASP calculations the vacuum distance perpendicular to the surface to the next periodic image was set to about 14.5 Å.

B TPT on 2 ML Co/Cu(111)

In addition to the case of TPT adsorbed on the 2 ML Fe/W(110) surface presented in Chapter 8 supplemental results were also obtained for this molecule on the 2 ML Co/Cu(111) substrate which are presented in this chapter. In the present case the symmetries of the TPT molecule and the surface are compatible in the sense that the adsorption position now shows threefold rotational symmetry as the isolated TPT. Consequently, in this case only two different magnetic units are formed below the molecule associated with the triazine-like and the phenyl rings, respectively.

B.1. Adsorption Geometries and Structural Properties

The adsorption positions investigated for TPT on 2 ML Co/Cu(111)[1] are presented in Fig. B.1. With respect to the central triazine-like ring the molecule can be positioned in the C-hollow site (Fig. B.1(a)) on the surface with the C atoms of the central ring occupying hcp hollow positions of the surface and the N atoms being positioned on top of Co atoms. From this position the molecule can be shifted such that two N-C bonds of the central ring lie on top of Co atoms giving rise to the N-C bond top site (Fig. B.1(b)). Moreover, also the N-hollow site (Fig. B.1(c)) was investigated in which the nitrogens occupy fcc hollow sites and the C atoms of the central ring are on top of surface Co atoms. In contrast to the adsorption position found for TPT on 2 ML Fe/W(110) all present adsorption positions retain a certain degree of symmetry. The C-hollow and N-hollow sites clearly show threefold rotational symmetry (with additional mirror planes) and the N-C bond top position has a mirror plane going through the upper N and lower C atom of the central triazine-like ring.

The stability of the different adsorption positions was first investigated using a reduced number of layers in the supercell, i. e. a slab with one Cu layer and two Co layers and the TPT molecule adsorbed on top. During the relaxation the uppermost Co layer and the molecular coordinates were allowed to relax. The adsorption energies obtained from this investigation are listed in Table B.1. Clearly, the C-hollow site is favored by about 0.6 eV over the N-hollow site and the N-C bond top site turns out to be no (local) minimum and hence the molecule moves towards the stable C-hollow site during the relaxation. The energetic preference of the C-hollow site was further confirmed when the relaxation was carried out using the rev-vdW-DF2 functional [99–103] corroborating the 0.6 eV energy difference between the two adsorption positions. The relaxation was also continued for a unit cell incorporating 5 Cu layers following the approach described in Section A.10 for both the C-hollow and the N-hollow

[1] In the present study an fcc-stacking of the two Co layers with respect to the underlying Cu(111) substrate was assumed.

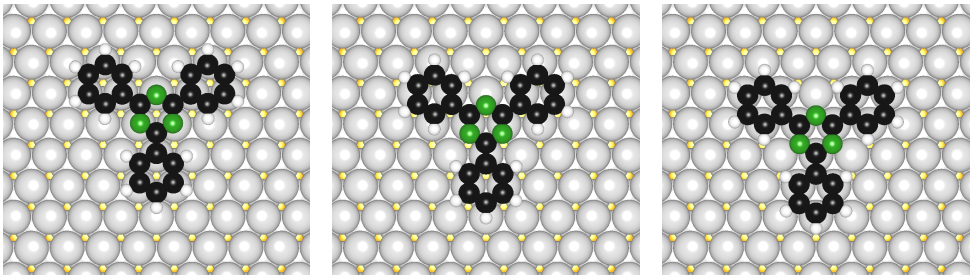

(a) C-hollow site (b) N-C bond top site (c) N-hollow site

Figure B.1.: Investigated adsorption sites for TPT on 2 ML Co/Cu(111). Color code for molecular atoms same as in Fig. 5.2. Color code of the surface atoms: light gray for Co and orange for Cu.

geometries. Once again the adsorption energies included in Table B.1 show a strong energetic preference of the C-hollow site. The relaxed C-hollow geometry is depicted in Fig. B.2(a) and (b) in both top and side view, respectively. This adsorption position is consistent with the general tendency of N to adsorb on top of surface atoms as found in Chapters 7 and 8[2]. If one performs a similar symmetry analysis as in Chapter 8 one finds that the isolated TPT molecule (D_{3h} symmetry) and the isolated surface (C_{3v} symmetry) combine to form a hybrid system showing C_{3v} symmetry, i. e. the symmetries of the two individual systems are more compatible than in the TPT on 2 ML Fe/W(110) case in the sense that not all symmetries of the D_{3h} group are broken in the hybrid system.

Table B.1.: Calculated adsorption energies E_{ads} for TPT on 2 ML Co/Cu(111) for the different adsorption sites with a slab containing one or five Cu layers. The adsorption energy is defined as in Equation (5.1).

position	E_{ads} (eV)
	1 Cu/5 Cu
C-hollow site	**2.79/3.55**
N-hollow site	2.18/3.05
N-C bond top site	moves towards C-hollow site

The hybrid system can be further characterized by the overview of the molecule-surface bond distances between the molecular C/N centers and the surface Co atoms given in Table B.2. All three N atoms of the central triazine-like ring and all C atoms of the phenyl rings sitting directly on top of surface Co atoms bind closely to the surface in that the corresponding molecule-surface distances are between 2.0 Å and 2.1 Å. This tight bonding of the TPT

[2]STM measurements performed by Taner Esat (PGI-3 and PGI-6, Forschungszentrum Jülich) also indicate that the adsorption geometry with the molecular nitrogens on top of surface Co atoms is most stable.

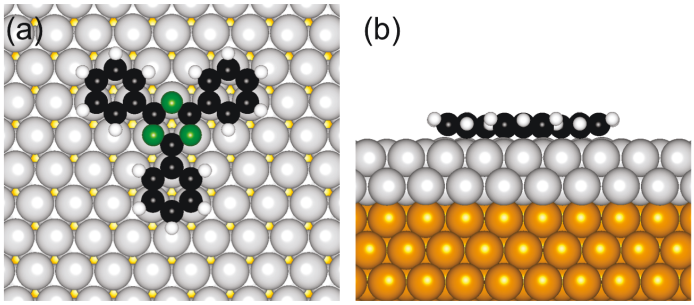

Figure B.2.: Optimized stable structure for TPT on 2 ML Co/Cu(111) in top view (a) and side view (b), respectively.

to the 2 ML Co/Cu(111) surface is also obvious in the side view in Fig. B.2(b) showing that the whole molecular plane is closely attached to the surface. As for the 2 ML Fe/W(110) surface these findings point to a chemisorption of the TPT molecule which is supported by the large adsorption energy given in Table B.1. When the two different types of molecular rings are compared, the central triazine-like ring is on average 0.05 Å lower in height above the surface than the peripheral phenyl rings.

Table B.2.: Overview of the molecule-surface distances between the molecular C/N atoms and the surface Co atoms for TPT on 2 ML Co/Cu(111).

distance range (Å)	number of bonds
2.0-2.1 (Co-N)	3
2.0-2.1 (Co-C)	9
2.4-2.6 (Co-C)	33
2.7-2.8 (Co-C)	3

When analyzing the distortions of the Co-Co distances on the surface induced by the adsorption of the TPT, in general the in-plane distances within the first Co layer below both the phenyl rings and the triazine-like ring are increased by 0.07 Å to 0.12 Å compared to the clean surface nearest neighbor in-plane Co-Co distance of 2.57 Å. This is supposed to be a consequence of (i) the rigid structure of the individual molecular rings and (ii) the favorable interaction when molecular atoms are placed directly above surface Co atoms. In addition, the inter-layer Co-Co distances between the first and second Co layer are in general increased compared to the clean surface inter-layer distance of 2.40 Å as indicated in Table B.3. Only the inter-layer distance of the Co atoms directly below the N atoms to their second layer nearest neighbor Co atoms not positioned underneath the molecular structure are slightly decreased. Hence it can be concluded that the molecular induced skyhook effect, i. e. the molecular induced detaching of the first layer magnetic surface atoms from the second layer below the molecule, established in Chapter 6, is also operational in the present case as can also be seen

when looking closely at the side view in Fig. B.2(b). In this figure also the retraction of the H atoms from the surface can be clearly seen. On average the Co-Co inter-layer distance below the triazine-like ring is 2.41 Å whereas it amounts to 2.44 Å underneath the phenyl rings[3]. This clearly underlines that the induced lift off of the first layer Co atoms is strongest below the parts of the molecule where the hydrogens are attached.

Table B.3.: Overview of the inter-layer Co-Co distances for TPT on 2 ML Co/Cu(111). The clean surface inter-layer Co-Co distance is 2.40 Å.

distance range (Å)	number of bonds
2.37-2.40	3
2.40-2.45	21
2.45-2.48	12

B.2. Simulated STM Images and Spin-polarized Projected Density of States

An overview of simulated STM topography images in Tersoff-Hamann approximation is presented Fig. B.3. Analogously to the description in Section 8.3 the images display isosurfaces of the charge density within the specific energy intervals given by the bias voltage. In all cases the images show a threefold rotational symmetry as expected from the threefold symmetric adsorption geometry in Fig. B.2(a). When looking more closely to the spin averaged images in the top row of Fig. B.3 for negative bias voltages the central triazine-like ring appears less bright than the peripheral phenyl based lobes[4]. On the other hand for +0.25 V and +0.5 V especially the nitrogen centers of the central ring show high intensity whereas for +1 V the central ring is less bright again. The general trend for a higher brightness of the phenyl based lobes compared to the central ring corresponding to a higher position of the isosurface above these lobes is in agreement with the closer binding of the central triazine-like ring to the surface as outlined in Section B.1.

The simulated images for the spin up and spin down channels given in the second and third rows of Fig. B.3 show that in general the molecule appears brighter in the up channel than in the down channel and that the increased brightness at the N centers for +0.25 V and +0.5 V originates from majority spin states. Most remarkably, at −0.15 V no majority spin states are present as can also be seen in the SP-PDOS in Fig. B.4 yielding a dark image[5]. However in

[3]The largest Co-Co inter-layer distance found below the phenyl rings is 2.47 Å.
[4]The terms 'lobe' and 'ring' are treated as synonyms in this chapter.
[5]This finding might be hard to prove experimentally because of the difficulty to measure zero current.

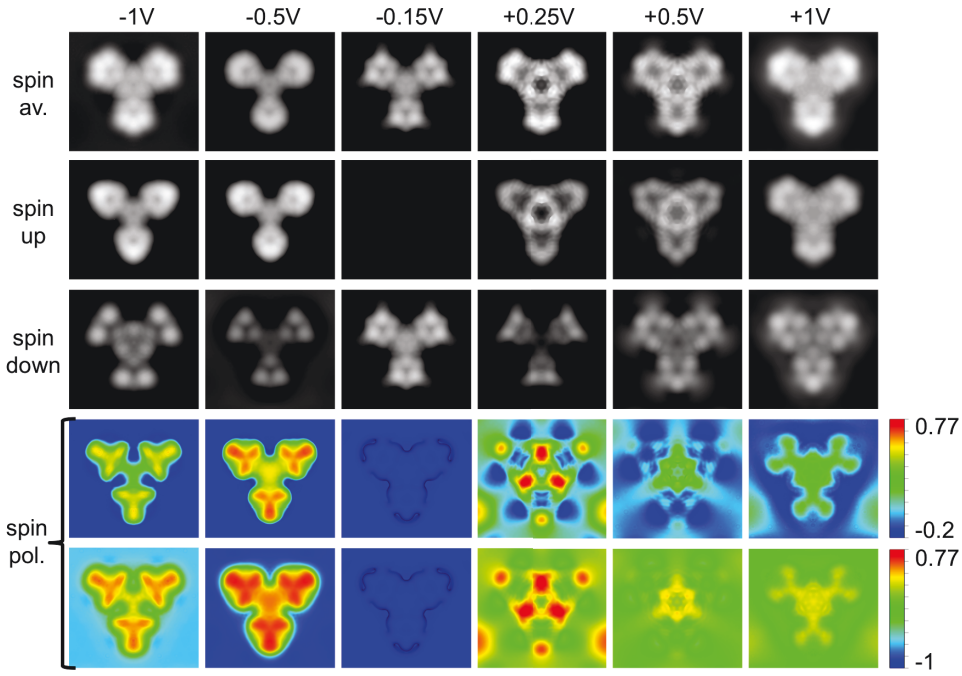

Figure B.3.: Overview of the simulated STM topography images for TPT on 2 ML Co/Cu(111) at different bias voltages. In the first row the spin averaged topography images are presented. In the second and third rows the images for the spin up and spin down channel are given, respectively. The last two rows show the deduced spin polarization at the different bias voltages. The spin averaged, spin up and spin down images at -1 V, -0.5 V and +0.5 V are displayed for an isovalue of $1.35 \cdot 10^{-5}$ $e/\text{Å}^3$, at -0.15 V for $3.37 \cdot 10^{-6}$ $e/\text{Å}^3$, at +0.25 V for $5.40 \cdot 10^{-6}$ $e/\text{Å}^3$ and at +1 V for $5.40 \cdot 10^{-5}$ $e/\text{Å}^3$. All images for the spin polarizations were made for an isovalue of $1.35 \cdot 10^{-5}$ $e/\text{Å}^3$ colored with the degree of spin polarization at each point. The scale bars to the right of the last two rows indicate the respective range of spin polarization. The orientation of the TPT molecule on the surface is in every case the same as in Fig. B.2(a). The dark contour seen in the spin polarization images at -0.15 V is caused by the proximity of the isosurface to the molecular structure resembling the periphery of TPT on the surface.

the minority spin channel states are available in this energy interval, i. e. the system shows half-metallic behavior at -0.15 V.

This has interesting consequences for the spin polarization according to Equation (4.4) as indicated in the last two rows in Fig. B.3. For most bias voltages the negative spin polarization of the substrate, for which minority spin states dominate at the Fermi level, is inverted above the molecule, i. e. there it is dominated by majority spin states consistent with the results of

Ref. [19] and Chapter 8. The largest degrees of inversion, i. e. the largest positive spin polarizations above the molecule are seen at −0.5 V and +0.25 V whereas for increased positive or negative voltages the effect is diminished. Remarkably, the highest positive spin polarization of about 77% is found in the area above the N centers at +0.25 V due to the localization of the states at these centers in the spin up channel within this energy interval. However the consequence of the half-metallic behavior at −0.15 V is that the spin polarization is exactly −100% over the whole unit cell. If analogously as in Chapter 8 the range of the scale bar for the spin polarization is extended as in the last row in Fig. B.3 it becomes evident that also the (negative) spin polarization of the substrate varies over a wide range for the different bias voltages.

Consequently, these results reveal on the one hand similar as in Chapter 8 a strongly spatially varying intramolecular spin polarization between the different triazine-like and phenyl based lobes. On the other hand also a strong energy dependence of the spin polarization is observed in that the type of spin picked up above the molecule can be switched almost completely from up to down when changing the bias voltage from for instance −0.5 V to −0.15 V.

In Fig. B.4 an overview of the SP-PDOS above the two types of molecular rings, the whole molecular part and for the d-states of selected surface Co atoms positioned directly below C or N is presented. The dashed lines in the figure indicate the bias ranges relative to the Fermi energy for which the simulated STM images in Fig. B.3 were generated. All diagrams show the strong hybridization of the TPT with the substrate indicating chemisorption as already concluded from the structural analysis in Section B.1. Clearly the half-metallic behavior in the energy range down to −0.15 eV below the Fermi energy can be identified in all diagrams since in every case only minority spin states can be found in this energy region. In case of the molecular SP-PDOS in addition to the total value also the contribution of σ- and π-states is given emphasizing again that the electronic structure at the molecular site near the Fermi energy is dominated by π-states. As explained in Chapter 8 these states are predominantly measured by STM due to their increased spatial extent perpendicular to the surface compared to the σ-states.

When comparing the PDOS derived from the two types of rings it can be seen that the SP-PDOS of the phenyl ring in Fig. B.4(b) is in general more strongly broadened than the SP-PDOS of the triazine-like ring in Fig. B.4(a) being consistent with the in general weaker interaction of N with the surface as compared to C found in Chapter 5. Especially the two peaks in the majority spin channel in the SP-PDOS derived from the triazine-like ring at about +0.1 V and +0.45 V are most remarkable giving rise to the observed brightness increase of this ring in the STM images at +0.25 V and +0.5 V. As in Chapter 8 the general inversion of the spin polarization above the molecule with respect to the substrate can be clearly seen when comparing Fig. B.4(c) and (d). Besides the half metallic region below E_F the spin polarization above the

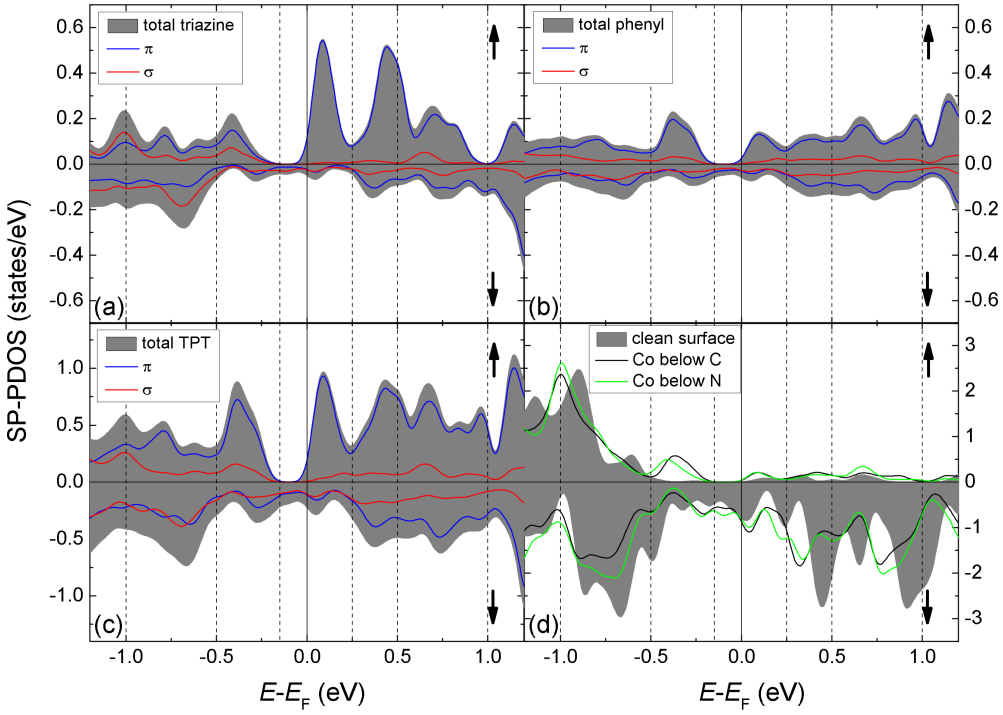

Figure B.4.: SP-PDOS of the individual molecular triazine-like (a) and phenyl (b) rings, total molecular SP-PDOS (c) and d-states of surface Co atoms positioned below a C or N atom (d) for TPT on 2 ML Co/Cu(111). As a reference, in (d) also the SP-PDOS of a clean surface Co atom is given as gray shaded area. The dashed lines indicate the bias voltages relative to the Fermi energy for which the images in Fig B.3 were simulated. The phenyl SP-PDOS in (b) was summed over all centers of one phenyl unit.

TPT is positive whereas it is negative even for the Co atoms below the molecule as outlined in Fig. B.4(d). The SP-PDOS of the Co d-states displayed over a larger energy region is given in Fig. B.5 explicitly indicating a strong molecule-surface hybridization over the whole energy range of the d-bands. As already noted in Chapter 8 it should be realized that the SP-PDOS visualized in Fig. B.4 is not directly comparable to the LDOS measured by STM since the tip is positioned at least several Å above the molecule and the SP-PDOS shown is obtained from the states within the PAW spheres centered around the nuclei.

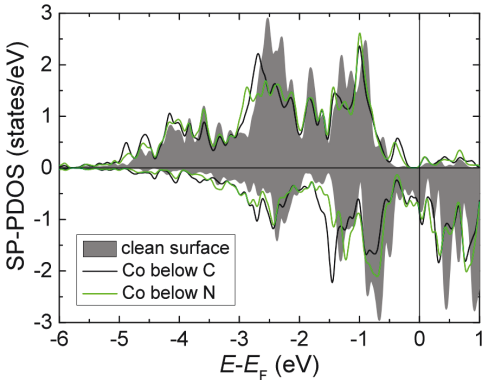

Figure B.5.: SP-PDOS of all d-states of Co atoms below N and C for TPT on 2 ML Co/Cu(111). As a reference, also the SP-PDOS of a clean surface Co atom is given as gray shaded area.

B.3. Magnetic Moments and Exchange Coupling Constants

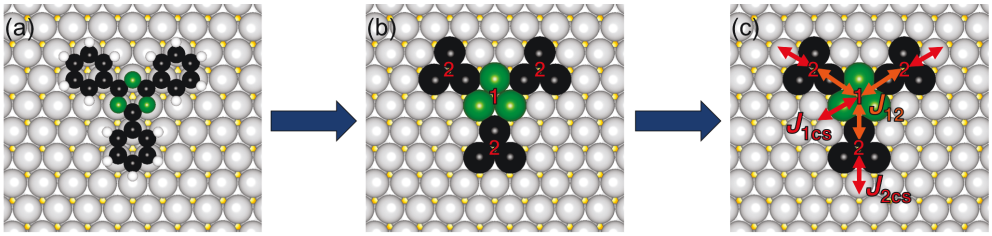

Figure B.6.: The interaction of TPT with the 2 ML Co/Cu(111) surface (a) is confined to the twelve Co atoms directly bound to it (b). Below the different rings of the molecule magnetic units are formed which are labeled as 1 and 2 since the phenyl based units are equivalent by symmetry. To calculate the magnetic exchange coupling constants for the different units the couplings between the units and from each unit to the clean surface need to be considered as assigned in (c).

The influence of the TPT adsorption onto the surface is confined to the twelve first layer Co atoms it is directly bound to as indicated in Fig. B.6(b) consistent with the results of Chapter 8 for TPT on 2 ML Fe/W(110). According to the concepts developed in Ref. [52] and Chapter 8, the surface Co atoms below each molecular ring can be grouped into strongly exchange coupled magnetic units below (i) the triazine-like ring (unit 1) and (ii) the phenyl rings (unit 2). The magnetic moments of the Co centers for the respective units are listed in Table B.4 and show as in all previous chapters that as a consequence of the molecule-surface hybridization

the values are reduced compared to the clean surface moment of 1.8 μ_B. In agreement with the findings of Chapter 5 the moments below N are 0.1 μ_B to 0.2 μ_B less diminished than the ones underneath C atoms.

Table B.4.: Overview of the magnetic moments of the surface Co atoms directly bound to TPT on 2 ML Co/Cu(111) assigned to the molecular-induced magnetic units defined in Fig. B.6(b). The clean surface first and second layer Co moments are 1.8 μ_B and 1.6 μ_B, respectively.

magnetic unit	moment per Co atom (μ_B)
1	1.6
2	1.4-1.5

When calculating the effective exchange coupling constants for this arrangement according to the procedure developed in Chapter 8, the internal coupling J_{12} between the two molecular-induced magnetic units and the coupling of each unit to the respective nearest neighbor clean surface unit J_{1cs} and J_{2cs} need to be taken into account (see Fig. B.6(c)). This can in principle be accomplished by using the AFM configurations displayed in Fig. B.7.

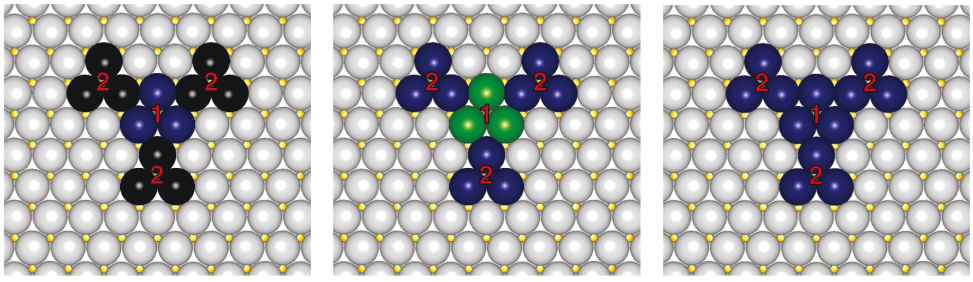

(a) AFM-unit1 (b) AFM-units2 (c) AFM-units1+2

Figure B.7.: Suitable AFM configurations to calculate the exchange coupling constants between the magnetic units for TPT on 2 ML Co/Cu(111). The atoms for which the moment is flipped in the respective configuration are displayed in dark blue.

C Graphene on 1 ML Fe/Co on Cu(111)

In order to gain further understanding of the influence of Gr adsorption onto the in-plane magnetic exchange coupling constants of a magnetic surface, in this appendix additional results for Gr on 1 ML Fe or Co on a Cu(111) substrate treated within the KKR formalism are presented. The usage of the KKR Green's function allows to calculate the exchange coupling constants via the method of infinitesimal rotations according to the Lichtenstein formula Equation (3.17) providing an alternative approach compared to the previous chapters. In addition this method allows to analyze the energy dependence of the coupling constant $J(E)$ favorably in terms of the Alexander-Anderson-model [173]. Moreover the results offer a way to further study and understand the role of the U in the DFT+U formalism for Co-based systems compared to Fe-based ones.

C.1. Adsorption Geometries

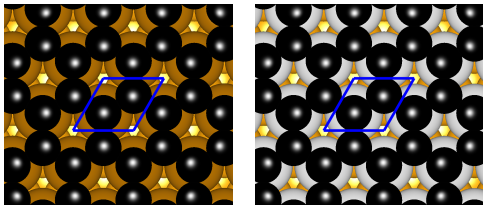

(a) top-hcp (b) top-hcp

Figure C.1.: Top-hcp adsorption position for Gr on 1 ML Fe (a) or Co (b) on the Cu(111) substrate. The unit cell of each system is marked by the blue parallelogram. Color code of the surface atoms same as in Figs. 5.2, 5.3, 7.2 and B.1.

In accordance with the results obtained in Chapter 7 for Gr on Co(111) the adsorption position in the present two cases was chosen to be the top-hcp geometry shown in Fig. C.1, i. e. the two C atoms in the unit cell of the commensurate Gr-layer on the surfaces reside on top of a surface atom and in an hcp hollow site 2.09 Å above the surface.

C.2. Spin-polarized Density of States and Coupling Constants of the Clean Surfaces

First, the properties of the clean 1 ML Fe or Co on Cu(111) surfaces were investigated. Within the KKR formalism a Voronoi construction for the atoms of the investigated system needs

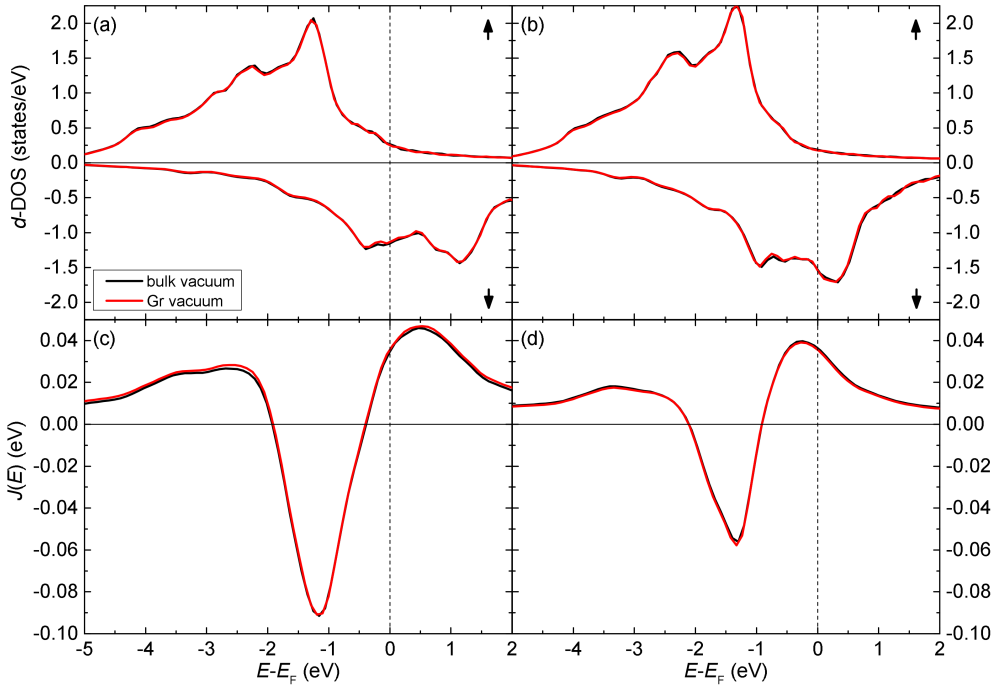

Figure C.2.: d-SP-DOS (a, b) and energy-dependent exchange coupling constants (c, d) for the first layer magnetic atoms of the clean 1 ML Fe, Co on Cu(111) surfaces, respectively. In all cases the results obtained from (i) structuring the vacuum region above and below the slab as continued bulk layers and (ii) by applying the Gr structure of the cells in the vacuum but leaving these cells empty, are included.

to be carried out [144]. For the method to yield reliable results the shape of the Voronoi cells should be as close to spherical as possible. In order to check whether the Voronoi construction for the systems with Gr adsorbed on the surfaces works reliably, the electronic structure of the clean systems was calculated in two ways: (i) by structuring the vacuum region above and below the slab as continued bulk layers and (ii) by applying already the Gr structure of the cells in the vacuum but leaving these cells empty. The equivalence of the results presented in Fig. C.2 using the two approaches shows that for both systems the treatment of the vacuum region is consistent guaranteeing reliability of the results for the hybrid Gr-surface systems. Notably, even the magnetic moments of the respective first layer magnetic atoms calculated from the different approaches coincide up to the second digit amounting to 2.62 μ_B in case of 1 ML Fe on Cu(111) and to 1.72 μ_B for 1 ML Co on Cu(111) (see also Table C.1).

More specifically, the d-SP-DOS of the first layer magnetic atoms in Figs. C.2 (a) and (b) clearly shows the exchange splitting for both systems with the minority (spin down) states dominating around E_F. However the exchange splitting is smaller in case of the 1 ML Co sur-

face and due to the additional valence electron compared to Fe the Fermi energy lies closer to the upper energy bound of the minority spin band. In contrast, for the 1 ML Fe surface it lies closer to the lower energy bound explaining also the larger magnetic moment in this case. The calculated energy-dependent exchange coupling constants $J(E)$ in Figs. C.2 (c) and (d) obtained from the method of infinitesimal rotations (Equation (3.17)) also reflect these differences. The general appearance of the curves can be understood in terms of the Alexander-Anderson-model [173, 174] briefly described in Section 3.1 in that when the Fermi energy crosses a band, the interaction is FM ($J > 0$) whereas it is AFM ($J < 0$) when E_F lies between bands. Most notably, although the coupling constants of both systems at the Fermi energy are similar (34.3 meV vs. 36.3 meV for the Fe and Co ML surfaces, respectively, see Table C.1), the Fermi energy crosses the $J(E)$-curve at an energy below the maximum in case of the 1 ML Fe surface as compared to the 1 ML Co surface where it crosses it at an energy above the maximum. This can be a significant difference since in case of the Fe ML small changes of the Fermi energy can lead to strong changes in the coupling constant and might eventually even turn it negative, i. e. inducing an AFM interaction. Also remarkable is the fact that the range of the energy-dependent coupling constant is larger in case of the Fe ML as compared to the Co ML. This can be understood as a direct consequence of the smaller exchange splitting in the latter case meaning that for the Co ML no clear regions in the d-DOS within and between the spin split d-bands occur and therefore the curve is 'smoothened' compared to the Fe ML case where the energetic separation of the bands is more clearly present.

C.3. Spin-polarized Density of States and Coupling Constants of the Hybrid Systems

Now the d-SP-DOS and the energy-dependent exchange coupling constants calculated for the hybrid Gr-surface systems depicted in Fig. C.3 will be discussed in comparison to the respective clean surface data. Firstly, the general influence of the Gr adsorption onto the magnetic surfaces is a hybridization induced broadening of the DOS as already known from Chapter 7 which also leads to a reduction of the magnetic moments of the surface atoms as listed in Table C.1. More precisely, the Gr adsorption reduces the clean surface first layer magnetic moments in case of the 1 ML Fe on Cu(111) surface from 2.62 μ_B to 2.35 μ_B and for the 1 ML Co on Cu(111) surface from 1.72 μ_B to 1.32 μ_B. This broadening of the d-SP-DOS leads to a 'smoothening' of the $J(E)$ curve, i. e. the FM and AFM maxima become less pronounced compared to the respective clean surface data. Most importantly, the exchange coupling constant at the Fermi energy listed in Table C.1 increases upon Gr adsorption in case of 1 ML Fe on Cu(111) from the clean surface value of 34.3 meV to 40.8 meV (see also Fig. C.3(c)). This

could be assigned to both a small down shift of the majority spin band maximum and a slight refocussing of spectral weight at E_F in the spin down channel in the d-SP-DOS for the hybrid system with respect to the clean surface (see Fig. C.3(a)). On the contrary, in case of 1 ML Co on Cu(111) the coupling constant at the Fermi energy decreases from 36.3 meV to 20.9 meV upon Gr adsorption indicating an in-plane magnetic softening in this case. This could be understood from the d-SP-DOS (see Fig. C.3(b)) based on the finding that in the hybrid system the majority spin band is shifted significantly closer to the Fermi energy compared to the clean surface strongly enhancing the AFM contribution in this energy region. Therefore the FM maximum close to E_F is significantly diminished and hence gives rise to a weakened exchange coupling compared to the clean surface.

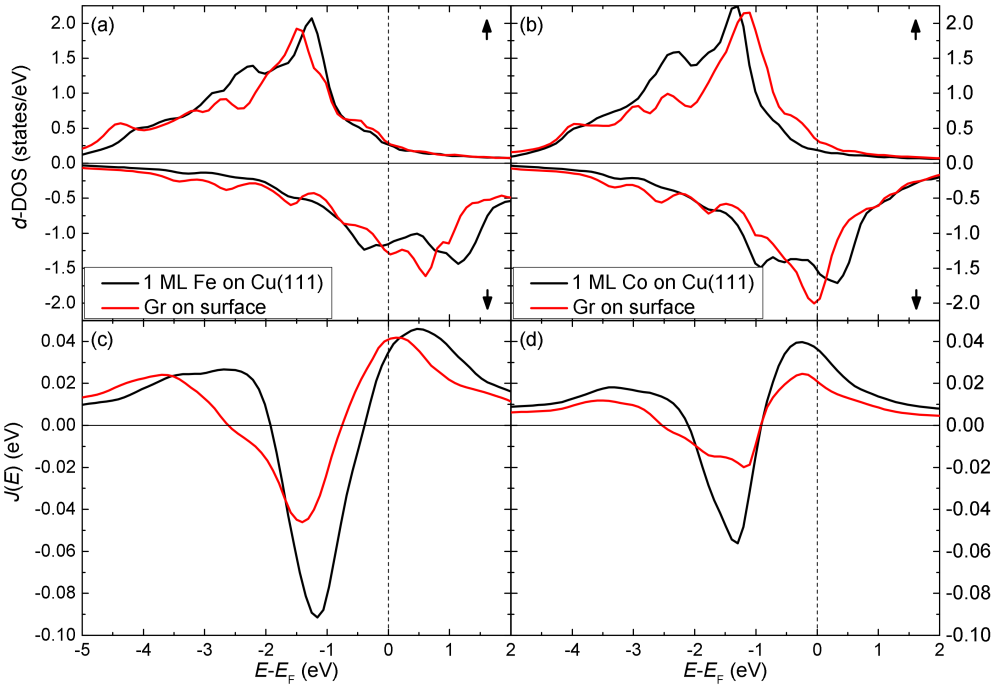

Figure C.3.: d-SP-DOS (a, b) and energy-dependent coupling constants (c, d) for the first layer magnetic atoms for Gr on 1 ML Fe, Co on the Cu(111) substrate, respectively. In addition the respective clean surface reference data are also included.

This result is in contrast to the in-plane magnetic hardening found for the Co(111) surface upon Gr and hBN adsorption in Chapter 7. In order to investigate the impact of the evaluation method of the coupling constants, the parameters have also been computed with the method of inverting selected moments as already applied in Chapters 5, 6 and 7 using the VASP program. The resulting values are included in Table C.1. First of all the magnetic moments calcu-

lated with the VASP program agree nicely with the ones of the KKR treatment especially for the clean surfaces where only differences up to 0.05 μ_B are observed and in both cases the moments are considerably reduced in the hybrid systems[1]. As regarding the coupling constants, the VASP results show the same trend as the data obtained from KKR, i. e. for the 1 ML Fe on Cu(111) surface an enhancement of the coupling from 30.2 meV to 58.6 meV is found upon Gr adsorption whereas a decrease from 49.8 meV to 36.6 meV is detected for the 1 ML Co on Cu(111) surface upon Gr adsorption. However in Chapter 7 it was outlined based on the comparison of experimental and theoretical data that for Co-based systems a DFT+U treatment of the Co d-states might be necessary. For this reason the VASP computations have been repeated for the 1 ML Co on Cu(111) surface by applying an effective Hubbard-like interaction parameter of $U_{\text{eff}} = 3$ eV on the Co d-states. The results included in Table C.1 as VASP PBE+U show firstly that the magnetic moment of the clean surface Co becomes enhanced due to the application of the U and that the reduction of the moment upon Gr adsorption becomes less pronounced. Even more importantly, within this approach the clean surface coupling constant is practically unaffected amounting to 49.9 meV but it is strongly enhanced by nearly a factor of 2 upon Gr adsorption to 97.9 meV. This qualitatively different behavior compared to the treatment without U might be understood from the fact that the on-site interaction term should shift the majority spin states to lower energies (see Equation (2.45)) removing the AFM contribution of these bands at the Fermi energy which has already been revealed in Ref. [172] for transition-metal dimers on Cu substrates. At the same time the on-site U term might possibly lead to a stronger FM contribution of the minority spin bands at E_F due to its shift to higher energies.

Table C.1.: Magnetic moments and exchange coupling constants for Gr on 1 ML Fe/Co on Cu(111) obtained using different methods.

system/surface	magnetic moments (μ_B)			J (meV)		
	KKR LDA	VASP PBE	VASP PBE+U	KKR LDA	VASP PBE	VASP PBE+U
1 ML Fe on Cu(111)	2.62	2.67	-	34.3	30.2	-
Gr on 1 ML Fe on Cu(111)	2.35	2.44	-	40.8	58.6	-
1 ML Co on Cu(111)	1.72	1.76	1.98	36.3	49.8	49.9
Gr on 1 ML Co on Cu(111)	1.32	1.50	1.91	20.9	36.6	97.9

In Fig. C.4 the distance dependence of the coupling constants with respect to nearest and more distant neighbors derived from the KKR results is presented for the two investigated systems. The curves depict the general oscillatory RKKY like behavior of the coupling as des-

[1] It should be noted that the KKR results were obtained using the LDA functional whereas for the VASP computations PBE was used.

cribed in Section 3.2.4. In addition it shows that in case of the 1 ML Fe on Cu(111) surface not only the nearest neighbor coupling constant discussed in detail before is modified but that also the next nearest neighbor coupling is influenced by the Gr adsorption, i. e. its value is increased with respect to the clean surface case from −17.3 meV to −6.2 meV. However the next next nearest neighbor coupling is practically unaffected and the coupling between farther distant neighbors is less significant since the energy scale of their coupling becomes very small. In case of the 1 ML Co on Cu(111) surface the size of the coupling constants decreases very rapidly with distance and is already negligible for next next nearest neighbors. Moreover the largest effect of the Gr is seen on the nearest neighbor coupling and the next nearest neighbor coupling is only slightly diminished from 6.5 meV for the clean surface to 4.2 meV for the hybrid system.

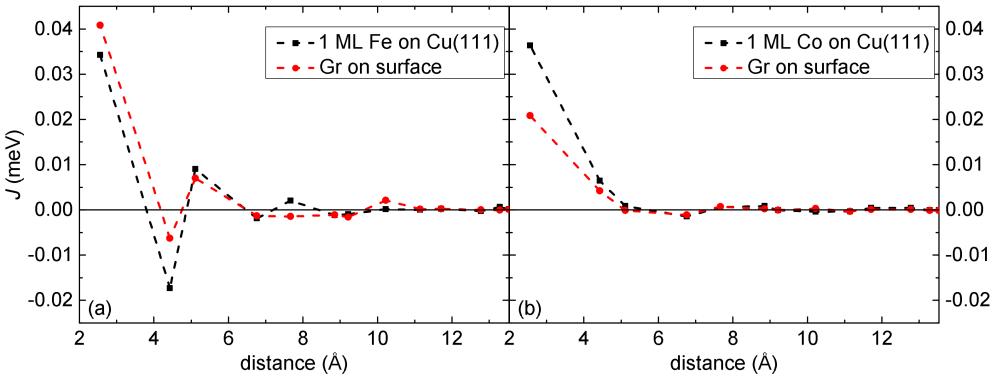

Figure C.4.: Distance dependence of the coupling constants for Gr on 1 ML Fe (a) and 1 ML Co (b) on the Cu(111) substrate. In addition also the respective clean surface data are included.

List of Figures

List of Tables

List of Abbreviations

DFT	density functional theory
HF	Hartree-Fock
CI	Configuration Interaction
CC	Coupled Cluster
QMC	Quantum Monte Carlo
MCSCF	multi-configuration self-consistent-field
TF	Thomas-Fermi
HK	Hohenberg-Kohn
KS	Kohn-Sham
HOMO	highest occupied molecular orbital
LUMO	lowest unoccupied molecular orbital
LDA	local density approximation
GGA	generalized gradient approximation
PBE	Perdew, Burke and Ernzerhof
ADA	average density approximation
WDA	weighted density approximation
vdW	van der Waals
vdW-DF	van der Waals density functional
SDFT	spin-DFT
LSDA	local spin density approximation
SOC	spin-orbit coupling
PP	pseudopotential
PAW	projector augmented-wave
KKR	Korringa-Kohn-Rostoker
NEGF	non-equilibrium Green's function
STM	scanning tunneling microscopy
LCAOMO	linear combination of atomic orbitals to molecular orbitals
STO	Slater-type orbital

GTO	Gaussian-type orbital	42
CGTO	contracted Gaussian-type orbital	42
PS	pseudo	44
OPW	orthogonalized plane wave	45
NC	norm-conserving	45
PDOS	projected density of states	51
BZ	Brillouin zone	57
STS	scanning tunneling spectroscopy	58
DOS	density of states	58
LDOS	local density of states	58
SP-STM	spin-polarized STM	62
FM	ferromagnetic	66
AFM	antiferromagnetic	66
LSMO	$La_{1-x}Sr_xMnO_3$	73
RKKY	Rudermann, Kittel, Kasuya and Yosida	74
MAE	magnetic anisotropy energy	76
MCA	magneto-crystalline anisotropy	76
MS	molecular spintronics	79
ME	molecular electronics	79
GMR	giant magnetoresistance	79
MCBJ	mechanically controllable break-junction	80
Bz	benzene	83
Py	pyridine	83
Pz	pyrazine	83
COT	cyclooctatetraene	83
MR	magnetoresistance	85
TMR	tunneling magnetoresistance	85
Alq_3	8-hydroxy-quinoline aluminium	87
OSV	organic spin-valve	88

SMM	single-molecule magnet 90
XMCD	X-ray magnetic circular dichroism 91
XAS	X-ray absorption spectroscopy 91
ML	monolayer 94
OMAR	organic magnetoresistance 99
IMR	interface magnetoresistance 101
ZMP	zinc methyl phenalenyl 101
PCP	2,2-paracyclophane 102
IP	ionization potential 111
SP-PDOS	spin-polarized projected DOS 121
MC	Monte Carlo 124
2D	two-dimensional 145
Gr	graphene 145
hBN	hexagonal boron nitride 145
TPT	2,4,6-triphenyl-1,3,5-triazine 159
2DEG	2D electron gas 178
ARPES	angle resolved photoemission spectroscopy 182
SCF	self-consistent field 191
VASP	Vienna *ab initio* simulation package 211
SPR-TB-KKR	spin-polarized relativistic tight-binding KKR 211
3D	three-dimensional 211
VESTA	Visualization for Electronic and STructural Analysis 212
PW91	Perdew and Wang 1991 214

Bibliography

[1] C. M. Schneider, in *Spintronics - from GMR to Quantum Information: Lecture Notes of the 40th IFF Spring School 2009* (Forschungszentrum Jülich GmbH, Intitut für Festkörperforschung, 2009), chap. Introduction, pp. I.1–I.19.

[2] S. Blügel, in *Computing Solids: Models, ab-initio methods and supercomputing: Lecture Notes of the 45th IFF Spring School 2014* (Forschungszentrum Jülich GmbH, IAS, PGI, JCNS, ICS, 2014), chap. Complex magnetism, pp. C4.1–C4.50.

[3] M. Bode, M. Heide, K. von Bergmann, P. Ferriani, S. Heinze, G. Bihlmayer, A. Kubetzka, O. Pietzsch, S. Blügel, and R. Wiesendanger, Nature **447**, 190 (2007).

[4] S. Heinze, K. von Bergmann, M. Menzel, J. Brede, A. Kubetzka, R. Wiesendanger, G. Bihlmayer, and S. Blügel, Nature Physics **7**, 713 (2011).

[5] G. Binasch, P. Grünberg, F. Saurenbach, and W. Zinn, Physical Review B **39**, 4828 (1989).

[6] M. N. Baibich, J. M. Broto, A. Fert, F. N. Van Dau, F. Petroff, P. Etienne, G. Creuzet, A. Friederich, and J. Chazelas, Physical Review Letters **61**, 2472 (1988).

[7] S. S. P. Parkin, N. More, and K. P. Roche, Physical Review Letters **64**, 2304 (1990).

[8] M. Julliere, Physics Letters A **54**, 225 (1975).

[9] T. Miyazaki and N. Tezuka, Journal of Magnetism and Magnetic Materials **151**, 403 (1995).

[10] J. S. Moodera, L. R. Kinder, T. M. Wong, and R. Meservey, Physical Review Letters **74**, 3273 (1995).

[11] W. H. Butler, X.-G. Zhang, T. C. Schulthess, and J. M. MacLaren, Physical Review B **63**, 054416 (2001).

[12] S. S. P. Parkin, C. Kaiser, A. Panchula, P. M. Rice, B. Hughes, M. Samant, and S.-H. Yang, Nature Materials **3**, 862 (2004).

[13] S. Yuasa, T. Nagahama, A. Fukushima, Y. Suzuki, and K. Ando, Nature Materials **3**, 868 (2004).

[14] Y. M. Lee, J. Hayakawa, S. Ikeda, F. Matsukura, and H. Ohno, Applied Physics Letters **90**, 212507 (2007).

[15] S. Ikeda, J. Hayakawa, Y. Ashizawa, Y. M. Lee, K. Miura, H. Hasegawa, M. Tsunoda, F. Matsukura, and H. Ohno, Applied Physics Letters **93**, 082508 (2008).

[16] S. Datta and B. Das, Applied Physics Letters **56**, 665 (1990).

[17] H. Munekata, I. Zutic, J. Fabian, S. Tarucha, M. Stopa, S. Sasaki, K. Ono, J. Martinek, J. Barnas, D. C. Ralph, et al., *Concepts in Spin Electronics* (Oxford University Press, 2006).

[18] S. Sanvito, Chemical Society Reviews **40**, 3336 (2011).

[19] N. Atodiresei, J. Brede, P. Lazic, V. Caciuc, G. Hoffmann, R. Wiesendanger, and S. Blügel, Physical Review Letters **105**, 066601 (2010).

[20] N. Atodiresei, V. Caciuc, P. Lazic, and S. Blügel, Physical Review B **84**, 172402 (2011).

[21] V. Dediu, M. Murgia, F. Matacotta, C. Taliani, and S. Barbanera, Solid State Communications **122**, 181 (2002).

[22] Z. H. Xiong, D. Wu, Z. V. Vardeny, and J. Shi, Nature **427**, 821 (2004).

[23] A. Scheybal, T. Ramsvik, R. Bertschinger, M. Putero, F. Nolting, and T. A. Jung, Chemical Physics Letters **411**, 214 (2005).

[24] H. Wende, M. Bernien, J. Luo, C. Sorg, N. Ponpandian, J. Kurde, J. Miguel, M. Piantek, X. Xu, P. Eckhold, et al., Nature Materials **6**, 516 (2007).

[25] E. G. Emberly and G. Kirczenow, Chemical Physics **281**, 311 (2002).

[26] J. Park, A. N. Pasupathy, J. I. Goldsmith, C. Chang, Y. Yaish, J. R. Petta, M. Rinkoski, J. P. Sethna, H. D. Abruna, P. L. McEuen, et al., Nature **417**, 722 (2002).

[27] W. Liang, M. P. Shores, M. Bockrath, J. R. Long, and H. Park, Nature **417**, 725 (2002).

[28] R. Pati, L. Senapati, P. M. Ajayan, and S. K. Nayak, Physical Review B **68**, 100407 (2003).

[29] J. R. Petta, S. K. Slater, and D. C. Ralph, Physical Review Letters **93**, 136601 (2004).

[30] G.-H. Kim and T.-S. Kim, Physical Review Letters **92**, 137203 (2004).

[31] A. R. Rocha, V. M. Garcia-Suarez, S. W. Bailey, C. J. Lambert, J. Ferrer, and S. Sanvito, Nature Materials **4**, 335 (2005).

[32] D. Waldron, P. Haney, B. Larade, A. MacDonald, and H. Guo, Physical Review Letters **96**, 166804 (2006).

[33] C. Iacovita, M. V. Rastei, B. W. Heinrich, T. Brumme, J. Kortus, L. Limot, and J. P. Bucher, Physical Review Letters **101**, 116602 (2008).

[34] M. Cinchetti, K. Heimer, J.-P. Wüstenberg, O. Andreyev, M. Bauer, S. Lach, C. Ziegler, Y. Gao, and M. Aeschlimann, Nature Materials **8**, 115 (2009).

[35] A. J. Drew, J. Hoppler, L. Schulz, F. L. Pratt, P. Desai, P. Shakya, T. Kreouzis, W. P. Gillin, A. Suter, N. A. Morley, et al., Nature Materials **8**, 109 (2009).

[36] S. Steil, N. Großmann, M. Laux, A. Ruffing, D. Steil, M. Wiesenmayer, S. Mathias, O. L. A. Monti, M. Cinchetti, and M. Aeschlimann, Nature Physics **9**, 242 (2013).

[37] S. Pramanik, C.-G. Stefanita, S. Patibandla, S. Bandyopadhyay, K. Garre, N. Harth, and M. Cahay, Nature Nanotechnology **2**, 216 (2007).

[38] T. S. Santos, J. S. Lee, P. Migdal, I. C. Lekshmi, B. Satpati, and J. S. Moodera, Physical Review Letters **98**, 016601 (2007).

[39] J. H. Shim, K. V. Raman, Y. J. Park, T. S. Santos, G. X. Miao, B. Satpati, and J. S. Moodera, Physical Review Letters **100**, 226603 (2008).

[40] J. Brede, N. Atodiresei, S. Kuck, P. Lazic, V. Caciuc, Y. Morikawa, G. Hoffmann, S. Blügel, and R. Wiesendanger, Physical Review Letters **105**, 047204 (2010).

[41] C. Barraud, P. Seneor, R. Mattana, S. Fusil, K. Bouzehouane, C. Deranlot, P. Graziosi, L. Hueso, I. Bergenti, V. Dediu, et al., Nature Physics **6**, 615 (2010).

[42] S. L. Kawahara, J. Lagoute, V. Repain, C. Chacon, Y. Girard, S. Rousset, A. Smogunov, and C. Barreteau, Nano Letters **12**, 4558 (2012).

[43] S. Schmaus, A. Bagrets, Y. Nahas, T. K. Yamada, A. Bork, M. Bowen, E. Beaurepaire, F. Evers, and W. Wulfhekel, Nature Nanotechnology **6**, 185 (2011).

[44] L. Bogani and W. Wernsdorfer, Nature Materials **7**, 179 (2008).

[45] M. Urdampilleta, S. Klyatskaya, J.-P. Cleuziou, M. Ruben, and W. Wernsdorfer, Nature Materials **10**, 502 (2011).

[46] M. Mannini, F. Pineider, P. Sainctavit, C. Danieli, E. Otero, C. Sciancalepore, A. M. Talarico, M.-A. Arrio, A. Cornia, D. Gatteschi, et al., Nature Materials **8**, 194 (2009).

[47] M. Mannini, F. Pineider, C. Danieli, F. Totti, L. Sorace, P. Sainctavit, M.-A. Arrio, E. Otero, L. Joly, J. C. Cezar, et al., Nature **468**, 417 (2010).

[48] R. Vincent, S. Klyatskaya, M. Ruben, W. Wernsdorfer, and F. Balestro, Nature **488**, 357 (2012).

[49] S. Thiele, F. Balestro, R. Ballou, S. Klyatskaya, M. Ruben, and W. Wernsdorfer, Science **344**, 1135 (2014).

[50] R. Decker, J. Brede, N. Atodiresei, V. Caciuc, S. Blügel, and R. Wiesendanger, Physical Review B **87**, 041403 (2013).

[51] K. V. Raman, A. M. Kamerbeek, A. Mukherjee, N. Atodiresei, T. K. Sen, P. Lazic, V. Caciuc, R. Michel, D. Stalke, S. K. Mandal, et al., Nature **493**, 509 (2013).

[52] M. Callsen, V. Caciuc, N. Kiselev, N. Atodiresei, and S. Blügel, Physical Review Letters **111**, 106805 (2013).

[53] E. Schrödinger, Annalen der Physik **384**, 361 (1926).

[54] T. Fließbach, *Quantenmechanik: Lehrbuch zur Theoretischen Physik III* (Spektrum Akademischer Verlag, Heidelberg, Berlin, 2005), 4th ed.

[55] J. Reinhold, *Quantentheorie der Moleküle: eine Einführung* (Teubner, Wiesbaden, 2006), 3rd ed.

[56] G. Czycholl, *Theoretische Festkörperphysik: Von den klassischen Modellen zu modernen Forschungsthemen.* (Springer, Berlin, Heidelberg, 2007), 3rd ed.

[57] R. M. Martin, *Electronic structure: Basic Theory and Practical Methods* (Cambridge Univ. Press, Cambridge, 2008).

[58] W. Demtröder, *Atoms, Molecules and Photons - An Introduction to Atomic-, Molecular- and Quantum Physics*, Graduate Texts in Physics (Springer, Berlin, Heidelberg, 2010), 2nd ed.

[59] F. Jensen, *Introduction to Computational Chemistry: Second Edition* (JW, Chichester, England ; Hoboken, NJ, 2011), 2nd ed.

[60] M. Born and R. Oppenheimer, Annalen der Physik **389**, 457 (1927).

[61] H. Eschrig, *The Fundamentals of Density Functional Theory*, Eagle 4 (EAGLE, Ed. am Gutenbergplatz Leipzig, Leipzig, 2003).

[62] H. Hellmann, *Einführung in die Quantenchemie* (Franz Deuticke, Leipzig, 1937).

[63] R. P. Feynman, Physical Review **56**, 340 (1939).

[64] K. Capelle, Brazilian Journal of Physics **36**, 1318 (2006).

[65] P. W. Anderson, Science **177**, 393 (1972).

[66] D. R. Hartree, Proceedings of the Cambridge Philosophical Society **24**, 89 (1928).

[67] V. Fock, Zeitschrift für Physik **61**, 126 (1930).

[68] J. C. Slater, Physical Review **81**, 385 (1951).

[69] S. Grimme, Journal of Computational Chemistry **27**, 1787 (2006).

[70] J. P. Perdew and A. Ruzsinszky, International Journal of Quantum Chemistry **110**, 2801 (2010).

[71] P. A. M. Dirac, Proceedings of the Royal Society of London A: Mathematical, Physical and Engineering Sciences **123**, 714 (1929).

[72] W. Kohn, Reviews of Modern Physics **71**, 1253 (1999).

[73] P. Hohenberg and W. Kohn, Physical Review B **136**, B864 (1964).

[74] W. Kohn and L. Sham, Physical Review **140**, 1133 (1965).

[75] L. Thomas, Proceedings of the Cambridge Philosophical Society **23**, 542 (1927).

[76] E. Fermi, Atti Accad. Naz. Lincei, Cl. Sci. Fis., Mat. Nat., Rend. **6**, 602 (1927).

[77] P. A. M. Dirac, Proceedings of the Cambridge Philosophical Society **26**, 376 (1930).

[78] R. O. Jones and O. Gunnarsson, Reviews of Modern Physics **61**, 689 (1989).

[79] C. Broyden, Mathematics of Computation **19**, 557 (1965).

[80] D. D. Johnson, Physical Review B **38**, 12807 (1988).

[81] P. Pulay, Chemical Physics Letters **73**, 393 (1980).

[82] G. P. Kerker, Physical Review B **23**, 3082 (1981).

[83] M. Levy, J. P. Perdew, and V. Sahni, Physical Review A **30**, 2745 (1984).

[84] R. Stowasser and R. Hoffmann, Journal of the American Chemical Society **121**, 3414 (1999).

[85] S. Lindner, M. Knupfer, R. Friedrich, T. Hahn, and J. Kortus, Physical Review Letters **109**, 027601 (2012).

[86] S. Lindner, B. Mahns, A. König, F. Roth, M. Knupfer, R. Friedrich, T. Hahn, and J. Kortus, The Journal of Chemical Physics **138**, 024707 (2013).

[87] J. P. Perdew and M. Levy, Physical Review Letters **51**, 1884 (1983).

[88] O. Gunnarsson and B. I. Lundqvist, Physical Review B **13**, 4274 (1976).

[89] D. C. Langreth and J. P. Perdew, Solid State Communications **17**, 1425 (1975).

[90] D. C. Langreth and J. P. Perdew, Physical Review B **15**, 2884 (1977).

[91] T. Asada and K. Terakura, Physical Review B **46**, 13599 (1992).

[92] J. Perdew, K. Burke, and M. Ernzerhof, Physical Review Letters **77**, 3865 (1996).

[93] M. Lezaic and Y. Mokrousov, in *Computing Solids: Models, ab-initio methods and supercomputing: Lecture Notes of the 45th IFF Spring School 2014* (Forschungszentrum Jülich GmbH, IAS, PGI, JCNS, ICS, 2014), chap. Introduction to Density Functional Theory, pp. A2.1–A2.21.

[94] O. Gunnarsson, M. Jonson, and B. I. Lundqvist, Physical Review B **20**, 3136 (1979).

[95] V. A. Parsegian, *Van der Waals Forces: A Handbook for Biologists, Chemists, Engineers, and Physicists* (Cambridge University Press, Cambridge, 2005).

[96] S. Braun, W. R. Salaneck, and M. Fahlman, Advanced Materials **21**, 1450 (2009).

[97] N. Ooi, A. Rairkar, and J. B. Adams, Carbon **44**, 231 (2006).

[98] N. Atodiresei, V. Caciuc, P. Lazic, and S. Blügel, Physical Review Letters **102**, 136809 (2009).

[99] M. Dion, H. Rydberg, E. Schröder, D. C. Langreth, and B. I. Lundqvist, Physical Review Letters **92**, 246401 (2004).

[100] J. Klimes, D. R. Bowler, and A. Michaelides, Journal of Physics: Condensed Matter **22**, 022201 (2010).

[101] J. Klimes, D. R. Bowler, and A. Michaelides, Physical Review B **83**, 195131 (2011).

[102] I. Hamada, Physical Review B **89**, 121103(R) (2014).

[103] K. Lee, E. D. Murray, L. Kong, B. I. Lundqvist, and D. C. Langreth, Physical Review B **82**, 081101 (2010).

[104] G. Roman-Perez and J. Soler, Physical Review Letters **103**, 096102 (2009).

[105] M. Callsen, Ph.D. thesis, RWTH Aachen University (2014).

[106] T. Thonhauser, S. Zuluaga, C. Arter, K. Berland, E. Schröder, and P. Hyldgaard, Physical Review Letters **115**, 136402 (2015).

[107] S. Grimme, Journal of Computational Chemistry **25**, 1463 (2004).

[108] A. Tkatchenko and M. Scheffler, Physical Review Letters **102**, 073005 (2009).

[109] S. Grimme, J. Antony, S. Ehrlich, and H. Krieg, The Journal of Chemical Physics **132**, 154104 (2010).

[110] X. Chu and A. Dalgarno, The Journal of Chemical Physics **121**, 4083 (2004).

[111] V. G. Ruiz, W. Liu, E. Zojer, M. Scheffler, and A. Tkatchenko, Physical Review Letters **108**, 146103 (2012).

[112] N. Ferri, R. A. DiStasio, A. Ambrosetti, R. Car, and A. Tkatchenko, Physical Review Letters **114**, 176802 (2015).

[113] U. von Barth and L. Hedin, Journal of Physics C: Solid State Physics **5**, 1629 (1972).

[114] D. D. Koelling and B. N. Harmon, Journal of Physics C: Solid State Physics **10**, 3107 (1977).

[115] A. H. MacDonald, W. E. Pickett, and D. D. Koelling, Journal of Physics C: Solid State Physics **13**, 2675 (1980).

[116] E. Runge and E. K. U. Gross, Physical Review Letters **52**, 997 (1984).

[117] L. Hedin, Physical Review **139**, A796 (1965).

[118] R. Car and M. Parrinello, Physical Review Letters **55**, 2471 (1985).

[119] J. Pople, Reviews of Modern Physics **71**, 1267 (1999).

[120] J. Junquera, O. Paz, D. Sanchez-Portal, and E. Artacho, Physical Review B **64**, 235111 (2001).

[121] F. Bloch, Zeitschrift für Physik **52**, 555 (1929).

[122] C. Kittel and S. Hunklinger, *Einführung in die Festkörperphysik* (Oldenbourg Verlag, München, Wien, 2006).

[123] P. Y. Yu and M. Cardona, *Fundamentals of Semiconductors - Physics and Materials Properties*, Graduate Texts in Physics (Springer, Berlin, Heidelberg, 2010), 4th ed.

[124] P. F. Baumeister, Ph.D. thesis, RWTH Aachen University (2012).

[125] C. Rostgaard, The Projector Augmented-wave Method (2009), URL `http://arxiv.org/abs/0910.1921`.

[126] https://wiki.fysik.dtu.dk/gpaw/setups/setups.html (March 25, 2015).

[127] M. H. Cohen and V. Heine, Physical Review **122**, 1821 (1961).

[128] M. L. Cohen and J. R. Chelikowsky, *Electronic Structure and Optical Properties of Semiconductors*, Springer series in solid state sciences ; 75 (Springer, Berlin, Heidelberg, 1989).

[129] C. Herring and A. G. Hill, Physical Review **58**, 132 (1940).

[130] C. Herring, Physical Review **57**, 1169 (1940).

[131] L. Kleinman and D. M. Bylander, Physical Review Letters **48**, 1425 (1982).

[132] W. Kromen, Ph.D. thesis, RWTH Aachen (2001).

[133] D. Vanderbilt, Physical Review B **41**, 7892 (1990).

[134] P. E. Blöchl, Physical Review B **41**, 5414 (1990).

[135] G. Kresse and D. Joubert, Physical Review B **59**, 1758 (1999).

[136] D. R. Hamann, M. Schlüter, and C. Chiang, Physical Review Letters **43**, 1494 (1979).

[137] P. A. Christiansen, Y. S. Lee, and K. S. Pitzer, The Journal of Chemical Physics **71**, 4445 (1979).

[138] G. B. Bachelet, D. R. Hamann, and M. Schlüter, Physical Review B **26**, 4199 (1982).

[139] D. Vanderbilt, Physical Review B **32**, 8412 (1985).

[140] G. P. Kerker, Journal of Physics C: Solid State Physics **13**, L189 (1980).

[141] N. Troullier and J. L. Martins, Physical Review B **43**, 1993 (1991).

[142] P. E. Blöchl, Physical Review B **50**, 17953 (1994).

[143] M. Marsman and G. Kresse, The Journal of Chemical Physics **125**, 104101 (2006).

[144] D. S. G. Bauer, Ph.D. thesis, RWTH Aachen University (2013).

[145] P. Mavropoulos and N. Papanikolaou, in *Computational Nanoscience: Do It Yourself! ; NIC Winter School, 14 - 22 February 2006, Forschungszentrum Jülich, Germany - Lecture Notes* (Forschungszentrum Jülich GmbH, John von Neumann Institute for Computing, 2006), chap. The Korringa-Kohn-Rostoker (KKR) Green Function Method, I. Electronic Structure of Periodic Systems, pp. 131–158.

[146] S. Blügel, in *Computational Condensed Matter Physics : Lecture manuscripts of the 37th Spring School of the Institute of Solid State Research* (Forschungszentrum Jülich GmbH, Institut für Festkörperforschung, 2006), chap. Density Functional Theory in Practice, pp. A8.1–A8.36.

[147] J. Korringa, Physica **13**, 392 (1947).

[148] W. Kohn and N. Rostoker, Physical Review **94**, 1111 (1954).

[149] R. Zeller, P. H. Dederichs, B. Ujfalussy, L. Szunyogh, and P. Weinberger, Physical Review B **52**, 8807 (1995).

[150] K. Wildberger, R. Zeller, and P. H. Dederichs, Physical Review B **55**, 10074 (1997).

[151] M. Paulsson, T. Frederiksen, and M. Brandbyge, Chimia **64**, 350 (2010).

[152] S. Lounis, in *Computing Solids: Models, ab-initio methods and supercomputing: Lecture Notes of the 45th IFF Spring School 2014* (Forschungszentrum Jülich GmbH, IAS, PGI, JCNS, ICS, 2014), chap. Theory of Scanning Tunneling Microscopy, pp. C6.1–C6.38.

[153] P. S. Damle, A. W. Ghosh, and S. Datta, Physical Review B **64**, 201403 (2001).

[154] E. G. Emberly and G. Kirczenow, Annals of the New York Academy of Sciences **852**, 54 (1998).

[155] S. Datta, Nanotechnology **15**, S433 (2004).

[156] S. Datta, *Electronic Transport in Mesoscopic Systems* (Cambridge University Press, Cambridge, 1995).

[157] A. R. Rocha, V. M. Garcia-Suarez, S. Bailey, C. Lambert, J. Ferrer, and S. Sanvito, Physical Review B **73**, 085414 (2006).

[158] S. Sanvito and A. R. Rocha, Journal of Computational and Theoretical Nanoscience **3**, 624 (2006).

[159] A.-P. Jauho, N. S. Wingreen, and Y. Meir, Physical Review B **50**, 5528 (1994).

[160] S. Datta, *Quantum Transport: Atom to Transistor* (Cambridge University Press, Cambridge, 2005).

[161] R. Wiesendanger, Reviews of Modern Physics **81**, 1495 (2009).

[162] J. Bardeen, Physical Review Letters **6**, 57 (1961).

[163] J. Tersoff and D. R. Hamann, Physical Review Letters **50**, 1998 (1983).

[164] C. J. Chen, Physical Review Letters **65**, 448 (1990).

[165] C. J. Chen, Physical Review B **42**, 8841 (1990).

[166] S. Blundell, *Magnetism in Condensed Matter* (Oxford University Press, Oxford, 2009).

[167] W. Nolting and A. Ramakanth, *Quantum Theory of Magnetism* (Springer, Berlin, Heidelberg, 2009).

[168] E. Koch, in *Computing Solids: Models, ab-initio methods and supercomputing: Lecture Notes of the 45th IFF Spring School 2014* (Forschungszentrum Jülich GmbH, IAS, PGI, JCNS, ICS, 2014), chap. Model Hamiltonians and Second Quantization, pp. B1.1–B1.31.

[169] T. Fließbach, *Statistische Physik: Lehrbuch zur Theoretischen Physik IV* (Spektrum Akademischer Verlag, Heidelberg, 2010), 5th ed.

[170] L. Noodleman, The Journal of Chemical Physics **74**, 5737 (1981).

[171] A. I. Liechtenstein, M. I. Katsnelson, V. P. Antropov, and V. A. Gubanov, Journal of Magnetism and Magnetic Materials **67**, 65 (1987).

[172] P. Mavropoulos, S. Lounis, and S. Blügel, Physica Status Solidi (b) **247**, 1187 (2010).

[173] S. Alexander and P. W. Anderson, Physical Review **133**, A1594 (1964).

[174] A. Oswald, R. Zeller, P. J. Braspenning, and P. H. Dederichs, Journal of Physics F: Metal Physics **15**, 193 (1985).

[175] D. Gatteschi, R. Sessoli, and J. Villain, *Molecular Nanomagnets*, Mesoscopic Physics and Nanotechnology ; 5 (Oxford University Press, Oxford, 2006).

[176] J. Kanamori, Journal of Physics and Chemistry of Solids **10**, 87 (1959).

[177] J. B. Goodenough, *Magnetism and the Chemical Bond*, Interscience Monographs on Chemistry. Inorganic Chemistry Section vol. 1 (Interscience, New York, 1963).

[178] J. C. Cuevas and E. Scheer, *Molecular Electronics: An Introduction to Theory and Experiment*, World Scientific Series in Nanoscience and Nanotechnology 1 (World Scientific, Hackensack, NJ, 2010).

[179] B. Mann and H. Kuhn, Journal of Applied Physics **42**, 4398 (1971).

[180] A. Aviram and M. A. Ratner, Chemical Physics Letters **29**, 277 (1974).

[181] K. Stokbro, J. Taylor, and M. Brandbyge, Journal of the American Chemical Society **125**, 3674 (2003).

[182] R. M. Metzger, B. Chen, U. Höpfner, M. V. Lakshmikantham, D. Vuillaume, T. Kawai, X. Wu, H. Tachibana, T. V. Hughes, H. Sakurai, et al., Journal of the American Chemical Society **119**, 10455 (1997).

[183] M. A. Reed, C. Zhou, C. J. Muller, T. P. Burgin, and J. M. Tour, Science **278**, 252 (1997).

[184] A. Aviram, C. Joachim, and M. Pomerantz, Chemical Physics Letters **146**, 490 (1988).

[185] C. Joachim and J. K. Gimzewski, Europhysics Letters **30**, 409 (1995).

[186] C. Joachim, J. K. Gimzewski, R. R. Schlittler, and C. Chavy, Physical Review Letters **74**, 2102 (1995).

[187] L. A. Bumm, J. J. Arnold, M. T. Cygan, T. D. Dunbar, T. P. Burgin, L. Jones, D. L. Allara, J. M. Tour, and P. S. Weiss, Science **271**, 1705 (1996).

[188] R. P. Andres, T. Bein, M. Dorogi, S. Feng, J. I. Henderson, C. P. Kubiak, W. Mahoney, R. G. Osifchin, and R. Reifenberger, Science **272**, 1323 (1996).

[189] E. G. Emberly and G. Kirczenow, Physical Review B **58**, 10911 (1998).

[190] M. Di Ventra, S. T. Pantelides, and N. D. Lang, Physical Review Letters **84**, 979 (2000).

[191] E. G. Emberly and G. Kirczenow, Physical Review Letters **87**, 269701 (2001).

[192] R. H. M. Smit, Y. Noat, C. Untiedt, N. D. Lang, M. C. van Hemert, and J. M. van Ruitenbeek, Nature **419**, 906 (2002).

[193] C. Joachim, J. K. Gimzewski, and A. Aviram, Nature **408**, 541 (2000).

[194] H. Park, J. Park, A. K. L. Lim, E. H. Anderson, A. P. Alivisatos, and P. L. McEuen, Nature **407**, 57 (2000).

[195] S. V. Aradhya and L. Venkataraman, Nature Nanotechnology **8**, 399 (2013).

[196] R. L. Carroll and C. B. Gorman, Angewandte Chemie International Edition **41**, 4378 (2002).

[197] J. Del Nero, F. M. de Souza, and R. B. Capaz, Journal of Computational and Theoretical Nanoscience **7**, 503 (2010).

[198] J. P. Bergfield and M. A. Ratner, Physica Status Solidi (b) **250**, 2249 (2013).

[199] C. Zhou, M. R. Deshpande, M. A. Reed, L. Jones, and J. M. Tour, Applied Physics Letters **71**, 611 (1997).

[200] P. Lazic, M. Alaei, N. Atodiresei, V. Caciuc, R. Brako, and S. Blügel, Physical Review B **81**, 045401 (2010).

[201] M. Callsen, N. Atodiresei, V. Caciuc, and S. Blügel, Physical Review B **86**, 085439 (2012).

[202] H. Harutyunyan, M. Callsen, T. Allmers, V. Caciuc, S. Blügel, N. Atodiresei, and D. Wegner, Chemical Communications **49**, 5993 (2013).

[203] P. Grünberg, in *Spintronics - from GMR to Quantum Information: Lecture Notes of the 40th IFF Spring School 2009* (Forschungszentrum Jülich GmbH, Intitut für Festkörperforschung, 2009), chap. Spin polarization: From the EPR paradox to the GMR effect, pp. B1.1–B1.14.

[204] C. Chappert, A. Fert, and F. N. Van Dau, Nature Materials **6**, 813 (2007).

[205] A. Fert, Reviews of Modern Physics **80**, 1517 (2008).

[206] S. Sanvito, Journal of Materials Chemistry **17**, 4455 (2007).

[207] P. A. Grünberg, Reviews of Modern Physics **80**, 1531 (2008).

[208] S. Blügel, D. Bürgler, M. Morgenstern, C. M. Schneider, and R. Waser, eds., *Spintronics - from GMR to Quantum Information: Lecture Notes of the 40th IFF Spring School 2009* (Forschungszentrum Jülich GmbH, Intitut für Festkörperforschung, 2009).

[209] I. Zutic, J. Fabian, and S. Das Sarma, Reviews of Modern Physics **76**, 323 (2004).

[210] K. Tsukagoshi, B. W. Alphenaar, and H. Ago, Nature **401**, 572 (1999).

[211] V. A. Dediu, L. E. Hueso, I. Bergenti, and C. Taliani, Nature Materials **8**, 707 (2009).

[212] H. Friebolin, *Ein- und zweidimensionale NMR-Spektroskopie: Eine Einführung* (Wiley-VCH, Weinheim, 2006).

[213] T. D. Nguyen, G. Hukic-Markosian, F. Wang, L. Wojcik, X.-G. Li, E. Ehrenfreund, and Z. V. Vardeny, Nature Materials **9**, 345 (2010).

[214] S. Bandyopadhyay, Physical Review B **81**, 153202 (2010).

[215] S. Sanvito, Nature Materials **6**, 803 (2007).

[216] D. Wu, Z. H. Xiong, X. G. Li, Z. V. Vardeny, and J. Shi, Physical Review Letters **95**, 016802 (2005).

[217] V. Dediu, L. E. Hueso, I. Bergenti, A. Riminucci, F. Borgatti, P. Graziosi, C. Newby, F. Casoli, M. P. De Jong, C. Taliani, et al., Physical Review B **78**, 115203 (2008).

[218] X. Sun, M. Gobbi, A. Bedoya-Pinto, O. Txoperena, F. Golmar, R. Llopis, A. Chuvilin, F. Casanova, and L. E. Hueso, Nature Communications **4**, 2794 (2013).

[219] S. Sanvito, Nature Physics **6**, 562 (2010).

[220] D. Sun, E. Ehrenfreund, and Z. V. Vardeny, Chemical Communications **50**, 1781 (2014).

[221] M. Shiraishi and T. Ikoma, Physica E **43**, 1295 (2011).

[222] G. Szulczewski, S. Sanvito, and M. Coey, Nature Materials **8**, 693 (2009).

[223] J. S. Jiang, J. E. Pearson, and S. D. Bader, Physical Review B **77**, 035303 (2008).

[224] M. Grünewald, R. Göckeritz, N. Homonnay, F. Würthner, L. W. Molenkamp, and G. Schmidt, Physical Review B **88**, 085319 (2013).

[225] S. Javaid, M. Bowen, S. Boukari, L. Joly, J.-B. Beaufrand, X. Chen, Y. J. Dappe, F. Scheurer, J.-P. Kappler, J. Arabski, et al., Physical Review Letters **105**, 077201 (2010).

[226] P. Gambardella, S. Stepanow, A. Dmitriev, J. Honolka, F. M. F. de Groot, M. Lingenfelder, S. S. Gupta, D. D. Sarma, P. Bencok, S. Stanescu, et al., Nature Materials **8**, 189 (2009).

[227] C. Wäckerlin, K. Tarafder, D. Siewert, J. Girovsky, T. Hählen, C. Iacovita, A. Kleibert, F. Nolting, T. A. Jung, P. M. Oppeneer, et al., Chemical Science **3**, 3154 (2012).

[228] S. Müller, S. Steil, A. Droghetti, N. Großmann, V. Meded, A. Magri, B. Schäfer, O. Fuhr, S. Sanvito, M. Ruben, et al., New Journal of Physics **15**, 113054 (2013).

[229] L. Schulz, L. Nuccio, M. Willis, P. Desai, P. Shakya, T. Kreouzis, V. K. Malik, C. Bernhard, F. L. Pratt, N. A. Morley, et al., Nature Materials **10**, 39 (2011).

[230] K. V. Raman, S. M. Watson, J. H. Shim, J. A. Borchers, J. Chang, and J. S. Moodera, Physical Review B **80**, 195212 (2009).

[231] C. Barraud, K. Bouzehouane, C. Deranlot, S. Fusil, H. Jabbar, J. Arabski, R. Rakshit, D.-J. Kim, C. Kieber, S. Boukari, et al., Physical Review Letters **114**, 206603 (2015).

[232] A. R. Rocha and S. Sanvito, Journal of Applied Physics **101**, 09B102 (2007).

[233] C. Herrmann, G. C. Solomon, and M. A. Ratner, Journal of the American Chemical Society **132**, 3682 (2010).

[234] N. Tsukahara, K.-i. Noto, M. Ohara, S. Shiraki, N. Takagi, Y. Takata, J. Miyawaki, M. Taguchi, A. Chainani, S. Shin, et al., Physical Review Letters **102**, 167203 (2009).

[235] N. Tsukahara, S. Shiraki, S. Itou, N. Ohta, N. Takagi, and M. Kawai, Physical Review Letters **106**, 187201 (2011).

[236] Y. Wang, J. G. Che, J. N. Fry, and H.-P. Cheng, The Journal of Physical Chemistry Letters **4**, 3508 (2013).

[237] N. M. Caffrey, P. Ferriani, S. Marocchi, and S. Heinze, Physical Review B **88**, 155403 (2013).

[238] J. Brede and R. Wiesendanger, Physical Review B **86**, 184423 (2012).

[239] S. Fahrendorf, N. Atodiresei, C. Besson, V. Caciuc, F. Matthes, S. Blügel, P. Kögerler, D. E. Bürgler, and C. M. Schneider, Nature Communications **4**, 2425 (2013).

[240] R. Sessoli, D. Gatteschi, A. Caneschi, and M. A. Novak, Nature **365**, 141 (1993).

[241] H. B. Heersche, Z. de Groot, J. A. Folk, H. S. J. van der Zant, C. Romeike, M. R. Wegewijs, L. Zobbi, D. Barreca, E. Tondello, and A. Cornia, Physical Review Letters **96**, 206801 (2006).

[242] S. Kyatskaya, J. R. G. Mascaros, L. Bogani, F. Hennrich, M. Kappes, W. Wernsdorfer, and M. Ruben, Journal of the American Chemical Society **131**, 15143 (2009).

[243] J. Schwöbel, Y. Fu, J. Brede, A. Dilullo, G. Hoffmann, S. Klyatskaya, M. Ruben, and R. Wiesendanger, Nature Communications **3**, 953 (2012).

[244] M. Mannini, P. Sainctavit, R. Sessoli, C. C. d. Moulin, F. Pineider, M.-A. Arrio, A. Cornia, and D. Gatteschi, Chemistry-A European Journal **14**, 7530 (2008).

[245] P. Gütlich and H. Goodwin, eds., *Spin Crossover in Transition Metal Compounds I*, vol. 233 of *Topics in Current Chemistry* (Springer, Berlin, Heidelberg, 2004).

[246] N. Baadji, M. Piacenza, T. Tugsuz, F. D. Sala, G. Maruccio, and S. Sanvito, Nature Materials **8**, 813 (2009).

[247] V. Niel, A. L. Thompson, M. C. Munoz, A. Galet, A. E. Goeta, and J. A. Real, Angewandte Chemie International Edition **42**, 3760 (2003).

[248] S. Sarkar, K. Tarafder, P. M. Oppeneer, and T. Saha-Dasgupta, Journal of Materials Chemistry **21**, 13832 (2011).

[249] K. Tarafder, S. Kanungo, P. M. Oppeneer, and T. Saha-Dasgupta, Physical Review Letters **109**, 077203 (2012).

[250] T. G. Gopakumar, F. Matino, H. Naggert, A. Bannwarth, F. Tuczek, and R. Berndt, Angewandte Chemie International Edition **51**, 6262 (2012).

[251] T. Miyamachi, M. Gruber, V. Davesne, M. Bowen, S. Boukari, L. Joly, F. Scheurer, G. Rogez, T. K. Yamada, P. Ohresser, et al., Nature Communications **3**, 938 (2012).

[252] J. Kalinowski, M. Cocchi, D. Virgili, P. Di Marco, and V. Fattori, Chemical Physics Letters **380**, 710 (2003).

[253] T. L. Francis, O. Mermer, G. Veeraraghavan, and M. Wohlgenannt, New Journal of Physics **6**, 185 (2004).

[254] B. Hu and Y. Wu, Nature Materials **6**, 985 (2007).

[255] F. L. Bloom, W. Wagemans, M. Kemerink, and B. Koopmans, Physical Review Letters **99**, 257201 (2007).

[256] O. Mermer, G. Veeraraghavan, T. L. Francis, Y. Sheng, D. T. Nguyen, M. Wohlgenannt, A. Köhler, M. K. Al-Suti, and M. S. Khan, Physical Review B **72**, 205202 (2005).

[257] P. A. Bobbert, T. D. Nguyen, F. W. A. van Oost, B. Koopmans, and M. Wohlgenannt, Physical Review Letters **99**, 216801 (2007).

[258] B. Göhler, V. Hamelbeck, T. Z. Markus, M. Kettner, G. F. Hanne, Z. Vager, R. Naaman, and H. Zacharias, Science **331**, 894 (2011).

[259] R. Gutierrez, E. Diaz, C. Gaul, T. Brumme, F. Dominguez-Adame, and G. Cuniberti, The Journal of Physical Chemistry C **117**, 22276 (2013).

[260] A.-M. Guo, E. Diaz, C. Gaul, R. Gutierrez, F. Dominguez-Adame, G. Cuniberti, and Q.-f. Sun, Physical Review B **89**, 205434 (2014).

[261] D. Rai and M. Galperin, The Journal of Physical Chemistry C **117**, 13730 (2013).

[262] R. Sessoli, M.-E. Boulon, A. Caneschi, M. Mannini, L. Poggini, F. Wilhelm, and A. Rogalev, Nature Physics **11**, 69 (2015).

[263] J. S. Moodera, B. Koopmans, and P. M. Oppeneer, MRS Bulletin **39**, 578 (2014).

[264] T. D. Nguyen, E. Ehrenfreund, and Z. V. Vardeny, MRS Bulletin **39**, 585 (2014).

[265] M. Wohlgenannt, P. A. Bobbert, and B. Koopmans, MRS Bulletin **39**, 590 (2014).

[266] N. Atodiresei and K. V. Raman, MRS Bulletin **39**, 596 (2014).

[267] M. Galbiati, S. Tatay, C. Barraud, A. V. Dediu, F. Petroff, R. Mattana, and P. Seneor, MRS Bulletin **39**, 602 (2014).

[268] J. Brede and R. Wiesendanger, MRS Bulletin **39**, 608 (2014).

[269] T. Saha-Dasgupta and P. M. Oppeneer, MRS Bulletin **39**, 614 (2014).

[270] J. E. Bickel, F. Meier, J. Brede, A. Kubetzka, K. von Bergmann, and R. Wiesendanger, Physical Review B **84**, 054454 (2011).

[271] A. B. Shick, S. C. Hong, F. Maca, and A. I. Lichtenstein, Journal of Physics: Condensed Matter **26**, 476003 (2014).

[272] J. Brede, N. Atodiresei, V. Caciuc, M. Bazarnik, A. Al-Zubi, S. Blügel, and R. Wiesendanger, Nature Nanotechnology **9**, 1018 (2014).

[273] P. Campiglio, R. Breitwieser, V. Repain, S. Guitteny, C. Chacon, Amandine Bellec, J. Lagoute, Y. Girard, S. Rousset, A. Sassella, et al., New Journal of Physics **17**, 063022 (2015).

[274] K. Bairagi, A. Bellec, V. Repain, C. Chacon, Y. Girard, Y. Garreau, J. Lagoute, S. Rousset, R. Breitwieser, Y.-C. Hu, et al., Physical Review Letters **114**, 247203 (2015).

[275] M. Gruber, F. Ibrahim, S. Boukari, H. Isshiki, L. Joly, M. Peter, M. Studniarek, V. Da Costa, H. Jabbar, V. Davesne, et al., Nature Materials **14**, 981 (2015).

[276] F. A. Ma'Mari, T. Moorsom, G. Teobaldi, W. Deacon, T. Prokscha, H. Luetkens, S. Lee, G. E. Sterbinsky, D. A. Arena, D. A. MacLaren, et al., Nature **524**, 69 (2015).

[277] R. Pang, X. Shi, and M. A. Van Hove, Journal of the American Chemical Society **138**, 4029 (2016).

[278] T. Andersen and W. Hübner, Physical Review B **74**, 184415 (2006).

[279] A. L. Allred and E. G. Rochow, Journal of Inorganic and Nuclear Chemistry **5**, 264 (1958).

[280] A. D. Yau, S. A. Perera, and R. J. Bartlett, Molecular Physics **100**, 835 (2002).

[281] C. E. Mortimer and U. Müller, *Chemie: Das Basiswissen der Chemie* (Thieme, Stuttgart, 2007), 9th ed.

[282] Vasile Caciuc, private communication.

[283] R. Friedrich, V. Caciuc, N. S. Kiselev, N. Atodiresei, and S. Blügel, Physical Review B **91**, 115432 (2015).

[284] D. Hinzke and U. Nowak, Computer Physics Communications **121–122**, 334 (1999).

[285] R. Friedrich, V. Caciuc, N. Atodiresei, and S. Blügel, Physical Review B **92**, 195407 (2015).

[286] E. Riedel and C. Janiak, *Anorganische Chemie* (de Gruyter, Berlin, 2007), 7th ed.

[287] A. H. Castro Neto, F. Guinea, N. M. R. Peres, K. S. Novoselov, and A. K. Geim, Reviews of Modern Physics **81**, 109 (2009).

[288] M. Gmitra, S. Konschuh, C. Ertler, C. Ambrosch-Draxl, and J. Fabian, Physical Review B **80**, 235431 (2009).

[289] L. Song, L. Ci, H. Lu, P. B. Sorokin, C. Jin, J. Ni, A. G. Kvashnin, D. G. Kvashnin, J. Lou, B. I. Yakobson, et al., Nano Letters **10**, 3209 (2010).

[290] K. Watanabe, T. Taniguchi, and H. Kanda, Nature Materials **3**, 404 (2004).

[291] K. S. Novoselov, D. Jiang, F. Schedin, T. J. Booth, V. V. Khotkevich, S. V. Morozov, and A. K. Geim, Proceedings of the National Academy of Sciences of the United States of America **102**, 10451 (2005).

[292] K. S. Novoselov, A. K. Geim, S. V. Morozov, D. Jiang, Y. Zhang, S. V. Dubonos, I. V. Grigorieva, and A. A. Firsov, Science **306**, 666 (2004).

[293] K. S. Novoselov, A. K. Geim, S. V. Morozov, D. Jiang, M. I. Katsnelson, I. V. Grigorieva, S. V. Dubonos, and A. A. Firsov, Nature **438**, 197 (2005).

[294] Y. Zhang, Y.-W. Tan, H. L. Stormer, and P. Kim, Nature **438**, 201 (2005).

[295] C. L. Kane and E. J. Mele, Physical Review Letters **95**, 226801 (2005).

[296] V. M. Karpan, G. Giovannetti, P. A. Khomyakov, M. Talanana, A. A. Starikov, M. Zwierzycki, J. van den Brink, G. Brocks, and P. J. Kelly, Physical Review Letters **99**, 176602 (2007).

[297] A. K. Geim and K. S. Novoselov, Nature Materials **6**, 183 (2007).

[298] G. M. Sipahi, I. Žutić, N. Atodiresei, R. K. Kawakami, and P. Lazic, Journal of Physics: Condensed Matter **26**, 104204 (2014).

[299] H. Sahin, S. Cahangirov, M. Topsakal, E. Bekaroglu, E. Akturk, R. T. Senger, and S. Ciraci, Physical Review B **80**, 155453 (2009).

[300] L. Van Hove, Physical Review **89**, 1189 (1953).

[301] M. Corral Valero and P. Raybaud, The Journal of Physical Chemistry C **118**, 22479 (2014).

[302] M. Lezaic, P. Mavropoulos, and S. Blügel, Applied Physics Letters **90**, 082504 (2007).

[303] R. Friedrich, V. Caciuc, N. Atodiresei, and S. Blügel, Physical Review B **93**, 220406(R) (2016).

[304] R. Decker, M. Bazarnik, N. Atodiresei, V. Caciuc, S. Blügel, and R. Wiesendanger, Journal of Physics: Condensed Matter **26**, 394004 (2014).

[305] B. Dlubak, M.-B. Martin, R. S. Weatherup, H. Yang, C. Deranlot, R. Blume, R. Schloegl, A. Fert, A. Anane, S. Hofmann, et al., ACS Nano **6**, 10930 (2012).

[306] V. Heß, Ph.D. thesis, Universität zu Köln (2016).

[307] S. M. Barlow and R. Raval, Surface Science Reports **50**, 201 (2003).

[308] Volkmar Heß, private communication.

[309] E. I. Rashba, Soviet Physics-Solid State **2**, 1109 (1960).

[310] Y. Bychkov and E. I. Rashba, Journal of Experimental and Theoretical Physics Letters **39**, 78 (1984).

[311] Y. A. Bychkov and E. I. Rashba, Journal of Physics C: Solid State Physics **17**, 6039 (1984).

[312] M. Heide, G. Bihlmayer, P. Mavropoulos, A. Bringer, and S. Blügel, Newsletter of the Psi-k Network **78** (2006), URL `www.psi-k.org/newsletters/News_78/Highlight_78.pdf`.

[313] T. Schäpers, J. Knobbe, and V. A. Guzenko, Physical Review B **69**, 235323 (2004).

[314] G. Bihlmayer, S. Blügel, and E. V. Chulkov, Physical Review B **75**, 195414 (2007).

[315] C. R. Ast, J. Henk, A. Ernst, L. Moreschini, M. C. Falub, D. Pacile, P. Bruno, K. Kern, and M. Grioni, Physical Review Letters **98**, 186807 (2007).

[316] G. Bihlmayer, Y. M. Koroteev, P. M. Echenique, E. V. Chulkov, and S. Blügel, Surface Science **600**, 3888 (2006).

[317] S. LaShell, B. A. McDougall, and E. Jensen, Physical Review Letters **77**, 3419 (1996).

[318] Y. M. Koroteev, G. Bihlmayer, J. E. Gayone, E. V. Chulkov, S. Blügel, P. M. Echenique, and P. Hofmann, Physical Review Letters **93**, 046403 (2004).

[319] O. Krupin, G. Bihlmayer, K. Starke, S. Gorovikov, J. E. Prieto, K. Döbrich, S. Blügel, and G. Kaindl, Physical Review B **71**, 201403 (2005).

[320] D. Pacile, C. R. Ast, M. Papagno, C. Da Silva, L. Moreschini, M. Falub, A. P. Seitsonen, and M. Grioni, Physical Review B **73**, 245429 (2006).

[321] C. R. Ast, G. Wittich, P. Wahl, R. Vogelgesang, D. Pacile, M. C. Falub, L. Moreschini, M. Papagno, M. Grioni, and K. Kern, Physical Review B **75**, 201401 (2007).

[322] A. Varykhalov, D. Marchenko, M. R. Scholz, E. D. L. Rienks, T. K. Kim, G. Bihlmayer, J. Sanchez-Barriga, and O. Rader, Physical Review Letters **108**, 066804 (2012).

[323] D. Marchenko, A. Varykhalov, M. R. Scholz, G. Bihlmayer, E. I. Rashba, A. Rybkin, A. M. Shikin, and O. Rader, Nature Communications **3**, 1232 (2012).

[324] M. C. Cottin, J. Lobo-Checa, J. Schaffert, C. A. Bobisch, R. Möller, J. E. Ortega, and A. L. Walter, New Journal of Physics **16**, 045002 (2014).

[325] N. Atodiresei, V. Caciuc, J.-H. Franke, and S. Blügel, Physical Review B **78**, 045411 (2008).

[326] J. Premper, M. Trautmann, J. Henk, and P. Bruno, Physical Review B **76**, 073310 (2007).

[327] K. H. L. Zhang, I. M. McLeod, M. Lahti, K. Pussi, and V. R. Dhanak, Journal of Physics: Condensed Matter **24**, 435502 (2012).

[328] Gregor Mussler, private communication.

[329] Markus Eschbach, private communication.

[330] G. Kresse and J. Hafner, Physical Review B **49**, 14251 (1994).

[331] G. Kresse and J. Furthmüller, Physical Review B **54**, 11169 (1996).

[332] G. Kresse and J. Furthmüller, Computational Materials Science **6**, 15 (1996).

[333] G. Kresse, M. Marsman, and J. Furthmüller, VASP the GUIDE (2014).

[334] H. Ebert and R. Zeller, SPR-TB-KKR package, URL `http://olymp.cup.uni-muenchen.de/ak/ebert/SPR-TB-KKR`.

[335] K. Momma and F. Izumi, Journal of Applied Crystallography **44**, 1272 (2011).

[336] J. Neugebauer and M. Scheffler, Physical Review B **46**, 16067 (1992).

[337] G. Makov and M. C. Payne, Physical Review B **51**, 4014 (1995).

[338] J. P. Perdew and Y. Wang, Physical Review B **45**, 13244 (1992).

[339] V. A. d. l. P. O'Shea, I. d. P. R. Moreira, A. Roldan, and F. Illas, The Journal of Chemical Physics **133**, 024701 (2010).

[340] V. I. Anisimov, J. Zaanen, and O. K. Andersen, Physical Review B **44**, 943 (1991).

[341] S. L. Dudarev, G. A. Botton, S. Y. Savrasov, C. J. Humphreys, and A. P. Sutton, Physical Review B **57**, 1505 (1998).

[342] Nicolae Atodiresei, private communication.

[343] D. Eom, D. Prezzi, K. T. Rim, H. Zhou, M. Lefenfeld, S. Xiao, C. Nuckolls, M. S. Hybertsen, T. F. Heinz, and G. W. Flynn, Nano Letters **9**, 2844 (2009).

[344] D. Prezzi, D. Eom, K. T. Rim, H. Zhou, S. Xiao, C. Nuckolls, T. F. Heinz, G. W. Flynn, and M. S. Hybertsen, ACS Nano **8**, 5765 (2014).

[345] M. B. Stearns, *3d, 4d and 5d Elements, Alloys and Compounds*, Landolt-Börnstein, New Series, Group III, Vol. 19, Pt. A (Springer, Berlin, Heidelberg, 1986).

[346] M. Pozzo, D. Alfe, P. Lacovig, P. Hofmann, S. Lizzit, and A. Baraldi, Physical Review Letters **106**, 135501 (2011).

[347] R. S. Pease, Acta Crystallographica **5**, 356 (1952).

[348] K.-A. N. Duerloo, M. T. Ong, and E. J. Reed, The Journal of Physical Chemistry Letters **3**, 2871 (2012).

[349] K. Jakobi, *Electronic and Vibrational Properties*, Landolt-Börnstein, New Series, Group III, Vol. 24, Pt. B (Springer, Berlin, Heidelberg, 1994).

Publications

Parts of this thesis and results from this thesis have already been published, are submitted for publication or a manuscript to be published is currently in preparation. The status of each article is indicated.

1. R. Friedrich, V. Caciuc, N. S. Kiselev, N. Atodiresei, and S. Blügel,
   'Chemically functionalized magnetic exchange interactions of hybrid organic-ferromagnetic metal interfaces',
   Physical Review B **91**, 115432 (2015).

2. R. Friedrich, V. Caciuc, N. Atodiresei, and S. Blügel,
   'Molecular induced skyhook effect for magnetic interlayer softening',
   Physical Review B **92**, 195407 (2015).

3. R. Friedrich, V. Caciuc, N. Atodiresei, and S. Blügel,
   'Exchange interactions of magnetic surfaces below two-dimensional materials',
   Physical Review B Rapid Communication **93**, 220406(R) (2016).

4. V. Heß, R. Friedrich, F. Matthes, V. Caciuc, N. Atodiresei, D. E. Bürgler, S. Blügel, and C. M. Schneider,
   'Magnetic subunits within a single molecule-surface hybrid',
   submitted manuscript.

5. R. Friedrich, V. Caciuc, G. Bihlmayer, N. Atodiresei, and S. Blügel,
   manuscript in preparation.

6. R. Friedrich, V. Caciuc, G. Bihlmayer, N. Atodiresei, and S. Blügel,
   manuscript in preparation.

Acknowledgment

I would like to deeply thank Prof. Dr. Stefan Blügel for giving me the unique opportunity to carry out my PhD in his group under his personal guidance of exceptional quality. It was really a great experience to work together with the world leading scientists from his group in the Peter Grünberg Institut and the Institute for Advanced simulation whose research achieves high international recognition.

A particular thanks deserves Dr. Nicolae Atodiresei for his continuous support and countless stimulating discussions about research projects, ideas and how to develop new concepts. I really profited a lot from his experience. I would also like to express my particular gratitude to Dr. Vasile Caciuc who always had an open door and the patience to discuss with me especially about the details of certain problems.

Moreover I appreciate many fruitful discussions with Dr. Phivos Mavropoulos, Dr. Gustav Bihlmayer, Dr. Hoang Long Nguyen, Dr. Nikolai S. Kiselev, Dr. Daniel Wortmann, Dr. Paul Baumeister, Dr. Shigeru Tsukamoto and Dr. Andrea Nobile who greatly helped me in understanding several things related to computing, electronic structure methods and gaining physical understanding on various phenomena.

I also would like to thank Dr. Volkmar Heß, Dr. Daniel Bürgler, Dr. Frank Matthes and Taner Esat for the conversations on STM results and organic-ferromagnetic interfaces.

A special thanks also goes to my long-term offices mates Dr. Martin Callsen, Johannes Kirchmair and especially Mathias Müller for the plenty scientific but also the more informal discussions we had. Particularly you, Mathias, helped me a lot over all the years to always keep up my motivation at the highest level.

I also would like to mention that I greatly enjoyed my lunch breaks with Dr. Nicolae Atodiresei, Dr. Vasile Caciuc, Dr. Konstantin Rushchanskii, Dr. Ivetta Slipukhina, Dr. Shigeru Tsukamoto and Dr. Martin Callsen.

At this point I would like to thank all members of the institute and in particular Ute Winkler for the nice time and friendly atmosphere over my PhD. Moreover I also want to acknowledge the continuous support from the members of the in-house IT over all the years and the computing time at the JUROPA, JURECA and JUQUEEN supercomputers provided by the Jülich Supercomputing Centre.

I would like to thank Prof. Dr. Jens Kortus for having agreed to be the second referee of this thesis.

Abschließend möchte ich meinen Eltern sowie meinen Großeltern für ihre unermessliche, immer liebevolle und fortwährende Unsterstützung während meines gesamten Lebens und im Besonderen während meiner Ausbildung danken. Ich bin überzeugt, dass ich ohne Euch nie so weit gekommen wäre.

Band / Volume 125
Nanocavity Arrays for Extracellular Recording and Stimulation of Electroactive Cell Systems
A. Czeschik (2016), x, 162 pp
ISBN: 978-3-95806-144-6

Band / Volume 126
Band Structure Engineering in 3D Topological Insulators Investigated by Angle-Resolved Photoemission Spectroscopy
M. Eschbach (2016), VIII, 153 pp
ISBN: 978-3-95806-149-1

Band / Volume 127
Dynamics in colloid and protein systems: Hydrodynamically structured particles, and dispersions with competing attractive and repulsive interactions
J. Riest (2016), ix, 226 pp
ISBN: 978-3-95806-153-8

Band / Volume 128
Self-purifying $La_{2/3}Sr_{1/3}MnO_3$ epitaxial films: Observation of surface precipitation of Mn_3O_4 particles for excess Mn ratios
A. Steffen (2016), 154 pp
ISBN: 978-3-95806-162-0

Band / Volume 129
Strain and electric field mediated manipulation of magnetism in $La_{(1-x)}Sr_xMnO_3/BaTiO_3$ heterostructures
M. Schmitz (2016), VI, 141 pp
ISBN: 978-3-95806-164-4

Band / Volume 130
High-Throughput Live-Cell Imaging for Investigations of Cellular Heterogeneity in *Corynebacterium glutamicum*
S. Helfrich (2016), xvi, 217 pp
ISBN: 978-3-95806-167-5

Band / Volume 131
Laser-Induced Ultrafast Electron- and Spin-Dynamics in the Electronic Band Structure of Co(001)
M. A. Plötzing (2016), ii, 109, XXXIV pp
ISBN: 978-3-95806-168-2

Band / Volume 132
Robot-Assisted Phenotyping of Genome-Reduced *Corynebacterium glutamicum* Strain Libraries to Draft a Chassis Organism
S. Unthan (2016), 122 pp
ISBN: 978-3-95806-169-9

Band / Volume 133
Characterization of amino acid ammonia lyases & aminomutases for the production of chiral α- and β-amino acids
A. Dreßen (2016), ix, 112 pp
ISBN: 978-3-95806-176-7

Band/Volume 134
7th Georgian-German School and Workshop in Basic Science
Kacharava, A. (Ed.) erscheint nur als CD (2016)
ISBN 978-3-95806-179-8

Band / Volume 135
Crystal growth and scattering studies on two ferrites
S. Adiga (2016), iv, 150 pp
ISBN: 978-3-95806-183-5

Band / Volume 136
Manipulating the Structural and Electronic Properties of Epitaxial $NaNbO_3$ Films via Strain and Stoichiometry
B. Cai (2016), VI, 114 pp
ISBN: 978-3-95806-185-9

Band / Volume 137
Surface Potential of Metallic Surfaces and Self-Assembling Organic Monolayers in Various Electrolytes
J. Wang (2016), ii, 58 pp
ISBN: 978-3-95806-188-0

Band / Volume 138
Ab initio investigation of hybrid molecular-metallic interfaces as a tool to design surface magnetic properties for molecular spintronics
R. Friedrich (2016), 277 pp
ISBN: 978-3-95806-194-1

Weitere ***Schriften des Verlags im Forschungszentrum Jülich*** unter
http://wwwzb1.fz-juelich.de/verlagextern1/index.asp

Schlüsseltechnologien /
Key Technologies
Band / Volume 138
ISBN 978-3-95806-194-1